The impact of melt supply on fault distribution, volcanism, and the thermal regime at slow spreading ridges

Jie Chen

▶ To cite this version:

Jie Chen. The impact of melt supply on fault distribution, volcanism, and the thermal regime at slow spreading ridges. Geophysics [physics.geo-ph]. Université Paris Cité, 2021. English. NNT : 2021UNIP7226 . tel-04004048

HAL Id: tel-04004048
https://theses.hal.science/tel-04004048v1

Submitted on 24 Feb 2023

Université de Paris
Institut de physique du globe de Paris

École doctorale Sciences de la Terre et de l’environnement et physique de l’Univers STEP’UP n°560

Laboratoire de Géosciences Marines

The impact of melt supply on fault distribution, volcanism, and the thermal regime at slow spreading ridges

Par **Jie CHEN**

Thèse de doctorat de Sciences de la Terre et de l’environnement
Dirigée par **Mathilde CANNAT**

présentée et soutenue publiquement le **8 décembre 2021**

Devant jury composé de:

Roger BUCK: Professeur (LDEO, Columbia University, USA)	Rapporteur
Lydéric FRANCE: Professeur associé (CRPG, Université de Lorraine, France)	Rapporteur
Satish SINGH Directeur de recherche (IPGP, Université de Paris, France)	Examinateur
Suzanne CARBOTTE Professeure (LDEO, Columbia University, USA)	Examinatrice
Mireille LAIGLE Directrice de recherche (GEOAZUR, France)	Examinatrice
Javier ESCARTIN Directeur de recherche (ENS, Université PSL, France)	Examinateur
Wayne CRAWFORD Directrice de recherche (IPGP, Université de Paris, France)	Invité
Jean-Arthur OLIVE Chargé de recherche (ENS, Université PSL, France)	Invité
Mathilde CANNAT Directrice de recherche (IPGP, Université de Paris, France)	Directrice de thèse

Acknowledgments

First and sincerely, I would like to thank my Ph.D. advisor, Mathilde Cannat, for her help and encouragement during the last three years, and for her thorough reviews and corrections of numerous drafts of this thesis. I also thank her for her constructive (and critical) guidance that always inspires me to broaden the scope of the work, make it in geological sense, and look for the philosophy in my work. I couldn't have asked for a better advisor.

I extend my gratitude to Chunhui Tao for allowing me to use the AUV data in Chapter 3, to Daniel Sauter and Marc Munschy for helping me to process and interpret magnetic data in Chapter 3, to Wayne Crawford for guiding me to process the earthquake in Chapter 4, and to Jean-Arthur Olive for his support with numerical thermal modelling in Chapter 5.

I thank Raphael Grandin and Daniel Sauter for giving me useful feedback in my annual thesis committee.

I would like to express my special gratitude to other members of the Cannat family: Ekeabino Momoh, Manon Bickert, Benjamin Wheeler, Souradeep Mahato, and Soumya Bohidar. The stay with you enriched my geological insights and my life in IPGP.

The data used in this thesis were collected thanks to captions, officers, crew, and scientific staff during the DY40 cruise aboard R/V Xiangyanghong-10, the DY34 cruise aboard R/V Dayangyihao, the SEISMOSMOOTH cruise aboard the R/V Marion Dufresne, and the ROVSMOOTH cruise aboard the R/V Pourquoi Pas?

Finally, I wish to express my endless gratitude to my family, who have supported me to stay oversea and explore my interests in geological research. Here I also would like to thank Yuan for her love, friendship, and her constant support and encouragement.

My three years of Ph.D. was funded by the China Scholarship Council. My two AGU conferences were funded by ANR project "Ridge-Factory-Slow".

Résumé

L'impact de l'apport magmatique sur la distribution des failles, du volcanisme et sur le régime thermique des dorsales lentes

Il a été démontré que l'apport de magma au niveau des dorsales lentes varie d’un volume suffisant pour produire une croûte entièrement volcanique, à presque amagmatique, conduisant à l'exposition généralisée de roches mantellique sur les fonds océaniques. Pour mieux comprendre le rôle de l'apport magmatique, j'étudie deux régions de la dorsale sud-ouest Indienne (SWIR) qui sont des cas extrêmes en termes d'apport magmatique : une section située à 50°28’E qui présente une croûte magmatique de 9.5 km d'épaisseur et une anomalie sismique à basse vitesse dans la croûte inférieure (Partie 1), et un couloir quasiamagmatique à 64°30'E (Partie 2) avec des failles de détachement successives à vergence opposée qui accommodent presque toute la divergence des plaques et exhument des roches mantelliques en surface. J'utilise enfin la modélisation numérique 2D pour relier le régime thermique déduit de ces deux cas extrêmes en apport magmatique à la fréquence et à la profondeur des injections de magma (Partie-3).

Dans la partie 1, j'utilise des données de bathymétrie et de réflectivité obtenues par AUV (Autonomous Underwater Vehicle) à une résolution de 2 m pour cartographier les morphologies du fond marin et la distribution des failles. J'utilise également des photographies du fond marin pour cartographier les morphologies de lave au niveau de la SWIR à 50°28'E au cours des derniers 780 milliers d’années. Les résultats de cette approche mettent en évidence des taux d'éruption élevés et une faible contrainte tectonique, proches de ce qui a été observé sur les dorsales intermédiaires et rapides. La cartographie montre que les modes d’accrétion de la croûte supérieure ont varié dans l'espace et dans le temps, probablement en réponse aux variations d’intensité de l’apport magmatique. En particulier, nous proposons que la croûte supérieure de cette section de dorsale lente magmatiquement robuste ait été construite par une alternance de phases croissantes et décroissantes en apport magmatique, sur des cycles d'environ 300 milliers d’années.

Dans la partie 2, je localise des microséismes à l'axe, près de la faille de détachement active sur le corridor presque amagmatique de la SWIR à 64°30'E, qui ont été enregistrés dans cette zone lors de deux courts déploiements de sismomètres. Les résultats suggèrent une lithosphère sismogène d'environ 15 km d'épaisseur. La distribution sismique met en évidence l'activité tectonique de la faille de détachement à pendage sud et de ses petites failles conjuguées à pendage nord dans le toit de la faille. Je documente également un essaim sismique de deux jours, interprété comme étant dû à une migration ponctuelle de magma dans le mur du détachement, déclenchant une séquence de tremblements de terre moins profonds le long du plan de la faille de détachement.

Dans la partie 3, j'utilise la modélisation numérique pour explorer la relation entre le régime thermique axial et les paramètres associés au flux de magma : le volume et la fréquence des injections de magma, ainsi que la profondeur de mise en place du magma. J'ai réussi à prédire les régimes thermiques au niveau de mes deux zones d'études, et j'extrapole ces résultats sur une dorsale ultralente à la variabilité du régime thermique au niveau des dorsales lentes.

Mots-clés : apport magmatique ; dorsale ultra-lente sud-ouest Indienne ; bathymétrie haute résolution ; microsismicité ; modélisation numérique ; dorsales lentes

Abstract

Melt supply at slow spreading ridges has been shown to vary from enough to produce a fully volcanic seafloor, to nearly amagmatic, leading to the widespread exposure of mantle-derived rocks on the seafloor. To better understand the role of melt supply, I study two regions of the ultraslow spreading Southwest Indian Ridge (SWIR) that are endmembers in terms of melt supply: the magmatically-robust SWIR 50°28'E (Part-1 of the thesis) with a 9.5 km-thick crust and a seismic low-velocity anomaly in the lower crust, and a nearly-amagmatic corridor at the SWIR 64°30'E (Part-2) with successive flip-flop detachment faults that accommodate almost 100% of plate divergence and continuously exhume mantle-derived rocks. I finally use 2D numerical modelling to relate the thermal regime inferred from these two endmembers to the frequency and depth of melt injections (Part-3).

In Part-1, I use AUV-based, 2-m resolution bathymetry and backscatter data to map seafloor morphologies and fault distributions and use seafloor photographs to map lava morphologies at the SWIR 50°28'E over the past 780 kyr. The results show evidence of high eruption rates and low tectonic strain, close to what has been observed at intermediate- and fast-spreading ridges. Mapping shows that the modes of upper-crustal construction have varied both in space and time, likely in response to changes in melt supply. Particularly, we propose that the upper crust at this magmatically-robust ridge section was constructed with alternating waxing and waning phases of melt supply over cycles of ~300 kyr.

In Part-2, I locate microearthquakes over the youngest, active detachment fault at the nearly-amagmatic SWIR 64°30'E, as recorded during two short ocean bottom seismometer deployments. The results suggest a ~15 km-thick seismogenic lithosphere. The earthquake distribution highlights the tectonic activity of the south-dipping detachment fault and of its conjugate, small, north-dipping faults in the hanging wall. I also document a two-day seismic swarm interpreted as due to an upward-migrating magmatic event in the footwall, triggering a sequence of shallower earthquakes on the detachment fault plane.

In Part-3, I use numerical modelling to explore the relation between the axial thermal regime and parameters associated with melt flux (the volume and frequency of melt injections) and with the depth of melt emplacement. I successfully predict the thermal regimes at two ultraslow-spreading endmember areas, and I extend these results to the variability of the thermal regime at slow spreading ridges.

Key words: melt supply; ultraslow spreading Southwest Indian Ridge; high-resolution bathymetry; microseismicity; numerical modelling; slow spreading ridges

Résumé Substantiel

Les dorsales médio-océaniques (MOR) sont les principales limites de plaques divergentes sur Terre. Elles forment une chaîne volcanique continue d'une longueur totale d'environ 65 000 km (Searle, 2013). En réponse à la divergence des plaques, le magma se forme dans le manteau asthénosphérique ascendant sous l'axe de la dorsale pour créer une nouvelle lithosphère océanique ; celle-ci devient symétriquement plus âgée, plus froide et plus dense au fur et à mesure qu'elle s'écarte de la zone axiale par divergence des plaques. Le magma joue un double rôle dans la formation de la lithosphère océanique : les intrusions magmatiques répétées accommodent une fraction de la divergence des plaques, et elles modifient également le régime thermique de la dorsale en libérant de la chaleur latente lors de leur refroidissement et de leur cristallisation (Buck et al., 2005 ; Cannat et al., 2019 ; Phipps Morgan et Chen, 1993 ; Theissen-Krah et al., 2011). Bien que l'apport de magma soit principalement sensible au taux d'écartement des plaques (Phipps Morgan et Chen, 1993; Theissen-Krah et al., 2011), il a été démontré que les dorsales lentes et ultralentes (taux d'écartement < 40 mm/an) ont un apport magmatique qui varie de suffisant pour produire un fond marin entièrement volcanique (e.g., Escartín et al., 2014; Sauter et al., 2002; Searle et al., 2010), à presque nul, conduisant à l'exposition généralisée de roches dérivées du manteau sur le fond marin (par exemple, Michael et al., 2003 ; Sauter et al., 2013).

Pour mieux comprendre le rôle de l'apport magmatique au niveau des dorsales lentes et ultralentes, j'étudie deux régions de la dorsale ultralente sud-ouest indienne (SWIR) qui sont des cas extrêmes en termes d'apport magmatique. La première région est une section située à 50°28'E qui présente une croûte magmatique de 9.5 km d'épaisseur et une anomalie sismique à faible vitesse dans la croûte inférieure (Jian et al., 2017a, 2017b ; Li et al., 2015 ; Niu et al., 2015). Cette région est présentée dans la partie 1 de la thèse. La seconde région est un couloir quasi-amagmatique à 64°30'E (présentée en partie 2 de la thèse) avec des failles de détachement successives à vergence opposée qui accommodent presque toute la divergence des plaques et exhument des roches mantelliques en surface (Cannat et al., 2019 ; Momoh et al., 2020 ; Sauter et al., 2013). J'utilise enfin la modélisation numérique 2D, adaptée de l'étude de Fan et al. (2021), pour relier le régime thermique déduit de ces deux régions ultralentes à apport magmatique contrasté à la fréquence et à la profondeur des injections magmatiques, ainsi que pour explorer la variabilité du régime thermique au niveau des dorsales lentes et ultralentes (Partie-3 de la thèse).

Dans la partie 1, j'utilise des données de bathymétrie et de réflectivité haute résolution (2 m) obtenues avec un véhicule sous-marin autonome (AUV) pour cartographier les morphologies du fond marin et la distribution des failles et j'utilise des photographies du fond marin pour cartographier les morphologies de laves à l'axe de la SWIR à 50°28' E, au cours des 780 kyr passés. La zone d'étude présente trois morphologies différentes de fonds marins volcaniques, correspondant à différentes morphologies de lave, qui sont principalement influencées par les taux d'effusion de la lave. Les morphologies de fonds marins dites smooth (lisses) et smooth-hummocky (lisses à bosselées) sont les plus répandues (64% de la zone cartographiée), formant des volcans en dôme, tandis que les laves en coussin à faible taux d'épanchement, correspondent à une morphologie dite "hummocky" (bosselée) du fond marin qui ne représente que 29 % (les 7 % restants sont recouverts de sédiments). La proportion de laves lobées et la déformation tectonique (inférée des à partir des escarpements de failles) sont respectivement de 41 % et < 8 %, proches de ce qui a été observé au niveau des dorsales intermédiaires et rapides.

La morphologie du fond marin le long de l'axe est donc caractérisée par une dominance de fond marin bosselé lisse et lisse dans un domaine d'environ 5 km de long au centre du segment, tandis que le fond marin bosselé prévaut à l'est et à l'ouest, indiquant une diminution substantielle le long de l'axe du taux d'éruption moyen. Les changements de morphologies du fond marin et du rejeu apparent des failles dans la direction d'accrétion (perpendiculaire à l'axe) indiquent deux cycles successifs de construction de la croûte supérieure. Ces cycles durent environ 300 000 ans, et sont interprétés comme des alternances de phases magmatiques croissantes et décroissantes qui résultent vraisemblablement de changements temporels dans la fréquence des réalimentations en magma de la croûte moyenne et inférieure.

Pendant les phases d'approvisionnement en magma croissant, des fréquences de réalimentation plus élevées maintiennent la croûte inférieure à des températures élevées, avec des lentilles magmatiques axiales (AML) relativement peu profondes et à longue durée de vie et une zone de mush dans la croûte inférieure, constituée de crystaux et de quelques % de magma. Des dykes localisés alimentent des éruptions à taux d'éruption élevé, formant des coulées de lave lisses et des volcans en dôme qui recouvrent de vastes zones du fond marin, avec peu ou pas de failles. Pendant les phases d'approvisionnement en magma décroissant, des fréquences de réalimentation plus faibles conduisent à des lentilles magmatiques axiales

(AML) plus profondes et à durée de vie plus courte, avec des zones de mush réduites dans la croûte inférieure, une lithosphère fragile plus épaisse et un domaine hydrothermal plus variable et généralement plus épais. La construction de la croûte supérieure se produit alors dans une zone plus large d'injection de filons, avec plus de failles, et des coulées de lave principalement bosselées. Je propose donc que les modes de construction de la croûte supérieure et les systèmes de plomberie magmatique dans la croûte myenne et inférieure des dorsales lentes et ultra-lentes sont contrôlés par les variations spatiales et temporelles de l'apport de magma plus que par le seul taux d'expansion de la dorsale.

Dans la partie 2, je présente des données de microsismicité acquises à partir de deux déploiements différents de sismomètres de fond de mer (8 jours pour le catalogue SMSMO et 19 jours pour le catalogue RVSMO) sur la faille de détachement « flip-flop » la plus jeune et active du segment SWIR presque amagmatique à 64°30'E. Je localise 309 microséismes et résous 8 mécanismes focaux, à l'aide d'un modèle de vitesse 1D extrait d'une expérience de sismique réfraction dans la même zone d'étude (Momoh et al., 2017). Les résultats montrent que la lithosphère sismogène a une épaisseur d'au moins 15 km, plus mince qu'à la faille du détachement du SWIR Dragon Flag (18 km d'épaisseur ; Yu et al., 2018) avec le même taux de propagation mais dans un contexte plus magmatique. Ceci est surprenant, parce que l'épaisseur de la lithosphère sismogénique et censé augmenter à mesure que le taux d'étalement diminue (Phipps Morgan et Chen, 1993) et/ou que l'apport de matière fondue diminue (Fan et al., 2021). Ce résultat indique qu'il faut affiner les modèles actuels sur la façon dont le taux d'étalement et l'apport de magma contrôlent le régime thermique des dorsales médio-océaniques.

Les microséismes avec des mécanismes focaux normaux sont colocalisés avec des zones de dommages de la faille de détachement et de failles conjuguées à faible décalage dans l'éponte supérieure, imagées par la sismique active. Cela confirme ces précédentes interprétations tectoniques, y compris les failles normales actives dans l'éponte supérieure du détachement, non observées dans les détachements plus magmatiques du SWIR ou de la dorsale médio-atlantique (par exemple, de Martin et al., 2007 ; Grevemeyer et al., 2013 ; Parnell-Turner et al., 2020, 2017 ; Tao et al., 2020 ; Yu et al., 2018). Je documente également un essaim sismique durant deux jours que j'interpréte comme étant dû à une intrusion de magma ascendante dans le mur du détachement (6-11 km), potentiellement déclenchant une séquence de tremblements de terre tectoniques moins profonds (~1,5 km) dans le plan de faille du détachement. Cela indique un lien possible entre le magmatisme épars et la défaillance tectonique au niveau des crêtes d'étalement ultra-lentes à faible fusion.

Dans la troisième partie, j'utilise un modèle numérique thermique à deux dimensions, couplant convection hydrothermale et intrusions magmatiques répétées (Fan et al., 2021), afin de tester plusieurs hypothèses formulées à partir d'observations géologiques aux dorsales lentes et ultralentes : (1) L'apport magmatique façonne substantiellement le régime thermique de la lithosphère en apportant chaleur spécifique de refroidissement et chaleur de cristallisation. (2) Le magma peut être mis en place à une large gamme de profondeurs, plus ou moins accessibles à un refroidissement hydrothermal efficace (Cannat et al., 2019, 1995). (3) Les temps de récurrence caractéristiques de l'apport magmatique peuvent varier le long de l'axe de la dorsale et en fonction du temps (par exemple, Chen et al., 2021 ; Klischies et al., 2019).

Je commence par caractériser et modéliser les régimes thermiques correspondants à deux cas extrêmes d'alimentation magmatique observés le long de la dorsale ultralente sud-ouest indienne (SWIR) : le segment 50°28'E, le plus robuste du point de vue magmatique, et le segment 64°30'E, presque amagmatique. Je fais varier systématiquement les paramètres associés à l'apport de magma (la fréquence et la profondeur des intrusions) et à la circulation hydrothermale (la profondeur maximale et la perméabilité du domaine hydrothermal) pour explorer la sensibilité du régime thermique de l'axe de la dorsales entre ces deux cas extrêmes.

Au premier ordre, des fréquences plus élevées d'intrusion magmatique produisent des régimes thermiques plus chauds. Cependant, pour une fréquence d'intrusion donnée, les intrusions moins profondes conduisent à une structure thermique plus froide dans les premiers kilomètres sous le plancher océanique, car elles donnent lieu à une circulation hydrothermale plus vigoureuse. Ce type d'effet peut permettre d'expliquer la forte épaisseur de la couche sismogénique dans la région dite "Dragon Flag" de la SWIR, qui reçoit pourtant un fort apport magmatique. En revanche, des intrusions de magma plus profondes favorisent un régime plus chaud et sont une condition nécessaire à la formation de zones partiellement fondues (mush) persistantes dans la croûte océanique inférieure. Par ailleurs, augmenter la perméabilité et la profondeur maximale du domaine hydrothermal entraîne une augmentation de l'efficacité de l'extraction de la chaleur, décalant vers le bas les profondeurs de la transition cassant-ductile et des zones de mush. Je modélise enfin l'effet de changements cycliques de l'alimentation en magma, alternant entre des phases de croissance et de décroissance, comme le suggèrent des observations géologiques au segment 50°28'E de la SWIR (partie 1). Ces simulations produisent une oscillation du régime thermique (par exemple, des variations cycliques des profondeurs de la transition cassant-ductile et de la zone de mush, ainsi que des températures des évents hydrothermaux. Ces modèles établissent des liens nouveaux entre les processus d'accrétion de la croûte océanique inférieure et l'état thermo-mécanique des dorsales lentes et ultra-lentes.

长风破浪会有时，直挂云帆济沧海。

Someday, with my sail piercing the clouds, I will mount the wind, break the waves, and traverse the vast, rolling sea.

Li Bai in 744 A.D.

Contents

List of Figures

List of Tables

List of Abbreviations

AAR	American-Antarctic Ridge
AML	Axial Melt Lense
AR	Arctic Ridge
AST	Axial Summit Trough
AUV	Autonomous Underwater Vehicle
AVR	Axial Volcanic Ridge
B-M	Brunhes-Matuyama
bsf	below seafloor
bsl	below sea level
BTJ	Bouvet Triple Junction
BDT	Brittle-Ductile Transition
CaR	Carlsberg Ridge
CBL	Conductive Boundary Layer
ChR	Chile Ridge
CIR	Central Indian Ridge
EPR	East Pacific Rise
ESR	Effective Spreading Rate
FAA	Free Air Gravity Anomaly
GSC	Galapagos Spreading Center
HF	Hydrothermal Field
HR	High-Resolution
HRBSSS	High-Resolution Bathymetric Sidescan Sonar System
IGRF	International Geomagnetic Reference Field
LVA	Low-Velocity Anomaly
MAR	Mid-Atlantic Ridge
MBA	Mantle Bouguer Anomaly
MCSC	Mid-Cayman Spreading Center
MOR	Mid-Ocean Ridge
NTD	Non-Transform Discontinuity
OBS	Ocean Bottom Seismometer

OSC	Overlapping Spreading Center
PAR	Pacific-Antarctic Rise
RMBA	Residual Mantle Bouguer Anomaly
RTJ	Rodriguez Triple Junction
RTP	Reduction-To-Pole
SMS	Smooth Seafloor
SWIR	Southwest Indian Ridge
SEIR	Southeast Indian Ridge
Ts	Tectonic strain
TF	Transform Fault
USBL	UltraShort BaseLine

Introduction

The Mid-Ocean ridges (MORs) are first-order components of the Earth's system with a volcanic chain extending to 65 000 km. As plates separate at the MORs, oceanic lithosphere is created by upwelling melt from the mantle, covering more than 60% of the Earth's surface. Melt supply at the MORs, expressed here as the melt flux (the volume of melt upwelling from the mantle to the crust per unit time), is a key control on lithosphere formation: when melt is injected into the lithosphere, it crystallizes to fill the gap due to plate divergence and meanwhile modifies the thermal regime (Buck et al., 2005; Cannat et al., 2019b). Although melt supply is most sensitive to spreading rates (faster spreading ridges generally corresponding to a higher melt supply), it can be regionally and locally decoupled at slow and ultraslow spreading ridges (full spreading rate of <40 mm/yr) (Cannat et al., 2008; Lin et al., 1990).

With the investigations of seismic experiments over the last three decades, the average magmatic crustal thickness, i.e., the overall amount of melt forming the crust per unit width of plate spreading, is ~6 km at all spreading rates (Chen, 1992; Christeson et al., 2019). However, at slow and ultraslow spreading ridges, melt supply is highly variable and even disappears at some ridge sections, resulting in a larger variability of crustal thickness than faster spreading ridges (Chen, 1992; Christeson et al., 2019; Momoh et al., 2017). Slow spreading ridges, therefore, are natural laboratories for exploring the impact of melt supply on faulting, volcanism, and the thermal regime, independent of spreading rate.

At the ultraslow spreading Southwest Indian Ridge (SWIR; full spreading rate of ~14 mm/yr), the magmatic crust has been shown to vary between two endmembers in terms of melt supply: a magmatically-robust endmember at the SWIR 50°28'E (Jian et al., 2017a; Mendel et al., 2003) and a nearly-amagmatic endmember at the SWIR 64°30'E (Cannat et al., 2006; Momoh et al., 2017; Sauter et al., 2013). At the magmatically-robust SWIR 50°28'E, the crust is at 9.5 km-thick with a lower-crustal mush zone and numerous volcanic constructs on the seafloor (Jian et al., 2017a; Mendel et al., 2003). At the nearly-amagmatic SWIR 64°30'E, successive flip-flop detachment faults accommodate almost 100% of plate divergence and exhume mantle-derived peridotites on the seafloor with only patches of basalts (Cannat et al., 2019b; Momoh et al., 2020, 2017; Sauter et al., 2013).

In this thesis, I study these two endmembers from multiple aspects to unravel the nature and influence of the melt supply at slow spreading ridges.

I study the magmatically-robust endmember at the SWIR 50°28'E, first using AUV-based high-resolution bathymetry and backscatter, near-bottom magnetic data, and visual observations to infer spatial and temporal variations in melt supply over the past 780 kyr and the impact of melt supply on volcanic upper-crustal construction. I study the nearly-amagmatic endmember at the SWIR 64°30'E, using ocean bottom seismometer (OBS) data over the youngest, active detachment fault to reveal its tectonic activities and provide a proxy for the thermal regime. I finally use 2D numerical modelling to constrain the thermal regimes inferred from these two endmembers, and then explore the variability of the thermal regimes at slow and ultraslow spreading ridges associated with parameters of melt supply (the frequency and depth of melt injections) and hydrothermal convection.

Thesis organization

This thesis comprises six chapters.

In chapter 1, I start introducing the state-of-art understanding and the key concepts of the global Mid-Ocean Ridge system and why I'm interested in this system. This chapter emphasizes the role of melt supply in axial morphology, ridge segmentation, lithosphere composition, faulting style, volcanism, hydrothermal circulation, and the thermal regimes, which forms the basis of the notions used in Chapters 3-5.

In chapter 2, I introduce the geological background of the SWIR, and then narrow to two endmembers in terms of melt supply: the magmatically-robust SWIR 50°28'E and the nearly-amagmatic SWIR 64°30'E.

In chapter 3, I focus on the magmatically-robust endmember at the SWIR 50°28'E segment, first using high-resolution bathymetry and backscatter data, near-bottom magnetic data, and seafloor photographs. This chapter was published as: Chen, J., Cannat, M., Tao, C., Sauter, D. & Munschy, M. (2021). *780 thousand years of upper-crustal construction at a melt-rich segment of the ultraslow spreading Southwest Indian Ridge 50°28'E*. Journal of Geophysical Research: Solid Earth (doi: 10.1029/2021JB022152). I carried out all the geological interpretations and mapping, produced all figures, and wrote the manuscript, under the supervision of Mathilde Cannat. Chunhui Tao led the data acquisition and bathymetry data processing. Daniel Sauter and Marc Munschy processed near-bottom magnetic data.

In chapter 4, I focus on microseismicity recorded during two short OBS deployments, over the youngest active detachment fault at the nearly-amagmatic SWIR 64°30'E. This chapter has been submitted to Nature Communications with a title of *Microseismicity and lithosphere thickness at a nearly amagmatic mid-ocean ridge*. I carried out all the data processing, produced all figures, and wrote the manuscript, under the supervision of Wayne Crawford and Mathilde Cannat.

In chapter 5, I focus on 2D numerical thermal modelling, modified from Fan et al. (2021). This chapter has been submitted to Journal of Geophysical Research: Solid Earth with a title of *Thermal regime of slow and ultraslow spreading ridges controlled by melt supply and modes of emplacement*. I carried out all the numerical simulations, produced all figures, and wrote the manuscript, under the supervision of Jean-Arthur Olive and Mathilde Cannat.

In chapter 6, I wrap up new findings of the understanding of volcanic eruptions, faulting, and the thermal regime associated with melt supply at ultraslow spreading mid-ocean ridge, followed by future perspectives based on the work done in this thesis.

Chapter 1

The Global Mid-Ocean Ridge System

In this chapter, I start introducing the state-of-art understanding and the key concepts of the global Mid-Ocean Ridge system and why I'm interested in this system. This chapter emphasizes the role of melt supply in axial morphology, ridge segmentation, lithosphere composition, faulting style, volcanism, hydrothermal circulation, and the thermal regimes, which forms the basis of the notions used in Chapters 3-5.

1.1 Mid-ocean ridge system

The global Mid-Ocean Ridge (MOR) system is one of the Earth's principal plate divergent boundaries. In response to plate divergence, magma forms in the upwelling mantle beneath the axis of the MOR to create new oceanic lithospheric plates that symmetrically become older, cooler, and denser (Figure 1.1). As this theory of seafloor spreading was first proposed by Hess (1962) and confirmed by oceanographic investigation over the last six decades, the global MOR has a total length of about 65,000 km (Figure 1.1a), which is marked by teleseismic earthquakes that reflect rifting episodes and magma intrusions (Figure 1.1b).

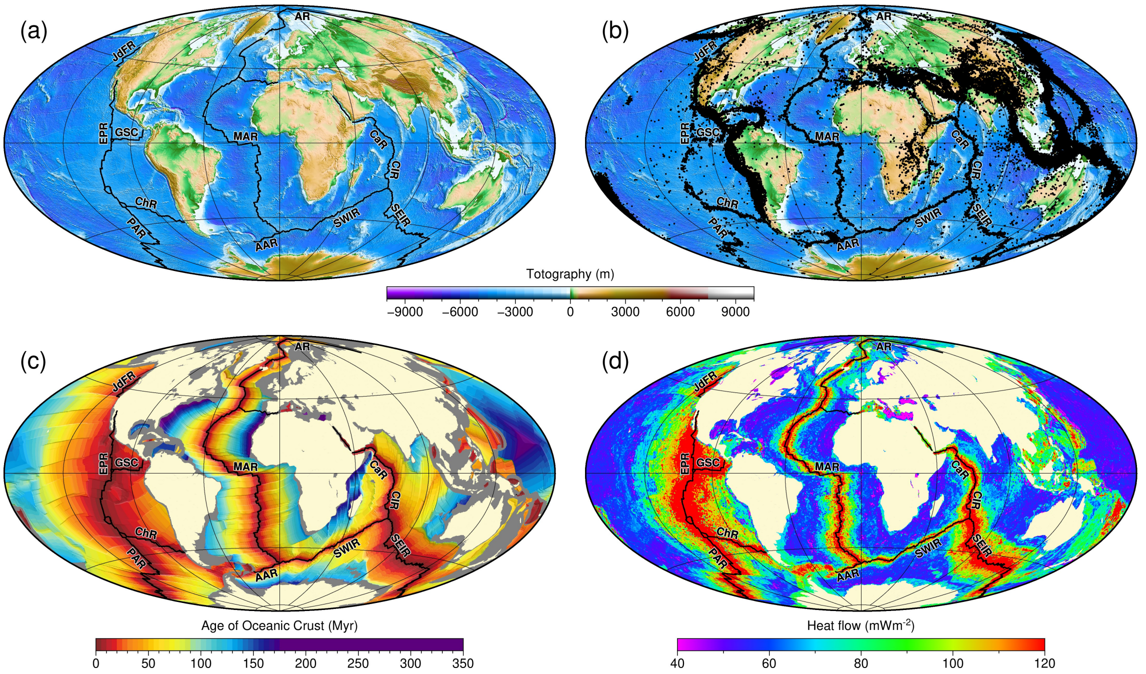

Figure 1.1. The global Mid-Ocean Ridge system

(a) Topography, (b) teleseismic earthquakes (Mb>4), (c) age of oceanic crust, and (d) heat flow. Datasets are from multiple sources: topography (Weatherall et al., 2015), teleseismic earthquakes (USGS, https://earthquake.usgs.gov/), crustal age (Seton et al., 2020), heat flow (Lucazeau, 2019), and the digital MOR locations (Coffin et al., 1997). AAR: American-Antarctic Ridge, AR: Arctic Ridge, CaR: Carlsberg Ridge, ChR: Chile Ridge, CIR: Central Indian Ridge, EPR: East Pacific Rise, GSC: Galapagos Spreading Center, MAR: Mid-Atlantic Ridge, PAR: Pacific-Antarctic Rise, SEIR: Southeast Indian Ridge, SWIR: Southwest Indian Ridge, JdFR: Juan de Fuca Ridge. Figure from Chen (2021a) at figshare.

Spreading rate is the primary control of seafloor spreading morphology, varying from the fastest up to 185 mm/yr at the East Pacific Rise (EPR) to the slowest down to nearly 0 mm/yr at the Gakkel Ridge (DeMets et al., 1994; Seton et al., 2020). The MOR can be generally classified into four types: fast spreading ridges (>80 mm/yr, e.g., East Pacific Rise), intermediate spreading ridges (40-80 mm/yr, e.g., Galapagos Spreading Center), slow spreading ridges (20-40 mm/yr, e.g., Mid-Atlantic Ridge), and ultraslow spreading ridges (<20 mm/yr, e.g., Southwest Indian Ridge) (Dick et al., 2003).

1.1.1 Axial morphology

Axial seafloor morphology is highly variable at different spreading rates, reflecting different faulting deformation (Chapter 1.2) and volcanic eruption styles (Chapter 1.3) (Buck et al., 2005; Cannat et al., 2006; Head et al., 1996; Macdonald, 1982; Perfit and Chadwick, 1998; Small, 1998).

Fast spreading ridges are characterized by axial highs, a few hundred meters high and a few kilometers wide (Figure 1.2a). Their crests typically have small linear grabens, i.e., axial summit troughs (ASTs), which are less than 500-m wide and 50-m deep (Fornari et al., 1998; Soule et al., 2009). Faults are small with throws of 10-20 m, and both inward- and outward-facing faults are observed, forming ridge-parallel horsts and graben (Bohnenstiehl and Carbotte, 2001; Cowie et al., 1993; Escartín et al., 2007).

Slow and ultraslow spreading ridges are characterized by a central median valley 1-3 km in depth and tens of kilometers in width (Figure 1.2c). The walls of the axial valley are usually two large, conjugate normal faults with throws of hundreds of meters or more, resulting in large ridge-parallel abyssal hills. Detachment faults (Chapter 1.2.2) are sometimes seen on one side of the axial valley (Figure 1.2c) (Cann et al., 1997; Escartín et al., 2008; MacLeod et al., 2009; Smith et al., 2006). Volcanic activity mainly takes place within the axial valley to form an axial volcanic ridge (AVR) (Mendel et al., 2003; Parson et al., 1993; Searle et al., 2010) or a dome-shaped central volcano (Escartín et al., 2014). The axial morphology of intermediate spreading ridges is intermediate between that of fast and slow spreading ridges (Figure 1.2b) (Perfit and Chadwick, 1998), depending on local melt supply (Colman et al., 2012; McClinton and White, 2015; Sinton et al., 2003).

1.1.2 Ridge segmentation

The axis of MOR is commonly segmented by first- to fourth-orders of discontinuities defined by transform faults (TFs), overlapping spreading centers (OSCs), and non-transform discontinuities (NTDs), with significant axial variations in seafloor morphology (Figure 1.3), reflecting spatial and temporal variations in magmatic and tectonic processes (Carbotte et al., 2015; Macdonald et al., 1991, 1988).

The most significant first-order segments are bounded by TFs, displaying a deep valley and off-axis fracture zones that are parallel to the spreading direction. The TFs could persist for >100 Ma and offset the ridge axis by up to hundreds of kilometers, e.g., the longest Romanche TF at the MAR. This type of discontinuity often plays a role as a boundary of magmatism, somtimes resulting in contrasting crustal thickness on both sides, e.g., the Gallieni and Andrew Bain TFs at the SWIR (Sauter et al., 2001; Takeuchi et al., 2010).

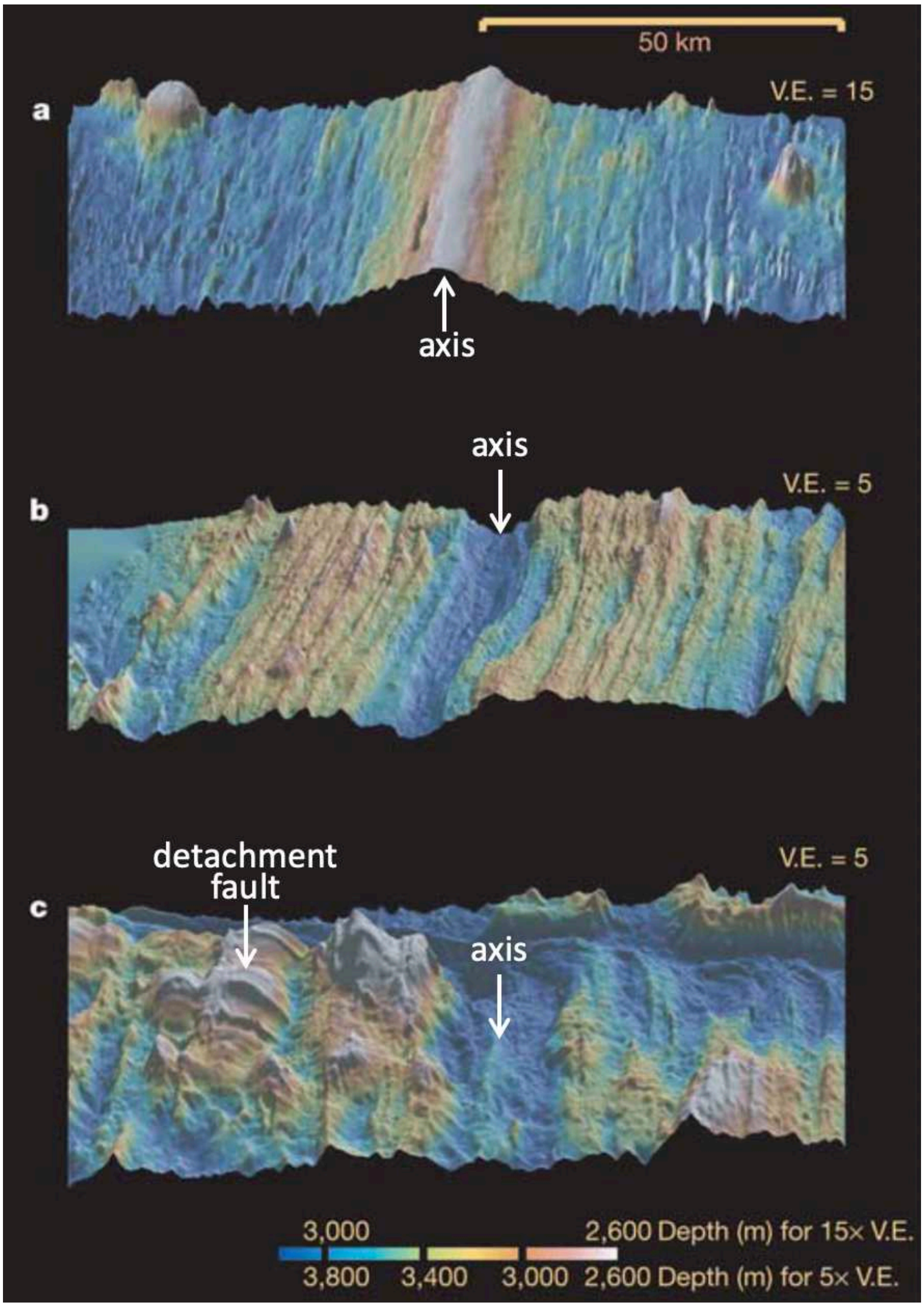

Figure 1.2. Contrasting axial morphology at fast, intermediate, and slow spreading ridges.

After Buck et al. (2005). (a) Axial high at 9°37'N of fast-spreading EPR (V.E.=15). (b) Axial valley and ridge-parallel abyssal hills at 115°E of intermediate-spreading SEIR (V.E.=5). (c) Axial valley at 23°25'N of slow-spreading MAR (V.E.=5). An axial volcanic ridge is located on axis. Ridge-parallel abyssal hills are on the right, and the detachment fault is on the left.

Second-order discontinuities offset the ridge axis by <30 km, including OSCs at fast spreading ridges and melt-rich intermediate spreading ridge sections, e.g., EPR 9°N (Carbotte and Macdonald, 1992), and NTDs at slow and ultraslow spreading ridges as well as melt-poor intermediate spreading ridges, e.g., MAR 24-31°N (Sempéré et al., 1990). OSCs are characterized by overlapping ridges enclosing a basin, while the NTDs are characterized by a nodal basin within the axial valley (Carbotte et al., 2015). OSCs and NTDs can persist for <10s Ma, and their off-axis traces may form V-shaped zones that are distinct from adjacent seafloor (Macdonald et al., 1991; Sempéré et al., 1993). At ultraslow spreading ridges, the NTDs can be defined by nearly avolcanic domains with a high obliquity (up to >50°) to the normal spreading, e.g., the SWIR 54-57°E (Sauter et al., 2001).

Second-order segments are considered as magmatic spreading cells (Figure 1.4) (Lin et al., 1990; Schouten et al., 1985; Schouten and Klitgord, 1982). Each spreading cell is an independent and long-lived unit of crustal accretion with a distinct magmatic plumbing system, corresponding to systematic variations in axial seafloor morphology and lithosphere structure (Figure 1.4) (Schouten et al., 1985). Early bathymetry and gravity studies at slow and ultraslow spreading ridges (Detrick et al., 1995; Kuo and Forsyth, 1988; Lin et al., 1990; Rommevaux-Jestin et al., 1997; Sauter et al., 2001) showed that segment centers typically correspond to topographic highs and Mantle Bouguer Anomaly (MBA) lows with a 'bull-eyes' pattern, reflecting thicker crust and/or lower density at segment centers than that their segment ends, e.g., the MAR 28-31°N (Lin et al., 1990) and the SWIR 49-57°E (Sauter et al., 2001). Therefore, melt supply is considered to be the highest at the segment center, decreasing towards segment ends, suggesting an along-axis melt focusing process (Figure 1.4b) (Lin et al., 1990). This focused melt was verified by later seismic observations (Dunn et al., 2005; Hooft et al., 2000; Li et al., 2015; Minshull et al., 2006; Seher et al., 2010).

On a fine scale of segmentation, third- and fourth-order discontinuities are defined by smaller OSCs at fast spreading ridges and melt-rich intermediate spreading ridges (Macdonald et al., 1988). These small offsets are <2 km, persisting for <1 Ma as third-order and <10 kyr as fourth-order discontinuities (Carbotte et al., 2015). At slow and ultraslow spreading ridges as well as melt-poor intermediate spreading ridges, third-order segmentation is defined by gaps between volcanic chains, and fourth-order segmentation might be defined by gaps within a single volcanic chain (Carbotte et al., 2015; Macdonald et al., 1991). However, using this criterion, it is nearly impossible to identify third- and fourth-order segmentation at slow and ultraslow spreading ridges, due to the complexity of the axial volcanic process (Carbotte et al., 2015).

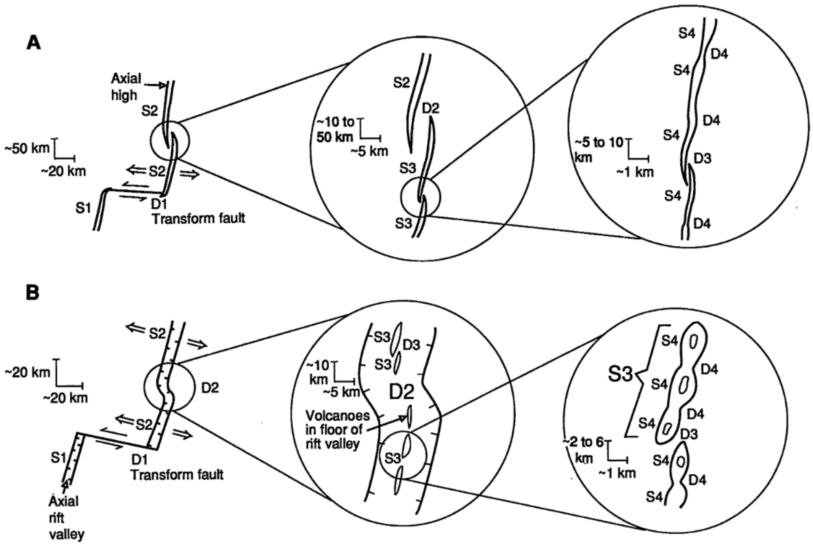

Figure 1.3. A hierarchy of segmentation defined by axial discontinuities.

After Macdonald et al., (1991). (a) Fast spreading ridges and melt-rich intermediate spreading ridges. (b) Slow and ultraslow spreading ridges as well as melt-poor intermediate spreading ridges. D1-D4 are first- to fourth-orders discontinuities, corresponding to segments S1-S4.

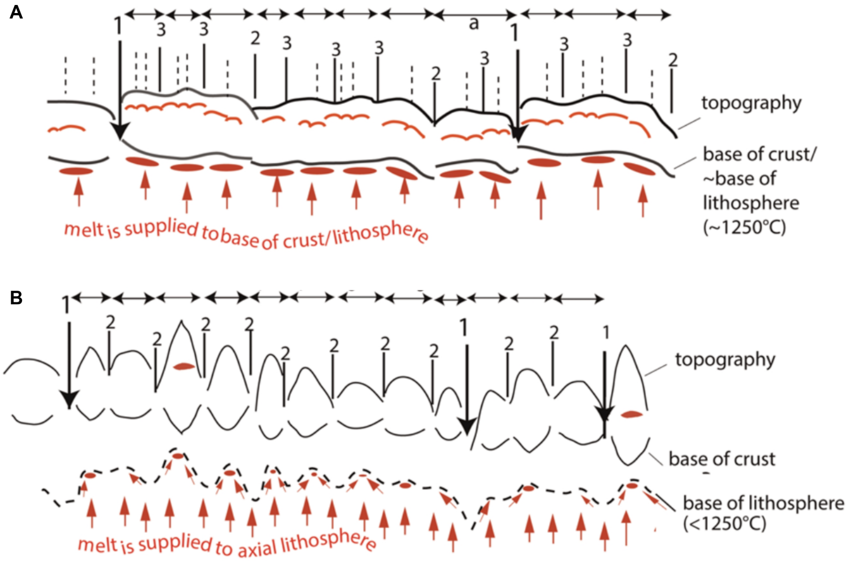

Figure 1.4. Schematic illustration of ridge segmentation.

After Carbotte et al., (2015). Numbered vertical lines indicate discontinuity order. (a) Fast spreading ridges and melt-rich intermediate spreading ridges. Crustal thickness is relatively constant except near transform faults. Melt upwells (red vertical arrows) from the base of the crust to feed each segment. Shallow AMLs (thin red lines) form within the crust/lithosphere, which define third- and fourth-orders discontinuities. (b) Slow and ultraslow spreading ridges and melt-poor intermediate spreading ridges. Only first- and second-orders discontinuities are numbered. Along-axis melt delivery from segment ends towards centers at the base of axial lithosphere results in variable segment-scale crustal thickness. Crustal mush zone (red ellipses in the crust) and/or AMLs occur at some magmatically-robust segments.

1.1.3 Oceanic lithosphere composition

Although there is no complete drilled section of oceanic lithosphere, it is conceptually composed of the crust and underlying upper-mantle, and the crust can be divided into three layers proposed at a Penrose conference (Penrose, 1972), based on petrological and seismic studies at fast spreading ridges (Figure 1.5) (Mével, 2003; Raitt, 1963; Spudich and Orcutt, 1980). Layer 1 is cumulated sediments, generally thickening with crustal age, so that layer 1 is nearly absent near the ridge axis. Alternatively, the upper-crustal layer 2 is the uppermost section of the new crust at a thickness of ~1.5 km (Christeson et al., 2019; Harding, 1989; Raitt, 1963), which is subdivided into layers 2A and 2B.

Layer 2A is made up of extrusive basaltic lavas, corresponding to P-wave seismic velocities of <4.5 km/s, and layer 2B is intrusive sheeted dike complex with seismic velocities of 5-6.5 km/s (Raitt, 1963). The boundary of layers 2A and 2B could be imaged by seismic reflections (Carbotte et al., 2006), which is interpreted as a transition from magma intrusion to extrusion (Harding et al., 1993). Below Layer 2 is crystallized gabbros of the lower-crustal layer 3 at a thickness of ~4.5 km (Christeson et al., 2019), corresponding to relatively uniform seismic velocities of 6.5-7 km/s (White et al., 1992). The layer 2/3 boundary can also be distinguished by a sharp change of velocity gradient from ~1-2 s^{-1} at layer 2 to only ~0.1 s^{-1} at layer 3 (White et al., 1992). The lowermost layer is upper-mantle peridotite with seismic velocities exceeding 8 km/s. The upper-mantle is defined as below the Moho interface (Canales et al., 2003) or mantle transition zone (Aghaei et al., 2014).

At slow and ultraslow spreading ridges, crustal composition estimated from seismic data is more heterogenous. There is either layered crustal structure at magmatic segment centers like fast spreading ridges, or heterogenous crust mixing with serpentinized peridotites at some segment ends (Figures 1.5 and 1.6). At segment ends where melt supply is not enough to keep up with plate spreading, the crust is thinner and the lithosphere is thicker relative to segment centers (Figure 1.6) (Cannat et al., 1995; Lin et al., 1990). The lower crust partially contains peridotites with discrete gabbroic bodies, and they could be uplifted to be exposed on the seafloor by deep-root, long-offset detachment faults (Cannat, 1993; Escartín et al., 2017; Ildefonse et al., 2007; Karson and Lawrence, 1997). Consequently, the ends of some (not all) melt-poor segments may not have strong contrast in seismic velocity gradients like layered curst (Figure 1.5). More recently, the seismic velocity profile at the nearly-amagmatic 64°E of the ultraslow spreading SWIR, where the seafloor is almost 100% composed of peridotite, shows a nearly linear gradient from the seafloor to mantle (Momoh et al., 2017).

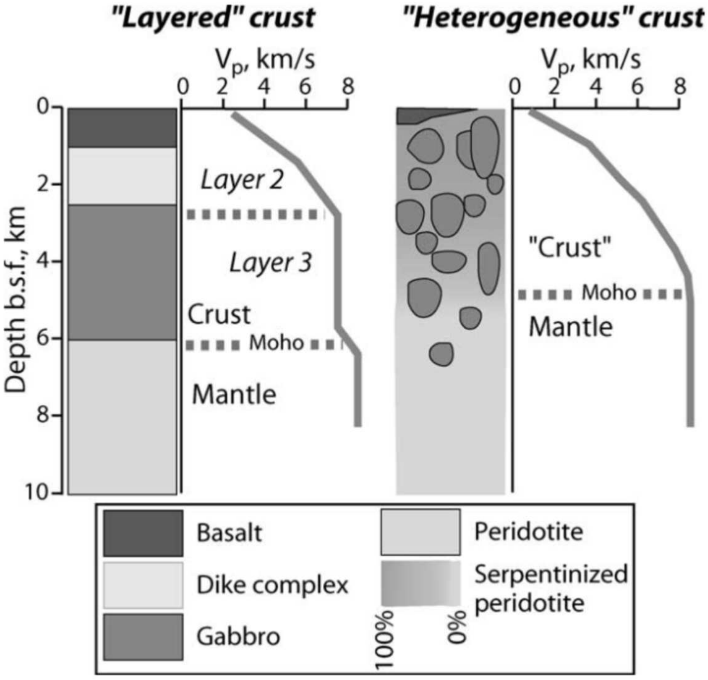

Figure 1.5. Conceptual models of layered and heterogeneous crusts, based on lithological interpretation and seismic velocity profiles.

After Mével (2003). See legend for symbols. (left) Layered crust beneath fast spreading ridges and its corresponding seismic velocity model. (right) Heterogeneous crust with serpentinized peridotites beneath slow and ultraslow spreading ridges and its possible seismic velocity model.

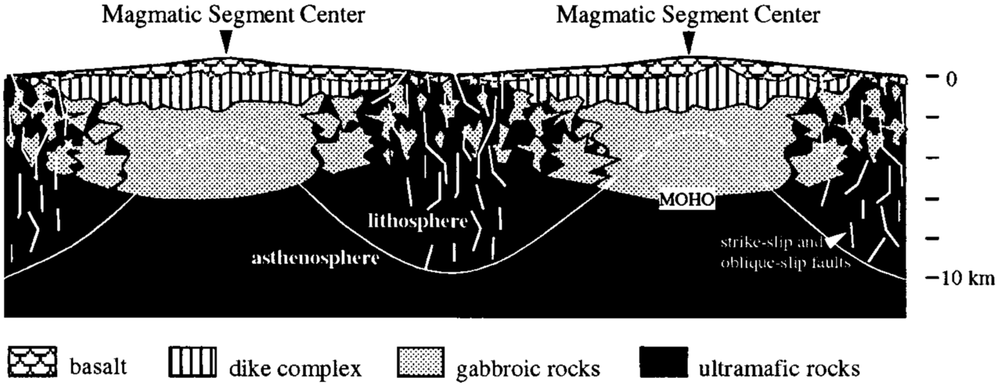

Figure 1.6. Interpretive sketch for two magmatic segments along the slow-spreading MAR between 22 and 24°N.

Adapted from Cannat et al. (1995). See legend for symbols. Crust at magmatic segment centers is shown as layered structure, becoming progressively thinner, more heterogenous, more faults towards melt-poor segment ends. The lithosphere above the white line is progressively thicker from segment centers to ends.

1.2 Faulting

As the young lithosphere of the MORs is built by magmatism, fractures occur to accommodate plate divergence due to tectonic deformation (e.g., detachment faults) or dike intrusions (e.g., graben bounding faults within the AST of fast spreading ridges; Soule et al., 2009), reshaping the seafloor morphology. These fractures vary from fissures (down to <1 m wide), normal faults (10s to 100s m in vertical throw and horizontal heave), to long-offset detachment faults (up to >10 km in horizontal heave). Faulting pattern is sensitive to spreading rate and melt supply through their impact on the thermal structure and hence the strength and thickness of the brittle lithosphere (Behn and Ito, 2008; Buck et al., 2005; Cannat et al., 2019b; Searle and Escartín, 2004).

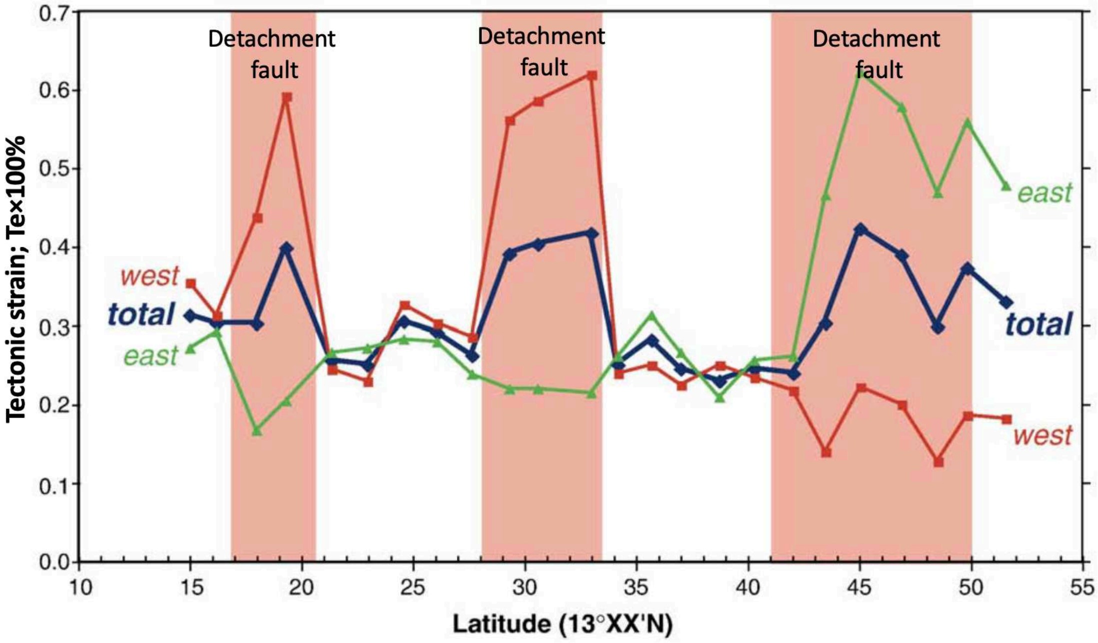

Figure 1.7. Along-axis variation in tectonic strain around the MAR 13°N

Modified from MacLeod et al. (2009). Tectonic strain (Te; left axis) is measured around MAR 13°N over the past 1.86 Ma. Pink shaded areas indicate the areas of detachment faults. Red and green lines are relative proportions of tectonic strain from the western and eastern flanks of the axis, respectively. Thick blue line is the total tectonic strain.

1.2.1 Apparent tectonic strain and M value

Apparent tectonic strain (Ts) could be tentatively quantified by summing heaves of normal faults along a flow line parallel to the spreading direction, which is believed to be the proportion of plate divergence accommodated by tectonic deformation (Bohnenstiehl and Carbotte, 2001; Cowie et al., 1993; Escartín et al., 1999). The proportion of plate divergence accommodated by magmatic extension is, therefore, expressed as 1-Ts, which is so-called M value (Buck et al., 2005). At fast spreading ridges, Ts is typically low at <5% (Bohnenstiehl and Carbotte, 2001; Cowie et al., 1993; Escartín et al., 2007). At intermediate spreading ridges, Ts ranges between 5-30% (Deschamps et al., 2007; Howell et al., 2016). Ts has the highest variability at slow and ultraslow spreading ridges, which can be up to almost 100% at a nearly-amagmatic corridor of the SWIR (Sauter et al., 2013), and be down to ~10% at magmatically-robust segments (Combier et al., 2015; Escartín et al., 1999). Ts ranges between 20 and 40% at volcanically and tectonically symmetric spreading segments, while at asymmetric spreading segments with detachment faults at one plate, Ts ranges between 40 and 80% (Figure 1.7) (Liu et al., 2020; MacLeod et al., 2009). Substantially increased Ts at detachment faults, where melt supply is lower compared to adjacent regions, indicates that the need for faulting to accommodate plate separation may increase as melt supply reduces (MacLeod et al., 2009).

However, the actual Ts may be misestimated by this apparent Ts. At fast spreading ridges, the actual Ts would be overestimated, because part of the fractures at the uppermost crust are triggered by dike intrusions (Soule et al., 2009). At slow spreading ridges, large-offset faults may be rotated to low dip angles, e.g., detachment faults, leading to gross underestimation of the actual Ts. Mass wasting and the overprint of lava flows may also result in the misestimation of the actual Ts (Deschamps et al., 2007; Escartín et al., 1999).

1.2.2 Oceanic detachment faults

Oceanic detachment faults play a significant role in tectonically accommodating plate divergence at slow spreading ridges, conceptually proposed in the 1980s and 1990s (Cannat, 1993; Dick, 1981; Karson and Dick, 1983) to explain the exposure of mantle-derived peridotites at the seafloor. Detachment faults are long-lived to slip the young lithosphere with corrugated surface and a dome shape at diameters of up to >10 km (Figures 1.2c and 1.8) (Cann et al., 1997; Escartín et al., 2017; Escartín and Canales, 2011; MacLeod et al., 2009; Reston and Ranero, 2012; Searle et al., 2003; Smith et al., 2008a; Tucholke et al., 2001). In contrast to their conjugate plates, the seafloor is characterized by volcanic abyssal cut by high-angle normal faults (Buck et al., 2005; Cannat et al., 2006; Escartín et al., 2008; MacLeod et al., 2009; Smith et al., 2008a). This asymmetric spreading mode is more widely distributed at segment ends than at segment centers of the MAR between 12° and 35°N, and these detachment faults presumably control plate separation over ~50% of the total length with a concentration of hydroacoustic and teleseismic events that are ~1.5 times more than symmetrical segments (Escartín et al., 2008).

It is widely accepted that detachment faults initiate as high-angle normal faults that cut through a significant thickness of a young lithosphere, and then rotate to a lower angle due to the flexure in the footwall (Escartín and Canales, 2011; Lavier et al., 1999; MacLeod et al., 2009; Smith et al., 2006). Oceanic core complexes (OCCs), including lower-crustal gabbros and mantle-derived peridotites, are exhumed on the footwall during fault development (Cannat, 1993; Dick et al., 2000; Escartín et al., 2017; Ildefonse et al., 2007; Tucholke et al., 2001). Gravity signals show higher anomalies associated with the OCCs, relative to the conjugate plates, reflecting denser rocks beneath the OCC (Blackman et al., 2009). Seismic refraction studies show a heterogenous velocity structure with a high velocity anomaly in the footwall, also correlating with detailed seafloor sampling of gabbros and peridotites in the footwall (Canales et al., 2008). Seismic reflection images of the subsurface (<5 km bsf) geometry of detachment faults, for example of the SWIR 64°E, show a concentration of damage zones with a dip of ~50° along the supposed continuation of an outcropping detachment fault (Momoh et al., 2017).

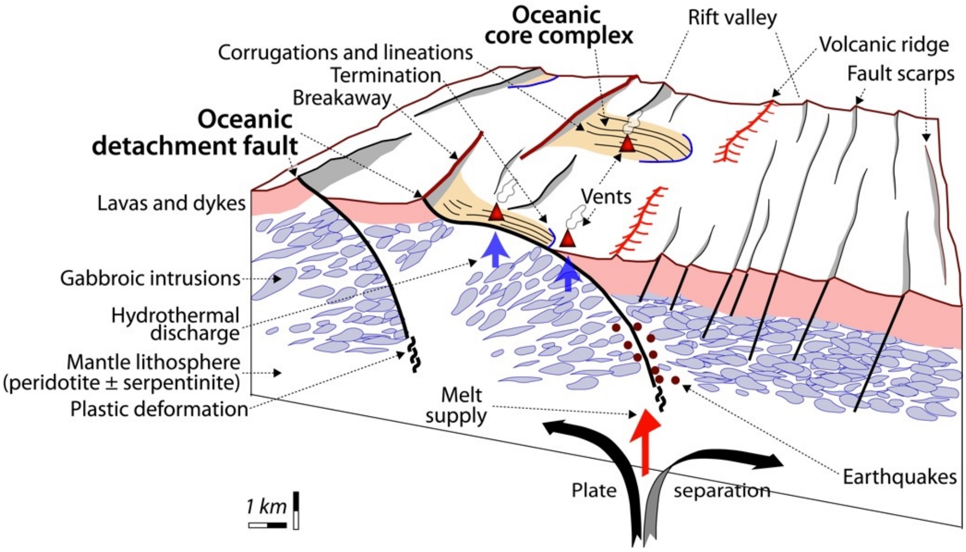

Figure 1.8. Sketch of oceanic detachment faults, OCCs, and related structures. *Adapted from Escartín and Canales (2011). Features are indicated in the figure.*

The deeper structure of detachment faults is evident from microearthquakes, using local ocean bottom seismometer (OBS) networks at slow and ultraslow spreading ridges, i.e., TAG (de Martin et al., 2007), Atlantis (Collins et al., 2012), Logatchev (Grevemeyer et al., 2013), MAR 13°N (Parnell-Turner et al., 2020, 2017), and Rainbow (Horning et al., 2018) at the MAR, Dragon Flag at the SWIR (Tao et al., 2020; Yu et al., 2018) and Mount Dent at the MCSC (Grevemeyer et al., 2019). The distribution of earthquakes at active detachment faults outlines the fault planes that penetrate thick lithospheres (>7 km), e.g., TAG, MAR 13°N, and Dragon Flag (Figure 1.10; de Martin et al., 2007; Parnell-Turner et al., 2017; Yu et al., 2018); Almost all earthquakes occurred along the faulting zone and in the footwall, while only few occurred in the hanging wall, which highlights the tectonic activity of detachment faults and the bending of the lithosphere as the footwall rolls over to a lower angle (de Martin et al., 2007; Parnell-Turner et al., 2017). This bending of lithosphere may correspond to compressive stresses that trigger reverse faulting at depths of 3-7 km bsf, which was observed only at the MAR 13°20'N detachment fault (Figure 1.10b; Parnell-Turner et al., 2017).

Numerical modelling suggests that the occurrence of detachment faults requires an M-value of less than ~50%, i.e., Ts>50% (Behn and Ito, 2008; Bickert et al., 2020; Buck et al., 2005; Liu and Buck, 2020; Olive and Dublanchet, 2020; Tucholke et al., 2008). Segment-scale melt focusing at slow and ultraslow spreading ridges leads to segment ends receiving a lesser melt supply; this increases the needs of faulting to accommodate plate divergence, triggering the development of long-lived detachment faults at a critical range of the M-value.

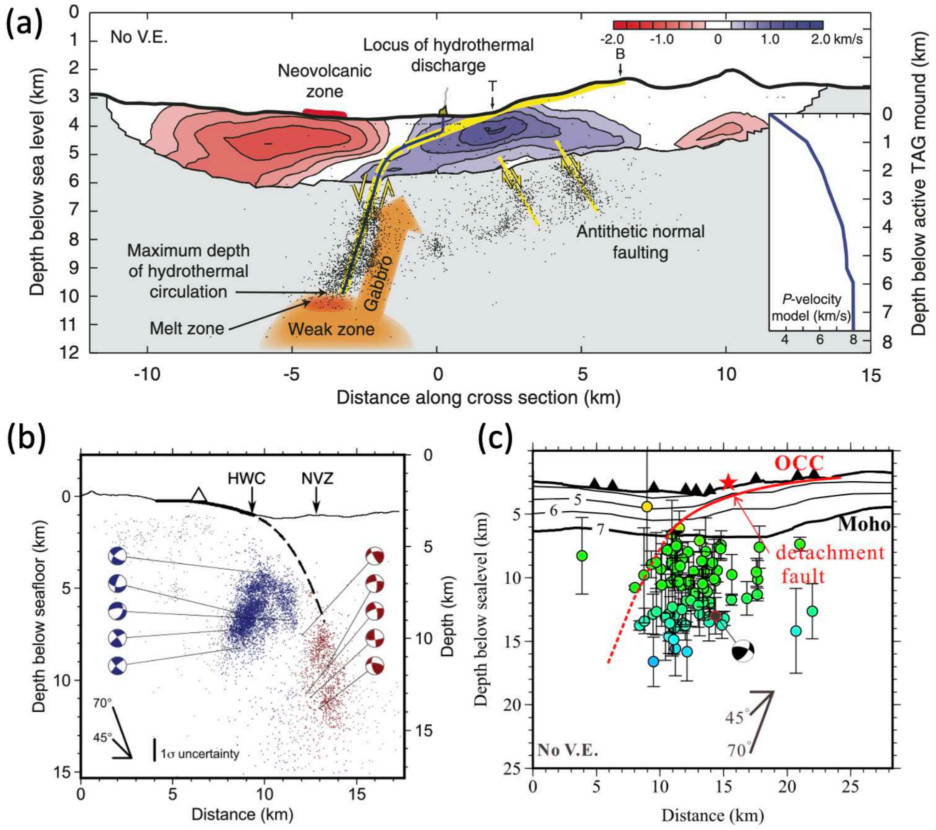

Figure 1.9. Microearthquakes at detachment faults

(a) Schematic crustal section of the MAR TAG detachment fault showing hypocenters and seismic velocity anomalies, adapted from de Martin et al. (2007). The fault plane is outlined by microearthquakes (black dots) rotating from ~70° below 3 km bsf to ~20° on the seafloor. T is the fault termination and B is the breakaway. (b) The MAR 13°20'N detachment fault with a rotated fault plane, outlined by microearthquakes (Parnell-Turner et al., 2017). Red dots represent microearthquakes due to normal faults and blue dots represent microearthquakes due to reserve faults, suggested by focal mechanisms. HWC: hanging wall cut-off. NVZ: neo-volcanic zone. (c) The SWIR Dragon Flag detachment fault with a rotated fault plane, outlined by microearthquakes (Yu et al., 2018).

1.3 Volcanism and magma plumbing system

Basaltic lavas are erupted onto the seafloor through dikes, crystallizing to form the uppermost crust. This process transfers heat and mass from the Earth's interior to surface through magma plumbing system and leads to the MOR being the Earth's largest volcanic system (Sinton and Detrick, 1992). Due to the great water depth and remote locations, ongoing submarine volcanic eruptions are rarely observed visually, but can be recorded by submarine earthquake observing networks, such as 2011 and 2015 eruptions at the Axial seamount (Dziak et al., 2012; Wilcock et al., 2016). The erupted lavas are cooled by seawater at an extremely high rate, forming distinct volcanic morphologies. This provides excellent opportunities to study historic volcanic eruptions at MOR, using seafloor videos and photographs, and high-resolution (<10 m) bathymetry and backscatter data (Cann and Smith, 2005; Colman et al., 2012; Deschamps et al., 2013; Escartín et al., 2014; Fundis et al., 2010; Searle et al., 2010; Stakes et al., 2006).

1.3.1 Lava morphology

Based on seafloor videos and photographs, the surface lava flow morphologies can be classified into three distinct types (i.e., pillow, lobate, and sheet), regarding the appearance of the individual unit and interconnected system (Kennish and Lutz, 1998; Perfit and Soule, 2016; Soule, 2015).

Pillow lavas are characterized by high relief with bulbous, spherical, or tubular lobes, usually associated with well-identified bread crust surface (Figures 1.1a-d). They are formed by an interconnected system: new pillows down-slope continuously growing from a larger feeding flow (Moore, 1975). Pillow mounds are generated by a top-to-bottom piling up of numerous pillows and elongated pillow tubes (Figures 1.1b-c).

Lobate lavas are similar to pillows but larger in width, and they are commonly inflated, leading to a flatter upper layer (intermediate relief) of crusts (Figures 1.1d-f). Later collapses commonly occur near eruptive vents (Figure 1.1f), possibly showing the interior lava pond system that lacks a direct interconnection like pillow lava flows.

Sheet lavas have a uniform and flat surface (low relief), displaying various morphologies, i.e., lineated, folded, jumbled, and hackly (Figures 1.1c, g-i). Sheet lavas tend to flow far away from eruptive vents, up to several kilometers (Sinton et al., 2002; Soule et al., 2007).

Lava effusion rate is the dominant factor governing lava morphologies at MORs (other potential factors are cooling rate, lava viscosity, and seafloor slope) (Colman et al., 2012; Griffiths and Fink, 1992; White et al., 2009). Based on a wax experiment (Gregg and Fink, 1995), the order of magnitude of lava effusion rate increases from pillow (<1 m^3/s), lobate (1-10 m^3/s) to sheet (>100 m^3/s) lavas, assuming a lava viscosity of 100 Pa s. The contacts, between distinct lava morphologies (e.g., Figure 1.1c: sheet lavas topped by pillow lavas), provide visual evidence for relative ages between two adjacent eruptions and their corresponding eruptive styles with distinct lava morphologies.

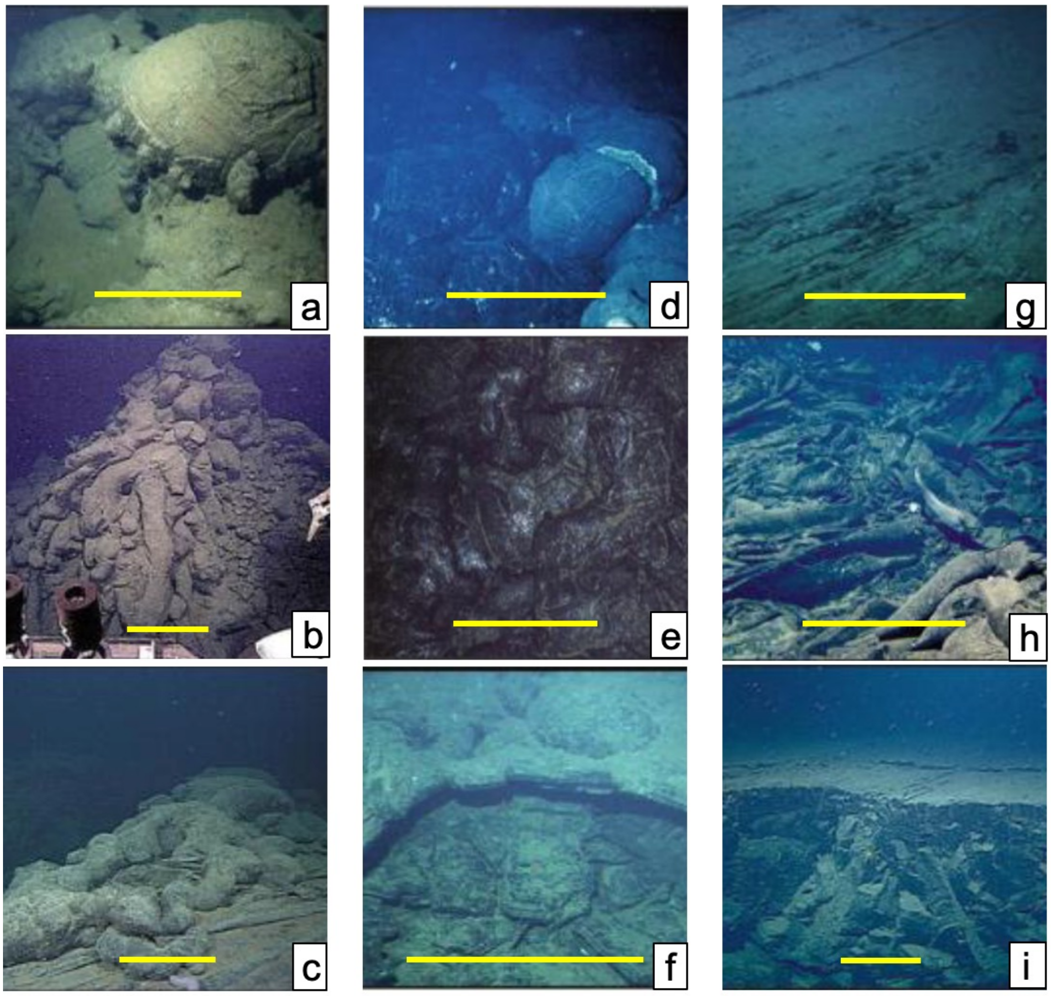

Figure 1.10. Photographs of lava morphologies.

Adapted from Perfit and Soule, (2016). (a) Pillow lava with bread crust surface. (b) Haystack of tubular pillow lava. (c) Pillow mound piled up by pillow and elongated tubes, overlying a sheet flow. (d) Young lobate lava flow (left) in contact with older pillow lava (right), observed at EPR 9°N in 1992 eruption. (e) Young glassy lobate lava, observed in the 2005-2006 eruption at the EPR 9°N. (f) Collapsed lobate lava with a thin roof. (g) Lineated sheet lava with thin sediment cover. (h) Folded to jumbled sheet lava. (i) Vertical exposure of sheet lava showing the flat upper layer. Horizontal scales (yellow) across the bottom of the photos are ~1 m.

1.3.2 Volcanic seafloor morphology

Seafloor morphology with distinct characteristics can be mapped using high-resolution bathymetry and backscatter data. Smooth and hummocky seafloor morphologies, as well as volcanic seamounts, are major seafloor types at the MORs (Cann and Smith, 2005; Escartín et al., 2014, 2007; Klein et al., 2013; Searle et al., 2010).

Smooth seafloor morphology (Figure 1.11a), also called flat seafloor, are characterized by very flat lava flow surface (typically slope <5-10°) and uniform backscatter (Escartín et al., 2007; Sinton et al., 2002). Smooth flows tend to travel from their eruptive sources to several kilometers away, covering a wide area (Soule et al., 2007). Their boundaries are commonly irregular and sometimes stopped by higher-relief structures, such as faults and hummocky ridges (Briais et al., 2000). Sinuous **lava tubes** and **lava channels** are observed on smooth terrain, which help transport lavas (Fornari, 1986; Soule et al., 2005). Sheet and lobate lavas are the most commonly observed lava morphologies on smooth terrains (Fundis et al., 2010).

Hummocky seafloor morphology (Figure 1.11b), also called pillow mounds, are characterized by a rough topography and patchy backscatter due to numerous **volcanic hummocks** (Klein et al., 2013; Searle et al., 2010; Smith and Cann, 1992, 1990). These hummocks are cone-shaped with typical heights of 30-300 m, diameters of 5-150 m, and flank slopes of >25° (Yeo et al., 2012). **Hummocky ridges** consist of linearly coalesced volcanic hummocks for a few to tens of kilometers along the ridge axis, associate with AVRs (Searle et al., 2010; Smith et al., 1995; Smith and Cann, 1992). Hummocky seafloor is dominated by pillow lavas (Cann and Smith, 2005; Klein et al., 2013; Yeo et al., 2012).

Seamounts (Figure 1.11c) are large (>500 m in diameter and >50 m in height normally) near-circular volcanoes with steep (15-40°) smooth flanks (Searle et al., 2010; Smith et al., 1995). The seamounts detected from shipboard bathymetry data have a typical height-to-diameter ratio of about 1:10 (Smith et al., 1995; Smith and Cann, 1992; Smith and Jordan, 1988). Flat-topped seamounts with distinct flat tops (<10°), e.g., at MAR 45°N, are composed of sheet and lobate lavas on their tops and pillow and elongated pillow lavas with breccias on their flanks (Yeo and Searle, 2013). Seamount volcanism also plays an essential role in crustal construction along the MORs, relating to isolated, local, small melt bodies within the brittle lithosphere (Smith and Cann, 1992, 1990).

The term 'eruption rate' describes the average lava output for the entire eruption over a classified seafloor morphology. With a dominance of sheet and lobate lavas, smooth morphology has a higher eruption rate than hummocky morphology that mainly consists of pillow lavas (Colman et al., 2012; McClinton and White, 2015). Like photo-scale lava morphology, the contacts between map-scale seafloor morphologies provide evidence of longer-term eruptive history in the timescale of 10 years to 10,000 years (Perfit and Chadwick, 1998).

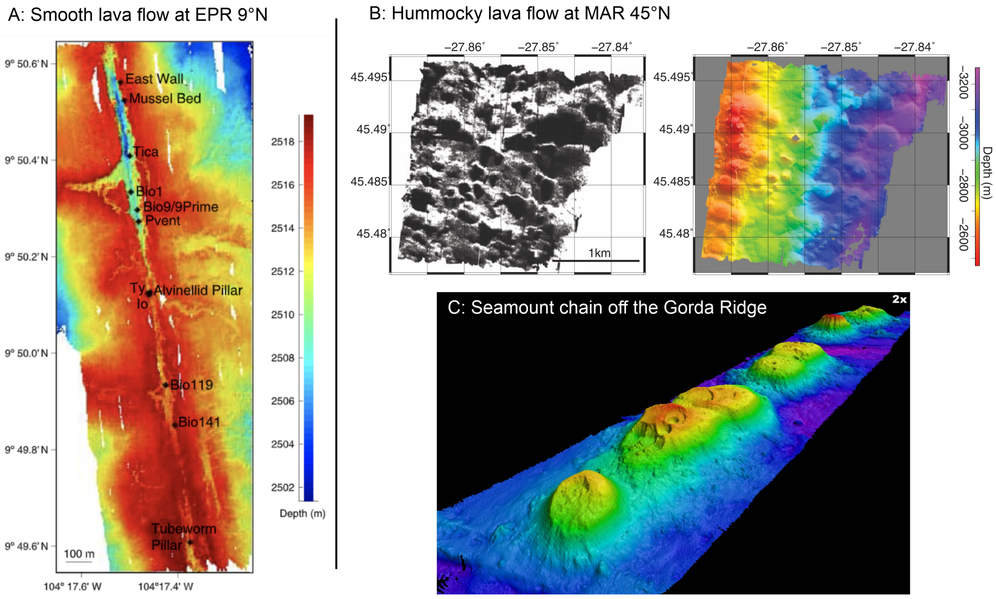

Figure 1.11. Examples of large-scale seafloor morphologies.

(a) Smooth flow at EPR 9°N (Ferrini et al., 2007). (b) hummocky flow at MAR 45°N (Yeo et al., 2012). (c) Flat-topped seamount chain off the Gorda ridge (Davis and Clague, 2000).

1.3.3 Volcanic deposits

The accumulation of erupted volcanic products leads to the identification of eruptive units; each eruptive unit is formed within an eruptive episode that consists of single or multiple cogenetic eruptive events and each event probably lasts hours to weeks (Clague et al., 2018; Colman et al., 2012; McClinton and White, 2015; Perfit and Chadwick, 1998).

Eruptive units can be spatially singled out by high-resolution bathymetry data, and their volumes are a key parameter to reflect eruptive dynamics (Colman et al., 2012; Perfit and Chadwick, 1998; Sinton et al., 2002). The most efficient and accurate way to obtain the eruptive volume is to observe the topographic differences by repeated high-resolution bathymetry surveys before and after a known eruption. Currently, at the MORs, Axial seamount has been bathymetrically investigated before and after 2011 and 2015 eruptions (Caress et al., 2012; Clague et al., 2017), and two known eruptions at the EPR 9°50'N in1991-1992 and 2005-2006 have been detected by digital seafloor imagery and Alvin dives

(Haymon et al., 1993; Soule et al., 2007). As for unknown submarine eruptions, volumes of the eruptive units are roughly estimated by a single bathymetry survey, according to the identification of natural contacts between seafloor morphologies, such as GSC 92°W and 95°W (Colman et al., 2012; McClinton and White, 2015). Due to the deformation of post lava flows and tectonics, the volume measurement should have considerable uncertainties.

1.3.4 Volcanism with respect to spreading rate

The abundance of photo-scale lava morphologies and eruptive unit volumes are generally associated with spreading rates (Figure 1.12). At fast spreading ridges, such as the EPR 9°30'N, a prevalence of sheet and lobate lavas forming smooth morphology is most commonly observed (Fundis et al., 2010; Sinton et al., 2002; Soule et al., 2007), and these smooth-dominated eruptions tend to produce small volumes of eruptive units (Perfit and Chadwick, 1998; Sinton et al., 2002). At intermediate spreading ridges, pillow lavas also occur to form hummocky ridges, resulting in a diversity of lava morphologies (Figure 1.12a), such as the GSC 92°W and 95°W (Colman et al., 2012). At slow spreading ridges, pillow lavas are most dominant, such as the MAR 45°N (Searle et al., 2010), and eruptive units usually have larger volumes, relative to intermediate and fast spreading ridges (Figure 1.12b). Additionally, volcanism can be very weak or nearly absent at some melt-poor sections of ultraslow spreading ridge, such as the SWIR 64°30'E. (Sauter et al., 2013).

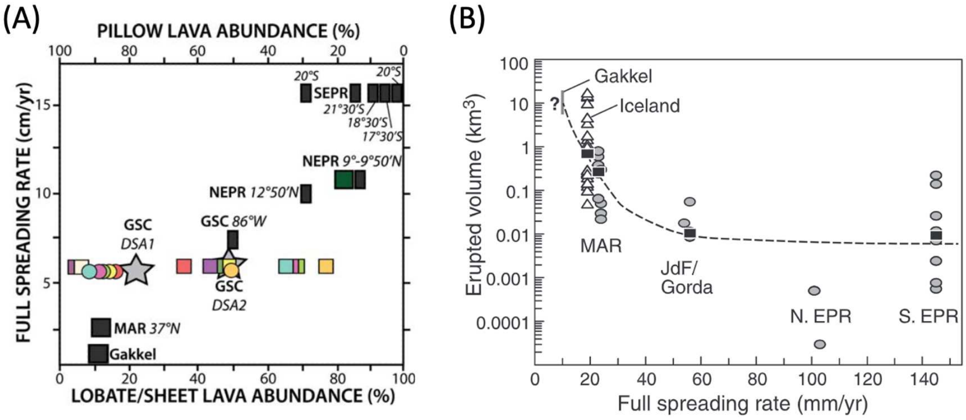

Figure 1.12. Compilation of (a) abundances of lava morphologies (McClinton et al., 2013) and (b) eruptive unit volume (Sinton et al., 2002) as functions of spreading rate.

1.3.5 Magma plumbing system

The styles of volcanic eruption are associated with the magma plumbing system (Sinton and Detrick, 1992). This system is mainly filled with crystal mush (Lissenberg et al., 2019; Sinton and Detrick, 1992). In a crystal mush zone, buoyant interstitial melts upward migrate by porous flow combined with sufficient compaction, resulting in nearly horizontal melt-rich sills that are probably connected by melt channels (Figure 1.13a) (Cashman et al., 2017; Lissenberg et al., 2019). Seismic reflection at the Axial Seamount of JdFR images a column of stacked AMLs (3-5-km wide and 300-450-m regular spacing), distributed from the topped AML to the mid-to-lower crust (Figure 1.13b) (Carbotte et al., 2020). These AMLs contain enough melt to lower seismic velocities that can be detected by seismic tomography if melt volume is large enough, i.e., 26-60 m^3 at the Axial Seamount with melt fraction up to 65% (Arnulf et al., 2018). Furthermore, reactions between melt sills and surrounding crystal framework and mixing between replenishing and interstitial melts lead to buffer and homogenize melt composition (Figure 1.13a) (Lissenberg et al., 2019 and references therein).

The best constrained magma plumbing system at MOR is located at fast spreading ridges and some magmatically-robust segments of intermediate spreading ridges, such as the EPR 9°N and Axial Seamount. The EPR 9°N has shallow (1.5 km), long-lived AMLs (Carbotte et al., 2013; Detrick et al., 1987) over a large crystal mush zone interpreted from a seismic low-velocity anomaly (LVA; Dunn et al., 2000). Consequently, internal, excess magma driving pressures can easily and frequently trigger dike intrusions to feed high-effusion-rate eruptions, i.e., sheet and lobate lavas (Fundis et al., 2010).

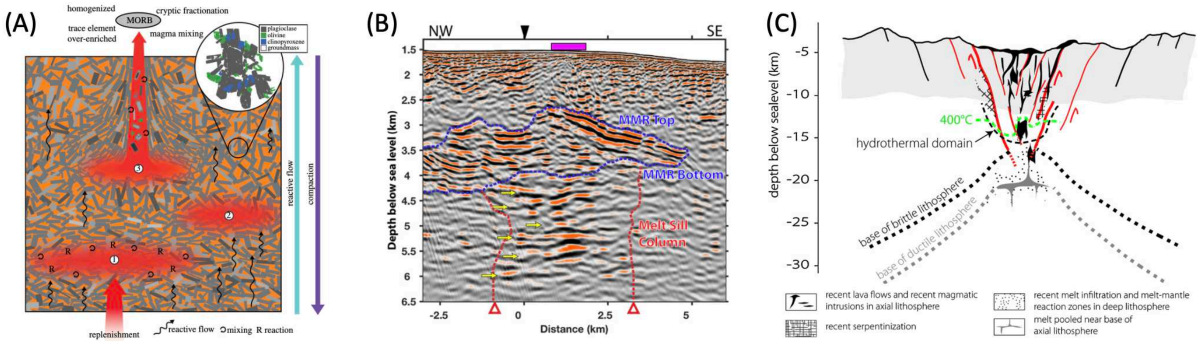

Figure 1.13. Crystal mush zone and magma plumbing systems

(a) Conceptual model of a crystal mush zone in the lower crust (Lissenberg et al., 2019). Melt lens 1 at the bottom is replenished by primary melt. Melt transport occurs both by porous flow, aided by compaction, and by channelized focused flow, forming melt lenses 2 and 3. Therefore, all the melt lenses are segregated in the shape of a nearly horizontal sill and have reactions with surrounding mush and mixing of interstitial melts into the melt lenses (inset). Melt lens 3 on the top is drained to feed eruptions of MORB (mid-ocean ridge basalt). (b) Close-up of stacked melt sills at the Axial Seamount of JdFR, imaged by seismic reflection (Carbotte et al., 2020). MMR: main magma reservoir. (c) Conceptual crustal sketch across the ridge axis of a slow spreading ridge (Cannat et al., 2019b). *See legend for symbols.*

Slow and ultraslow spreading ridges generally have thicker and colder lithosphere (Phipps Morgan and Chen, 1993a), leading to deeper and more complex magma plumbing systems (Cannat, 1993; Cannat et al., 1995; Sinton and Detrick, 1992). The thick brittle lid may impede magma transport to the crust to form a long-lived crystal mush zone and/or AML (Detrick et al., 1990). Instead, melt may crystalize as long as it intrudes into colder rocks at any depths of the lithosphere through faults, and the crystallization of the melt releases heat to probably drive black-smoker hydrothermal circulation (Figure 1.13c) (Cannat, 1993; Cannat et al., 2019b, 1995). Consequently, a complex magma plumbing system is expected to be shaped by free melt intrusions at both melt-poor and melt-rich areas.

1.3.6 Central domal volcano at slow and ultraslow spreading ridges

However, there are a few exceptions at the center of magmatically-robust segments of slow and ultraslow spreading ridges, with seismic LVAs and/or AMLs, i.e., the MAR Lucky Strike (Combier et al., 2015; Seher et al., 2010; Singh et al., 2006), the Reyjanes Ridge 57°N (Sinha et al., 1997), and the SWIR 50°28'E (Jian et al., 2017b, 2017a). In these areas, domal volcanos are commonly constructed within the axial valley at heights of hundreds of meters or up to >1 km. At the Lucky Strike (Figure 1.14), the central domal volcano corresponds to a 3.5 km-deep AML at the top of a seismic LVA (Combier et al., 2015; Seher et al., 2010; Singh et al., 2006), and the seafloor within the volcanic summit is dominated by high-eruption-rate smooth lava flows (Escartín et al., 2014; Humphris et al., 2002). Rifting of the domal volcanos by axial graben faults is also observed (Figure 1.14c), relating to non-steady-state melt supply (Escartín et al., 2014; Klischies et al., 2019).

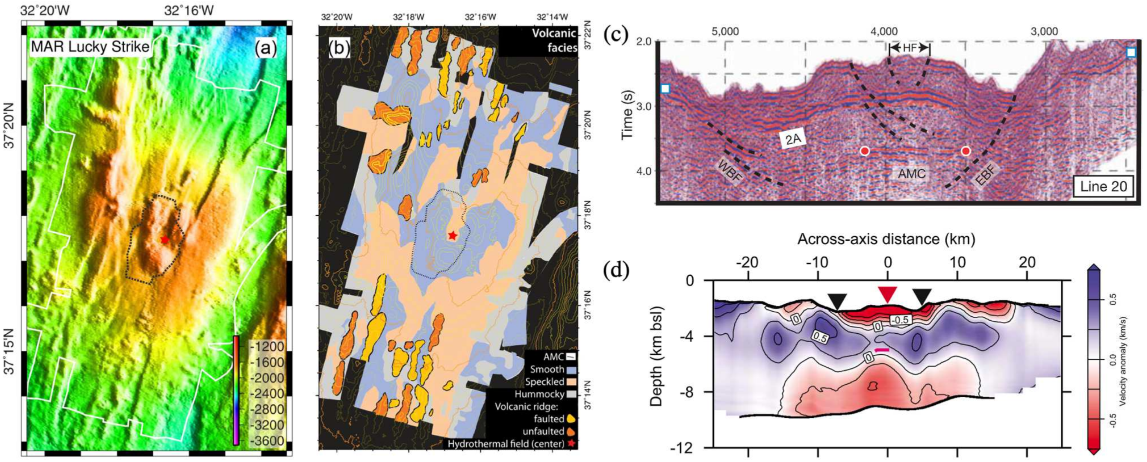

Figure 1.14. Central domal volcano at the MAR Lucky Strike.

(a) Bathymetric map (Escartín et al., 2014). (b) Volcanic seafloor morphologies interpreted from sidescan data, showing a prevalence of smooth seafloor morphology at the domal volcano (Escartín et al., 2014). (c) Seismic multi-channel reflection across the domal volcano, showing a horizontal AML reflector and oblique faulting reflectors (Singh et al., 2006). (d) Seismic velocity anomaly across the domal volcano (Seher et al., 2010), contoured at every 0.25 km/s and labelled at every 0.5 km/s. The AML is shown as a red line above the LVA area. The Moho interfaces at the bottom are shown as a thick black curve.

1.4 Hydrothermal circulation

As the first seafloor hydrothermal vent was discovered at the Galapagos Rift in the late 1970s (Corliss et al., 1979; Lonsdale, 1977), more than 600 hydrothermal vents along the global MORs have been reported (Beaulieu et al., 2015), with venting temperatures up to >400°C (Koschinsky et al., 2008). These discoveries provide straightforward evidence for hydrothermal circulation transporting heat and chemicals from the interior of the Earth to the ocean (e.g., Lowell et al., 1995). As the heated hydrothermal fluid is buoyant to the seafloor, hydrothermal vents occur with visual impressions, accompanied by diverse biological communities (e.g., Figure 1.15). High-temperature (>300°C) hydrothermal vents with black smoker chimneys (e.g., Figure 1.15) have highly enriched minerals and metals from the crust at depth. Low-temperature (<200°C) hydrothermal vents are diffuse flows, usually occurring near high-temperature vents.

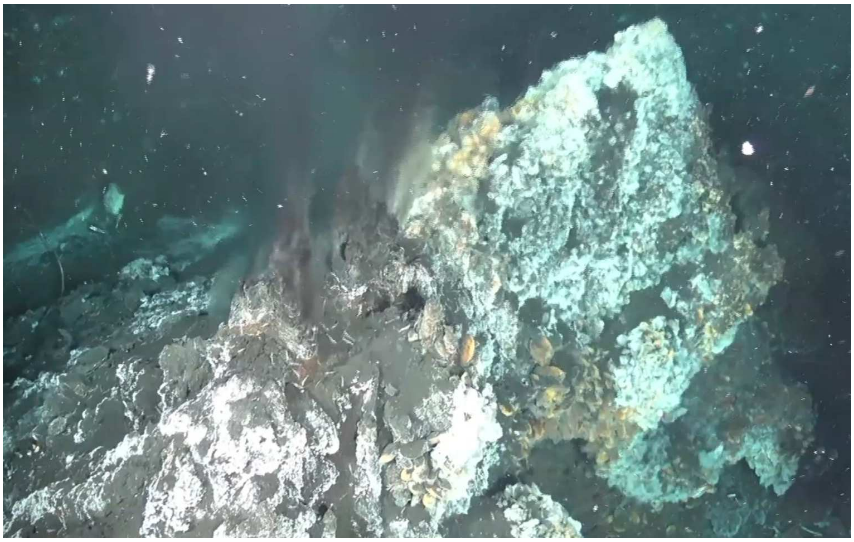

Figure 1.15. Black smoker chimneys in the Lucky Strike hydrothermal field

Image by the HOV Nautile during the MOMARSAT cruise in 2019, in which the author participated. The hydrothermal vents are surrounded by numerous mussels and shrimps.

The convection of black-smoker hydrothermal fluids is driven by a magmatic heat source, e.g., axial magma chamber (Lowell, 1991; Lowell et al., 1995). As cold and dense seawater percolates into permeable oceanic crust along pathways, i.e., faults and fissures, it keeps being heated with depth and reacts with surrounding rocks to produce hydrothermal fluids (Lowell, 1991; Lowell et al., 1995). These fluids rise to the seafloor by buoyancy at temperatures of <400°C (Jupp and Schultz, 2000, 2004), resulting in heat and chemical exchanges between oceanic lithosphere and seawater. Hydrothermal circulation accounts for approximately one third of the global oceanic crust heat flux, and ~30% of the hydrothermal heat flux occurred at axial crust younger than 1 Ma (Figure 1.1d) (Lucazeau, 2019; Stein and Stein, 1994). The heat flux estimated at a hydrothermal field, e.g., the Lucky Strike, ranges from ~200 to 1000 MW, and 75->90% of this flux is taken up by low-temperature diffuse flows (Barreyre et al., 2012).

Hydrothermal circulation can be locally enhanced at detachment fault systems with more frequent high-temperature hydrothermal venting (McCaig et al., 2007). Damage zones due to detachment faulting may provide specific pathways for hydrothermal fluids to reach deep heat sources (Andersen et al., 2015; Tao et al., 2020), or melt intruding into a shallow depth could act as heat sources to drive hydrothermal circulation (Canales et al., 2017; Cannat et al., 2009; McCaig et al., 2007).

1.5 The axial thermal regime

The thermal regime at MORs is believed to be divided into two layers with different heat transfer mechanisms. The upper layer is fractured and permeable, where hydrothermal fluids could circulate along cracks to transport heat, while the lower layer is impermeable, and the heat is purely transported by conduction. These two layers are separated by a cracking front that is the base of hydrothermal circulation. A conductive boundary layer (CBL), between the cracking front and the injected AMLs (Lowell and Germanovich, 2004; Wilcock et al., 2009), allows heat to be extracted from the AMLs (heat from magma advection, magma cooling, and latent heat of magma crystallization) to the hydrothermal system, corresponding to a high temperature gradient (Olive and Crone, 2018; Wilcock et al., 2009).

The grain-scale cracking front migrates progressively downward into hot rocks if they remain permeable (Lister, 1974; Manning et al., 2000; Wilcock and Delaney, 1996). However, the increase of confining pressure makes rocks less permeable, and the cracking front migrates downward more slowly and eventually reaches a limit depth. In a waning phase of melt supply, hydrothermal circulation could thus be driven by a downward-migrating cracking front (Wilcock and Delaney, 1996).

As the lithosphere is simultaneously cooled by hydrothermal circulation (heat output) and heated by injected AMLs (heat input), the thermal regime hardly reaches a steady state, probably leading to temporal changes of the thickness and rheology of the lithosphere (Fan et al., 2021). The hotter thermal regime corresponds to a thinner and weaker lithosphere, hence producing less brittle deformation (Figure 1.6).

1.5.1 Seismic proxies for the thermal regime

Passive seismic methods are most powerful and precise to investigate the lithosphere thermal regime (McKenzie et al., 2005). The maximum depth of earthquakes in the oceanic lithosphere, i.e., the location of the base of the seismogenic lithosphere or the Brittle-Ductile Transition (BDT), is a straightforward proxy for the 650±100°C isotherm (Anderson, 1995; Boettcher et al., 2007; McKenzie et al., 2005; Wang-Pin Chen and Molnar, 1983; Wiens and Stein, 1983). This isotherm gradually deepen with crustal ages (Figure 1.16) (McKenzie et al., 2005).

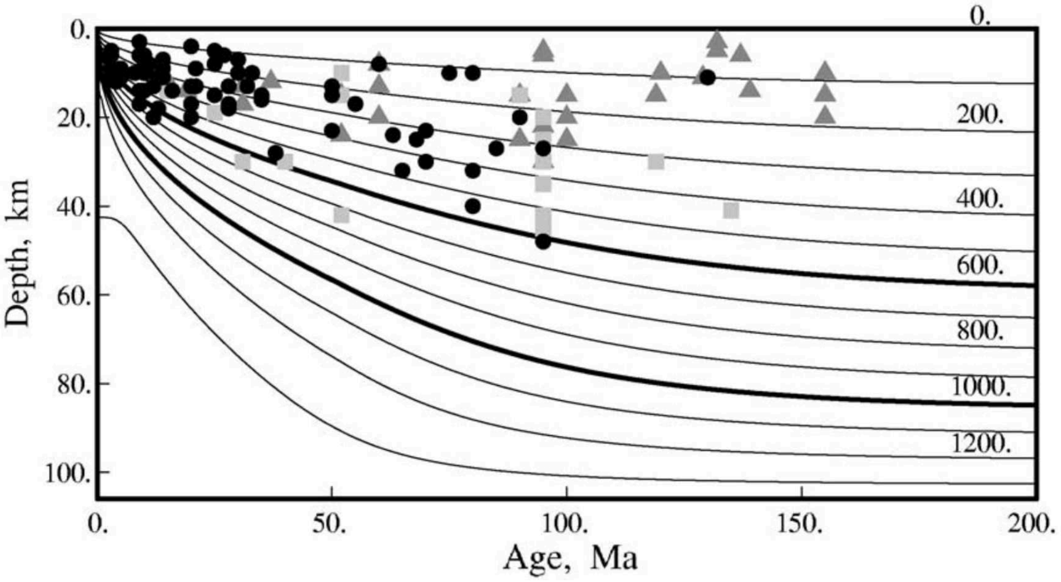

Figure 1.16. Isotherms of the oceanic lithosphere with the deepest earthquakes. *Adapted from the plate model of McKenzie et al. (2005). Black contours show isotherms every 100℃ and the 600℃ and 1000℃ contours are marked by thicker lines. Circles, triangles, and squares show depths of earthquakes.*

The deepest on-axis earthquakes of the MOR can be down to only 1.8 km at the fast-spreading EPR 9°N (Tolstoy et al., 2008), ≤12 km at the slow spreading MAR (de Martin et al., 2007; Grevemeyer et al., 2013; Kong et al., 1992; Parnell-Turner et al., 2017; Tilmann et al., 2004; Wolfe et al., 1995), and >15 km at ultraslow spreading ridges (Grevemeyer et al., 2019; Korger and Schlindwein, 2013; Meier et al., 2021; Yu et al., 2018). At slow and ultraslow spreading ridges, the maximum depth of earthquakes within a segment have been shown to vary distinctly along the axis (Meier et al., 2021; Wolfe et al., 1995). For example, the deepest earthquakes shallow toward the Logachev volcanic center over 70 km along the axis of the Knipovich Ridge (Meier et al., 2021). This may be attributed to the process of along-axis melt focusing toward the segment center (Cannat et al., 1995; Lin et al., 1990), where the thermal regime is heated by large amount of melt injections to uplift the isotherms and hence thinning the seismogenic lithosphere.

The second proxy, determined by active seismic methods and referring to the basaltic solidus or the 1000°C isotherm, is the depth to the AMLs and/or to the top of the lower-crustal LVAs (Fontaine et al., 2011; Sinton and Detrick, 1992). The best example is the EPR 9°N, where a crystal mush zone (interpreted from a seismic lower-crustal LVA) is capped by an AML reflector at a depth of 1.5 km (Carbotte et al., 2013; Detrick et al., 1987; Dunn et al., 2000). Thermal models of slow and ultraslow spreading ridges have led to the prediction that they should not have long-lived AMLs or LVAs at crustal depths (Morgan and Chen, 1993). However, such LVAs and AML have been discovered at the centers of some magmatically-robust slow and ultraslow segments, such as the Lucky Strike at the MAR and SWIR 50°28'E (Chapter 1.3.6).

1.5.2 The thermal regime with respect to spreading rate

A strong correlation between the axial thermal regime and spreading rate has been shown by seismic studies over the last three decades (Christeson et al., 2019; Grevemeyer et al., 2019). The maximum depth of earthquakes and AML depths at the MORs tend to be greater as spreading rate decreases, which could be predicted by numerical thermal models. Phipps Morgan and Chen (1993) parameterized the effect of hydrothermal circulation on heat transfer by an increased effective thermal conductivity by a factor Nu, the Nusselt number, that ranges between 1 and 12. With Nu=8 and a cut-off temperature of hydrothermal circulation of 600°C, the 750°C isotherm fits with the observed base of the seismogenic lithosphere at the MOR (Figure 1.17). The observed AML depths at fast and intermediate spreading ridges also fit with simulations of Nu between 8 and 12 (Figure 1.17) (Chen and Lin, 2004; Phipps Morgan and Chen, 1993b). However, these simulations cannot precisely produce the axial thermal regime, especially because of the artificially parameterized hydrothermal convection.

Theissen-Krah et al. (2011) coupled magmatic (described by the Stokes equation) and hydrothermal (solved by Darcy-type convection of pure water) processes in crustal accretion by a 2D numerical model. Their model results also fit with the AML depths at fast and intermediate spreading for permeabilities between $4\text{-}6\times10^{-14}$ m^2. However, both numerical models cannot predict the presence of the AMLs and/or LVAs at the Lucky Strike and SWIR 50°28'E.

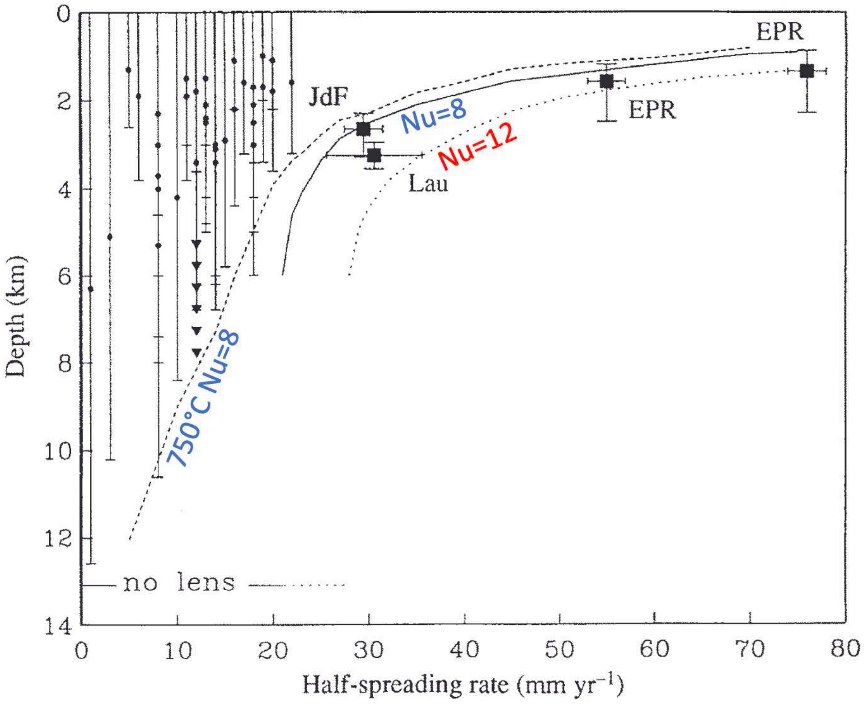

Figure 1.17. Depth vs. half spreading rate from Phipps Morgan and Chen (1993).

Curves are produced by numerical simulations with Nu=8 and Nu=12 and a cut-off temperature of hydrothermal circulation of 600°C. Filled squares with uncertainties represent the depth to the AMLs from multichannel seismic reflections at the EPR, JdFR, and Lau Basin. Vertical lines with small dots or triangles are earthquake depths at the MOR.

Chapter 2

Geological background of the Southwest Indian Ridge

In this chapter, I introduce the geological background of the SWIR, and then narrow to two endmembers in terms of melt supply: the magmatically-robust SWIR 50°28'E and the nearly-amagmatic SWIR 64°30'E.

2.1 The ultraslow-spreading Southwest Indian Ridge

The Southwest Indian Ridge (SWIR) accommodates the divergence between the Antarctic and Nubian/Somalian plates from the Bouvet Triple Junction (BTJ; 0°E) north-eastward to the Rodrigues Triple Junction (RTJ; 70°E), with a total length of about 7700 km (Figure 2.1). The SWIR is an ultraslow-spreading ridge with a full spreading rate of 12-16 mm/yr (Horner-Johnson et al., 2005; Patriat and Segoufin, 1988). At such a low spreading rate, melt supply has been shown to be highly variable on regional (Cannat et al., 2008; Georgen et al., 2001; Sauter and Cannat, 2010) and segment (Cannat et al., 1999; Grindlay et al., 1998; Sauter et al., 2001; Takeuchi et al., 2010) scales, displaying contrasting features in geomorphology, geophysics, and geochemistry.

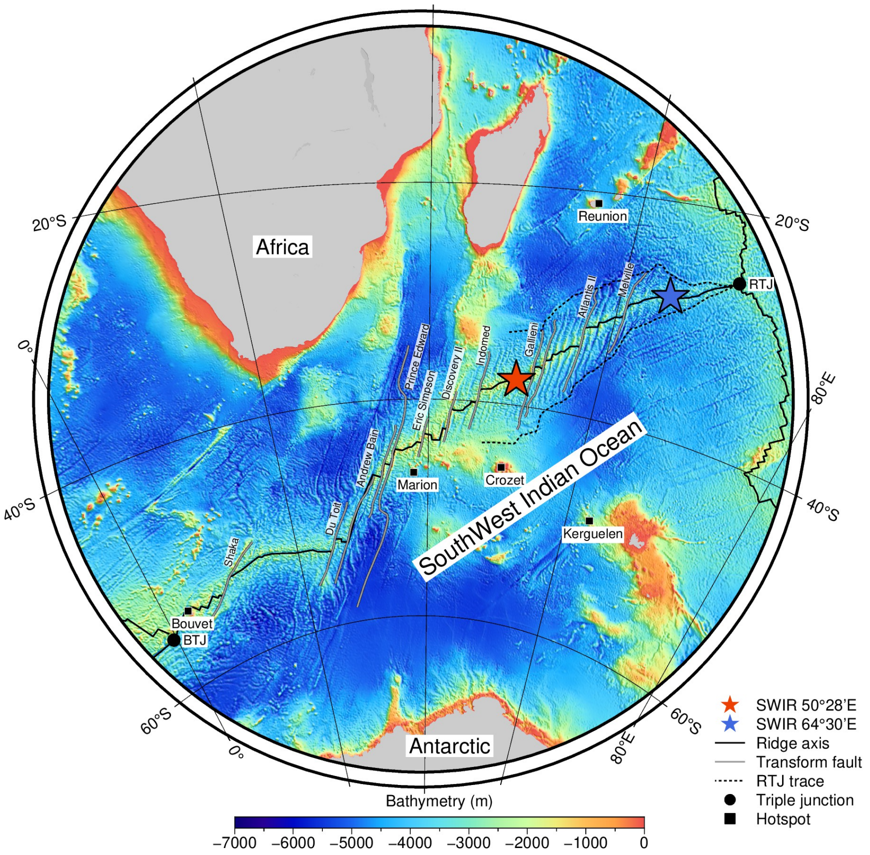

Figure 2.1. Bathymetric map showing the Southwest Indian Ridge.

See legend for symbols. Bathymetry data are derived from Weatherall et al. (2015). Red and blue stars indicate the locations of the SWIR 50°28'E and SWIR 64°30'E, respectively. BTJ: Bouvet Triple Junction; RTJ: Rodrigues Triple Junction. Figure from Chen (2021b) at figshare.

On the regional scale, the SWIR can be divided into 11 regions by major transform faults (TFs), showing abrupt changes in axial depth, Mantle Bouguer gravity Anomaly (MBA), and basalt Na8.0 (Cannat et al., 2008; Sauter and Cannat, 2010). In ridge regions with overall poor melt supply, the ridge axis is characterized by a deep axial valley with wide exposure of ultramafic rocks, positive MBA, and low degrees of melting, such as the eastern SWIR between the Melville TF and RTJ (Figure 2.2; Brunelli et al., 2018; Cannat et al., 2008; Sauter et al., 2013; Sauter and Cannat, 2010). In contrast to ridge regions with rich melt supply, the ridge is characterized by a shallower axial valley, active volcanism producing mafic rocks on the seafloor, negative MBA, and high degrees of melting, such as the SWIR between the Indomed and Gallieni TF, so-called Indomed-Gallieni supersegment (Figure 2.2; Brunelli et al., 2018; Sauter et al., 2009; Sauter and Cannat, 2010; Wang et al., 2020; Yu and Dick, 2020).

In segment scale, melt supply is apparently subject to along-axis focusing on discrete magmatic spreading cells (Lin et al., 1990), appearing in both melt-poor and melt-rich regions of the SWIR (Cannat et al., 1999; Grindlay et al., 1998; Sauter et al., 2001; Takeuchi et al., 2010). This melt focusing leads to segment centers receiving more melt than their corresponding ends, as observed in the MAR (Lin et al., 1990), associated with shallower depths and lower MBAs at segment centers (Figures 2.2a and 2.2b).

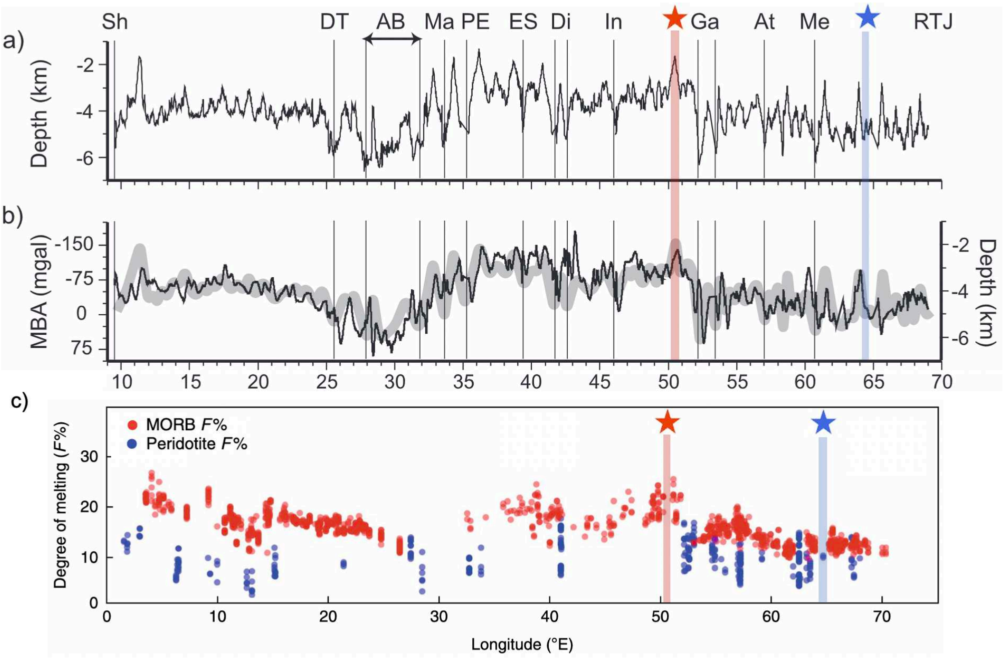

Figure 2.2. Variations of depth, MBA, and degree of melting along the SWIR axis.

(a) Depth profile. (b) Mantle Bouguer gravity Anomaly (MBA). (c) Degree of melting estimated from dredged basalts and peridotite. (a) and (b) are modified from Sauter and Cannat (2010), and (c) is modified from Brunelli et al. (2018). Red and blue stars with shadows indicate the locations of the SWIR 50°28'E and SWIR 64°30'E, respectively. Sh: Shaka TF; DT: Du Toit TF; AB: Andrew Bain TF; Ma: Marion TF; PE: Prince Edward TF; ES: Eric Simpson TF; Di: Discovery I and II TFs; In: Indomed TF; Ga: Gallieni and Gazelle TFs; At: Atlantis II TF; Me: Melville TF; RTJ: Rodrigues Triple Junction.

To better understand the impact of melt supply, in this thesis, I study two regions of the SWIR that are endmembers in terms of melt supply: the magmatically-robust SWIR 50°28'E located in the melt-rich Indomed-Gallieni supersegment and the nearly-amagmatic SWIR 64°30'E located in the melt-poor eastern SWIR (Figures 2.1 and 2.2). Geological backgrounds of both endmembers are introduced in the following chapters 2.2 and 2.3, respectively.

2.2 The magmatically-robust SWIR 50°28'E

The SWIR 50°28'E is located at the center of segment #27 (Figure 2.3a), named by Cannat et al. (1999b). The central volcano is bounded by two elevated volcanic regions that extend over almost the entire present-day ridge segment (Figure 2.3a), which are interpreted as the conjugate rifted remnants produced during a more magmatically-robust period (Mendel et al., 2003). This is likely associated with an event of mantle melting anomaly occurring in the Indomed-Gallieni supersegment at 11-8 Ma ago (Sauter et al., 2009). The excess melt propagated eastward with a velocity of 30 km/Ma, resulting in V-shaped elevation of seafloor and a reduction of MBA (Sauter et al., 2009). The SWIR 50°28'E has been the magmatic apex of this melting event after ~6 Ma ago, although the present-day magmatism is weaker (Mendel et al., 2003). The origin of the melting event is still in debate by recent studies: 1) interaction between the SWIR and Crozet hotspot (Breton et al., 2013; Li et al., 2021; Sauter et al., 2009; A. Y. Yang et al., 2017; Zhang et al., 2013), 2) a local micro hotspot (Yu and Dick, 2020), or the involvement of subarc depleted mantle (Li et al., 2017; Wang et al., 2020, 2021).

The crust at the SWIR 50°28'E, indicated by seismic tomography (Jian et al., 2017a), is uniquely thick at 9.5 km with a low-velocity anomaly (LVA) at depths of ~4-9 km (Figures 2.3b-2.3e). This LVA is interpreted as an axial magma chamber (AMC), composed of mostly crystallized gabbros with up to 10% melt (Jian et al., 2017b). The across-axis section over the segment center (Figures 2.3d and 2.3d) shows that the depth to the Moho is constant at 9.5 km within at least 3 Ma (20 km off the axis; Jian et al., 2017a). This Moho depth in the along-axis section is reduced to ~7 km, 20 km away from segment center (Figures 2.3c and 2.3c), and even reduced to only 4 km at the western end of the segment, indicating an extremely focused melt supply at the segment center (Li et al., 2015). Seismicity is low at the SWIR 50°28'E, with only a few microearthquakes on the axis (Yu et al., 2018). Extensive hydrothermal plumes anomalies were detected over the segment (Yue et al., 2019), including the nearly extinct Duanqiao hydrothermal field at the segment center (Tao et al., 2014, 2012), presumably associated with sufficient heat sources provided by the AMC underneath (Jian et al., 2017b; Yue et al., 2019).

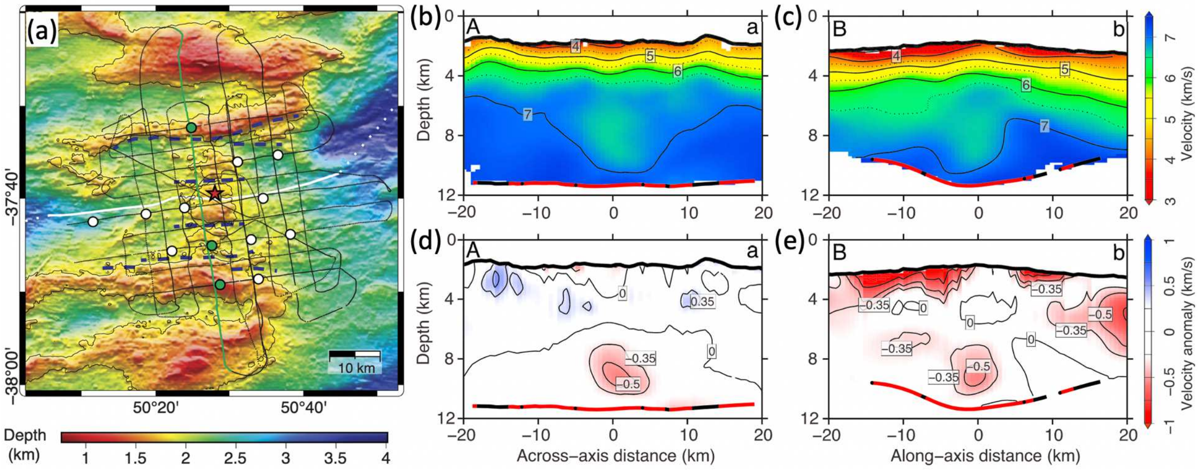

Figure 2.3. Geological background of the SWIR 50°28'E.

(a) Bathymetric map with a 3D seismic refraction survey, modified from Jian et al. (2017b). Solid white lines show the ridge axis, and dashed white lines indicate NTDs. Dark blue dashed curves are the bounding faults. The black contour marks the 1800 m water depth, delimiting the central volcano. The red star indicates the location of the Duanqiao hydrothermal field. Thin dotted curves and circles represent the tracks of shots and locations of ocean-bottom seismometers (OBSs), respectively. Across- and along-axis depth profiles showing seismic velocity in (b) and (c) and seismic velocity anomalies in (d) and (e), modified from Jian et al. (2017a). The Moho interfaces at the bottom are shown as thick curves, in which the red color marks the PmP reflection points. (b) and (c) The velocities are contoured at every 0.5 km/s and labelled at every 1 km/s. (d) and (e) Velocity anomalies are calculated by subtracting an average velocity-depth profile within the along-axis distance of ±15 km (Jian et al., 2017a). The anomalies are contoured at 0, ±0.35, and ±0.5 km/s.

2.3 The nearly-amagmatic SWIR 64°30'E

The SWIR 64°30'E is a corridor of spreading located between the two large axial volcanos of segments #8 and #11 (Figure 2.4a). In this corridor, geological and geophysical observations converge to suggest that melt supply is nearly zero (Cannat et al., 2006). Mantle-derived peridotites are extensively observed on the seafloor with only a few isolated patches of hummocky basalts (Figure 2.4b; Sauter et al., 2013). The seafloor near the SWIR 64°30'E corridor is called smooth seafloor: it is characterized by a series of axis-parallel ridges with a rounded, smooth topography at wavelengths of 15-30 km and heights of 500-2000 m (Figure 2.4a), corresponding to positive gravity anomalies (Cannat et al., 2006). These ridges are hypothesized as successive flip-flop detachment faults, accommodating nearly 100% of the plate divergence and continuously exhuming mantle-derived rocks (Cannat et al., 2019b; Reston, 2018; Sauter et al., 2013).

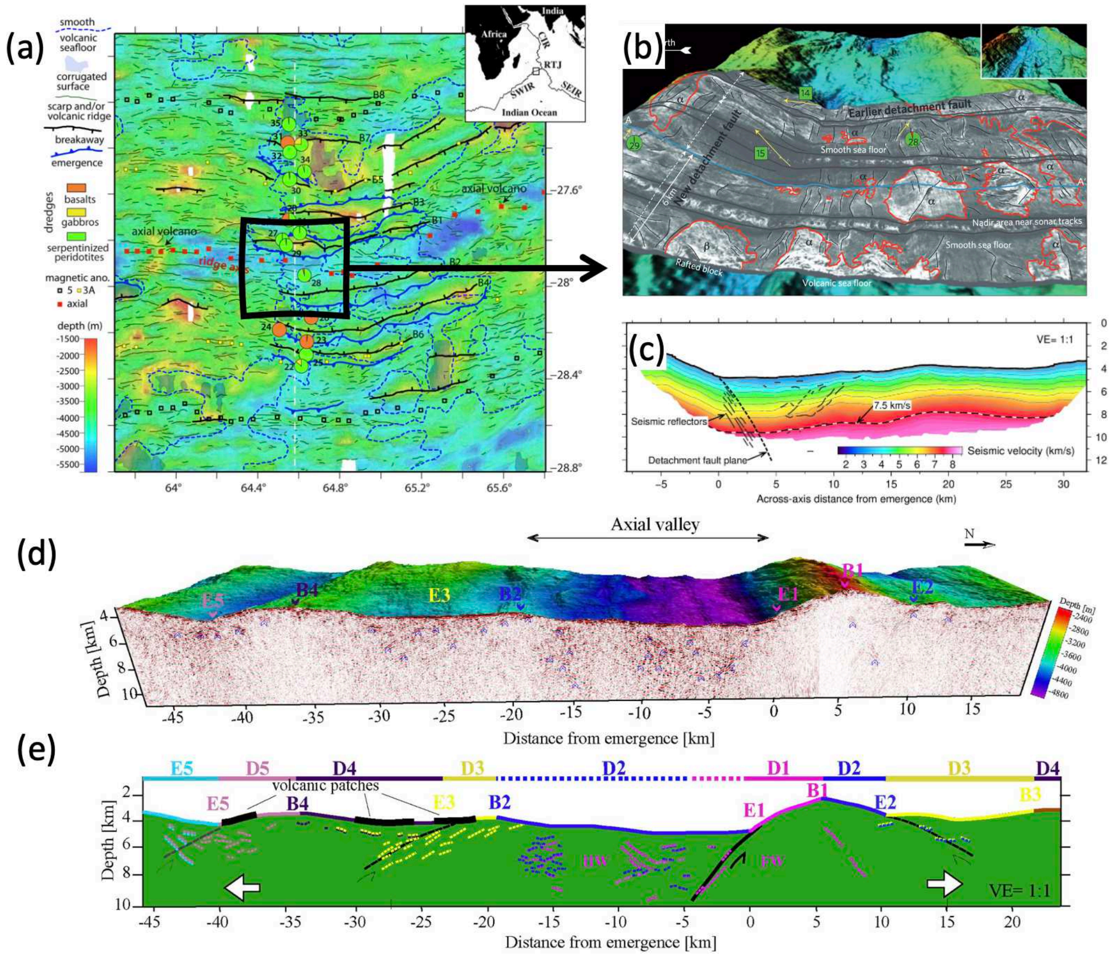

Figure 2.4. Geological background of the SWIR 64°30'E.

(a) Geological map of the SWIR 64°30'E, modified from Cannat et al. (2019). See legend for symbols. Detachment faults breakaways (B) and emergences are numbered from 1 (presently active) to 8 (initiated at ~11 Ma ago). (b) 3-D view of TOBI reflectivity draped on bathymetry for the youngest detachment fault, modified from Sauter et al. (2013). Extensive smooth seafloor corresponds to low reflectivity. Small patches of hummocky basalts with high reflectivity are indicated as α and β for the older and the youngest detachment faults, respectively. (c) Seismic velocity model across the youngest detachment fault, modified from Momoh et al. (2017). The velocity contour of 7.5 km/s is used for the base of the crust. (d) Seismic reflection data along the cross-section in Figure 2.4a (dashed white line) with the bathymetry overlain, modified from Momoh et al. (2020). Breakaways (B) and emergences (E) of detachment faults are as indicated in Figure 2.4a. (f) Simplified interpretation based on Figure 2.4d. The black lines indicate the inferred fault planes for the active and inactive (dashed) detachments. Different colors correspond to the active time of successive detachment faults, indicated by colored lines and labels atop the figure. Black lines on the seafloor indicate isolated basaltic patches.

The detachments continuously cut into the footwall of their predecessors by flipping polarities with a lifetime of 0.6-1.5 Ma (Bickert et al., 2020; Cannat et al., 2019b; Sauter et al., 2013). This hypothesis was recently confined by seismic reflection (Momoh et al., 2020, 2017), which imaged the detachment fault planes down to at least 5 km below the seafloor with intensive damage zones at a dip of 50° for the youngest detachment fault and dips of 25° for the older detachment faults (Figures 2.4d and 2.4e). There are some seismic reflectors also imaged in the hanging walls of the flip-flop detachment faults, interpreted as conjugate, small-offset normal faults and sparse melt sills (Figure 2.4a; Momoh et al., 2020, 2017). Consequently, there is no classic crust (basaltic layer 2A, sheeted dike complex layer 2B, and gabbroic layer 3) at the SWIR 64°30'E, but mostly peridotite with different extents of serpentinization, although a 5 km-thick crust is defined by the seismic velocity contour of 7.5 km/s (Figure 2.4c; Momoh et al., 2017).

Chapter 3

780 thousand years of upper-crustal construction at a melt-rich segment of the ultraslow spreading Southwest Indian Ridge 50°28'E

In this chapter, I focus on the magmatically-robust endmember at the center of the SWIR 50°28'E segment, first using high-resolution bathymetry and backscatter data, near-bottom magnetic data, and seafloor photographs. This chapter was published as: Chen, J., Cannat, M., Tao, C., Sauter, D. & Munschy, M. (2021). 780 thousand years of upper-crustal construction at a melt-rich segment of the ultraslow spreading Southwest Indian Ridge 50°28’E. Journal of Geophysical Research: Solid Earth (doi: 10.1029/2021JB022152). I carried out all the geological interpretations and mapping, produced all figures, and wrote the manuscript, under the supervision of Mathilde Cannat. Chunhui Tao led the data acquisition and bathymetry data processing. Daniel Sauter and Marc Munschy processed near-bottom magnetic data.

3.1 Abstract

Melt supply at the ultraslow-spreading Southwest Indian Ridge (SWIR) has been shown to vary from nearly-amagmatic, leading to ultramafic seafloor, to magmatically-robust, producing fully volcanic seafloor. The center of the SWIR 50°28'E segment represents a magmatically-robust endmember. High-resolution bathymetry and backscatter, near-bottom magnetic data, and visual observations were acquired to infer spatiotemporal variations in upper-crustal construction over the past 780 kyr. Tectonic strain inferred from observed faults represents <8% of the total plate divergence during this period. Mapped seafloor and lava morphologies show a prevalence of smooth seafloor and smooth hummocky seafloor (64% mapped area), corresponding to a dominance of high-effusion-rate, sheet-lobate lavas, over hummocky seafloor (29%) that mostly comprises low-effusion-rate pillow lavas. This prevalence is most pronounced within a ~5 km-long domain at the segment center, while hummocky seafloor prevails to its east and west, indicating a substantial along-axis decrease in average eruption rate. Across-axis changes of seafloor morphologies and faulting pattern indicate two successive cycles of upper-crustal construction. These cycles last ~300 kyr, interpreted as waxing and waning magmatic phases. During waxing phases, shallow axial melt lenses (AMLs) form beneath the segment center, feeding narrow diking systems that build high-eruption-rate smooth domal volcanos. During waning phases, lower frequencies of melt replenishment may cause the AML to become deeper and ultimately disappear. This configuration triggers diking and hummocky-dominated eruptions over a wider axial domain, with more faults. We propose that modes of upper-crustal construction at slow and ultraslow mid-ocean ridges are influenced by melt supply more than spreading rate.

3.2 Introduction

Mid-Ocean Ridges (MORs) are one of the Earth's principal volcanic systems: magma forms in the upwelling mantle in response to plate divergence, and dike intrusions and volcanic eruptions build the upper crust. Modes of upper-crustal construction have been shown to vary as functions of spreading rate, magma supply, and tectonic deformation (Cannat et al., 2019b; Colman et al., 2012; Perfit and Chadwick, 1998). At those ridge segments that have a crustal magma mush zone capped by a shallow axial melt lens (AML), e.g., 9°30'N of fast spreading East Pacific Rise (EPR), as inferred from the detection of a seismic low-velocity anomaly (LVA; Dunn et al., 2000) and an AML reflector (Detrick et al., 1987), volcanic eruptions mostly produce high-eruption-rate, sheet-lobate dominated, smooth lava flows (Fundis et al., 2010). When the AML reflector gets deeper, e.g., 91-95°W of intermediate spreading Galapagos Spreading Center (GSC; Blacic et al., 2004), low-eruption-rate hummocky lava flows (pillow dominated) also occur, and meanwhile faults contribute to a larger part of plate divergence (Colman et al., 2012). Key characteristics of the ridge's magma plumbing system possibly can therefore be indirectly inferred from seafloor and lava morphologies, if bathymetry and backscatter data are available at sufficient resolution, and backed by seafloor videos or photographs (Colman et al., 2012; Escartín et al., 2014; Fundis et al., 2010; Sauter et al., 2002; Searle et al., 2010).

Shallow AMLs typically characterize fast spreading ridges, while intermediate spreading ridges tend to have deeper AMLs (Chen and Morgan, 1990). Crustal LVA and/or AML reflectors have not been found as frequently at slow and ultraslow spreading ridges (Detrick et al., 1990; Hooft et al., 2000; Minshull et al., 2006), and hummocky lava flows dominate (Sauter et al., 2002; Searle et al., 2010). However, crustal LVAs and/or AML reflectors that extend only a few kilometers from their segment centers have been documented at a few magmatically-robust slow spreading segments, such as the Lucky Strike segment at the Mid Atlantic Ridge (MAR; Combier et al., 2015; Seher et al., 2010; Singh et al., 2006) and the 50°28'E segment at the ultraslow spreading Southwest Indian Ridge (SWIR; Jian et al., 2017a; Jian et al., 2017b). These segments display large along-axis variations in both seismic velocity structure and seafloor morphology. Lucky Strike has a dome-shaped volcanic construct built by smooth lava flows above the documented AML at the segment center while ridge-parallel hummocky ridges form towards segment ends (Escartín et al., 2014). This characteristic is consistent with a strong focusing of melt supply on the segment center (Lin et al., 1990). Escartín et al. (2014) listed 16 examples of dome-shaped volcanos at the center of slow and ultraslow spreading ridge segments, and suggested that a crustal melt mush zone is likely to be the key to form such large volcanic constructions and that their common fate is to become rifted by axial graben faults.

Seismic tomography results obtained at the center of the SWIR 50°28'E segment (segment #27 in Cannat et al., 1999; Figure 3.1a) show a uniquely thick crust (9.5 km) and a rounded crustal LVA ~4-9 km below the seafloor (bsf) with a horizontal diameter of 5-6 km at the -0.4 km/s contour (Jian et al., 2017a; Jian et al., 2017b). Seismic reflection data are not available to confirm the existence of an AML on top of this LVA. However, Full Waveform Inversion results show a sharp decrease in seismic velocity at a depth of about 4 km, which is interpreted to be due to mostly crystallized gabbros with up to 10% melt (Jian et al., 2017a).

The depth to the Moho indicates that crustal thickness is reduced to 6.6-7.6 km midway to the segment ends (profile B-B' of Jian et al., 2017b located in Figure 3.1a). Seismicity is low beneath the SWIR 50°28'E segment, yet a few microearthquakes have been located down to ~10 km bsf on or close to the ridge axis and at least 3 km laterally to the west of the LVA (Yu et al., 2018), indicating that the brittle lithosphere there is a bit thicker than the crust. The axial domain is bounded by two elevated regions that extend over the full length of the present-day ridge segment (prominent scarps near magnetic anomaly 2A in Figure 3.1a), and are interpreted by Mendel et al. (2003) as the conjugate rifted remnants of a yet more magmatically-robust period of spreading. This period of very high melt influx has been interpreted as due to the eastward migration of a mantle melting anomaly (Sauter et al., 2009). Present-day magmatism at the 50°28'E segment is a bit weaker, even at the segment center (Mendel et al., 2003), but remains more magmatically-robust than at other SWIR segments.

Here, we report on high-resolution (HR) bathymetry and backscatter, seafloor videos and photographs, and near-bottom magnetic data, collected over a 13 by 12 km area at the center of the SWIR 50°28'E segment (Figure 3.1). This survey is located above the LVA and is bounded by the Brunhes-Matuyama (B-M) reversal (780 kyr). It includes the Duanqiao extinct black-smoker hydrothermal field (HF; Tao et al., 2012) and several hydrothermal plume anomalies (Yue et al., 2019). The variations of seafloor and lava flow morphologies at the center of the SWIR 50°28'E segment over the past 780 kyr provide constraints in space and time to improve the general understanding of the effects of spreading rate and melt supply on upper-crustal construction at MORs.

3.3 Data and methods

3.3.1 AUV surveys

The autonomous underwater vehicle (AUV) QianLong-II investigated the center of the SWIR 50°28'E segment during the DY40 cruise aboard R/V Xiangyanghong-10 in 2016. The AUV was equipped with a newly-developed High-Resolution Bathymetric Sidescan Sonar System (HRBSSS; Liu et al., 2016) and a three-component magnetometer (Wu et al., 2019). During dives 27, 29, and 30, the AUV surveyed at an altitude of ~100 m above the seafloor at a speed of 1-2 kt with a track spacing of 400 m (Figure 3.1b). A short AUV-borne camera survey (dive 20) was conducted at ~5 m above the seafloor near the Duanqiao HF. Navigation was achieved by combining the inertial navigation system (IXBLUE PHINS-

6000) with a long baseline system (Wu et al., 2019).

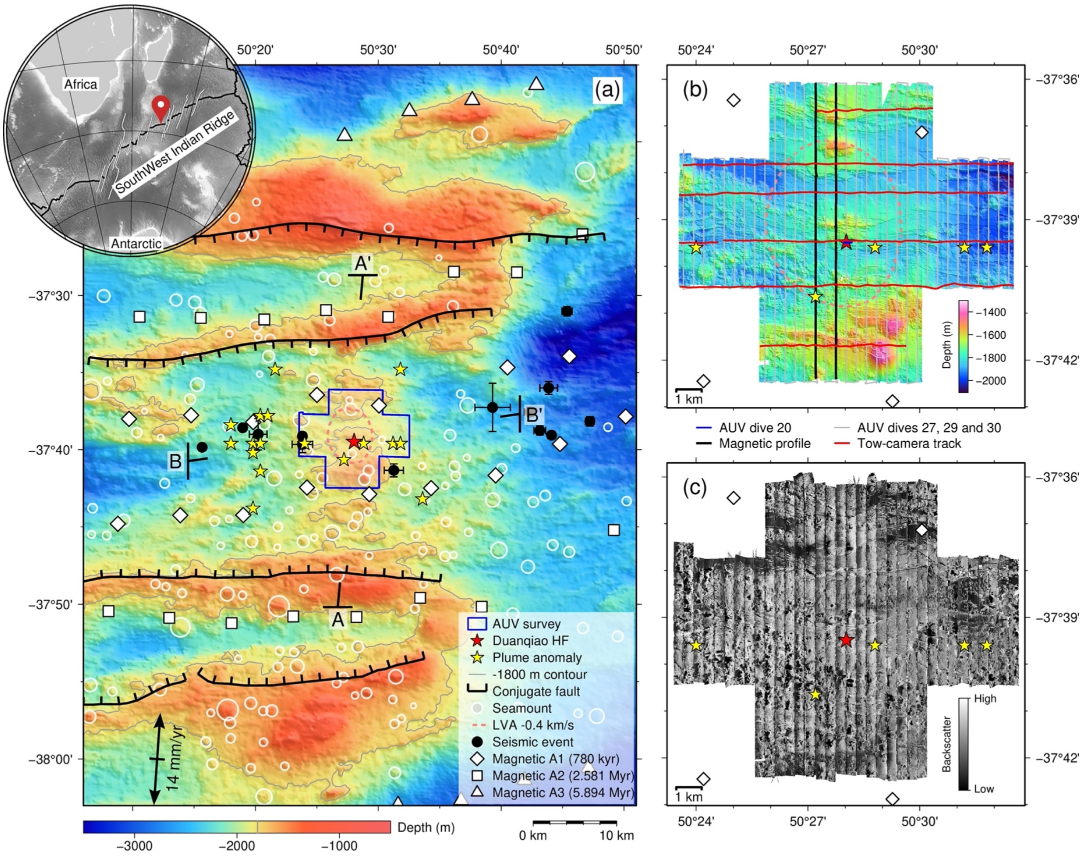

Figure 3.1. Shipboard bathymetric map of the SWIR 50°28'E segment and high-resolution bathymetry and backscatter at the center segment.

(a) Shipboard bathymetric map of 50°28'E segment (segment #27 in Cannat et al., 1999) at the Southwest Indian Ridge (SWIR). Conjugated faults mark the rifted remnants of elevated seafloor regions. Red star is the location of the Duanqiao hydrothermal field, and yellow stars indicate hydrothermal plume anomalies (Yue et al., 2019). Magnetic A1 (Brunhes-Matuyama reversal), A2, and A3 (white-filled symbols) are pickings from sea-surface magnetic anomaly (Sauter et al., 2009). The dashed pink line in (a) and (b) outlines the P-wave low-velocity anomaly (LVA) of -0.4 km/s at 7 km bsf, which is calculated by subtracting an average velocity-depth profile within along-axis distance of ±15 km (Jian et al., 2017b). AA' and BB' mark locations of seismic profiles across and along the ridge axis from Jian et al., (2017b). Black dots with error bars indicate the epicenters of microearthquakes (Yu et al., 2018). (b) and (c) High-resolution (gridded at 2m) bathymetry and backscatter at the center of 50°28'E segment. Grey lines are tracks of AUV QianLong-II dives 27, 29, and 30. Thick black lines are two magnetic profiles shown in Figure 3.7. Red lines show the deep-tow camera tracks. Short blue line near the Duanqiao hydrothermal field is a camera track during AUV dive 20.

3.3.1.1 High-resolution bathymetry and backscatter data

The HRBSSS was operated at 150 kHz with a swath width of 250 m during dives 27, 29, and 30. The bathymetry and backscatter data were processed using the CleanSweep software to create a 2-m resolution grid (Figures 3.1b and 3.1c). The combined bathymetry data cover

~110 km^2 of seafloor (13 km along axis and 12 km across axis). The data remain noisy despite processing (the DY40 cruise was the first deep sea operation for the HRBSSS system of the AUV). We were cautious to adapt the scale and scope of our observations to the relatively poor quality of the data.

3.3.1.2 Magnetic anomalies

For this study, we processed two across-axis magnetic profiles in the center of the AUV map, collected with a 1 Hz sampling frequency (Figure 3.1b). The magnetic effect from the AUV was estimated and removed (Wu et al., 2019). The local geomagnetic field predicted by International Geomagnetic Reference Field (IGRF) was removed (Thébault et al., 2015), and Reduction-To-Pole (RTP) was applied to locate the anomalies directly above their possible sources by correcting the inclination and declination of the geomagnetic field.

3.3.2 Deep-tow video and seafloor photographs

In this study, we analyzed 24 hours of video and 3647 photographs covering 6 ridge-parallel transects within the AUV survey area (Figure 3.1b). These data were collected in 2015 during the DY34 cruise aboard R/V Dayangyihao (Yue et al., 2019) with the Deep-tow Hydrothermal Detection System, navigated with an ultrashort-baseline (USBL) system (Yue et al., 2019).

3.3.3 Geomorphological analysis

Following previously published geomorphological studies of the MORs (Colman et al., 2012; Escartín et al., 2014; Fundis et al., 2010; Sauter et al., 2002; Searle et al., 2010), we used HR bathymetry and backscatter data to classify distinct seafloor morphologies and to map fault scarps and fissures (Figure 3.2). Optical seafloor imagery was used to identify lava morphologies, with the occurrence of pillow, lobate, and sheet lavas that have been interpreted as mainly resulting from low, intermediate, and high effusion rates, respectively (Colman et al., 2012; Fundis et al., 2010; Gregg and Fink, 1995). We also tentatively identified eruptive units, which we infer formed during a given eruptive sequence, characterized by similar eruptive dynamics (e.g., Colman et al., 2012), based on seafloor morphology and the nature of their contacts with the surrounding seafloor.

3.3.3.1 Seafloor morphology classification

Four distinct seafloor morphologies, i.e., smooth, hummocky, smooth hummocky, and sedimented terrains, were visually identified on HR bathymetry and backscatter maps. Each is described below and in Table 3.1.

Smooth terrain is characterized by dominantly flat seafloor with higher backscatter than sedimented areas, which displays volcanic features, such as ***lava flow fronts***, ***lava tubes***, and ***lava channels***. Lava flow fronts are associated with the edges of individual sequences of smooth lava flows (Figure 3.2d). Lava tubes are narrow and sinuous with different extents of collapse (Figure 3.2e), which is called uplifted tumuli (Appelgate and Embley, 1992). Lava channels have wider (up to 100 m) and sinuous depressions (Figure 3.2f).

Hummocky terrain has a rough topography with numerous individual ***volcanic cones***. Volcanic cones are defined as cone-shaped volcanic edifices 2 to 415 m in diameter and up to 96 m in height (Figures 3.2b and 3.3b). Backscatter is generally high in hummocky terrain but patchy due to the rough relief. Hummocky terrains commonly occur as ridges, elongated sub-parallel to the ridge axis (e.g., l in Figure 3.2a).

Smooth hummocky terrain mixes the characteristics of hummocky and smooth terrains: rougher topography than smooth terrain but less so than hummocky terrain (Figure 3.2c). In the mapping of these terrains, we took scale into consideration: for example, in Figure 3.2c: flat seafloor in the center extends >500 m with very few volcanic cones and is therefore identified as smooth, while flat seafloor in the south is relatively elevated and extends <300 m between volcanic cones, leading to classification as smooth hummocky.

Sedimented terrains are characterized by flat seafloor with uniformly low backscatter (Figure 3.2c).

Seamounts are defined here as volcanic cones with diameters of >500 m (Searle et al., 2010). They can be flat-topped (j in Figure 3.2a), bowl-shaped, display collapsed ***craters*** (Figure 3.2g), or fissured summit domes (Figure 3.2h).

3.3.3.2 Fault scarps and fissures

Linear features, i.e., ***fault scarps*** and ***fissures***, were automatically detected from bathymetry, using the method by Panagiotakis and Kokinou (2015), then confirmed visually and digitized using backscatter and slope maps (Figure 3.1). Fault scarps are linear and correspond to sharp changes in bathymetry, slope, and backscatter (Figures 3.2f and 3.2i). Digitized fault scarps (Figure 3.4a) trace the scarp tops. Fissures correspond to narrow (<40 m) and linear depressions (Figures 3.2f, 3.2h, and 3.2i). Digitized fissures trace the bottom of the fissure gaps. Fracture density (Figure 3.4b), including both fault scarps and fissures, was calculated as a kernel density with a grid size of 10 m and a search radius of 250 m.

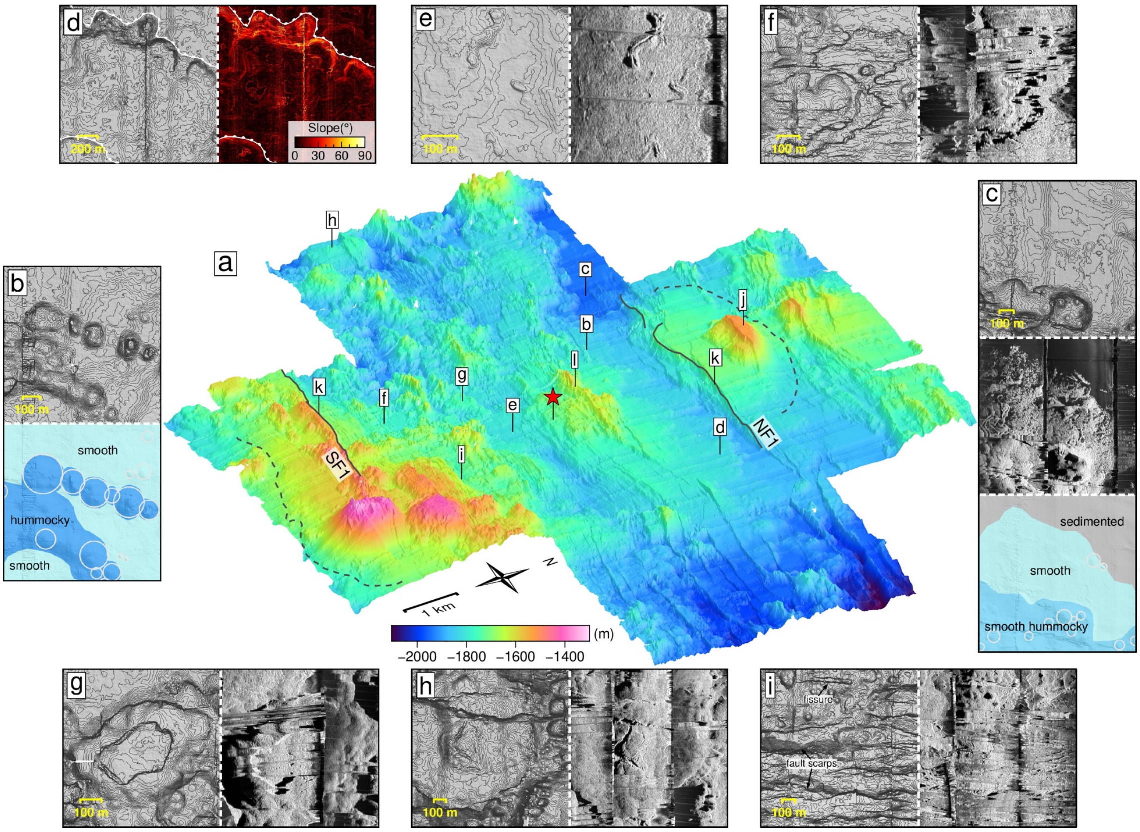

Figure 3.2. 3-D view bathymetric map of the SWIR 50°28'E and close-up views.

(a) 3-D view of HR bathymetry at the center of the SWIR 50°28'E segment, viewed from the ESE. Letters refer to locations of close-up views (b) to (i), and of features (j) to (l). Dashed lines show the approximate contour of the north and south flank of a rifted domal volcanic feature. Solid lines trace the top of conjugate fault scarps NF1 and SF1. Red star is the location of the Duanqiao hydrothermal field. (b) Example of seafloor morphologies for hummocky and smooth terrains (contours in 2 m and the same below). White circles represent volcanic cones. (c) Example of seafloor morphologies and backscatter for smooth hummocky, smooth, and sedimented terrains. (d) Lava flow fronts on smooth terrain in bathymetry (left) and slope (right) maps. (e) Lava tubes on smooth terrain in bathymetry (left) and backscatter (right) maps (the same below), with different extents of collapse (uplifted tumuli; Appelgate & Embley, 1992). (f) Collapsed lava channel with a dense network of fault scarps and fissures on smooth terrain. (g) Seamount with a central collapsed crater. (h) Seamount with a summit dome and radial fissures. (i) Dense network of fault scarps and fissures.

3.3.4 Tectonic strain estimation

Fault scarps and fissures exposed on the seafloor allow an estimation of the tectonic contribution to plate divergence at the upper crustal level, because successive lava flows potentially bury pre-existing faults and fissures. This upper crustal tectonic strain is not necessarily representative of the tectonic strain at the scale of the axial lithosphere: upper-crustal faults and fissures may also form as a response to the emplacement of dikes that do not reach the seafloor (Rubin and Pollard, 1988). The tectonic strain was estimated on the basis of the measurements of vertical fault throw (D) and fault dip (α) along axis-perpendicular profiles. Fault throw is defined as the depth difference between the top and bottom of the scarp, and its cumulative frequency theoretically fits an exponential distribution if the picking process provides a good record of small fault scarps (Deschamps et al., 2007). Because fault dip could be sharply decreased at the scarp bottom by the presence of mass wasting and/or post-faulting lava flows, the dip is defined as the largest value along the scarp. The cumulative horizontal fault heave (H) along the profiles is calculated by the equation:

$$H = D/tan(\alpha)$$

The tectonic strain (Ts) along profiles is then calculated from the equation:

$$Ts = 100\% \times H/L,$$

where L is the length of profiles. Fissures are neglected due to their small openings.

3.4 Results

The most prominent topographic features at the center of the SWIR 50°28'E segment are two elevated regions rifted by a pair of conjugate fault scarps with throws >100 m, NF1 and SF1 (k in Figure 3.2a). These elevated regions include several large seamounts (e.g., j in Figure 3.2a) that rest on a rifted domal structure (dashed lines in Figure 3.2a). The contours of this domal structure are more visible in the northern flank. They are obscured in the southern flank by a large seamount and several hummocky ridges (Figure 3.2a). Several flat-topped seamounts have been dissected by normal faults, with one half still visible (e.g., j in Figure 3.2a). Seamounts are less frequent in the near-axis region between fault zones NF1 and SF1, where the dominant topographic features are axis-parallel hummocky ridges and low-throw fault scarps (Figure 3.2a). In this near-axis region, there is no clear contrast in backscatter (Figure 3.1c) that would indicate where the most recent eruptions have occurred. In the following paragraphs, we analyze the distributions of the map-scale seafloor morphologies, photo-scale lava morphologies, eruptive units, and fault scarps and fissures (Figures 3.3 and 3.4).

3.4.1 Distribution of map-scale seafloor morphologies

The smooth seafloor morphology represents 38% of the total AUV-mapped area, smooth hummocky morphology 26%, hummocky morphology 29%, and sedimented seafloor 7% (Figure 3.3a). The smooth morphology covers vast expanses of the seafloor, particularly in the center and north parts of the map. The smooth hummocky morphology covers most of the relatively lower backscatter region in the south-eastern part of the map. The hummocky morphology is more abundant in the west of the map and is associated with elongated ridges and isolated patches of seafloor that are more elevated than their surroundings. Sedimented seafloor mainly occurs in the distal parts of the mapped area. The density of volcanic cones in the entire mapped area is 13.9 /km^2 with a total of 1529 cones, and this value increases from smooth (4.2 /km^2), smooth hummocky (17.2 /km^2), to hummocky (26.9 /km^2) morphologies. The average cone height in the map is 17.2 m, with the same trend increasing from smooth (8.0 m), smooth hummocky (12.4 m), to hummocky (22.1 m) morphologies.

Along-axis statistics of seafloor morphology and volcanic cones in the near-axis region between conjugate fault zones NF1 and SF1 are shown in Figure 3.3b. Smooth and smooth hummocky seafloor (>70%) are dominant within a ~5 km-long central domain (6-11 km in Figure 3.3b), while hummocky seafloor becomes prevalent to the east and west of this central domain. The distribution of volcanic cones is coincident with this trend of seafloor morphology: lower cone density and height (mostly <20 m) in the central domain, and larger cone density and height (2-96 m) outside this domain (Figure 3.3b).

3.4.2 Distribution of photo-scale lava morphologies

Lava morphologies (pillow, lobate, and sheet lavas) were identified from seafloor photographs along 6 ridge-parallel transects (Figures 3.3c and 3.5). The distribution of lava morphologies is consistent with the seafloor morphologies identified from HR mapping over these 6 transects (Figures 3.3c and 3.3d). Smooth terrain along the documented transects is characterized by 50% lobate-sheet lavas and 28% pillow lavas, while hummocky terrain is mainly composed of pillow lavas (65%) with only 23% lobate-sheet lavas (the rest are talus or sediments). Smooth hummocky terrain has 57% pillows and 32% lobate-sheet lavas. Seafloor mapped as sedimented corresponds to seafloor photographs that show 65% are fully covered by sediment, the rest being made up of heavily sedimented pillows, lobate lava or sheet lavas (Figure 3.3d). Omitting photographs of talus and complete sediment cover, the normalized proportions of pillow lava and lobate-sheet lava flows are 59% and 41%, respectively, along the 6 investigated transects (Figure 3.3d).

3.4.3 Eruptive units

39 eruptive units are proposed in Figure 3.3c. Most (29) correspond to small hummocky ridges or portions of larger hummocky ridges, for which contrasts in morphology or seafloor reflectivity suggest a chronology in volcanic construction. The 8 mapped seamounts are also

identified as eruptive units. The remaining 2 eruptive units are successive sequences of smooth terrain bounded by 15-75 m high, lobate, and up to 8 km-long lava flow fronts, that are located just south of fault zone NF1 (Figure 3.2d).

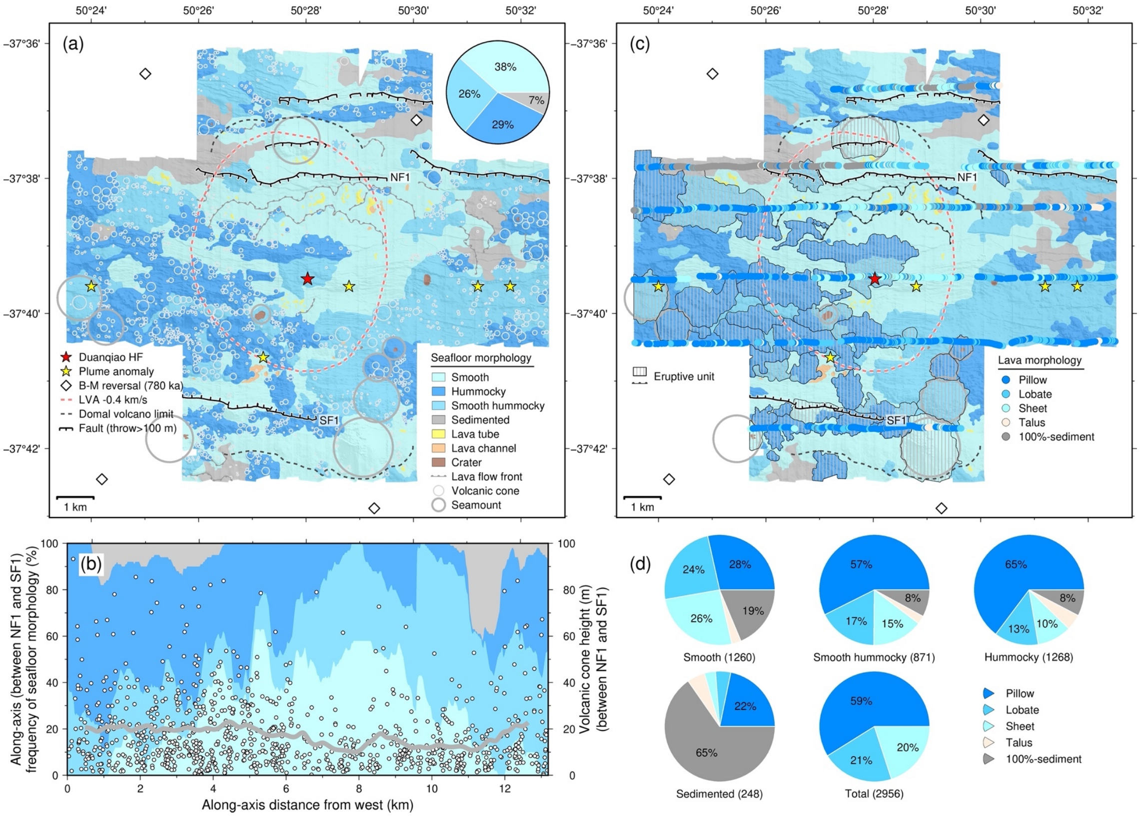

Figure 3.3. Interpretations in seafloor and lava morphologies.

(a) Bathymetric interpretation in seafloor morphologies of smooth (38%), smooth hummocky (26%), and hummocky (29%) and sedimented (7%) seafloor, as well as lava tubes, lava channels, craters, volcanic cones, and seamounts. NF1 and SF1 are two conjugate normal faults. Dashed pink line outlines the P wave LVA of -0.4 km/s at 7 km bsf (Jian et al., 2017b). Dashed black lines show the limit of the domal volcano, identified in Figure 3.2a. Red star is the location of the Duanqiao hydrothermal field. B-M reversal: magnetic anomaly pickings for Brunhes-Matuyama reversal (Sauter et al., 2009). (b) Along-axis statistics of seafloor morphology and volcanic cones between the conjugate NF1 and SF1. Lava tubes, lava channels, and craters are omitted in seafloor morphology. Circles indicate heights of individual cones. Thick gray line indicates the moving average of cone height with a window of 1 km and a step of 0.2 km. (c) Lava morphologies interpreted from seafloor photographs superimposed on the map of seafloor morphology. Pillow, lobate, and sheet lava, as well as talus and 100%-sediment are classified. 37 proposed eruptive units of hummocky ridges and seamounts are presented as closed and vertical-bar filled areas. 2 proposed eruptive units of smooth lava flows are presented as unclosed lava flow fronts. (d) Proportion of seafloor photographs showing the distribution of lava morphologies on each type of seafloor morphology over the same transects. The normalized proportion in total is calculated by omitting photographs of 100%-sedimented seafloor and talus.

3.4.4 Pattern of fault scarps and fissures

923 fault scarps and 441 fissures were recognized in the HR bathymetry map (Figure 3.4). Seafloor photographs show talus at the base of some fault scarps (e.g., Figure 3.5h). Fault scarps were classified into three groups according to their maximum throws: >100 m, 10-100 m, and <10 m (Figure 3.4a). The larger fault scarps include the conjugate NF1 and SF1. Individual fault scarps extend 0.05 to >4 km. NF1, and SF1, the most prominent fault scarps, are comprised of several individual faults (Figure 3.4a). Fissures are 20-530 m long, up to 38 m wide and up to 20 m deep. They are more abundant in smooth and smooth hummocky seafloor than in hummocky seafloor. Cumulative frequency of lengths of fault scarps and fissures fit exponential laws (Figure 3.13).

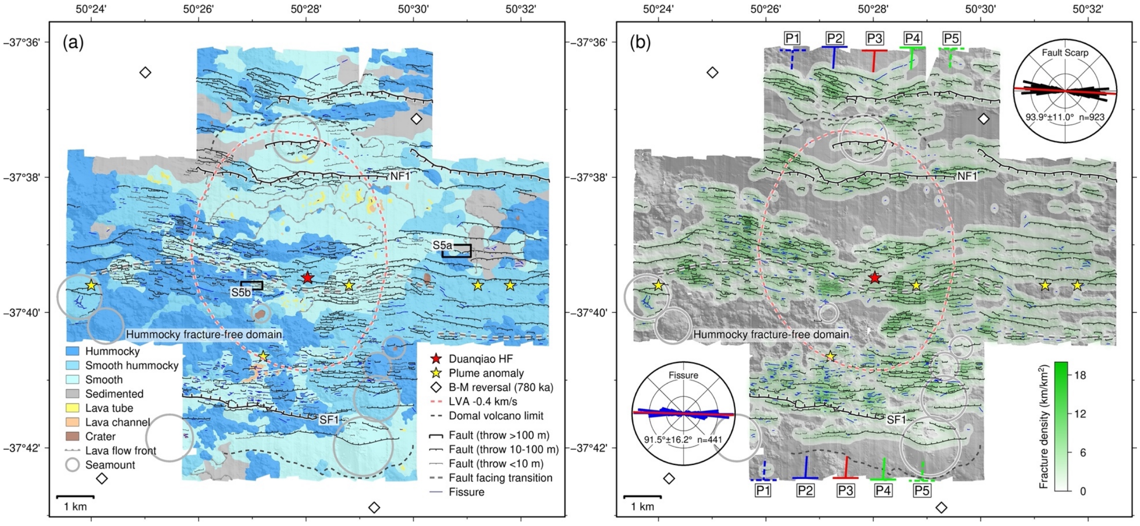

Figure 3.4. Interpretations in fault scarps and fissures.

(a) Fault scarps and fissures superimposed on the map of seafloor morphology. Three categories of faults are shown, based on their maximum fault throw (>100 m, 10-100 m, and <10 m). Dashed gray lines indicate the locations of fault-facing transition, from north-facing (south of the axis) to south-facing (north of the axis). Red star is the location of the Duanqiao hydrothermal field. (b) Fracture density calculated as a kernel density with a grid size of 10 m and a search radius of 250 m. Rose diagrams indicate azimuth distribution of fault scarps (top right) and fissures (bottom left). Cross-axis profiles P1-P5 are used for estimating tectonic strain in Figure 3.6.

The average fault orientation is 93.9°±11.0°, roughly orthogonal to the spreading direction, and the average fissure orientation is 91.5°±16.2° (Figure 3.4b), the higher deviation is due to radial fissures in volcanic edifices (e.g., Figure 3.2h). Fault scarps are dominantly south-facing in the north and north-facing in the south of the mapped area, and the transition, i.e., the location of ridge axis from the point of view of surface tectonics, is located at the latitude of the Duanqiao HF, except to the east of 50°30'E, where it is offset to the south by ~1.5 km (Figure 3.4a). Close examination of the HR bathymetry and slope maps reveals age relationships between faulting and lava emplacement: some fault scarps cut through pre-existing seafloor, while others are partially buried by later lava flows (e.g., Figure 3.14).

The fracture density varies between 0 and 18 km/km^2 in the mapped area (Figure 3.4b), and the average density is ~3 km/km^2. Three relatively broad ridge-parallel domains are fracture-free: a 1.3-2 km-wide, smooth domain with the two well-preserved lava flow fronts south of the NF1 scarp, a >1 km-wide mostly smooth domain in the southernmost part of the mapped area, and a 1.3-1.8 km-wide and 6 km-long hummocky domain to the south and southwest of the Duanqiao HF (Figures 3.4a and 3.4b). This fracture-free hummocky domain does not extend into the eastern part of the map, but ends eastward into an extensively faulted domain of smooth hummocky terrain.

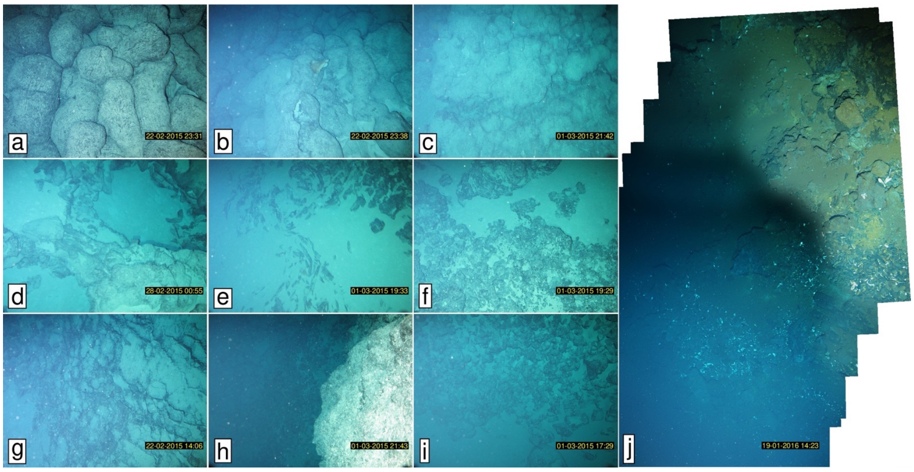

Figure 3.5. Representative seafloor photographs for lava morphologies and features. *(a) pillow lava; (b) elongated pillow lava on steep flanks; (c) lobate lava; (d) collapsed lobate lava; (e) folded sheet lava; (f) hackly sheet lava; (g) broken sheet lava; (h) fault scarp; (i) talus with rubble; (j) sulfide and dead mussel around the Duanqiao hydrothermal field.*

3.4.5 Tectonic strain

Based on the pattern of faulting, the surface tectonic strain was estimated along five axis-perpendicular profiles (P1-P5 from west to east in Figure 3.4b). Cumulative fault throws along each profile were measured between the northern and southern extremities (Figure 3.6a), and between the bottoms of the conjugate NF1 and SF1 fault scarps (Figure 3.6b). The cumulative frequency of fault throw fits an exponential law (Figure 3.6c). Individual fault scarps have dips between 30° and 80° (95% confidence interval; sketch of the measurements shown in the inset of Figure 3.6a), and have mean dip values of 55 to 65°. The calculated apparent tectonic strain over the whole length of the five profiles, ranges between 4.4 and 7.7% for a fault dip of 55°, and 3.6 and 5.1% for a fault dip of 65° (Figure 3.6a). Between the conjugate NF1 and SF1 scarps, tectonic strain ranges between 2.6 and 13.4% for a fault dip of 55°, and 1.8 and 8.9% for a fault dip of 65° (Figure 3.6b). Profile P4, near the eastern tip of the fracture-free hummocky domain (Figure 3.4b), yields the maximum tectonic strain.

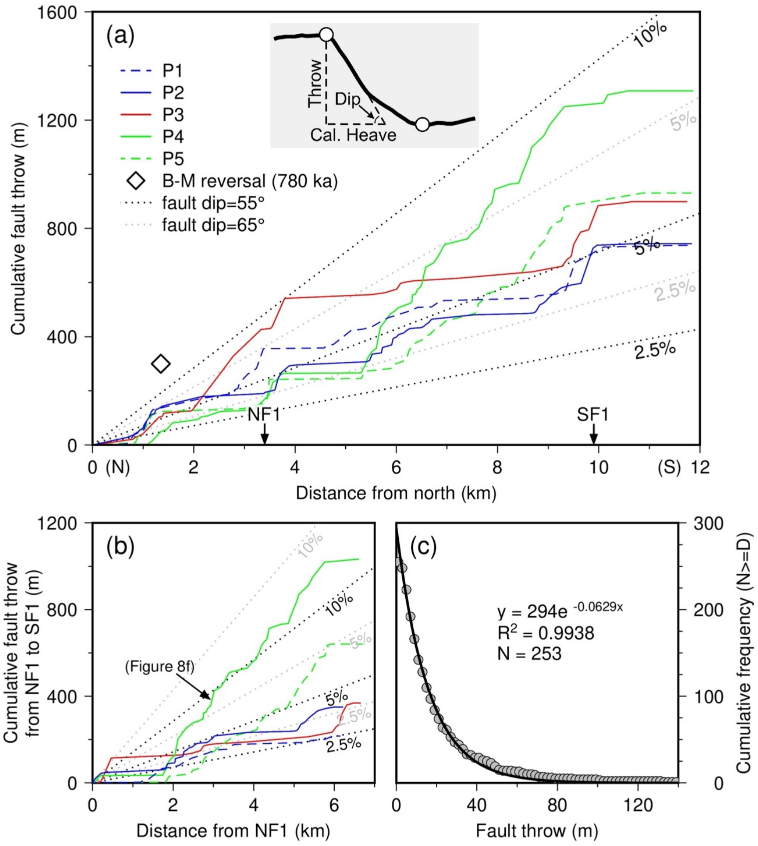

Figure 3.6. Tectonic strain estimated from cumulative fault throw.

(a) Cumulative fault throw measured between the northern (0 km) and southern extremities along five profiles (P1-P5) located in Figure 3.4b. Fissures are neglected. Black and grey dotted lines represent the estimation using fault dips of 55° and 65°, respectively, for tectonic strain of 2.5%, 5%, and 10%. The definitions of throw, maximum dip, and calculated heave of fault scarp are shown in the inset sketch. (b) Cumulative fault throw measured between the bottoms of conjugate NF1 and SF1. (c) Cumulative frequency of fault throw (N=253) binned by 2 m along five profiles (P1-P5). The exponential fit follows a law of the form: $y = 294e^{-0.0629x}$*, with the correlation coefficient (*R^2*) of 0.9938.*

3.4.6 Near-bottom magnetic anomalies

The two AUV magnetic profiles are located in the center of the study area (Figures 3.1b and 3.7a). To the north, they extend over the location of the B-M reversal as picked from sea-surface magnetic anomalies (magnetic A1 in Figure 3.1a; Sauter et al., 2009). This anomaly corresponds to clear lows in both near-bottom magnetic profiles (Figure 3.7b). The two profiles, distant by 0.8 km, record similar patterns of magnetic anomalies: magnetic highs are located outward from the conjugate NF1 and SF1 scarps, while magnetic lows are found inward of these two scarps (Figure 3.7b). The hummocky fracture-free domain corresponds to magnetic highs (red arrows in Figure 3.7b). The highly fractured domain to the north of this fracture-free domain corresponds to a magnetic low, while the smooth fracture-free domain with the two lava flow fronts (Figure 3.2d), and hummocky ridge on top of it (l in Figure 3.2a) correspond to weak magnetic anomalies (Figure 3.7b).

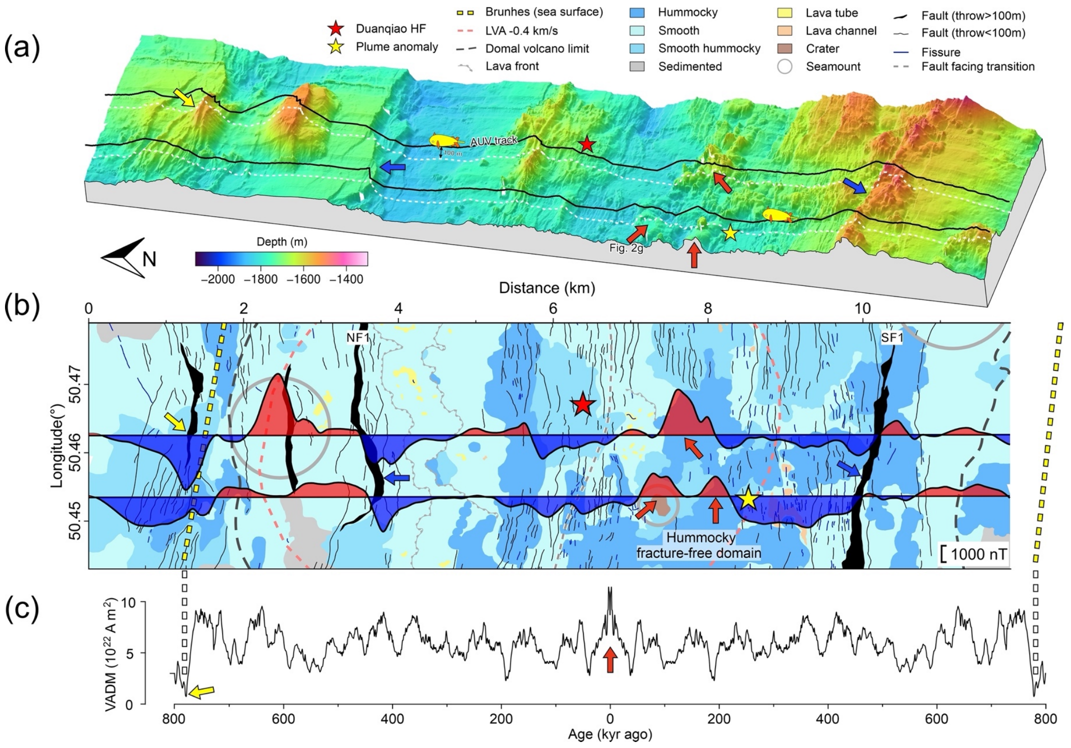

Figure 3.7. Near-bottom magnetic anomalies.

(a) 3-D seafloor topography with tracks of AUV survey ~100 m above the seafloor at a velocity of 1-2 kt. Yellow, blue, and red arrows respectively mark the interpreted locations of Brunhes, the conjugate NF1 and SF1, and the most recent hummocky eruptions. Red star is the location of the Duanqiao hydrothermal field. (b) Total magnetic anomaly plotted along AUV track lines, superimposed on geological interpretation (after Figure 3.4a). Reduction-To-Pole (RTP) was applied to locate the magnetic anomalies above their sources.

3.5 Discussion

Our results provide new insights into volcanic and tectonic processes at the center of the magmatically-robust SWIR 50°28'E segment. These results inform the spatial and temporal evolution of upper-crustal construction since the Brunhes-Matuyama reversal, ca 780 kyr ago (Cande and Kent, 1995). We propose an interpretation of this evolution, calling for phases of waxing and waning magmatic activity. We then examine the implications of our findings for the relation between upper-crustal construction and magmatic activity in the global MOR.

3.5.1 780 kyr of upper-crustal construction at the center of the magmatically-robust SWIR 50°28'E segment

3.5.1.1 Eruptive phases and modes of upper-crustal construction

Based on the mapped seafloor morphologies, eruptive units, and faults distribution, we propose that the upper crust formed at the center of the SWIR 50°28'E segment has experienced at least 6 eruptive phases, V0 to V5, within the past 780 kyr (Figure 3.8a). V0 corresponds to the construction of the upper crust on which the smooth domal volcano that is now rifted to the north of NF1 and to the south of SF1 (dashed lines in Figures 3.2a and 3.8a) was built. A faulted flat-topped seamount that is partially covered by smooth lava to the north of NF1 (j in Figure 3.2a), could have formed during the V0 phase. The V1 domal volcano (Figure 3.8b) originally had a diameter of 5-8 km. Its contours are now obscured in the south by several younger hummocky ridges and seamounts (Figures 3.2a and 3.8a). We interpret these as having formed during the V2 eruptive phase, together with the rifting of the V1 domal volcano along the conjugate NF1 and SF1 fault zones (Figures 3.8a and 3.8c). This 'split-volcano' configuration is commonly observed in the center of magmatically-robust slow and ultraslow spreading ridge segments (Escartín et al., 2014).

V1 is interpreted as a phase of high magma supply. The prevalence of smooth lava flows in the V1 domal volcano domain points to elevated eruptive rates, with feeding dikes centered within a narrow injection zone (Figure 3.8b). By contrast, V2 corresponds to the formation of several hummocky ridges and seamounts and the rifting of the V1 domal volcano. This points to lower eruptive rates during individual eruptions, to a wider zone of dike injection (Figure 3.8c), and to a more significant tectonic contribution to plate divergence. We, therefore, relate the transition from V1 to V2 to a waning magma supply. Early V2 volcanic constructions are mostly found in the southern flank of the rifted V1 domal volcano (Figure 3.8a). After the initial stages depicted in Figure 3.8c, the V2 eruptive phase presumably built the substratum for the lava flow fronts that are visible to the south of the NF1 scarp (Figures 3.2d and 3.8a). These lava flow fronts were formed during the V3 eruptive phase, and they bound eruptive units that extend up to 2 km downslope from their eruptive sources (inferred to have been located near a later hummocky ridge, marked as l in Figure 3.2a). It is likely that these smooth lavas also flowed to the south during V3, and currently form the substratum for later lava flows. The predominance of smooth lava, flowing significant distances from a localized inferred eruptive source, is similar to the V1 phase

(Figure 3.8b) and suggests that V3 was a phase of renewed (waxing) magma supply.

The hummocky ridge that tops the V3 lava flows (l in Figure 3.2a) suggests lower effusion rates. We attribute its formation to the onset of the V4 eruptive phase, characterized by a waning magma supply. Similar to what happened during the V2 waning phase, V4 eruptions appear to have mainly occurred to the south, so that the V3 seafloor was preserved only in the north (Figure 3.8a). The chronology of volcanic phases is more difficult to unravel in the 4.4 km-wide domain between the early V4 hummocky ridge (l in Figure 3.2a) and the SF1 fault zone (Figure 3.8a). The seafloor there is significantly fractured, with the notable exception of the hummocky fracture-free domain to the south and southwest of the Duanqiao HF (Figures 3.4a and 3.4b). This elongated, ridge-parallel, and fracture-free domain also corresponds to magnetic highs (Figure 3.7b). We propose that it is the product of the most recent, V5, eruptive phase. This V5 hummocky fracture-free domain ends eastward into extensively fractured smooth hummocky seafloor that probably formed during V4 (Figure 3.8a). Most scarps in this fractured area face to the north at the latitude of the hummocky fracture-free domain, then face to the south just 1 km to the north at the latitude of Duanqiao HF. We interpret the resulting narrow graben (Figure 3.8d) as being due to recent tectonically-accommodated plate divergence in the mapped area. Therefore, the most recent spreading would be mostly magmatic in the west and tectonic in the east.

The spatial distributions of eruptive products indicate that eruptive centers during magmatically-robust (waxing) phases V1 and V3 were located near the center of the mapped area, just north of the latitude of the Duanqiao HF. By contrast, during less magmatically-robust (waning) phases V2, V4, and V5, most eruptions occurred in the south, near the latitude of the hummocky fracture-free domain.

3.5.1.2 Constraints on crustal ages

The B-M reversal, at 780 kyr, is identified in sea-surface (Sauter et al., 2009) and in near-bottom magnetic anomalies (Figure 3.7b), providing the strongest constraint on crustal ages in the mapped area. Its traces on the south and north plates are separated by ~11 km, consistent within error to the ~14 mm/yr regional spreading rate (Patriat et al., 2008). This leads to interpret the maximum age of the onset of V0 phase (near the B-M reversal) as 780 kyr (Figure 3.8a). The next age constraint comes from the distance between the conjugate NF1 and SF1 scarps, which we interpreted as having initiated near the top of the V1 domal volcano (Figure 3.8b). This distance, 6.6 km (Figure 3.8a), would suggest a spreading age of

~471 kyr, corresponding to the onset of the V2 phase. However, parts of V2 eruptive products were emplaced on V1 seafloor (to the south of SF1 in Figure 3.8c), and their corresponding plate divergence, which is unknown, should be added to the 6.6 km to get a more accurate spreading age for the onset of the V2 phase.

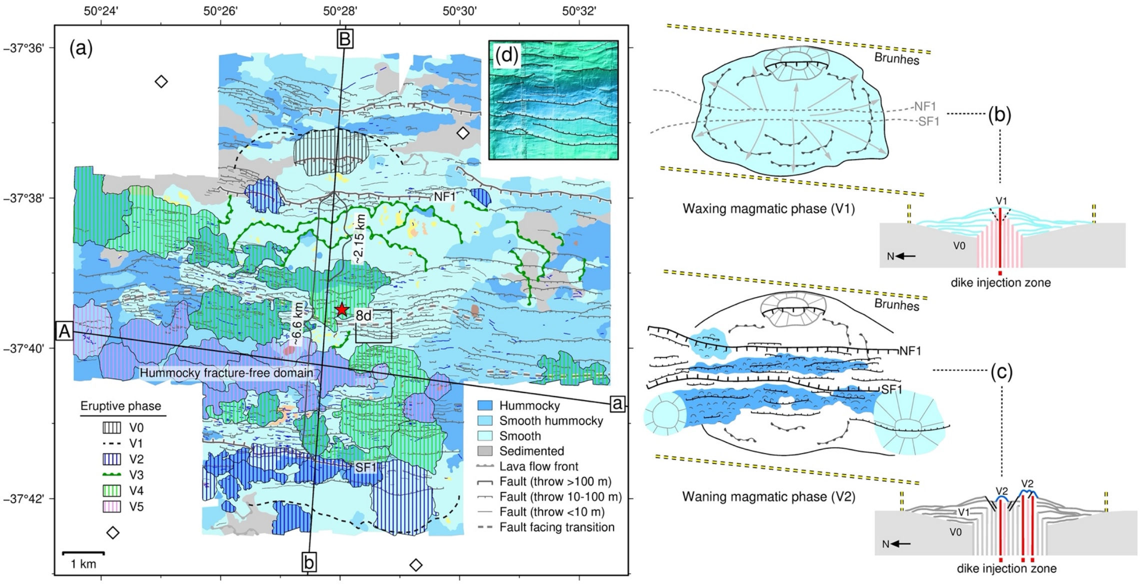

Figure 3.8. Interpretative map for eruptive phases and sketches for upper-crustal construction in waxing and waning magmatic phases.

(a) Interpretative map showing the distribution of eruptive units for the six proposed eruptive phases of upper-crustal construction (V0 to V5 from older to younger), superimposed on the geological map (after Figure 3.4a). Profiles A-a and B-b, along and across the most recent eruptive phase V5, refer to the locations of seismic profile in Figures 3.9a and 3.9b, respectively. Red star is the location of the Duanqiao hydrothermal field. (b) Sketches showing the construction of the domal volcano toward the end of magmatically-robust eruptive phase V1. In cross section, the most recent feeding dikes are in red, previous dikes in pink or gray. (c) Sketches showing the early stage of less magmatically-robust eruptive phase V2. (d) close-up view of the central, narrow graben (location in Figure 3.8a).

The age of the onset of the next magma waning phase (V4) can be estimated based on the 2.15 km across-axis distance between the early V4 hummocky ridge (l in Figure 3.2a) and the top of the NF1 scarp (Figure 3.8a). This suggests a total duration of 307 kyr for V2 and V3 together, and an age of 164 kyr for the onset of V4. The age of the onset of V5 is tentatively estimated as only 19 kyr, based on the cumulative heave of fault scarps of 0.27 km (calculated for a fault dip of 55°; Figure 3.6b) within 1-km to the north and south of the small graben shown in Figure 3.8d. This is one order of magnitude lower than the total estimated duration of V4+V5 (164 kyr), so that it seems more consistent to interpret V5 as just the most recent episode of the V4 eruptive phase.

3.5.2 Cycles of magmatic activity

Our interpretation of the eruptive phases associated with the past 780 kyr of plate spreading at the center of the SWIR 50°28'E segment, involves significant changes in magma supply, with alternating periods of more robust, waxing magmatism (V1 and V3), and of less robust, waning magmatism (V2 and V4+V5). Age constraints suggest a periodicity of about 300 kyr for these variations: up to 310 kyr from the start of V0 to the start of V2, and 307 kyr from the start of V2 to the start of V4.

Mendel et al. (2003) used the width of abyssal hills off-axis from our study area (Figure 3.1a), to propose a longer period (2-3 myr) magmatic cyclicity. These abyssal hills are interpreted as large split axial volcanos and correspond to changes of ~1 km in gravity-derived crustal thickness (Mendel et al., 2003). These 2-3 myr-long magmatic cycles occurred at the apex of a regional mantle melting anomaly, which is currently at its waning stage (Sauter et al., 2009). Our fine-scale geological observations document shorter magmatic cycles that occur during this waning stage, and with no detectable changes in crustal thickness, as revealed by the across-axis seismic velocity profile A-A' in Figure 3.1a (Jian et al., 2017b). Since crustal construction is a protracted process with more recent eruptions piling up over older seafloor (Figures 3.8b and 3.8c), and because of the very slow spreading rate, this is likely to dampen crustal thickness variation signals with periods of only a few 100s kyr.

Magmatic cycles with periods of the same order of magnitude have been documented at other sections of slow to ultraslow spreading ridges. At 19°S on the slow-spreading Central Indian Ridge, cyclic variations in basalt geochemistry suggest magmatic cycles of 150-200 kyr (Cordier et al., 2010). The cyclic occurrence of off-axis topographic highs at the Menez Gwen segment of the slow-spreading MAR points to magmatic cycles of 300-500 kyr (Klischies et al., 2019). At the ultraslow-spreading SWIR, melt replenishment cycles occurring over 180-250 kyr were proposed based on zircon dating of the gabbroic sequence drilled (ODP Holes 735B and 1105A) at the Atlantis Bank (Rioux et al., 2016). These cycles could be controlled by compaction processes in the melt-rich mantle below the ridge, or in the lowermost-crustal mush zone (Cordier et al., 2010; Rabinowicz and Toplis, 2009).

3.5.3 Upper-crustal construction and the magma plumbing system

In Figure 3.9c, we propose a conceptual sketch to relate the recent upper-crustal construction documented in this paper, to the deeper characteristics of the axial magma plumbing system, based on seismic velocity (Jian et al., 2017a; Jian et al., 2017b) and microseismicity (Yu et al., 2018) constraints. The boundary between the upper and lower crust i.e., layers 2 and 3, is defined by a vertical velocity gradient of 0.3 s^{-1}, and the Moho interface is defined by PmP arrivals (Jian et al., 2017b). Based on the full waveform inversion results of Jian et al. (2017a), we propose that the LVA documented beneath the SWIR 50°28’E segment center (Figures 3.9a and 3.9b), corresponds to partially crystallized gabbro, at temperatures greater than 1000°C and with residual melt contents increasing from less than 10% at a depth of 4 km bsf, to probably greater values in the LVA center. We tentatively draw the contours of this hot and melt-bearing domain down to Moho depth, where we propose that it roots into the melt-bearing upper mantle (Figure 3.9c). Inspired by observations of stacked melt sills at fast and intermediate spreading ridges (Carbotte et al., 2021, 2020; Marjanović et al., 2014), and by a conceptual model of the transcrustal magma plumbing system beneath subaerial volcanos (Cashman et al., 2017), we also propose that some of the melt in this hot lower crustal region resides in vertically stacked melt lenses (Figure 3.9c), and that these lenses play a role in transferring melt from the mantle to the upper crust to feed eruptions. In Figure 3.9c, we also infer that most hydrothermal cooling occurs in a domain that is limited both by temperature (ca 600°C) and pressure (corresponding to depths <6 km) as proposed by Morgan and Chen (1993). This limit is not meant to define the base of the fluid penetration in the lithosphere, but the domain of potentially vigorous hydrothermal circulation.

Moving just a few kilometers away from the hot central LVA region toward the ridge segment ends, we infer, based on the lateral increase of seismic velocities (Jian et al., 2017b), that lower crustal temperatures drop laterally below the solidus, yielding solidified and cooled gabbros. A smaller LVA, which we similarly interpret as a melt-mush zone, is documented in the shallow lower crust, ~6 km to the west of the segment center (Figure 3.9a; Jian et al., 2017b). This small mid-crustal mush zone is located just below, and may have fed, the fissured, dome-topped seamount (Figure 3.2h). In Figure 3.9c, we follow the implicit interpretation of Yu et al. (2018) that the mid-segment axial earthquakes are tectonic, and therefore reveal an along-axis deepening of the brittle lithosphere to the west. If these events are in fact magmatic, corresponding to diking associated with melt transport through the crust, the thermal regime need not be that cold beneath the smaller, western LVA.

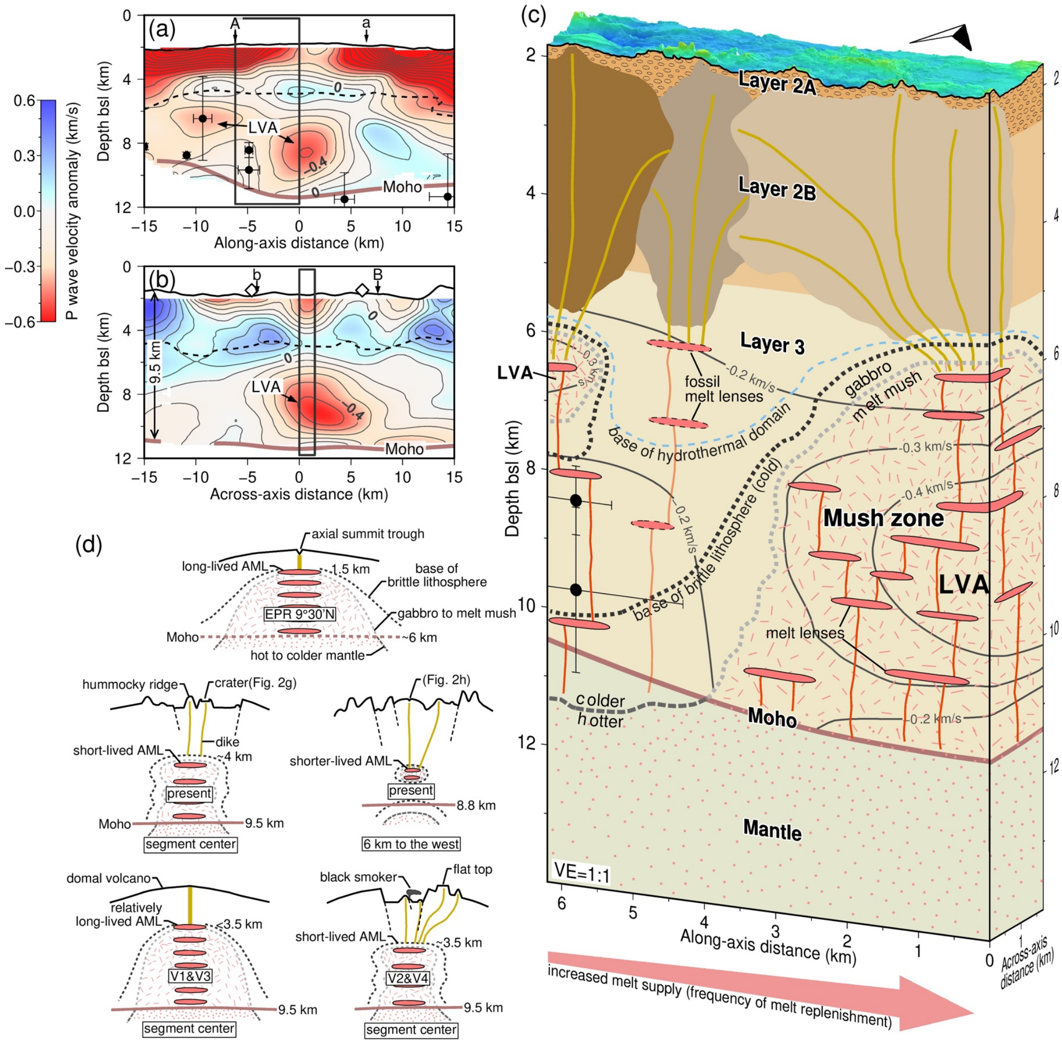

Figure 3.9. Magma plumbing system of the SWIR 50°28'E.

P wave velocity anomaly along (a) and across (b) the recent eruptive phase V5 (contours in 0.1 km/s), data extracted from 3-D seismic tomography (Jian et al., 2017b). Locations of A-a and B-b are shown in the map of Figure 3.8a. Dashed lines are the boundary of crustal layers 2 and 3, defined by the vertical velocity gradient of 0.3 s^{-1} *(Jian et al., 2017b). Moho interface based on PmP arrivals is shown as thick brown lines (Jian et al., 2017b). Two LVAs are shown at segment center within the lower crust (minimum <-0.6 km/s) and in the west within the mid crust (minimum <-0.35 km/s), respectively. Black dots with error bars indicate the hypocenters of microearthquakes (Yu et al., 2018). Closed squares outline the area of the 3-D model in Figure 3.9c. (c) Magma plumbing system for the recent eruptive phase (V5) showing the topography, crustal structure, dike injection, mush zone, mantle, and thermal structure, constrained by seismic velocity and microseismicity (Jian et al., 2017b; Yu et al., 2018). Vertically stacked melt lenses connected by dikes are inferred in the hot lower-crustal mush zone. Dots and dashes indicate crystal mushes. (d) Sketches showing magma plumbing systems for EPR 9°30'N, the present-day center of the SWIR 50°28'E segment and 6 km to the west to the segment center, and segment center during V1&V3 and V2&V4.*

The present-day along-axis configuration sketched in Figure 3.9c is heterogeneous, with significant variations in the thermal regime over distances of a few kilometers, which we propose are directly related to along-axis variations in the recent history of melt supply, and more specifically of the replenishment rates in the lower-crustal magma plumbing system of melt mush and stacked melt lenses (Figure 3.9c). This interpretation emphasizes the role of melt supply variations as a control of the thermal regime of slow and ultraslow spreading ridges (Cannat et al., 2019b). Frequent melt replenishment keeps the lower crust hot, pushing up the base of the brittle lithosphere and the base of the hydrothermally cooled domain (Fan et al., 2021). Less frequent melt replenishment results in deep and shorter-lived AMLs, a thicker brittle domain, and more variable but generally deeper hydrothermal circulation (Figure 3.9c).

The whole segment at 50°28'E is a magmatically-robust endmember for the ultraslow spreading SWIR. The configuration sketched in Figure 3.9c corresponds to a relatively large time-averaged melt supply, enough to make a magmatic crust ≥8.8 km-thick (Figure 3.9a). The contrasted present-day, across-axis settings in Figure 3.9d, one for the main LVA region at the segment center, and the other for the smaller, mid-crustal LVA region 6 km to the west of the segment center, corresponds to a relatively low melt supply. They likely prevailed during the most recent eruptive phase, forming the V5 hummocky ridges and seamounts, as part of the V4-V5 magma supply waning phase. We propose that the axial thermal regime and magma plumbing system was similar during the other documented magma waning phase (V2), with short-lived AMLs above shrinking mush zones (Figure 3.9d). Waxing phases V1 and V3, forming domal volcanos with predominantly high-effusion-rate smooth and smooth hummocky lava, probably corresponded to hotter axial regimes, with larger volumes of melt readily accessible in shallower, more frequently replenished, and thus relatively long-lived AMLs (Figure 3.9d). These relatively long-lived AMLs probably resided at depths shallower than the top of the current mush zone at ~4 km bsf (Jian et al., 2017a), or than the AML depth at the center of the MAR Lucky Strike segment (Combier et al., 2015; Singh et al., 2006), which is currently experiencing the early stages of rifting of a domal volcano formed during a more magmatically-robust recent phase of spreading (Escartín et al., 2014; Humphris et al., 2002).

3.5.4 Implications for the modes of upper-crustal construction and magma plumbing systems at MORs

Our model for the magma dynamics of the melt-rich SWIR 50°28'E segment suggests cyclic variations in both the modes of upper-crustal construction (construction of a domal volcano with a localized dike injection zone, or predominance of hummocky ridges with a broader dike injection zone; Figures 3.8b and 3.8c) and the magma plumbing system (relatively long-lived and frequently replenished AMLs above broad melt mush zones, or shorter-lived AMLs on top of narrower and shrinking mush zones; Figure 3.9d). We now extend this model to a comparison with other well-documented magmatically-robust ridge sections where both HR bathymetry data and seismic data are available.

Fast spreading ridges, like the EPR 9°30'N, are characterized by a predominance of high-effusion-rate smooth lava flows (Fundis et al., 2010), fed by a dike injection zone that is mostly localized in a few 100s meters-wide Axial Summit Trough (Fornari et al., 1998). The hotter thermal structure of the EPR at 9°30'N (Figure 3.9d) is nearly 2D and steady-state, with a 1.5 km-deep, long-lived AML on top of a mush zone (Detrick et al., 1987; Dunn et al., 2000) that contains stacked melt lenses (Marjanović et al., 2014).

Intermediate spreading ridges tend to have variable lava morphologies (Figure 3.15a), from Axial Seamount at the Juan de Fuca Ridge with smooth-dominated lava flows and a shallow AML similar to that of fast-spreading ridges (Arnulf et al., 2018; Clague et al., 2017), to GSC 95°W with a prevalence of hummocky seafloor and no detectable AML (Blacic et al., 2004; Colman et al., 2012).

Slow and ultraslow spreading ridges have a yet larger spectrum of upper-crustal construction modes and magma plumbing systems. Ridge sections with moderate and low melt supply are typically characterized by hummocky ridges (e.g., Cann and Smith, 2005; Searle et al., 2010), with no detectable AML (Detrick et al., 1990). At melt-rich segments, the construction of smooth domal volcanos at segment centers corresponds to a local AML and/or crustal melt mush zone, such as at the MAR Lucky Strike segment (Escartín et al., 2014; Singh et al., 2006) and at the SWIR 50°28'E (Jian et al., 2017b; this study). The magmatically-robust, ultraslow spreading endmember documented at the center of the SWIR 50°28'E segment is characterized by the highest proportion of lobate-sheet lava morphology among slow and ultraslow spreading ridges (Figure 3.15a), and by very low (<8%) apparent tectonic strain (Figure 3.15b). Indeed, the apparent tectonic strain at the center of the SWIR 50°28'E segment and at the center of the Lucky Strike segment are similar to what has been observed at fast and intermediate spreading ridges (Figure 3.15b). Yet, the mid and lower crustal thermal and geological structure inferred for these slow and ultraslow ridge segment centers on the basis of seismic data differs from that of a fast-spreading ridge (Figure 3.9d). Melt supply, although in the highest range, fails to maintain a steady-state melt mush and shallow AML. The combination of a well-developed melt mush domain and a relatively long-lived AML that allows for a fast spreading-type mode of upper crustal construction (axial dome, localized dike injection, prevalence of high-effusion-rate lava, and very little faulting) is transient (with time scales of a few 100s kyr) and limited to a few kilometers at the very center of the most magmatically-robust slow and ultraslow spreading segments.

3.6 Conclusions

We mapped the fine-scale volcanic and tectonic features at the center of the magmatically-robust SWIR 50°28'E segment, and their evolution over the past 780 kyr, based on HR bathymetry and backscatter data, near-bottom magnetic data, and optical seafloor imagery. Our geological observations and interpretations support the following conclusions.

(1) The study area displays three different volcanic seafloor morphologies, corresponding to different patterns of lava morphologies that are mainly influenced by lava effusion rates. High-effusion-rate, lobate-sheet lavas dominated, smooth and smooth hummocky morphologies are the most prevalent (64% of the mapped area), forming smooth domal volcanos, while low-effusion-rate, pillow lavas dominated, hummocky morphology accounts for only 29% (the remaining 7% is covered by sediments). The proportion of lobate-sheet lavas and the apparent tectonic strain are respectively 41% and <8%, similar to values measured at fast-spreading ridges.

(2) We recognize six eruptive phases (V0-V5 from old to young), each corresponding to waxing or waning melt supply. Cycles that include a waxing and a waning phase last about 300 kyr. We propose that they result from temporal changes in the frequency of melt replenishment in the mid and lower crust. The most recent eruptions produce a ridge-parallel, fracture-free, hummocky domain that may have formed over the past ~19 kyr.

(3) During waxing phases in magma supply, higher frequencies of melt replenishment keep the lower-crust hot, with relatively shallow, and long-lived AMLs and a melt-crystal mush zone. Narrow and localized dikes feed high-eruption-rate eruptions, forming smooth lava flows and domal volcanos that cover large areas of the seafloor, with little to no faulting. Waxing phases at the SWIR 50°28'E segment represent the most magmatically-robust endmember for ultraslow spreading ridges.

(4) During waning phases in magma supply, lower frequencies of melt replenishment lead to deeper and shorter-lived AMLs, reduced melt-mush zones in the lower crust, a thicker brittle lithosphere, and a more variable and generally thicker hydrothermal domain. Crustal construction occurs within a wider zone of dike injection with more faults, producing dominantly hummocky lava flows.

(5) The modes of upper-crustal construction and the magma plumbing systems at slow and ultraslow spreading ridges are controlled by spatial and temporal variations in magma supply more than by spreading rate alone.

3.7 Supplementary material

Bathymetry and backscatter data used in this study are available at https://doi.org/10.5281/zenodo.5147241.

Table 3.1. Overview of geological features

Feature name	Seafloor morphology (HR bathymetry, slope, and backscatter)	Lava morphology (ground truth by deep-tow camera)	Comments	Seafloor example	Photo example
Smooth	Flat seafloor (homogeneous low slope) and higher backscatter than sedimented seafloor without shadow. Very few volcanic cones occur.	Pillow (28%), lobate (24%), sheet (26%), talus (3%) and 100%-sedimented (19%)	Contacts with sedimented seafloor can be obscure.	Figures 3.2b-3.2f	Figures 3.5c-3.5g
Hummocky	Composed of numerous elevated and rounded volcanic cones. Backscatter is usually high on one side and deep shadow on the other side.	Pillow (65%), lobate (13%), sheet (10%), talus (4%) and 100%-sedimented (8%)	Contacts with smooth and smooth hummocky seafloor are sharp.	Figure 3.2b	Figures 3.5a and 3.5b
Smooth hummocky	Rougher topography than the smooth but less so than the hummocky.	Pillow (57%), lobate (17%), sheet (15%), talus (3%) and 100%-sedimented (8%)	In small scale, flat seafloor areas extend less than 300 m between volcanic cones.	Figures 3.2c and 3.2i	Figure 3.5
Sedimented	Flat and very low backscatter in a wide area.	Pillow (22%), lobate (4%), sheet (3%), talus (6%) and 100%-sedimented (65%)	Hummocky seafloor with shadow in backscatter is not included.	Figure 3.2c	Figures 3.5d and 3.5e
Volcanic cone	Elevated and rounded volcanos with circular contours in bathymetry and slope.	Built by pillow lavas.	Height >2 m. Bases of cones on hummocky seafloor can be obscure.	Figures 3.2b and 3.2c	Figures 3.5a and 3.5b
Eruptive unit	Formed during a period characterized by similar eruptive dynamics, based on seafloor morphology and of the nature of their contact with the surrounding seafloor.	-	Two smooth lava units have constraints only in their north halves.	Figure 3.3c	-
Seamount	Large volcanos with diameters of >500 m and relatively uniformly high backscatter.	A few photographs show the appearance of talus on seamount flanks.	Bases of seamounts can be obscure.	Figures 3.2g and 3.2h	Figures 3.5d, 3.5e, and 3.5i
Crater	Bowl-shaped depression on the top of the volcano. The bottom is usually flat with high backscatter.	No data.	-	Figure 3.2g	-
Lava tube (uplifted tumulus)	Narrow and sinuous on smooth lava flows. 30-500 m long. Distinct in backscatter.	No data.	Positive relief and usually collapsed.	Figure 3.2e	-
Lava channel	Wide (up to 100 m) and sinuous with depression on smooth lava flows.	No data.	Negative relief.	Figure 3.2f	-
Lava flow front	Edges of individual smooth lava flow up to several kilometers long.	Mixing pillow, lobate, and sheet lava.	Difficult to distinguish which are overprinted by post eruptions.	Figure 3.2d	-
Fault scarp	Linear and narrow variations in bathymetry, slopes, and backscatter.	Talus is observed.	Classified by maximum fault throw >100 m, 10-100 m, and <10 m.	Figures 3.2i, 3.4c, and 3.4d	Figure 3.5h
Fissure	Narrow and linear change in bathymetry and slope with negative relief, consistent with shadow zones in backscatter.	No data.	-	Figures 3.2h and 3.2i	-

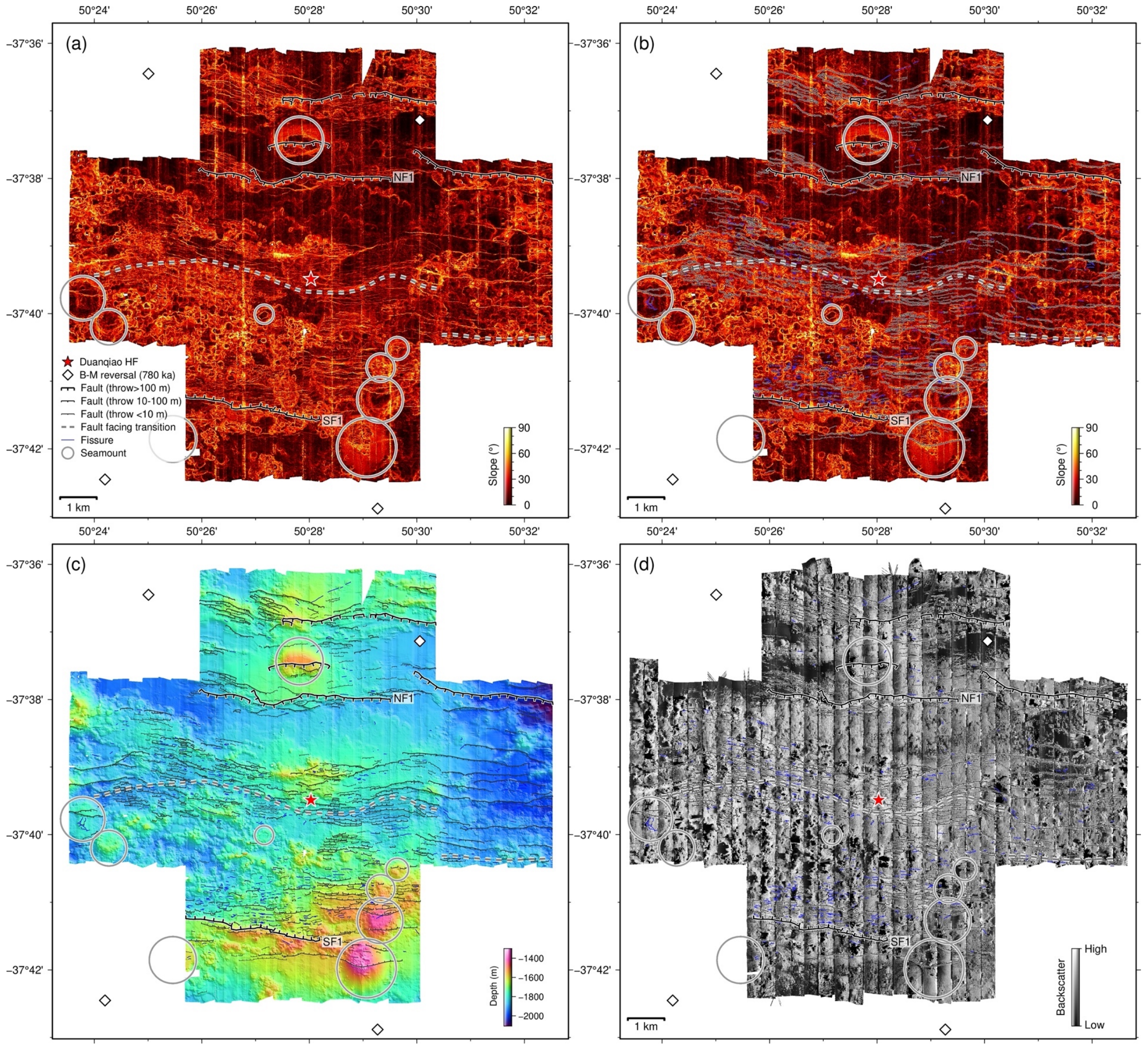

Figure 3.10. Slope map and maps with fault scarps and fissures.

Slope map calculated from bathymetry (a) and (b), bathymetry (c), and backscatter (d), with faults, fissures, fault facing transition, and seamounts and landmarks of NF1, SF1, B-M reversals, and the Duanqiao hydrothermal field. Slope map was computed from bathymetry with GMT software 'grdgradient' (Wessel et al., 2019).

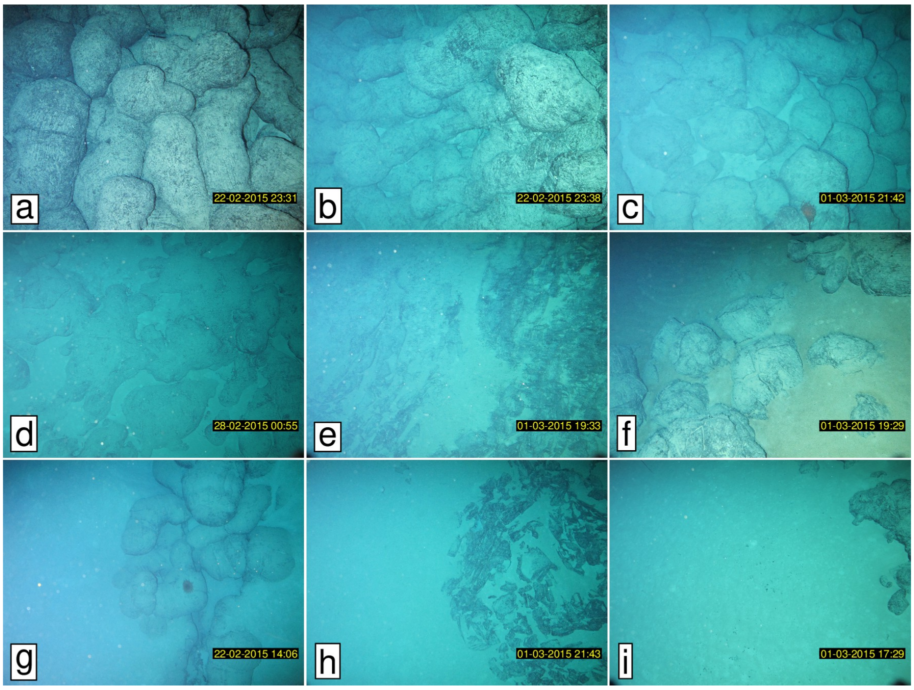

Figure 3.11. Representative seafloor photographs for sediment cover.

Sediment cover is thus classified into five groups. (a) and (b): <10%; (c) and (d): 10-30%; (e) and (f): 30-60%; (g) and (h): 60-90%; (i): >90%.

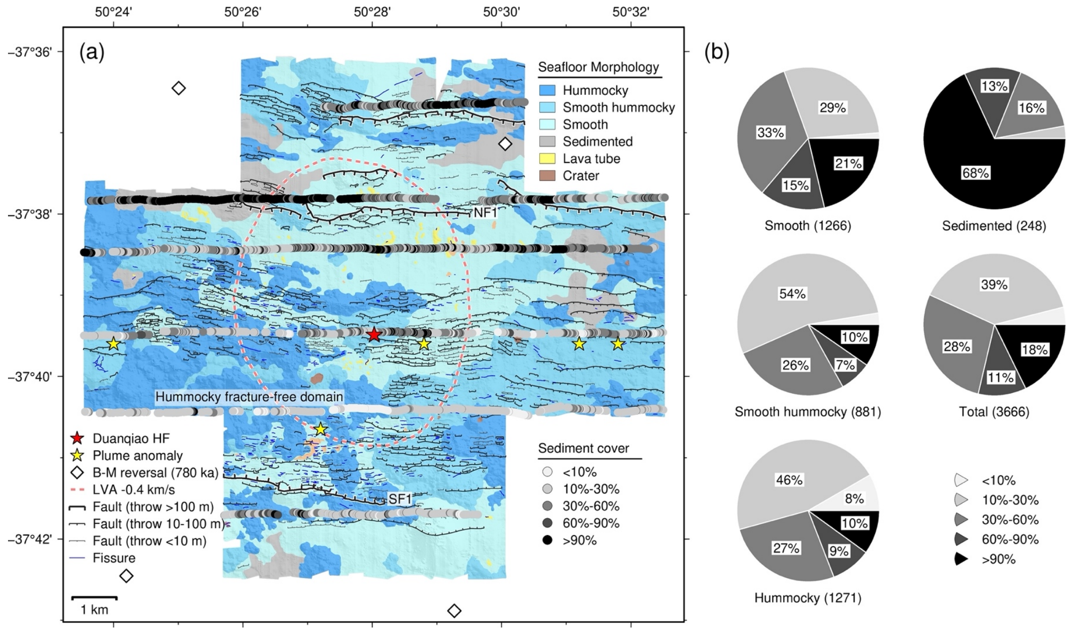

Figure 3.12. Interpretations in sediment cover.

(a) Distribution of sediment cover superimposed on the map of seafloor morphology. Classification of sediment cover is interpreted from seafloor photographs (Figure 3.11), into five groups: <10%, 10-30%, 30-60%, 60-90%, and >90%. (b) The proportion of seafloor photographs showing each sediment group for each type of seafloor morphology identified from HR mapping over the same transects.

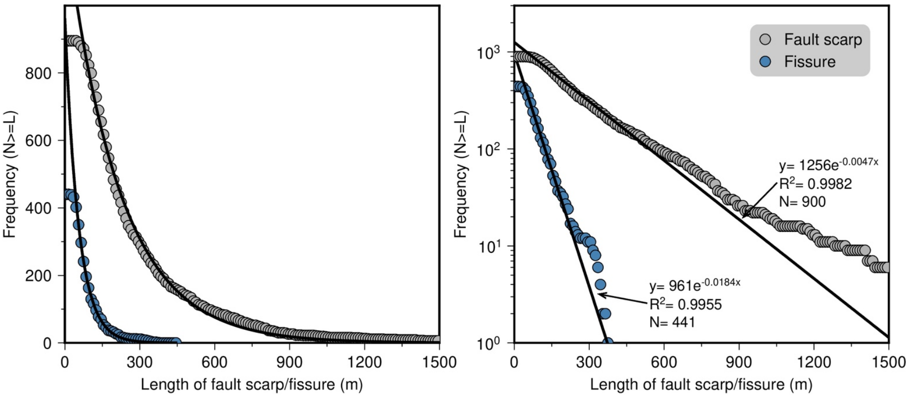

Figure 3.13. Cumulative frequency of lengths of fault scarps and fissures.

Binned by 10 m (omitting fault scarps and fissures that extend out of the HR map). Exponential fits of fault scarp and fissure follow laws of the forms: $y=1256e^{-0.0047x}$ *(*$R^2=0.9982$*) and* $y=961e^{-0.0184x}$ *(*$R^2=0.9955$*), respectively.*

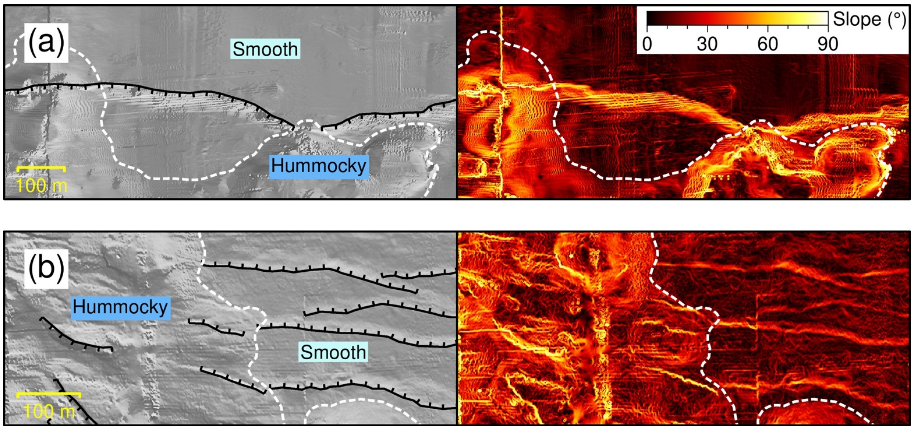

Figure 3.14. Close-up views of buried faults.

Shaded (left) and slope (right) maps are located in Figure 3.4a. White lines indicate the boundaries of seafloor morphology.

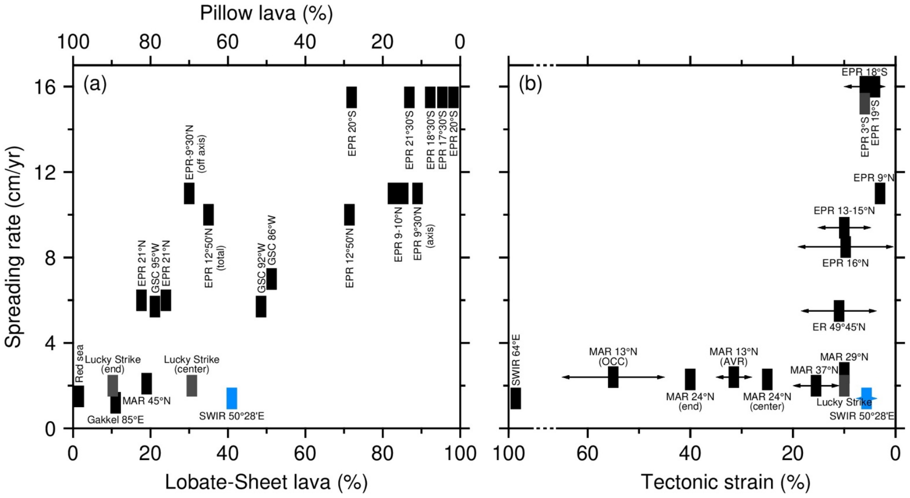

Figure 3.15. Compilation of abundances of lava morphologies (a) and tectonic strain (b) as functions of spreading rate.

Blue squares and (pale) blue circles represent the values of SWIR 50°28'E. (a) is modified and expanded from Perfit and Chadwick (1998). Additional values of the abundance of lava morphologies constrained by visual or bathymetric observations, including Gakkel 85°E: (Jokat et al., 2003; Pontbriand et al., 2012), MAR 45°N: (Yeo, 2012), segment center and end of Lucky Strike: (Escartín et al., 2014), GSC 92°W and 95°W: (McClinton et al., 2013), and EPR 9-10°N: (Engels et al., 2003; Fundis et al., 2010; Kurras et al., 2000; Meyer and White, 2007; White et al., 2002)*. (b) is compiled from high-resolution bathymetry or backscatter data, including SWIR 64°E (Sauter et al., 2013), oceanic core complex (OCC) and axial volcanic ridge (AVR) of MAR 13°N (MacLeod et al., 2009), segment center and end of MAR 24°N (Allerton et al., 1996), MAR 37°N (Macdonald and Luyendyk, 1977), MAR 29°N (Escartín et al., 1999), Lucky Strike (Combier et al., 2015), Explorer Ridge (ER) 49°45'N (Deschamps et al., 2007), EPR 16°N (Le Saout et al., 2018), EPR 3°S and 13-15°N (Cowie et al., 1993), EPR 9°N (Escartín et al., 2007), EPR 18°S (Carbotte and Macdonald, 1994), and EPR 19°S (Bohnenstiehl and Carbotte, 2001).*

Chapter 4

Microseismicity and lithosphere thickness at a nearly amagmatic mid-ocean ridge

In this chapter, I focus on microseismicity recorded during two short OBS deployments, over the youngest active detachment fault at the nearly-amagmatic SWIR 64°30'E. This chapter has been submitted to Nature Communications with a title of *Microseismicity and lithosphere thickness at a nearly amagmatic mid-ocean ridge*. I carried out all the data processing, produced all figures, and wrote the manuscript, under the supervision of Wayne Crawford and Mathilde Cannat.

4.1 Abstract

Successive flip-flop detachment faults in a nearly-amagmatic region of the ultraslow-spreading Southwest Indian Ridge (SWIR) at 64°30'E accommodate ~100% of plate divergence, with mostly ultramafic seafloor. As magma is the main heat carrier to the oceanic lithosphere, the nearly-amagmatic SWIR 64°30'E is expected to have a very thick lithosphere. Here, our microseismicity data shows a 15-km thick seismogenic lithosphere, actually thinner than the more magmatic SWIR Dragon Flag detachment with the same spreading rate. This challenges current models of how spreading rate and melt supply control the thermal regime of mid-ocean ridges. Microearthquakes with normal focal mechanisms are colocated with seismically imaged damage zones of the detachment and reveal hanging-wall normal faulting, which is not seen at more magmatic detachments at the SWIR or the Mid-Atlantic Ridge. We also document a two-day seismic swarm, interpret as caused by an upward-migrating melt intrusion in the detachment footwall (6-11 km), triggering a sequence of shallower (~1.5 km) tectonic earthquakes in the detachment fault plane. This points to a possible link between sparse magmatism and tectonic failure at melt-poor ultraslow ridges.

4.2 Introduction

A successive flip-flop detachment fault system discovered in 2013 at a nearly-amagmatic region of the ultraslow spreading Southwest Indian Ridge (SWIR; full spreading rate of 14 mm/yr) 64°30'E reveals a previously unknown seafloor spreading mode (Cannat et al., 2019b; Reston, 2018; Sauter et al., 2013) (Figure 4.1a). In this mode, the detachments accommodate nearly 100% of plate divergence, continuously cutting into the footwalls of their predecessors, with flipping polarities every 0.6-1.5 Ma (Cannat et al., 2019b; Sauter et al., 2013) (Figure 4.1). The resulting seafloor morphology is so-called smooth seafloor (Cannat et al., 2006), with extensive exposure of mantle-derived peridotites and only patches of hummocky basalts (Sauter et al., 2013). This newly-defined seafloor spreading mode differs from the "classic" detachment-volcanic and volcanic-volcanic modes at slow spreading ridges and at more magmatically-robust portions of ultraslow spreading ridges, where at least one plate is dominated by abyssal-hill volcanic seafloor (Buck et al., 2005; Cannat et al., 2006; Escartín et al., 2008; MacLeod et al., 2009; Olive and Dublanchet, 2020; Smith et al., 2008b; Tucholke et al., 2008).

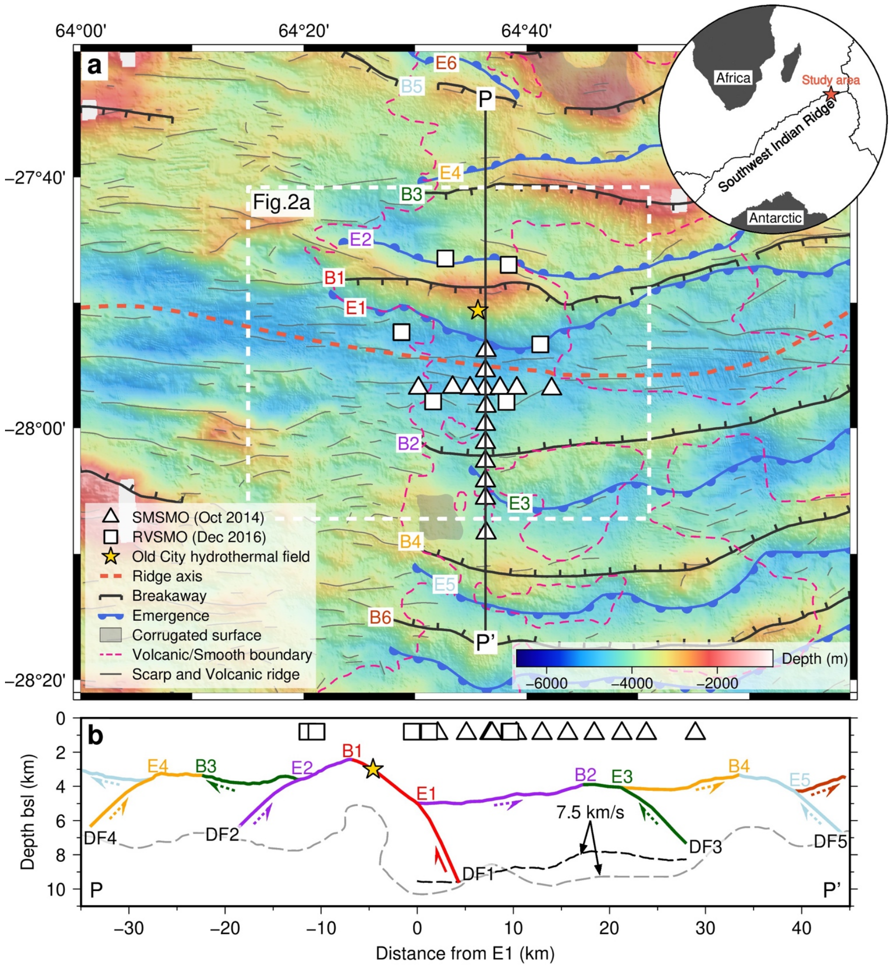

Figure 4.1. OBS locations and tectonic interpretation of the flip-flop detachment fault system at the eastern SWIR.

(a) Tectonic map with locations of the two OBS networks, SMSMO (14 OBSs in triangles) and RVSMO (6 OBSs in squares). Geological and tectonic information (see legend for symbols) includes breakaways (B1-B6) and emergences (E1-E6) of successive detachment faults, corrugated surface, the boundary between volcanic and smooth seafloor, and linear sketches of scarps and volcanic ridges (Cannat et al., 2019b). Yellow star is the Old City hydrothermal field (Cannat et al., 2019a). White dashed square marks the location of Figure 4.2a. (b) Tectonic interpretation of the successive flip-flop detachment fault system along the PP' cross-section (Cannat et al., 2019b). Black (Momoh et al., 2017) and gray (Corbalán et al., 2021) dashed lines are the 7.5 km/s velocity contours. Locations of OBSs are projected to the PP' cross-section. bsl: below sea level.

Seismicity provides a means to study magmatic, tectonic, and hydrothermal processes within the lithosphere of mid-ocean ridges (de Martin et al., 2007; Kong et al., 1992; Meier and Schlindwein, 2018; Parnell-Turner et al., 2017; Pontbriand and Sohn, 2014; Tan et al., 2016; Tilmann et al., 2004) (MORs), and is an indirect proxy for the thermal regime by constraining the depth to the base of the seismogenic lithosphere (McKenzie et al., 2005; Phipps Morgan and Chen, 1993a). The thickness of the axial seismogenic lithosphere is numerically predicted to increase as spreading rate decreases (Phipps Morgan and Chen, 1993a) and/or as melt supply decreases (Fan et al., 2021). The ultraslow spreading SWIR 64°30'E, being nearly amagmatic, may be regarded as a geothermal calibration for the MOR system.

In this study, we present 309 microearthquakes and 8 focal mechanisms associated with the youngest, active detachment system (DF1) at the SWIR 64°30'E (Methods), as recorded during two short (8 days for the SMSMO catalog and 19 days for the RVSMO catalog) ocean bottom seismometer (OBS) deployments (Figures 4.1 and 4.2a). Our results demonstrate tectonic activities at the detachment damage zones and provide constraints on the thickness of the seismogenic lithosphere. We also document a two-day seismic swarm which we propose is related to the incipient volcanism witnessed by patches of hummocky basalts resting on the ultramafic seafloor.

4.3 Seismicity of the detachment fault system

The two short OBS deployments we report on offer snapshots in time of the seismic activity. Most microearthquakes occurred in the axial valley (Figure 4.2) between the emergence of DF1 (E1) and the breakaway of DF2 (B2), with an average seismicity rate of 11.4 events per day (8.4 and 12.7 events per day in the SMSMO and RVSMO catalogs, respectively). The highest number of events is recorded near the longitude of the P2-P2' profile, and there is an apparent seismic gap to the west of the P1-P1' profile (Figures 4.2a and 4.2c). Earthquake hypocenters have depths between 0 and 15 km below the seafloor (bsf), and events in the shorter SMSMO catalog were mostly at less than 10 km bsf (Figure 4.2b). Local magnitudes (M_L) range between -0.5 and 3.2, with a magnitude of completeness of 1.1 and a b-value of 0.9, based on the Gutenberg-Richter relation (Gutenberg and Richter, 1944) (Methods and Figure 4.9). Focal mechanisms correspond to normal faulting, as expected in an extensional context, except for one strike-slip faulting event (Figure 4.2a).

Many microearthquake hypocenters plotted in the cross-axis sections P1-P1' and P2-P2' (Figures 4.2d and 4.2e) are aligned with the trace of the subseafloor detachment fault plane as inferred from a series of subparallel seismic reflectors with a dip of 50-60° (Momoh et al., 2020, 2017). In the three profiles, and particularly along P3-P3', there are several events scattered in the detachment footwall and hanging wall. This differs from the seismicity recorded at more magmatically active detachment systems, such as the 13°20'N, TAG, and Logatchev detachment faults at the Mid-Atlantic Ridge (de Martin et al., 2007; Grevemeyer et al., 2013; Parnell-Turner et al., 2020, 2017) and the Dragon Flag detachment fault of the

SWIR (Tao et al., 2020; Yu et al., 2018), where there are very few earthquakes in the hanging wall. Focal mechanisms of the hanging-wall earthquakes display a prevalence of normal faults with an average dip of 50° at 2-7 km bsf (Figures 4.2e and 4.2f). These dips are consistent with the geometry of nearby north-dipping seismic reflectors (Momoh et al., 2017) (Figure 4.2f) and with small-offset fault scarps at the seafloor (Sauter et al., 2013), suggesting that these small faults are conjugate with the detachment fault.

We also observe a larger number of earthquakes in the detachment damage zone and in the hanging wall, at the transition between volcanic and smooth seafloor (Figures 4.2c and 4.2e), where intrusive magmatic sills were proposed to explain subhorizontal seismic reflectors (Momoh et al., 2020). Due to the low friction coefficients associated with partial serpentinization, the brittle ultramafic basement may be less prone to seismogenic rupture than the more competent crystallized basalts or gabbros. Our observations may thus provide a framework to examine earthquake generation at detachment systems, interacting with sparse magmatism.

4.4 Thickness of seismogenic lithosphere and the axial thermal regime

The microearthquakes constrain the thickness of the seismogenic lithosphere to be at least 15 km in this nearly-amagmatic, ultraslow spreading MOR context (Figure 4.2b), and this thickness is mostly uniform along the ridge axis, across the transition from smooth to volcanic seafloor (Figure 4.2c). The thickness of the seismogenic lithosphere is believed to be mainly controlled by the thermal regime, with its base roughly corresponding to the 650℃ isotherm (Anderson, 1995; McKenzie et al., 2005; Wang-Pin Chen and Molnar, 1983). This is consistent with the minimum depth of 18 km bsf and 800 to 1000℃ temperature conditions, determined from petrological constraints for the high-stress ductile deformation of sheared peridotites dredged in the same area (Bickert et al., 2021, 2020). A greater maximum depth of microearthquakes (>20 km) was documented at the adjacent magma-poor SWIR 65°10'E (Schlindwein and Schmid, 2016), but these deep earthquakes are way out of the OBS network (>10 km) and were located using a velocity model derived from the magmatically-robust segment #8 volcano (Minshull et al., 2006) (Methods and Figure 4.10), which could bias their depths.

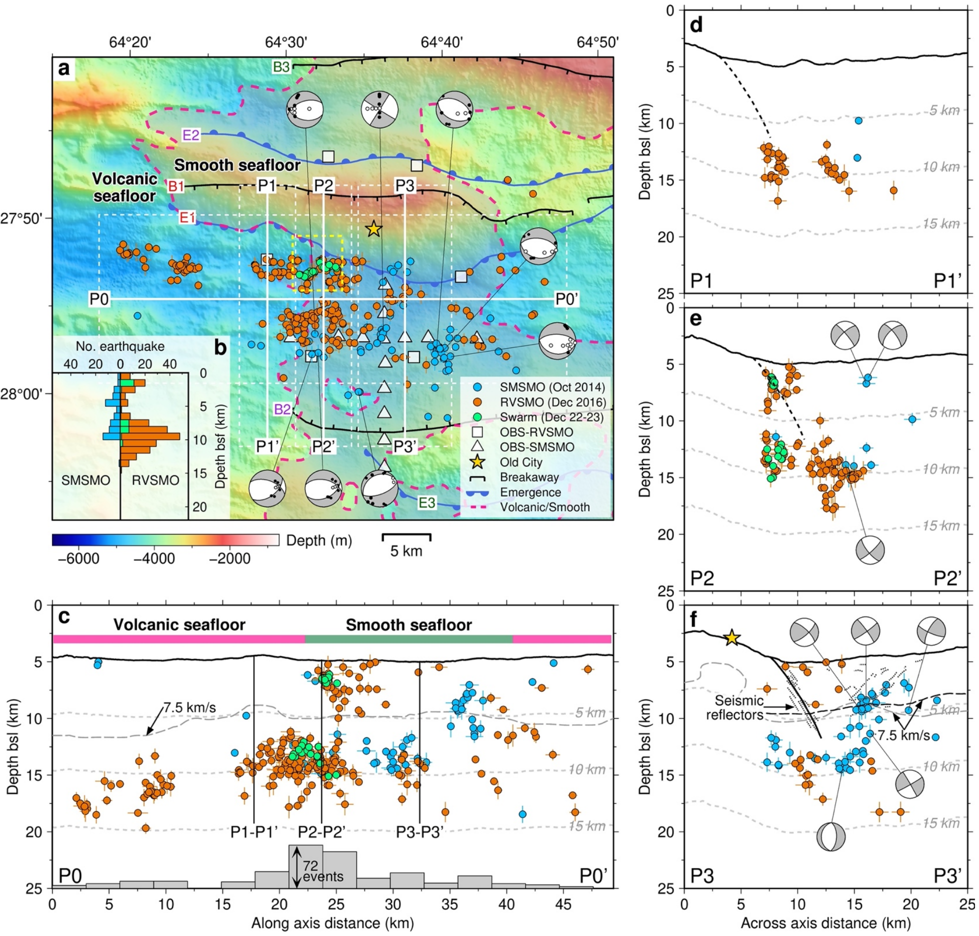

Figure 4.2. Distribution of earthquakes and focal mechanisms.

(a) Bathymetric map of the SWIR 64°30'E area showing the events of the SMSMO (blue circles) and RVSMO catalogs (orange circles), seismic swarm (green circles), and their focal mechanisms. Geological information (see legend for symbols) includes breakaways, emergences, and the boundary between volcanic and smooth seafloor (Cannat et al., 2019b). Best-fitting focal mechanisms have clear upward (black dots) and downward (white dots) first motions of P-wave onsets (Methods). Depth profiles (P0-P0' to P3-P3') are marked as labelled white lines in Figure 4.2a, with white dashed squares showing the corresponding boundaries for projected earthquakes in Figures 4.2c-4.2f. Yellow dashed square in Figure 4.2a marks the location of Figure 4.3b. (b) Histograms of earthquake depths below seafloor for the SMSMO (blue) and RVSMO (orange) catalogs, including the seismic swarm (green). (c) Along-axis depth profile P0-P0' projecting earthquakes within ±8 km off the profile (VE=1 and the same below). The classification of volcanic (pink) and smooth (green) seafloor is indicated (Cannat et al., 2006). Gray dashed line is the 7.5 km/s velocity contour (Corbalán et al., 2021). Labelled gray dashed lines show depths below the seafloor (the same below). (d) and (e) Across-axis depth profiles P1-P1' and P2-P2' projecting earthquakes within ±3 km off the profiles. Black dashed lines indicate the fault plane adapted from Figure 4.2f. (f) Across-axis depth profile P3-P3' projecting earthquakes within ±5 km off the profile. Dotted lines represent seismic reflectors, interpreted as DF1 damage zone (Momoh et al., 2017), with the main detachment fault plane tentatively drawn in the center (subseafloor solid black line). Black (Momoh et al., 2017) and gray (Corbalán et al., 2021) dashed lines are the 7.5 km/s velocity contours. Focal mechanisms are projected to profiles P2-P2' and P3-P3'.

At slow spreading ridges detachments, the maximum depth of earthquakes reaches 6-7 km bsf at the MAR 14°75'N and TAG (de Martin et al., 2007; Grevemeyer et al., 2013) and 12 km bsf at the MAR 13°N (Parnell-Turner et al., 2020, 2017). At ultraslow spreading ridges, this depth reaches 17-18 km at the Knipovich Ridge and at the SWIR 13°E (Grevemeyer et al., 2019; Meier et al., 2021), where highly oblique spreading produces effective spreading rates of only 7-8 mm/yr. Seismic events are reported down to 18 km bsf at the magmatically-robust Dragon Flag detachment system (Tao et al., 2020; Yu et al., 2018) and 10 km bsf at the Mount Dent detachment of the Mid-Cayman Spreading Center (Grevemeyer et al., 2019). Intriguingly, the more magmatically-robust Dragon Flag has a seismogenic lithosphere that is equivalent or greater in thickness to that determined here for the nearly-amagmatic SWIR 64°30'E with the same spreading rate. This questions current numerical models of the links between spreading rate, melt supply, and the thermal regime of MOR (Fan et al., 2021; Phipps Morgan and Chen, 1993a). We propose that hydrothermal removal of magmatic heat at Dragon Flag is more efficient than modelled, as evidenced by numerous black smokers (Copley et al., 2016; Tao et al., 2012).

4.5 Seismicity induced by melt intrusions in the ultramafic basement

A swarm of 34 earthquakes with a mean M_L of 0.9 and no identifiable mainshock was observed at the transition between volcanic and smooth seafloor in the RVSMO catalog during Dec 22-23, 2016 (Figs. 4.3a and 4.3b). We did not obtain well-constrained focal mechanisms due to the lesser number of OBSs in the RVSMO deployment (Methods). Earthquakes of this swarm are divided into three nearly simultaneous clusters based on spatial distribution: deep-west (14 events), deep-east (8 events), and shallow (12 events). The deep-west and deep-east clusters occurred 6 to 11 km into the detachment footwall (Fig. 4.3c). The shallow cluster was concentrated at ~1.5 km bsf near the detachment fault (Fig. 4.3c). All three clusters extend 1 to 2 km in the east-west, along-axis direction, with no lateral migration of the activity in time within each cluster. The swarm initiated in the deep-west cluster, with events starting in the other two clusters within 6 hours. The last 3 events of the deep-west cluster are located upward and to the north (Figs. 4.3b and 4.3c), indicating an upward migration of activity by about 2 km during the last ~8 hours of the migration (Figs. 4.3b and 4.3c). This, and its location underneath the volcanic hummocky seafloor (Fig. 4.3b), leads us to interpret this deep-west cluster as related to a magma injection. The nature of the deep-east cluster is not clear, but it is expected for a melt injection in this extensional context. The near-fault location of the shallow cluster and the lack of events joining it to the deeper events lead us to propose that the shallow cluster is tectonic. The swarm may thus be of mixed magmatic and tectonic origins, with tectonic activity at ~1.5 km bsf in the detachment being triggered by a magma injection at 11 to 6 km bsf in the detachment footwall. This could mean that melt intruding into the brittle peridotites at depths altered the stresses in the detachment footwall, so that a shallow portion of the fault which was near to rupture broke.

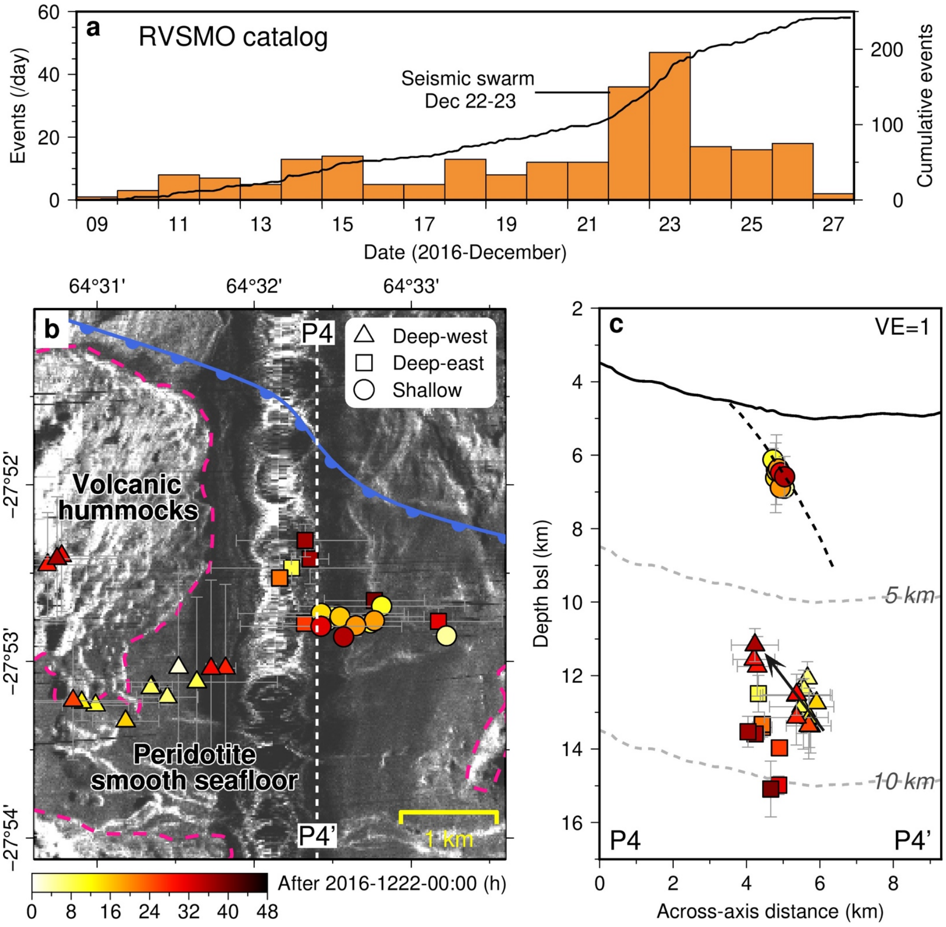

Figure 4.3. Temporal and spatial distribution of the seismic swarm.

(a) Histogram and cumulative histogram of located earthquakes for the RVSMO catalog. A seismic swarm with a total of 34 earthquakes occurred during December 22-23, 2016. (b) Epicenters of the seismic swarm, superimposed on the map of seafloor reflectivity showing the distribution of volcanic hummocks (dashed pink line on less reflective peridotite smooth seafloor (Sauter et al., 2013)). The swarm earthquakes are divided into three clusters: deep-west (triangles), deep-east (squares), and shallow (circles). Fill color of symbols indicates the time after 00:00, December 22nd, 2016. (c) Across-axis depth profile P4-P4' (dashed white line in Figure 4.3b) with projected swarm earthquakes (VE=1). Arrow indicates upward migration over time for the deep-west cluster. Black dashed line shows detachment fault as in Figure 4.2e. Labelled gray dashed lines show depths below the seafloor.

4.6 Methods

4.6.1 Microearthquake experiments

The first experiment, using 14 OBSs in a cross configuration, recorded 8 days of microearthquakes in between shots during the SISMOSMOOTH active seismic survey in October 2014 (R/V *Marion Dufresne*; SMSMO catalog; Figure 1.10). The second experiment, using 6 OBSs in a hexagon configuration, continuously recorded 19 days of microearthquakes during the ROVSMOOTH cruise in December 2016 (R/V *Pourquoi Pas?*; RVSMO catalog; Figure 1.10). Each OBS recorded three orthogonal ground motions and pressure signals.

4.6.2 Earthquake detection

The internal clocks of the OBSs were synchronized on deployment and recovery, and a linear drift was applied to eliminate the time lapse, which was verified by the final clock offset. Seismic wave sections with a high probability of earthquake events were detected by the CONDET program in the SEISAN software (Havskov and Ottemöller, 1999), and then an automatic picking procedure (Baillard et al., 2014) was used to pick P and S wave arrival onsets. These events were then registered in the SEISAN database, and P- and S-wave arrival onsets were then manually refined (Figure 4.4).

4.6.3 1-D velocity model

The 1-D P-wave velocity model was calculated using the VELEST program(Kissling et al., 1994). The initial velocity model was extracted from a seismic refraction experiment across DF1 during the SISMOSMOOTH cruise (Momoh et al., 2017), which is in general agreement with a broader velocity model at the same area (Corbalán et al., 2021) (Figure 4.5). Only events with OBS ≥6 and GAP≤180° were used in the VELEST program. The best-fitting P-wave velocity model was iteratively searched (Figure 4.5). The final root-mean-square (RMS) is acceptable low at 107 ms. The S-wave velocity (Vs) model is calculated using a best-fitting Vp/Vs ratio of 1.7 (ranging from 1.5 to 2.1), based on the Wadati diagram that plots travel time of P-wave versus travel time differences of P- and S- waves (S-P time; Figure 4.6).

4.6.4 Earthquake location and relocation

The initial earthquake locations were searched by the NonLinLoc software with the Oct-tree algorithm (Lomax et al., 2000) and the SWIR 64°30'E velocity model (Figure 4.5). 402

events of SMSMO (92) and RVSMO (292) catalogs were located with four or more stations (Figures 4.10a-1 to 4.10d-1). Station corrections were applied for the P and S phases (Figure 4.7), and the mean absolute station correction is only 60±40 ms in both catalogs. P- and S-waves travel time residuals follow the Gaussian distribution with an average RMS misfit of 34 ms (Figure 4.11).

We also applied the SWIR 65-66°E velocity model (Schlindwein and Schmid, 2016) (Figure 4.5), derived from a more magmatically-robust area than our study area (Minshull et al., 2006; Momoh et al., 2017), to locate earthquakes recorded in our study area using the NonLinLoc software (Figures 4.10a-2 to 4.10d-2). Earthquakes with more distant epicenters to the OBS network tend to have deeper hypocenters to form an inverted V shape of along-axis hypocenter depth distribution (Figure 4.10b-2), which is similar to what was documented at the SWIR 65-66°E (Schlindwein and Schmid, 2016).

309 events, with horizontal and depth errors of <5 km and RMS residual of <100 ms, were relocated using the Double-Difference Hypocenter (HypoDD) algorithm (Waldhauser and Ellsworth, 2000). The relocation uses both catalog and cross-correlation (Figures 4.12a-3 to 4.12d-3) and runs using the python module HypoDDpy (Krischer, 2015). A time window of 300 ms was applied based on pickings of P and S arrival onsets, and a correlation coefficient lower than 0.6 was rejected in cross-correlation. We also tested catalog only (Figures 4.12a-1 to 4.12d-1) and cross-correlation only (Figures 4.12a-2 to 4.12d-2) in HypoDD algorithm, which show stable seismicity patterns for both SMSMO and RVSMO catalogs and the improvement after relocation with applying both catalog and cross-correlation.

The 18 km-thick seismogenic lithosphere at the Dragon Flag detachment system of the SWIR is derived from two different microearthquake catalogs (Tao et al., 2020; Yu et al., 2018). The early one (Yu et al., 2018) recorded 17.5 days on average of microearthquakes in between airgun shots in 2010 (similar to the SMSMO catalog). Hypocenters were located using the least-squares HYPOSAT routine (Schweitzer, 2001) with a 1-D velocity model (an average value taken from several active-source tomography velocity models (Jian et al., 2017a; Niu et al., 2015; Zhao et al., 2013) and relocated using the Tomog3D (Zhao et al., 1992) with a 3-D velocity model (Yu et al., 2018). The Vp/Vs ratio was assumed as $\sqrt{3}$ (Yu et al., 2018). 214 well-located earthquake hypocenters have depths between 0 and 18 km bsf (Yu et al., 2018). The late one (Tao et al., 2020) recorded more than 9 months in total of microearthquakes during three different cruises in 2015-2017. Hypocenters were also located using the HYPOSAT routine (Schweitzer, 2001) with a 1-D velocity model taken from Zhao et al. (2013) but relocated using the HypoDD algorithm (Waldhauser and Ellsworth, 2000) with the same velocity model. The Vp/Vs ratio was not provided (Tao et al., 2020). 512 well-located earthquake hypocenters have a maximum depth of 13±2 km (Tao et al., 2020). We adopt the maximum depth (18 km) of two earthquake catalogs in the discussion.

4.6.5 Earthquake magnitude calculation

The definition of local magnitudes (M_L) is given by Richter (Richter, 1935):

$$M_L = \log(A) + n \log(r) + K r + C,$$

where A (in nm) is the maximum amplitude of horizontal components picked in the Wood-Anderson seismogram (Anderson and Wood, 1925), r (in km) is the hypocentral distance, C is a correction for each OBS, and n and K are constants to be calculated and relate to geometrical spreading and attenuation of seismic waves, respectively. The local magnitudes, parameters n and K, and station correction can be solved by a least-squares criterion that produces an optimal solution (Illsley-Kemp et al., 2017; Keir et al., 2006). For the SMSMO and RVSMO catalogs together, we obtain n of -2.923 and K of 5.85×10^{-3}.

4.6.6 First-motion focal mechanism

To assume best-fitting focal mechanisms, we use two first-motion-based algorithms, HASH (Hardebeck and Shearer, 2002) and FOCMEC (Snoke et al., 1984). Multiple criteria were applied: apparent first-motions polarities of P-wave arrival ≥8, azimuthal gaps ≤250°, the weighted fraction of misfit polarities <10%, RMS of fault plane uncertainty from HASH ≤35°, and similar reasonable solutions generated by both approaches. Eight acceptable focal mechanisms in the SMSMO catalog were shown in Figure 4.2. We did not obtain focal mechanisms in the RVSMO deployment due to the lesser number of OBSs.

4.7 Supplementary material

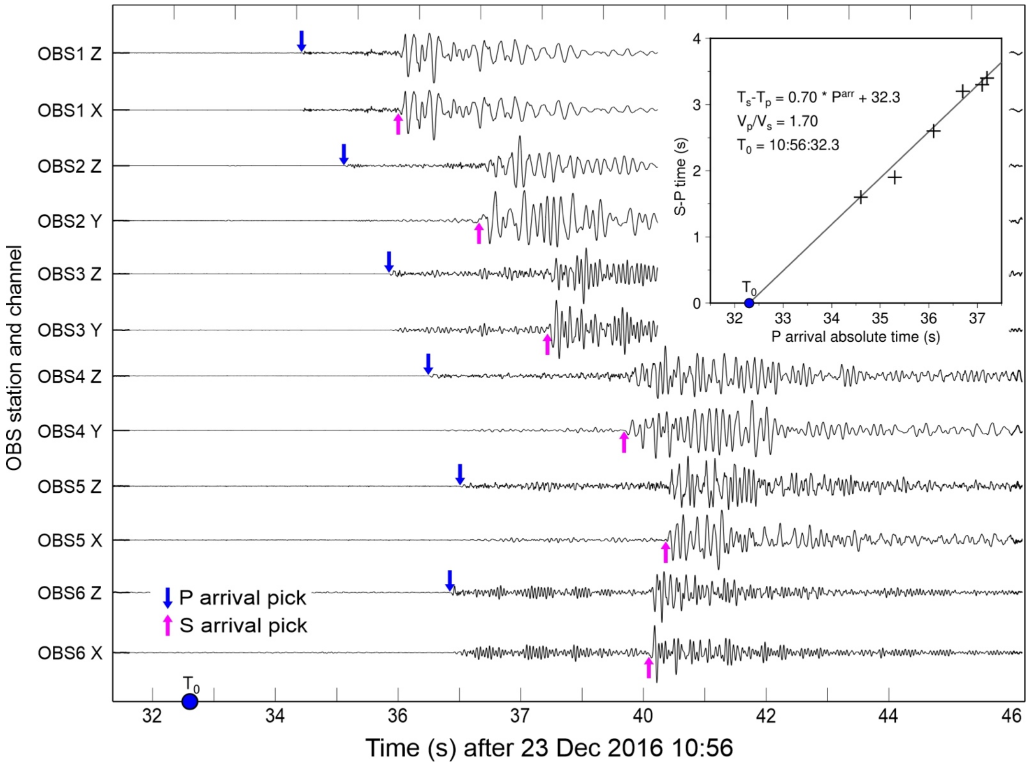

Figure 4.4. Typical waveforms of an exemplary event.

The event occurred at 64.394°E/27.883°S 11.6 km below seafloor with a local magnitude of 2.3, at 10:56, 23 Dec 2016 in RVSMO catalog. The inset shows the P-wave arrival absolute time versus arrival time differences of P- and S-waves (S-P time), yielding the origin time (T0) of 10:56:32.3 and a Vp/Vs ratio of 1.7.

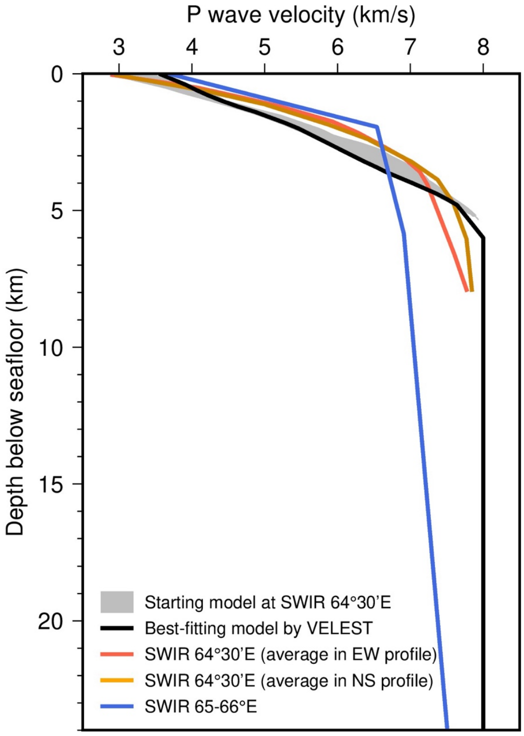

Figure 4.5. 1-D P wave velocity model.

Starting model (gray area) at the SWIR 64°30'E is extracted from a seismic refraction experiment (Momoh et al., 2017). The best-fitting model (black line) is iteratively searched by the VELEST program (Kissling et al., 1994). Red and orange lines are average velocity models in EW and NS profiles at the SWIR 64°30'E (Corbalán et al., 2021). Blue line is the velocity model at the SWIR 65-66°E (Schlindwein and Schmid, 2016).

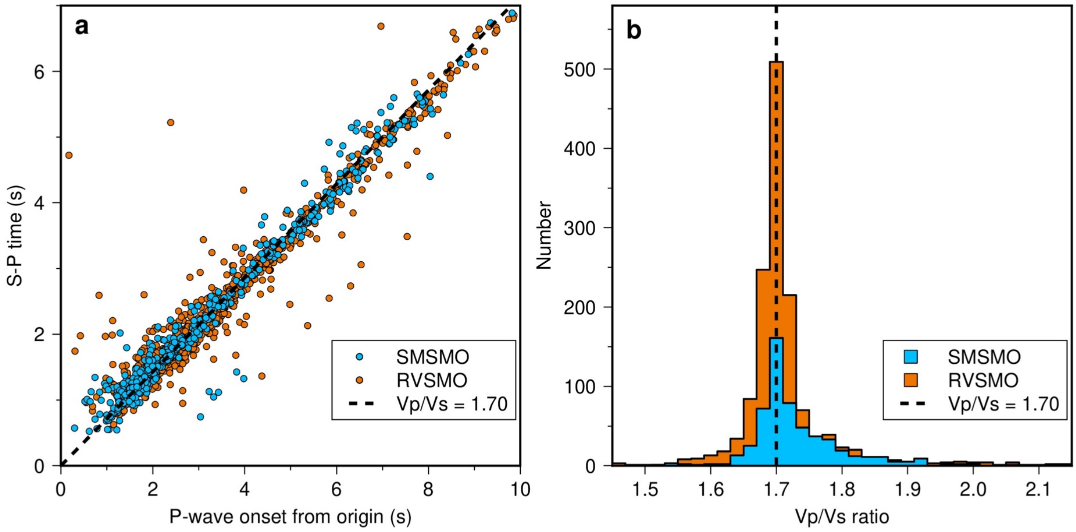

Figure 4.6. Wadati diagram.

(a) P-wave onset from origin versus S-P time (Wadati diagram) for both SMSMO (orange) and RVSMO (blue) catalogs. (b) Histogram of Vp/Vs ratio Vp/Vs ratio is calculated from the slopes of the Wadati diagram. The best-fitting Vp/Vs ratio is 1.7.

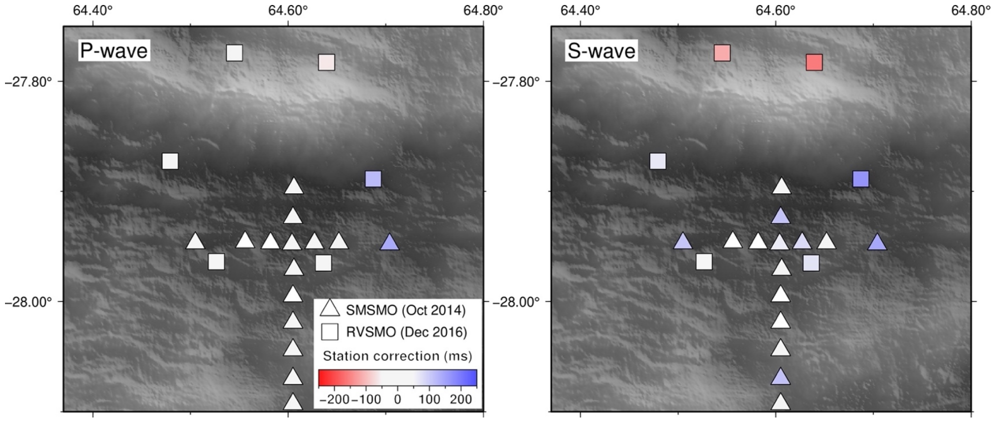

Figure 4.7. Station corrections of P- and S-wave after NonLinLoc location.

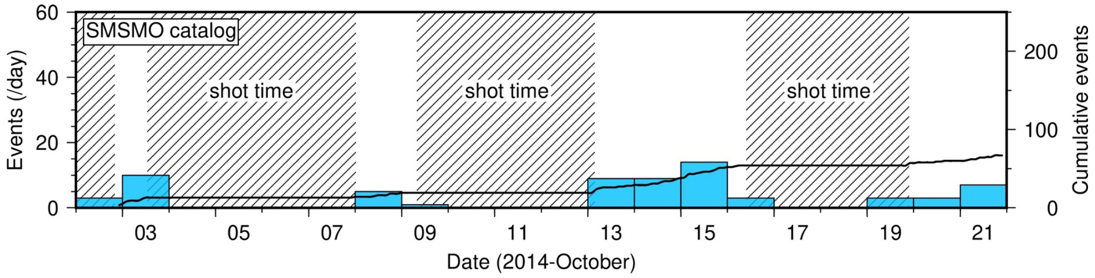

Figure 4.8. Histogram and cumulative histogram of earthquakes for the SMSMO catalog.

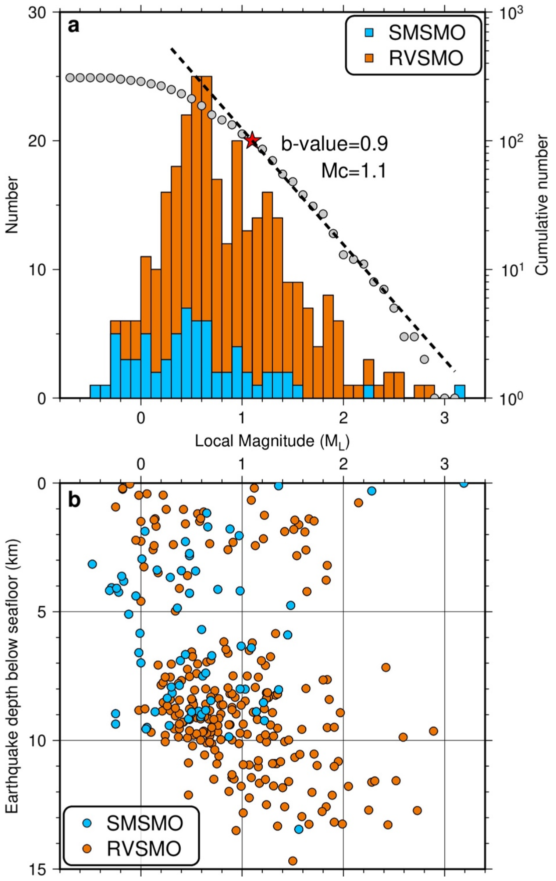

Figure 4.9. Distribution of local magnitude (M_L).

(a) Histograms of local magnitude for the SMSMO (blue) and RVSMO (orange) catalogs (left Y-axis). The cumulative number of earthquakes for both catalogs (gray circles) as a function of local magnitude (right Y-axis). Magnitude completeness (Mc) is determined as 1.1 (red star), resulting in a b-value of 0.9 (slope of the dashed line). (b) Local magnitude as a function of earthquake depth for the SMSMO (blue) and RVSMO (orange) catalogs.

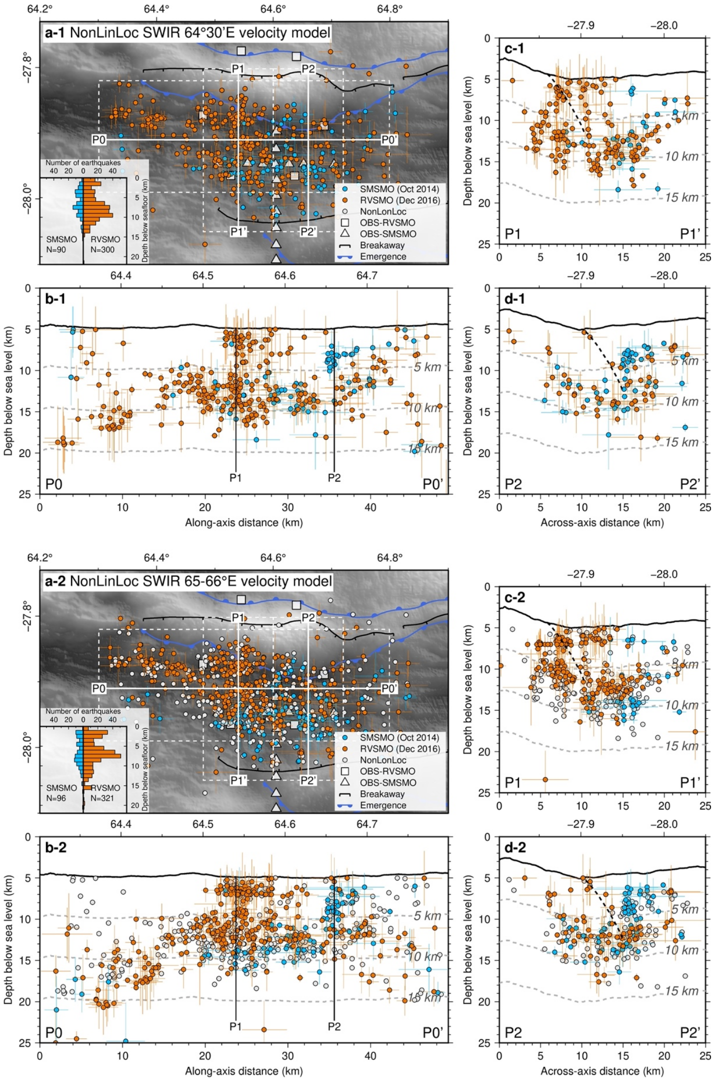

Figure 4.10. Earthquake locations.

See legend for symbols. Earthquake locations using the NonLinLoc with the SWIR 64°30'E velocity model (a-1 to d-1). Earthquake locations using the NonLinLoc with the SWIR 65-66°E velocity model (a-2 to d-2), compared with the NonLinLoc results with the SWIR 64°30'E velocity model (pale gray). Velocity models see Figure 4.5.

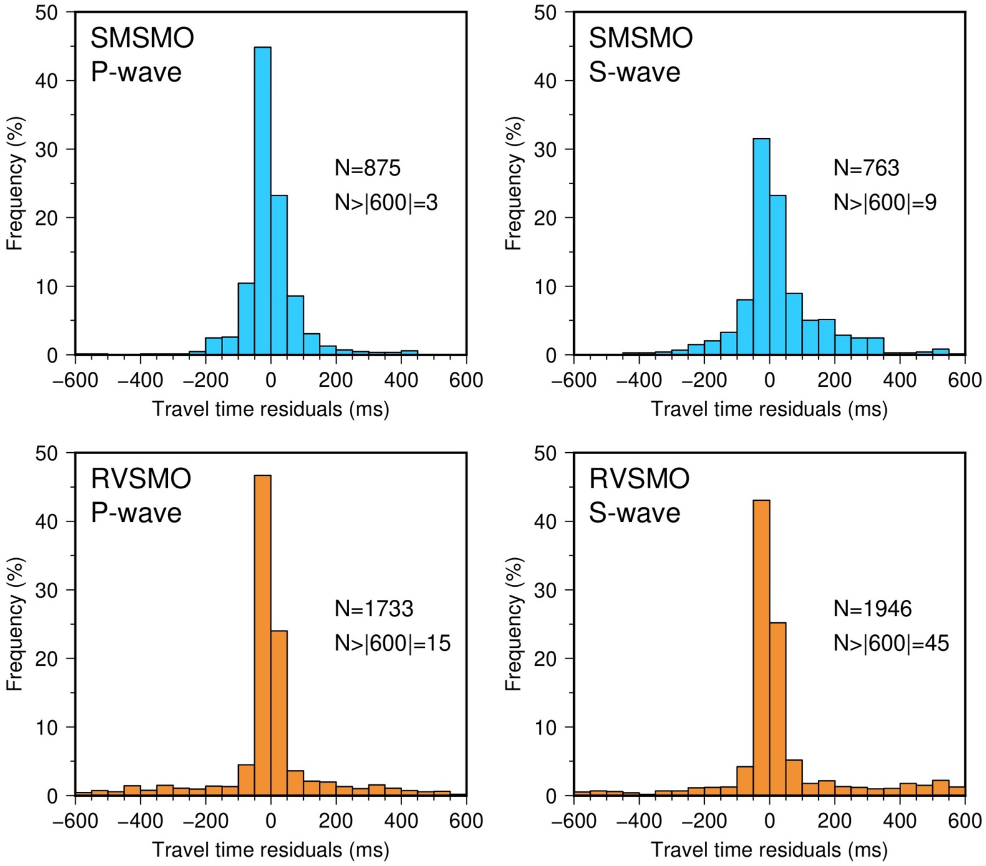

Figure 4.11. Frequency distribution of P- and S-wave travel time residuals for the SMSMO (blue) and RVSMO (orange) catalogs.

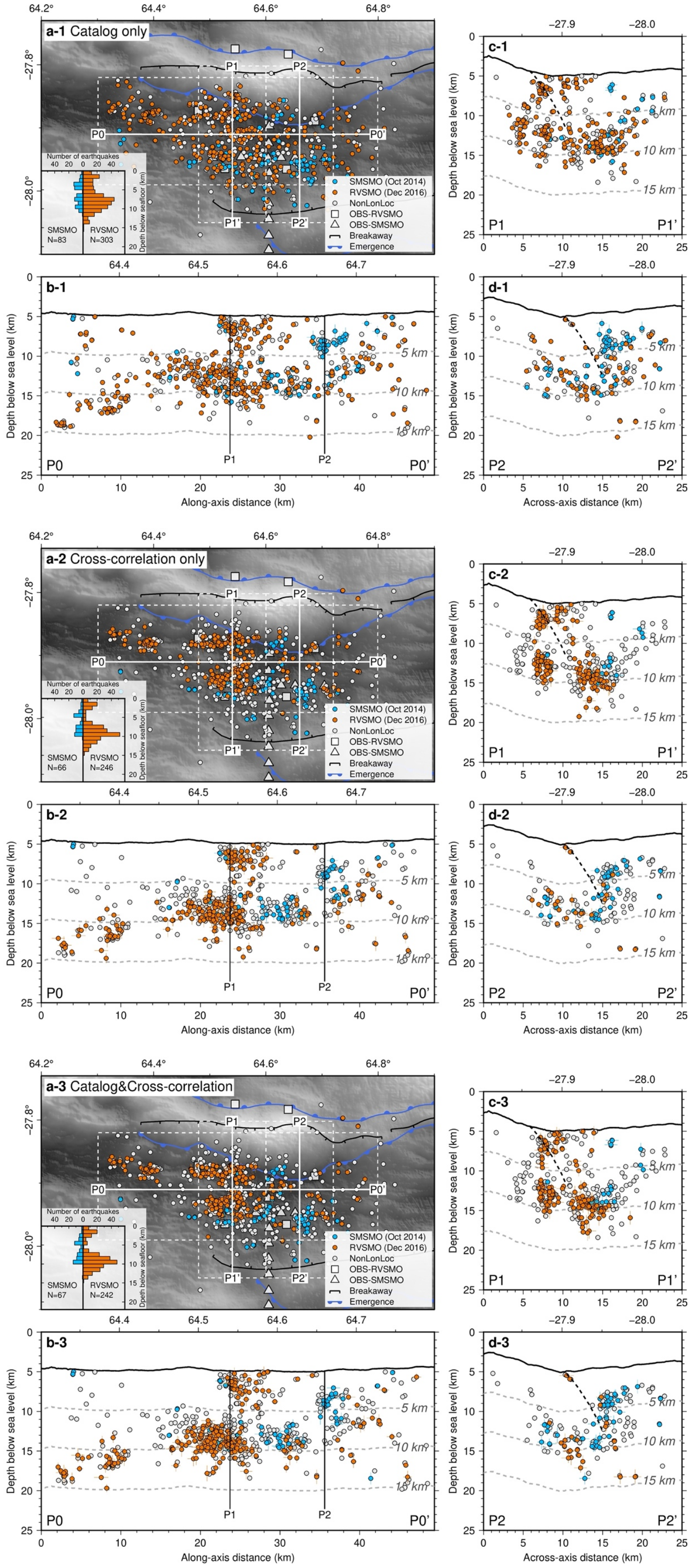

Figure 4.12. Earthquake relocations.

See legend for symbols. Tests of earthquake relocation using the HypoDD with catalog only (a-1 to d-1), cross-correlation only (a-2 to d-2), and catalog&cross-correlation (a-3 to d-3; same results as Figure 4.2). All are compared with the NonLinLoc results (pale gray) with the SWIR 64°30'E velocity model (Figures 4.10a-1 to 4.10d-1).

Chapter 5

Thermal regime of slow and ultraslow spreading ridges controlled by melt supply and modes of emplacement

In this chapter, I focus on 2D numerical thermal modelling, modified from Fan et al. (2021). This chapter has been submitted to Journal of Geophysical Research: Solid Earth with a title of *Thermal regime of slow and ultraslow spreading ridges controlled by melt supply and modes of emplacement*. I carried out all the numerical simulations, produced all figures, and wrote the manuscript, under the supervision of Jean-Arthur Olive and Mathilde Cannat.

5.1 Abstract

Melt supply at slow and ultraslow spreading ridges is overall reduced and highly variable, producing a large spectrum of magmatic crustal thickness. This melt heats the lithosphere owing to magma cooling and crystallization, substantially shaping the thermal regime. Geological data suggest that melt is emplaced over a wide range of depths, variably accessible to efficient hydrothermal cooling, and that periods of higher and lower melt supply may alternate at a given ridge location. Here we present results from a 2D numerical thermal model that couples repeated melt injections and hydrothermal convection to test these hypotheses. We first constrain thermal regimes inferred from two ultraslow spreading endmembers in melt supply at the Southwest Indian Ridge (SWIR): a magmatically-robust endmember at 50°28'E and a nearly-amagmatic endmember at 64°30'E. We adjust parameters associated with melt supply (the frequency of melt injections and the temperature of the host rocks upon melt emplacement) and hydrothermal circulation (the extent and the permeability of the hydrothermal system). Our simulations predict that higher frequencies of melt injections unsurprisingly produce hotter thermal regimes. However, at a given melt injection frequency, melt emplacement in cooler host rocks causes a cooler thermal regime with black-smoker hydrothermal circulation that extracts heat efficiently. Cyclic changes of melt supply with alternating waxing and waning phases, as proposed from geological data at the SWIR 50°28'E, is successfully predicted by constraining the range of melt injection frequencies, illustrating an oscillatory thermal regime and providing insight into lower-crustal construction at magmatically-robust slow and ultraslow ridge regions.

5.2 Introduction

Melt supply at mid-ocean ridges (MORs), i.e., the volume flux of magma ascending from the asthenosphere to the ridge axis to form the oceanic crust, is a key control on seafloor spreading modes. Melt plays a dual role in the formation of oceanic lithosphere: repeated magmatic intrusions accommodate a fraction of the plate divergence, and they also alter the thermal regime of the ridge by releasing specific and latent heat upon cooling and crystallizing (Buck et al., 2005; Cannat et al., 2019; Phipps Morgan and Chen, 1993a). At slow and ultraslow spreading ridges (full spreading rate of < 40 mm/yr), melt supply is highly variable (Chen, 1992; Christeson et al., 2019) due to along-axis melt focusing from segment ends to segment center (Cannat et al., 1995; Lin et al., 1990; Kuo and Forsyth, 1988). This melt may be emplaced over a wide range of depths, from lava flows on the seafloor to isolated gabbro bodies crystallized from unextracted melt that remains trapped in the mantle (Cannat et al., 1995). Cannat et al. (2019) proposed that the variability of melt supply (both in volume flux and depth of emplacement) could result in sharp along-axis transitions in the thermal regime, resulting in dramatic shifts in lithospheric thickness and strength over along-axis distances < 30 km, for example, the transition from volcanic to ultramafic seafloor in the eastern part of the ultraslow spreading Southwest Indian Ridge (SWIR in Figure 5.1a; full spreading rate of ~14 mm/yr). Magmatic heat is extracted to the ocean by hydrothermal circulation, which is enabled by tectonic processes and pervasive fracturing of the lithosphere, and manifests at the seafloor as clusters of hydrothermal vents (e.g., Lowell et al., 2013). The resulting thermal regime reflects a balance between magmatic heat supply and hydrothermal heat removal (Phipps Morgan and Chen, 1993a; Theissen-Krah et al., 2011).

The thermal structure of MOR axes includes two isotherms of interest at 650°C and 1000°C, which should outline regions of brittle deformation and crystal mush zones, respectively (McKenzie et al., 2005; Phipps Morgan and Chen, 1993a; Sinton and Detrick, 1992). The maximum depth of earthquakes is believed to be a proxy for the location of the brittle-ductile transition (BDT), roughly corresponding to the 650°C isotherm (Anderson, 1995; McKenzie et al., 2005). Seismically imaged low-velocity anomalies (LVAs) topped by axial melt lens (AML) reflectors can be an additional proxy for persistent crystal mush zones that are enclosed by the basaltic solidus at 1000°C (Fontaine et al., 2011; Sinton and Detrick, 1992). Thermal models of MOR axes typically predict a colder thermal regime as spreading rate decreases, with the impossibility to sustain long-lived magmatic mush zones at crustal depths at slow and ultraslow MORs (Phipps Morgan and Chen, 1993; Theissen-Krah et al., 2011).

However, several seismic observations appear to contradict this expectation. The thermal regime of the SWIR, for example, is inferred to vary between two magma supply endmembers: a magmatically-robust endmember (e.g., at 50°28'E: Chen et al., 2021) and a nearly-amagmatic endmember (e.g., at 64°30'E: Sauter et al., 2013). The center of the 50°28'E segment (Figure 5.1b) is characterized by a low-velocity mush zone between ~4 and 9 km below seafloor (bsf) with an along-axis extent of 7-8 km, and its magmatic crustal thickness has remained 9.5 km over the last > 3 Myr (Jian et al., 2017). At 64°30'E (Figure 5.1c), the deepest earthquake lies at ~15 km (Chen et al., 2020) in a context of nearly zero magmatic crust (Cannat et al., 2006; Momoh et al., 2017; Sauter et al., 2013), and seismic velocity gradients increase almost linearly with depth, which has been interpreted to reflect a decrease in serpentinization and fracturing with depth (Corbalán et al., 2021; Momoh et al., 2017). Surprisingly, the more magmatic detachment system in the "Dragon Flag" section of the SWIR at 49°39'E has the same spreading rate but features earthquakes that occur even deeper than at this nearly-amagmatic SWIR 64°30'E section (18 vs. 15 km; Chen et al., 2020; Tao et al., 2020; Yu et al., 2018). Thermal models of slow and ultraslow MORs must therefore account for the possibility of extensive regions of crystal mush at crustal depths, as well as for a possible decorrelation between the depth of the 650ºC isotherm and magma supply, at a given spreading rate.

The thermal regime of fast spreading MOR axes is often considered to be near steady-state over geological time, as evidenced by shallow, nearly continuous AMLs (Detrick et al., 1987; Marjanović et al., 2014) and nearly uniform off-axis seafloor morphology (Soule et al., 2009). By contrast, the axial thermal regime at slow and ultraslow spreading ridges appears temporally variable, and cyclic changes in melt supply with alternating waxing and waning phases over a few 100s of kyrs have been documented at a few slow and ultraslow spreading, magmatically-robust ridge sections, such as the centers of the SWIR 50°28'E segment (Chen et al., 2021) and the Menez Gwen segment of the Mid-Atlantic Ridge (MAR; Klischies et al., 2019). Cyclic melt supply at the SWIR 50°28'E results in the accretion of smooth domal volcanos during waxing phases and of hummocky ridges during waning phases (Chen et al., 2021). Interestingly, the thickness of the magmatic crust does not appear to vary significantly at these time scales (Jian et al., 2017), which may reflect a damping process characteristic of ultraslow settings (Chen et al., 2021).

Consequently, slow and ultraslow spreading ridges are natural laboratories for identifying key controls on the variability of the axial thermal regime that is documented across sections that spread at similar rates, and for assessing the impact of a transient melt supply on the thermal regime. This paper applies a modified version of a 2-D numerical thermal model (Fan et al., 2021) that couples repeated magma intrusions and hydrothermal convection (Figure 5.2b). The previous version in Fan et al. (2021) focused on simulating the cold thermal regimes of ultraslow spreading ridge sections with low to nearly zero melt supply, but did not consider sections with robust melt supply, where the thermal regimes show especially high sensitivity to melt injection frequencies (e.g., Figure 4 in Fan et al., 2021).

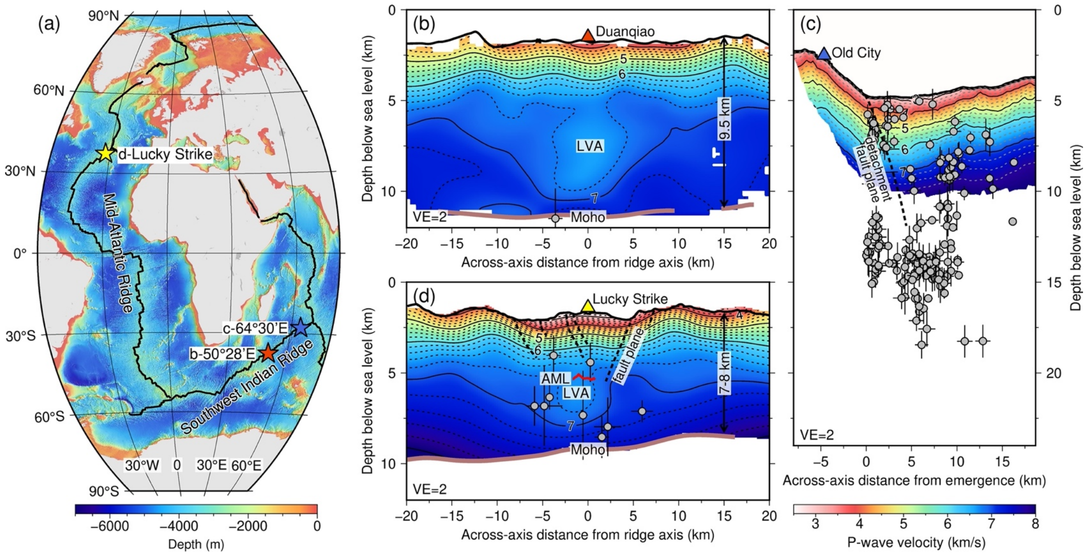

Figure 5.1. The SWIR and MAR, and across-axis depth profiles for the SWIR 50°28'E, SWIR 64°30'E, and Lucky Strike.

(a) Bathymetric map for the Southwest Indian Ridge (SWIR) and Mid-Atlantic Ridge (MAR). Stars show the locations of the SWIR 50°28'E, SWIR 64°30'E, and MAR Lucky Strike. (b) P-wave seismic velocity structure (VE = 2 and the same below) across the ridge axis at the SWIR 50°28'E (Jian et al., 2017). Contours are in 0.2 km/s intervals (the same below). LVA: low-velocity anomaly. The Moho interface (thick brown lines) is based on PmP arrivals (Jian et al., 2017). Gray circles with error bars are microearthquakes (Yu et al., 2018). The Duanqiao hydrothermal field exposes relict black-smoker chimneys (Chen et al., 2021; Yang et al., 2017). (c) P-wave seismic velocity structure across the active detachment fault at the SWIR 64°30'E (Momoh et al., 2017). Detachment fault plane is drawn by seismic reflection (Momoh et al., 2020, 2017). Microearthquakes are from Chen et al. (2020). The Old City hydrothermal field has active low-temperature, carbonate-brucite chimneys. (d) P-wave seismic velocity structure across the ridge axis at the Lucky Strike (Seher et al., 2010). The Moho interface is based on PmP arrivals (Seher et al., 2010). Microearthquakes are from Dusunur et al. (2009). The AML (red line) and normal fault planes (dashed lines) are imaged by seismic reflection (Combier et al., 2015; Singh et al., 2006). The Lucky Strike hydrothermal field has active high-temperature black smokers (Langmuir et al., 1997).

We use the modified model to constrain the thermal regimes of two melt supply endmembers of ultraslow spreading ridges (the most magmatically-robust SWIR 50°28'E and the nearly-amagmatic SWIR 64°30'E; Figure 5.1). We then take the SWIR 50°28'E as a reference in our numerical simulations of cyclic changes in melt supply. To do so, we adjust parameters associated with how much and/or at what depth the melt is emplaced, and we vary the impact of hydrothermal circulation by adjusting the maximum depth and the permeability of the hydrothermal domain. To explore the impact of the depth at which melt is emplaced, we periodically intrude melt as a lens centered in the model, whose top coincides with an isotherm. We call this isotherm the magma emplacement temperature. More precisely, it is the temperature of the host rock upon melt emplacement. This allows us to distinguish between repeated intrusions into the cold/shallow vs. the hot/deep lithosphere. With four groups of simulations (Figure 5.2) and two important observables in the model, e.g., the depths to the BDT (650℃ isotherm) and the mush zone (1000℃ isotherm), we successfully account for the thermal regimes of two ultraslow spreading endmembers and for the variability of the thermal regimes at ultraslow (extending to slow) spreading ridges. We also constrain the range of melt injection frequencies, exploring the thermal impact of the cyclic changes of melt supply inferred from geological data at the SWIR 50°28'E.

5.3 Methods

5.3.1 Model setup

We model a 2-D section of young oceanic lithosphere through which heat can be transferred conductively, as well as advected by hydrothermal fluids in a shallow, permeable region (Figure 5.2). We follow the numerical approach of Fan et al. (2021) and Olive and Crone (2018), who used a finite volume method to solve for conservation of mass and energy in fluid-saturated, non-deforming porous medium obeying Darcy's law:

$$\boldsymbol{\nabla} \cdot \left(-\frac{k}{\mu_f} \left(\boldsymbol{\nabla P} - \rho_f \boldsymbol{g} \right) \right) = 0, \tag{1}$$

where k is the permeability of the hydrothermal layer, μ_f is the viscosity of the fluids, and ρ_f is the density of the fluids. The gradient of pressure ($\boldsymbol{\nabla P}$) and the acceleration of gravity ($\boldsymbol{g}$) in bold are vectors. The fluid velocity ($\boldsymbol{v_f}$) corresponds to the term inside the divergence operator. To evolve the temperature field T, we solve Equation (1) with the heat equation:

$$\rho_{eff} C_{eff} \frac{\partial T}{\partial t} + \rho_f C_f \boldsymbol{v_f} \cdot \boldsymbol{\nabla T} = \lambda_{eff} \nabla^2 T + H_M, \tag{2}$$

where C is the specific heat, and λ is the thermal conductivity. ρ_{eff}, C_{eff}, and λ_{eff} are effective properties of water-saturated rocks, obtained by averaging the properties of the hydrothermal fluids (weighted by the porosity ϕ) and the dry matrix ($1-\phi$). H_M is the term for latent heat from magma crystallization.

Our numerical domain is 24 km high and 10 km wide (discretized as 100-m wide cells). It allows no conductive heat flow through its sides and is heated at its base to a constant temperature of 1250ºC. The top boundary represents the seafloor corresponding to a hydrostatic pressure P_0 = 20 MPa, which allows fluids to escape with no conductive flux and 0ºC fluids to enter the lithosphere. The thermodynamic properties of the fluids correspond to those of a 3.2 wt% NaCl-H_2O mixture (Anderko and Pitzer, 1993; Pitzer et al., 1984). The viscosity of the fluid is approximated as pure water, following the parameterization of Holzbecher (1998). The initial temperature field (at $t = 0$) is set to linearly increase from 0°C to 1000°C (basaltic solidus) between the seafloor and a depth of 10 km, and to linearly increase from 1000°C to the imposed bottom temperature of 1250°C between the 10 km depth and the bottom of the domain (Figure 5.2a).

5.3.2 Permeable hydrothermal system

Hydrothermal circulation (Darcy flow) is confined to a shallow domain of uniform permeability k (Figure 5.2b), bounded by a percolation front that separates it from the underlying impermeable layer (Olive and Crone, 2018). This approach constitutes a middle ground between imposing temperature and imposing heat flow at the base of the convective domain. It also allows the base of the convective region (at depth Z_H) to evolve through time in a manner that depends on its temperature (T_H). We adopt the parameterization of Olive and Crone (2018) and Fan et al. (2021), which treats the percolation front as a cracking front consisting of mineral-scale fractures driven by thermo-elastic stresses which accumulate when rocks cool below a visco-elastic transition temperature T_{ve}, as initially proposed by Demartin et al. (2004). The underlying assumption is that rocks become permeable as soon as the stress intensity factor associated with the aforementioned fractures reaches its critical value (K_{IC}), allowing rapid crack propagation and the establishment of connected fluid pathways. The stresses driving crack propagation increase as T_H decreases below T_{ve}, but are resisted by the effect of confining pressure as the cracking front deepens (Z_H increases). Olive and Crone (2018) expressed this balance between cooling stresses and confining pressure as:

$$A_T(T_{ve} - T_H) - A_P(P_0 + \rho g Z_H) = K_{IC}, \tag{3}$$

where A_T and A_P are sensitivity coefficients of the cooling stress and confining pressure, respectively (which depend on micro-mechanical parameters such as grain size), and ρ is the lithosphere density. Rather than exploring the effect of micro-mechanical parameters on the values of A_T, A_P, and the resulting dynamics of the cracking front (e.g., Demartin et al., 2004; Olive and Crone, 2018), we use the same value of A_T as Fan et al. (2021) and empirically adjust A_P to define the maximum hydrothermal domain depth (Z_{H0}; dashed blue lines in Figure 5.2a), i.e., the maximum depth of the cracking front (corresponding to $T_H = 0$°C in equation 3). According to equation (3), a lower A_P corresponds to a higher slope of the straight line between (T_{ve}, 0) and (0, Z_H) (solid blue lines in Figure 5.2a), suggesting that for the same accumulated cooling stress (i.e., the same T_H), fractures experience less resistance from confining pressure, and the cracking front can reach greater depths.

5.3.3 Magmatic heat input

In addition to heating the base of the domain, magmatic heat is supplied in the form of repeated AML injection events. These consist of instantaneously resetting temperature to the liquidus T_M = 1200ºC within a domain of vertical and horizontal extents H_{AML} and W_{AML}, respectively, every time interval τ (Fan et al., 2021). The imposed AML is always centered in the horizontal direction, and its top coincides with the isotherm Tr. Tr is the melt emplacement temperature, or more explicitly, the temperature of the isotherm at which melt is emplaced. Tr is a key parameter which we will systematically vary in this work. Our simulations keep tracks of melt fraction, assumed to be a linear function of temperature between the basaltic solidus T_S = 1000ºC and the liquidus at T_M. Following the approach of Fontaine et al. (2011) and Fan et al. (2021), a latent heat term, i.e., the H_M term in Equation (2), is expressed in the energy equation when rocks cool between T_M and T_S:

$$H_M = \frac{-L\rho_M}{T_M - T_S}\frac{\partial T}{\partial t}\lceil x_L \rceil, \tag{4}$$

where L is the latent heat, ρ_M is the magma density, and x_L is the local melt fraction, which is updated every time step to match the evolving temperature field ($x_L = 0$ at $T = T_S$, and $x_L = 1$ at $T = T_M$). We use the $\lceil x_L \rceil$ term in equation (4) to make sure that the latent heat is considered only where the melt is present ($0<x_L \leq 1$, i.e., $\lceil x_L \rceil = 1$). The latent heat, in addition to the specific heat of magma and hot rocks, fuels hydrothermal convection above depth Z_H.

The dimensions and frequency of melt intrusions are not set arbitrarily, as they must be compatible with the inferred melt supply of slow and ultraslow spreading ridges. Melt flux at a ridge section can be expressed as:

$$UHc = \frac{W_{AML}H_{AML}}{\tau}, \tag{5}$$

where U is the full spreading rate, and Hc is the equivalent magmatic (crustal) thickness. Assuming W_{AML} = 4 km and H_{AML} = 0.2 km, the 9.5-km thick crust at the SWIR 50°28'E (Jian et al., 2017a) corresponds to a time interval of τ = 6 kyr, and the ~7.5-km thick crust at the Lucky Strike segment of the MAR (U = 21 mm/yr; Figure 5.1d) (Seher et al., 2010) corresponds to a time interval of τ = 5.1 kyr (Figure 5.2c).

We chose the model height of 24 km by running initial simulations with a maximum hydrothermal domain depth of Z_{H0} = 6 km, a permeability of $k = 10^{-15}$ m^2, and varied model heights. We ran these simulations with no melt injection until stationary states were reached, and selected the model heights that placed the 650ºC isotherm at a depth of 15 km, corresponding to the inferred BDT at the nearly-amagmatic SWIR 64°30'E section (Figure 5.10b) (Chen et al., 2020). We note that this depth can also be obtained with a different model setup (e.g., Fan et al., 2021), in which the domain height is 30 km with an adiabatic bottom, the AML dimensions are set to W_{AML} = 5 km and H_{AML} = 0.4 km, and magmatic emplacement occurs every τ = 75 kyr beneath the isotherm Tr = 1000°C (Figure 4b in Fan et al., 2021 and reproduced by this study in Figure 5.10a).

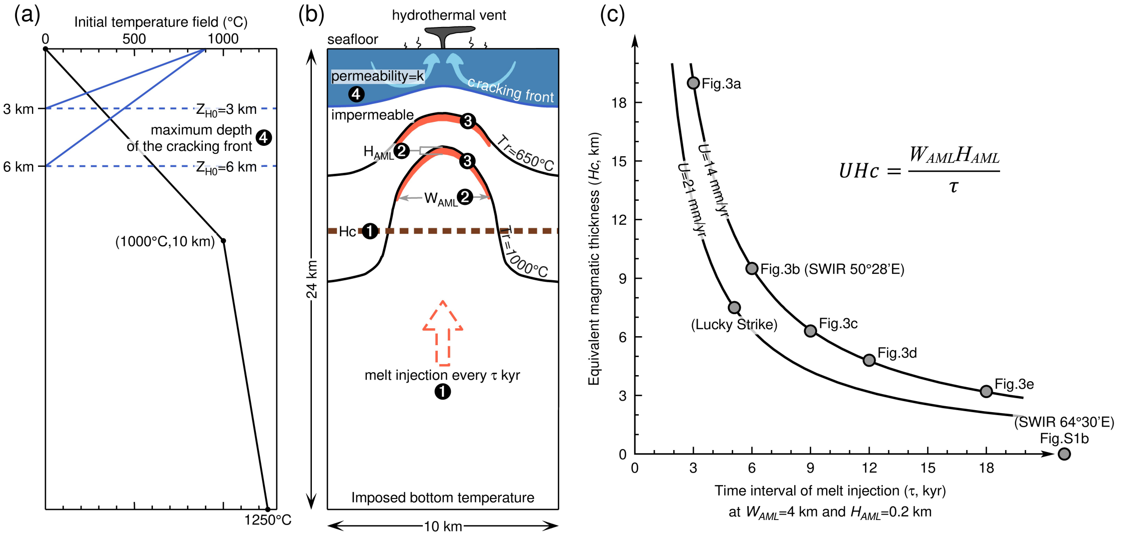

Figure 5.2. Model setup.

(a) Initial temperature field and the setting of the maximum depth of the cracking front (Z_{H0}). (b) Cartoon of the thermal model setup, modified from Fan et al. (2021). Numerical labels correspond to the four groups of simulations. (c) Equivalent magmatic thickness (Hc) vs. time interval of melt injection (τ) at W_{AML} = 4 km and H_{AML} = 0.2 km, according to Equation (5).

We conducted four groups of simulations to explore different parameters associated with melt supply and hydrothermal circulation. These parameters correspond to numerical labels in Figures 5.2a and 5.2b. We take the magmatically-robust SWIR 50°28'E, with its 9.5-km thick magmatic crust as a reference case. All simulations are run until reaching stationary states. The key parameters we vary are:

1) The frequency of melt injection ($1/\tau$; Figure 5.3 and Movie S1),

2) AML dimensions with constant Hc (W_{AML} and H_{AML}; Figures 5.4 and 5.12 and Movies S2-S5),

3) The temperature of the host rock upon melt emplacement (Tr; Figures 5.5, 5.6, and

5.13 and Movies S6-S14),

4) The maximum hydrothermal domain depth (Z_{H0}) and its permeability (*k*; Figures 5.7 and 5.14 and Movies S15-S18).

We also simulate cyclic variations in melt supply by alternately changing the frequency of melt injections (higher frequency during waxing magmatic phases, and lower frequency during waning phases; Figures 5.8, 5.9, and 5.15-5.22 and Movies S19-S27). The model outputs of interest in all simulations include hydrothermal venting temperatures, the depths to the BDT (650°C isotherms) and to the mush zone (1000°C isotherms), and the occurrence of mush zones at crustal depths.

5.4 Results

5.4.1 Frequency of melt injection

The first group of simulations explore the effect of varying the time interval between magmatic injections from τ = 3, 6, 9, 12, to 18 kyr, corresponding to equivalent magmatic thicknesses of Hc = 19, 9.5, 6.3, 4.8, and 3.2 km at the SWIR spreading rate of 14 mm/yr, respectively (Figures 5.3a-5.3e). AML dimensions are set to W_{AML} = 4 km and H_{AML} = 0.2 km, and AMLs are emplaced beneath the Tr = 1000°C isotherm, coinciding with the basaltic solidus. Another simulation with no melt injection is also run for reference (Figure 5.3f). Hydrothermal domains are confined above Z_{H0} = 3 km and have a permeability of $k = 10^{-15}$ m^2.

The melt-injection simulations are carried out for 3 Myr and the no-melt simulation for 20 Myr to ensure that all the thermal regimes reach stationary states independent from the initial condition. As the time interval increases from Figures 5.3a to 5.3e (i.e., the frequency of melt injection and the equivalent magmatic thickness decrease), the stationary-state thermal regimes become cooler and are characterized by a nonlinear decrease in hydrothermal vent (outflow) temperatures and a linear deepening of the 650°C and 1000°C isotherms (squares in Figures 5.5a and 5.5b, respectively). In simulations with τ = 3 and 6 kyr, extensive mush zones enclosed by the solidus (1000°C) isotherms develop and persist at depths that match those of the lower crust for the corresponding equivalent crustal thicknesses of Hc = 19 and 9.5 km at the SWIR spreading rate (Figures 5.3a and 5.3b). By contrast, in simulations with τ = 12 and 18 kyr, the 1000ºC isotherms equilibrate at depths greater than the equivalent magmatic thickness of the crust at the SWIR spreading rate (Figures 5.3d, and 5.3e).

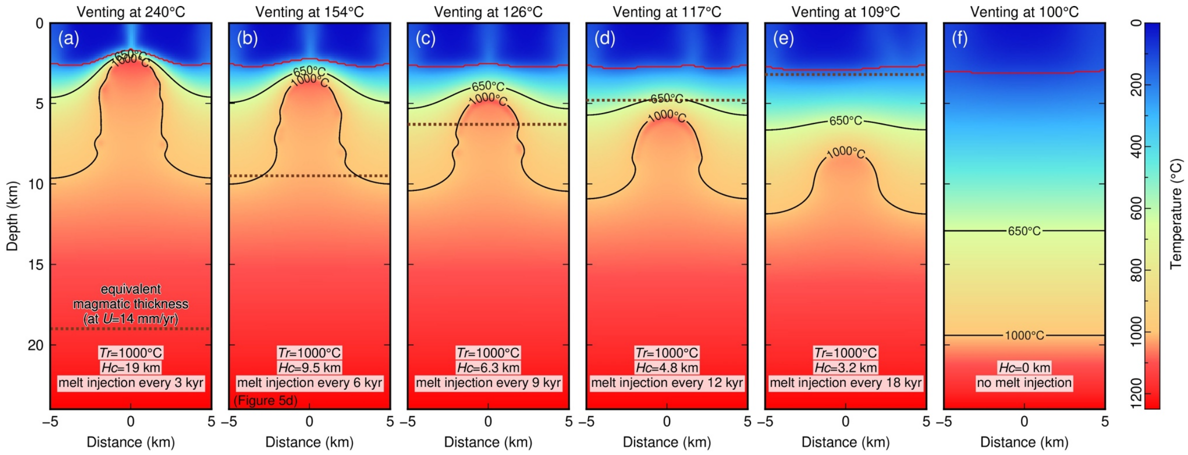

Figure 5.3. Snapshots of stationary-state thermal regimes for simulations with varying time interval of melt injection.

(a)-(e) Snapshots of stationary-state thermal regimes for simulations, varying time intervals of melt injection from τ = 3, 6, 9, 12, to 18 kyr, corresponding to Hc = 19, 9.5, 6.3, 4.8, and 3.2 km at the SWIR spreading rate of 14 mm/yr (from Figures 5.3a to 5.3e). The AML dimension is set to W_{AML} = 4 km and H_{AML} = 0.2 km, emplaced beneath Tr = 1000°C. Hydrothermal domains are confined above Z_{H0} = 3 km with a permeability of $k = 10^{-15}$ m^2. Red lines indicate cracking fronts. Black lines indicate the 650°C and 1000°C isotherms. The equivalent magmatic thicknesses are between the seafloor and dashed brown lines. (f) Snapshot of the stationary-state thermal regime with the same configuration of the hydrothermal domain but no melt injection.

5.4.2 AML dimensions with constant Hc

The second group of simulations examines the effect of varying W_{AML} from 1 to 5 km with a constant H_{AML} = 0.2 km (Figures 5.4a and 5.4b), as well as varying H_{AML} varying from 0.1 to 0.5 km with a constant W_{AML} = 4 km (Figures 5.4d and 5.4e). We adjust τ to keep the overall magma supply constant across these simulations, corresponding to an equivalent Hc = 9.5 km as set by Equation (5) for the SWIR spreading rate of 14 mm/yr. The AMLs are emplaced beneath Tr = 1000°C, and hydrothermal domains are confined above Z_{H0} = 3 km with a permeability of $k = 10^{-15}$ m^2. We ran simulations for 3 Myr to reach stationary states. Hydrothermal vent temperatures and depths to the 650°C and 1000°C isotherms are found to slightly decrease with both the widening of W_{AML} at constant H_{AML}, and the thickening of H_{AML} at constant W_{AML} (Figure 5.4). Repeating these runs with a different reference magma supply (corresponding to Hc = 6.3 km at the SWIR spreading rate) and the same range of W_{AML} and H_{AML} gives very similar results in an overall cooler thermal regime (Figure 5.12). We conclude that the exact shape of the AML has little influence on the thermal regime associated with a given magma flux, and we fix W_{AML} = 4 km and H_{AML} = 0.2 km in the following simulations.

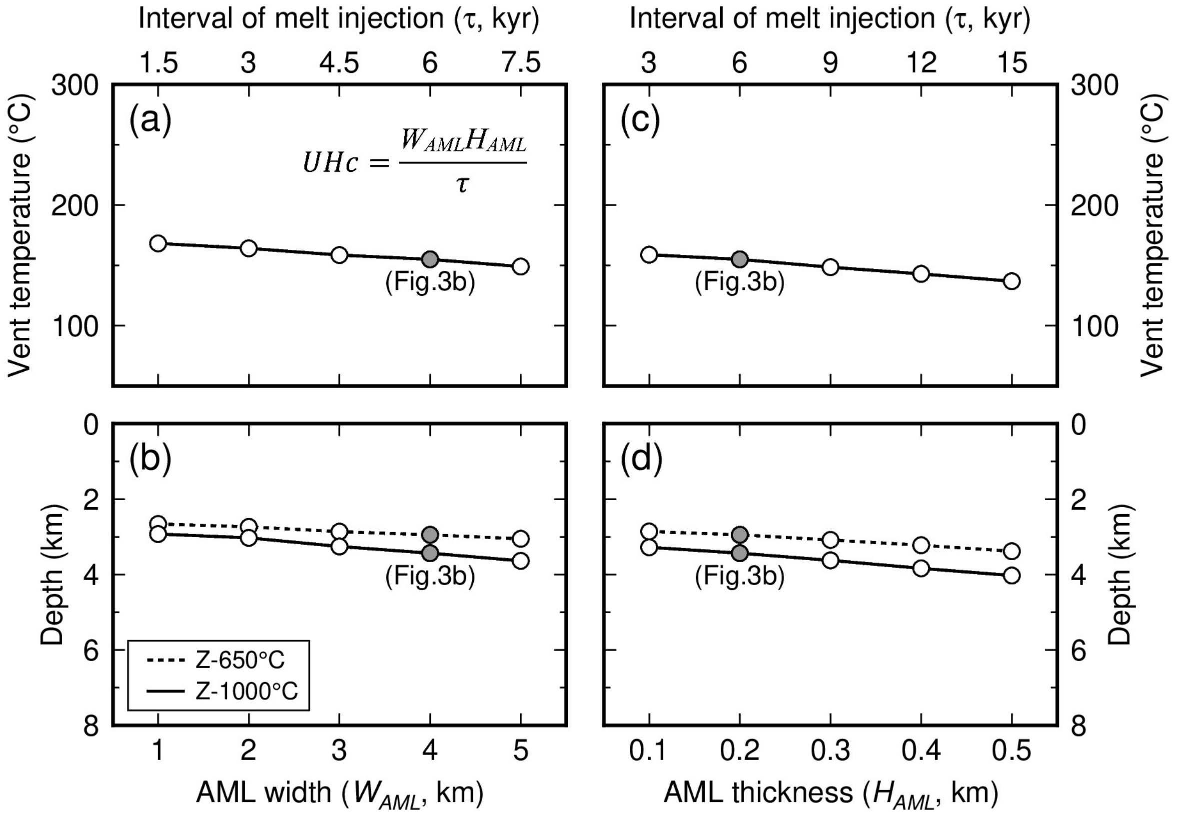

Figure 5.4. Effect of AML dimensions on key model outputs.

(a) and (b) Simulations of changing W_{AML} *from 1 to 5 km with a constant* $H_{AML} = 0.2$ *km. (c) and (d) Simulations of changing* H_{AML} *from 0.1 to 0.5 km with a constant* $W_{AML} = 4$ *km. In all simulations,* τ *is adjusted to keep a constant Hc = 9.5 km for the SWIR spreading rate of 14 mm/yr, according to Equation (5). AMLs are emplaced beneath Tr = 1000°C, and hydrothermal domains are confined above* $Z_{H0} = 3$ *km with a permeability of* $k = 10^{-15}$ m^2*. (a) and (c) Maximum vent temperatures in stationary states. (b) and (d) Depths to the isotherms of 650°C (dashed lines) and 1000°C (solid lines). See Figure 5.12 for the same configurations of AML dimensions but with a constant Hc = 6.3 km (for the SWIR spreading rate of 14 mm/yr).*

5.4.3 Temperature of the host rock upon melt emplacement

The third group of simulations (Figures 5.5 and 5.13) explores the effect of three selected temperatures of host rock upon melt emplacement (*Tr*): *Tr* = 650°C (a single AML emplaced beneath the 650°C isotherm during each injection event), *Tr* = 1000°C (a single AML emplaced beneath the 1000°C isotherm), and *Tr* = 650/1000°C (two stacked half-thick AMLs emplaced beneath the 650°C and 1000°C isotherms at the same time during each injection event). Simulations with a given *Tr* have injection periods varying from $\tau = 3, 6, 9, 12$, to 18 kyr. The AMLs are set to $W_{AML} = 4$ km and $H_{AML} = 0.2$ km (which amounts to two 0.1-km thick AMLs in the *Tr* = 650/1000°C simulations). Hydrothermal domains are confined above $Z_{H0} = 3$ km with a permeability of $k = 10^{-15}$ m². Simulations with *Tr* = 1000°C were previously presented as part of the first group of simulations (Figures 5.3a-5.3e). A control set of simulations was run with no melt injection (Figures 5.3f, 5.5a, and 5.5b).

As in the *Tr* = 1000°C simulations, the *Tr* = 650°C and *Tr* = 650/1000°C simulations show nonlinear decreases in vent temperatures with increasing *τ*, and linear decreases in the depths to the 650ºC isotherms (Figures 5.5a and 5.5b). The 1000°C isotherms in the *Tr*=650/1000°C simulations also linearly deepen with increasing *τ*, while in the *Tr* = 650°C simulations, the depth to the 1000°C isotherm is constant at 16.5 km with no sensitivity to *τ* (Figure 5.5b). The *Tr* = 650°C and *Tr* = 650/1000°C simulations also develop a transient, shallow region at temperatures in excess of 1000°C, which appears just below the 650°C isotherm whenever melt is emplaced (Movie S6).

Keeping *τ* constant at 6 kyr (*Hc* = 9.5 km at the SWIR spreading rate), the *Tr* = 650°C simulations produce the shallowest 650°C isotherms but the deepest 1000°C isotherms (Figures 5.5c-5.5e; see Figure 5.13 for other *τ*). The conductive boundary layer separating the cracking front from the 650ºC isotherm is thinnest in the *Tr* = 650°C simulations, efficiently transporting heat from the AML to the hydrothermal system and hence producing the hottest vent temperatures (Figure 5.5a). In other words, the *Tr* = 650°C simulations produce the hottest upper lithospheres and the coldest lower lithospheres, alongside the highest hydrothermal vent temperatures and transient shallow mush zones (Figure 5.5c). In contrast, the *Tr* = 1000°C simulations produce the coldest upper lithospheres, the lowest vent temperatures, and persistent crystal mush zones (regions in excess of 1000ºC) at depths shallower than the corresponding equivalent crustal thickness (Figure 5.5d).

The thermal regimes of the *Tr* = 650/1000°C simulations have characters of the other two (Figure 5.5e). Like the *Tr* = 650°C simulations, the shallow half-AML produces a transient mush zone and moderate vent temperatures. Like the *Tr* = 1000°C simulations, the deep half-AML enables a persistent mush zone at crustal depths (Figures 5.5a and 5.5b).

A wider range of *Tr* is explored with emplacements of a single AML and of two stacked half-thick AMLs (Figure 5.6). Both modes of AML emplacements show increased vent temperatures with the decrease of *Tr* (i.e., increasing *Hc* at a given spreading rate; Figures 5.6a and 5.6d). In the simulations with a single AML emplacement at *Tr* ≥ 650°C, melt emplaced closer to the 650°C and 1000°C isotherms leads to shallower 650°C and 1000°C isotherms, respectively (Figures 5.6b and 5.6c). The simulations with *Tr* < 1000°C produce deep 1000°C isotherms with no sensitivity to *τ*, and the larger the deviation from *Tr* = 1000°C, the deeper the 1000°C isotherm (Figure 5.6c). The simulations with *Tr* > 1000°C produce overall colder thermal regimes than the Tr = 1000°C simulations, because less heat is released by magma cooling and crystallization. The Tr = 400°C simulations produce the deepest 650°C isotherms with no sensitivity to τ (no measurements at τ = 3 kyr because the 400°C isotherm in the model reaches the seafloor at such high equivalent melt supply). In the simulations of stacked AML emplacements, the changes of Tr have less impact on the depths to the 650°C and 1000°C isotherms, relative to the single AML emplacement, and this impact decreases as τ decreases until the differences are nearly zero at τ = 3 kyr (Figures 5.6e and 5.6f).

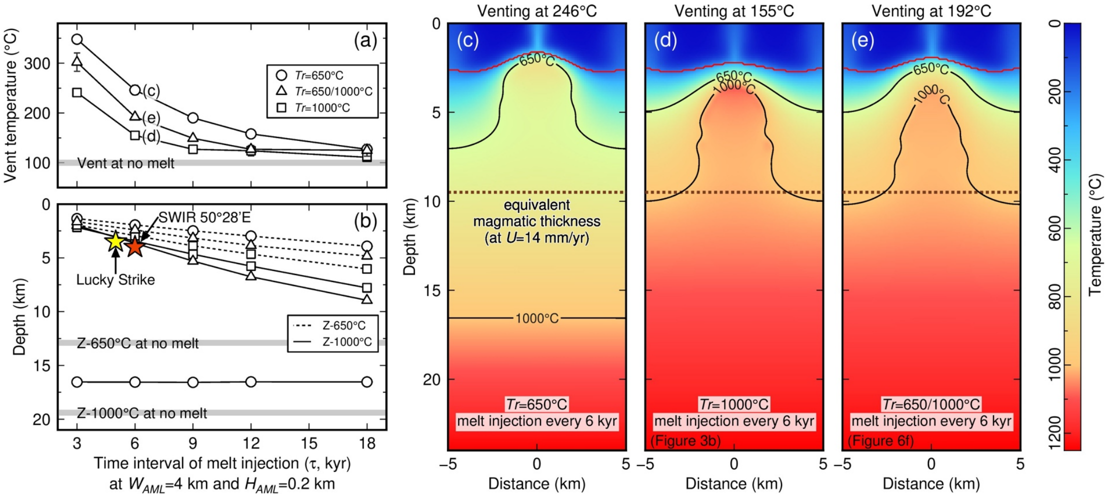

Figure 5.5. Simulations varying the temperature of the host rock upon melt emplacement. *Tr = 650°C, Tr = 1000°C, and Tr = 650/1000°C (half of the melt emplaced at Tr = 650°C, and the other half at Tr = 1000°C). See legend for symbols. Simulations with a given Tr have time intervals of melt injection varying from τ = 3, 6, 9, 12, to 18 kyr. The AML dimension is set to W_{AML} = 4 km and H_{AML} = 0.2 km in total. Hydrothermal domains are confined above Z_{H0} = 3 km with a permeability of $k = 10^{-15}$ m^2. (a) Maximum vent temperatures in stationary states. Thick gray line represents the no-melt simulation (Figure 5.3f). (b) Depths to the 650°C (dashed lines) and 1000°C (solid lines) isotherms. Red and yellow stars represent the depths to the mush zones of the SWIR 50°28'E and the Lucky Strike. (c)-(e) Snapshots of stationary-state thermal regimes for three selected Tr at τ = 6 kyr. Equivalent magmatic thickness is shown for the SWIR spreading rate of 14 mm/yr. See Figure 5.13 for snapshots of τ = 3, 9, 12, and 18 kyr.*

5.4.4 Hydrothermal system extent and permeability

The fourth group of simulations explores four combinations of two maximum hydrothermal domain depths Z_{H0} (3 and 6 km) and two permeabilities k (10^{-15} and 10^{-14} m^2; Figure 5.7). AML sizes are set to W_{AML} = 4 km and H_{AML} = 0.2 km in total, and AMLs are emplaced in a stacked mode beneath Tr = 650/1000°C. Each combination has injection periods varying from τ = 3, 6, 9, 12, to 18 kyr (corresponding to Hc = 19, 9.5, 6.3, 4.8, and 3.2 km, respectively, for the SWIR spreading rate).

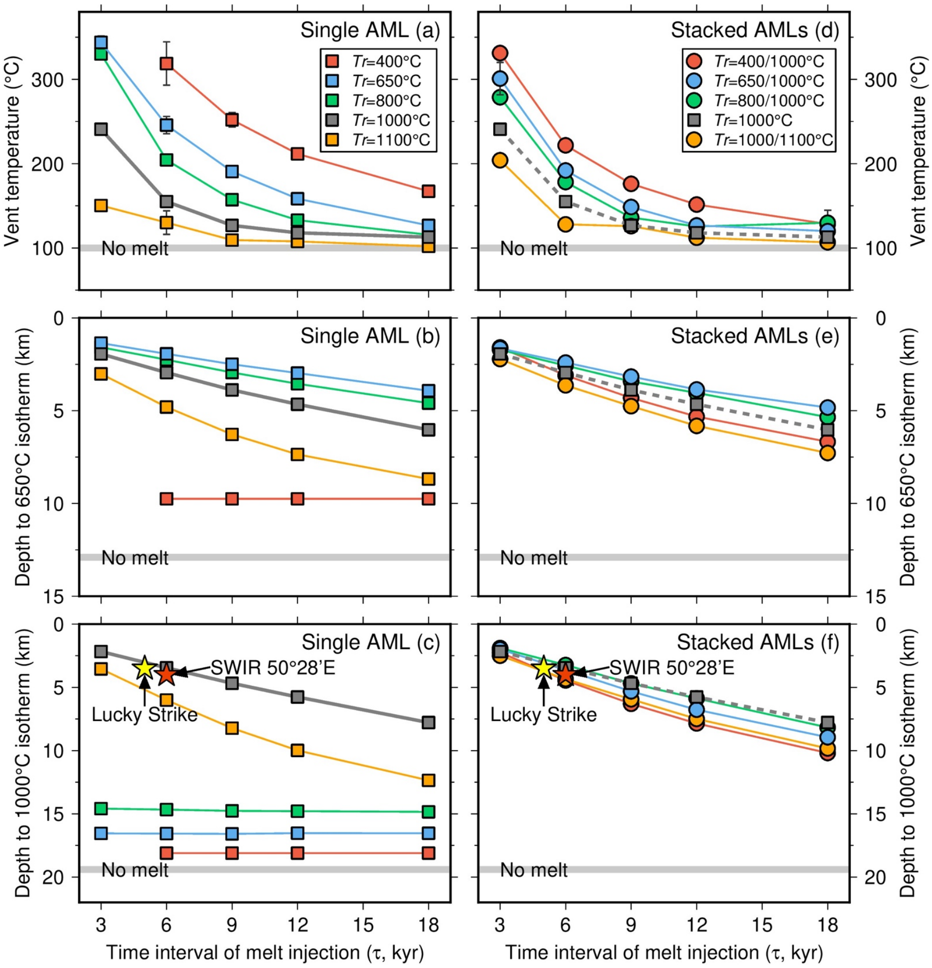

Figure 5.6. Key model outputs of simulations that vary the temperature of the host rock upon melt emplacement (*Tr*).

See legend for the corresponding Tr values. Simulations with a given Tr have time intervals of melt injection varying from τ = 3, 6, 9, 12, to 18 kyr. The AML dimension is set to W_{AML} *= 4 km and* H_{AML} *= 0.2 km in total. Hydrothermal domains are confined above* Z_{H0} *= 3 km with a permeability of k =* 10^{-15} m^2*. (a)-(c) Single AML emplacement. (d)-(e) Two stacked half-thick AMLs emplacements.*

Each combination shows a nonlinear decrease in vent temperature and a linear increase in depths to the 650°C and 1000°C isotherms as time interval increases (Figures 5.7a and 5.7b). For a given value of *τ* (i.e., for the same magma supply at a constant spreading rate), e.g., *τ* = 6 kyr (Figures 5.7c-5.7f; see Figure 5.14 for other injection periods), increasing the permeability or the maximum depth of the hydrothermal domain essentially shifts the thermal regime downward (Figures 5.7a and 5.7b). However, increasing the hydrothermal domain maximum depth, while reducing its permeability leads to higher venting temperatures (Figure 5.7a). Allowing a greater maximum depth for the hydrothermal circulation region also leads to a more dynamic convective system with more upwelling plumes (Figures 5.7c and 5.7d). A higher permeability leads to more unstable hydrothermal vent temperatures (Figure 5.7g), and this stability is also controlled by the maximum depth of the hydrothermal domain and the time intervals of melt injection (Figures 5.14g-1 to 5.14g-4).

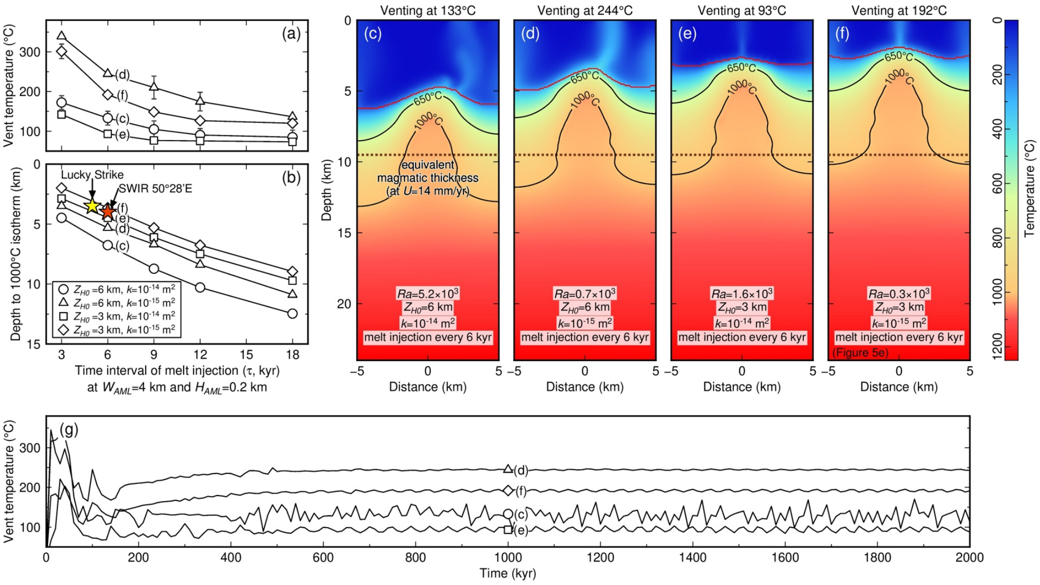

Figure 5.7. Simulations of four combinations of the maximum hydrothermal domain depths (Z_{H0} = 3 and 6 km) and permeabilities ($k = 10^{-15}$ and 10^{-14} m^2).

See legend for symbols. Each combination has time intervals of melt injection varying from τ *= 3, 6, 9, 12, to 18 kyr. The AML dimension is set to* W_{AML} *= 4 km and* H_{AML} *= 0.2 km in total, emplaced beneath Tr = 650/1000°C. (a) Maximum vent temperatures in stationary states. (b) Depths to the 1000°C isotherms. (c)-(f) Snapshots of stationary-state thermal regimes for four combinations at* τ *= 6 kyr. The equivalent magmatic thickness is calculated for the SWIR spreading rate of 14 mm/yr. (g) Maximum vent temperatures throughout the first 2000 kyr of simulations for four combinations. See Figure 5.14 for snapshots of* τ *= 3, 9, 12, and 18 kyr.*

5.5 Cyclic changes in frequencies of melt injection

Here we simulate cyclic changes in magma supply with alternating waxing and waning phases over a cycle of 300 kyr (D_{cycle}), which have been inferred from geological observations at the SWIR 50°28'E (Chen et al., 2021). We first define the time-average time interval of melt injection as $\overline{\tau}$ = 6 kyr according to Equation (5), by setting Hc = 9.5 km, W_{AML} = 4 km, H_{AML} = 0.2 km, and U = 14 mm/yr. A cycle of magma supply fluctuation comprises a waxing phase (duration D_{wax}) and a waning phase (duration D_{wan}), amounting to a total duration (or period):

$$D_{cycle} = D_{wax} + D_{wan}. \tag{6}$$

To account for a given time-average magma supply over the entire cycle (corresponding to a cycle-averaged magmatic thickness Hc = 9.5 km), the injection periodicities during the waxing and waning phase (τ_{wax} and τ_{wan}) must satisfy the following relation (e.g., Ito and

Behn, 2008):

$$\frac{D_{cycle}}{\overline{\tau}} = \frac{D_{wax}}{\tau_{wax}} + \frac{D_{wan}}{\tau_{wan}}. \tag{7}$$

We ran simulations for a total of 3 Myr. During the first 1.5 Myr, we set $\tau = \overline{\tau}$ to make sure the thermal regime reaches the stationary state associated with the long-term averaged magma supply. During the next 1.5 Myr, we alternately change τ to $\tau = \tau_{wax}$ for a duration D_{wax} and then to $\tau = \tau_{wan}$ for a duration D_{wan}. We examine 9 combinations of the above parameters by setting τ_{wax} = 3, 4, and 5 kyr and τ_{wan} = 8, 10, and 12 kyr (Figure 5.8a). We also ran two control simulations for each configuration with $\tau = \tau_{wax}$ and $\tau = \tau_{wan}$, corresponding to the high and low endmembers in magma supply of oscillating cases and to equivalent magmatic thicknesses Hc_{wax} and Hc_{wan}, respectively. In all simulations, two stacked half-thick AMLs are simultaneously emplaced beneath the 650°C and 1000°C isotherms (i.e., Tr = 650/1000°C). The hydrothermal domain is confined above Z_{H0} = 3 km and is assigned a permeability of $k = 10^{-15}$ m^2.

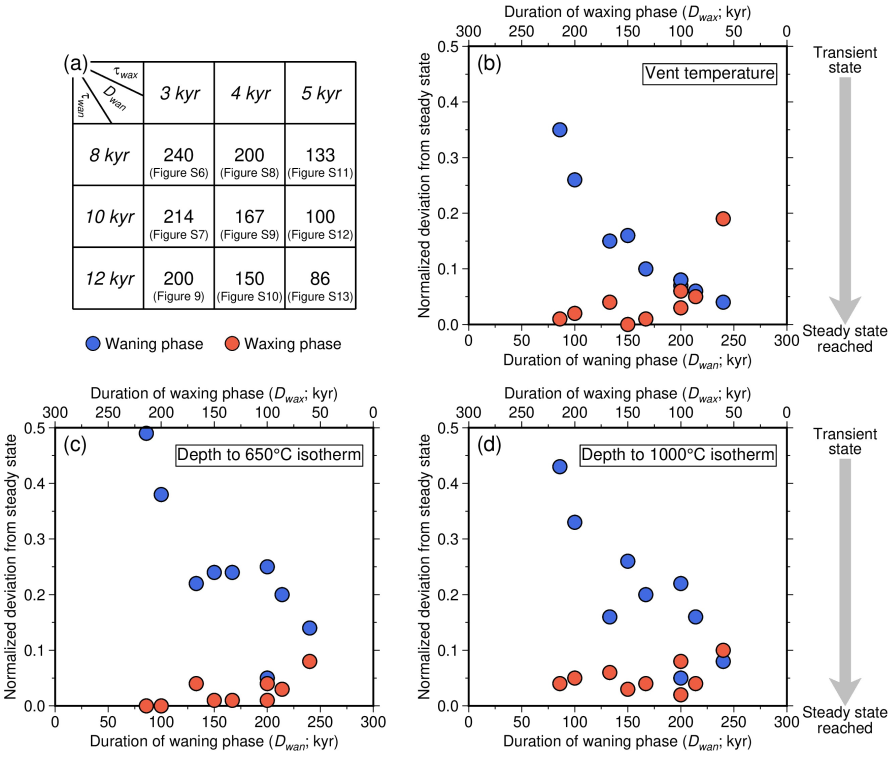

(a) τ_{wax} D_{wan} τ_{wan}	3 kyr	4 kyr	5 kyr
8 kyr	240 (Figure S6)	200 (Figure S8)	133 (Figure S11)
10 kyr	214 (Figure S7)	167 (Figure S9)	100 (Figure S12)
12 kyr	200 (Figure 9)	150 (Figure S10)	86 (Figure S13)

Figure 5.8. Configurations of τ_{wax} and τ_{wan} and normalized deviation

(a) 3×3 matrix of configurations of τ_{wax} = 3, 4, and 5 kyr and τ_{wan} = 8, 10, and 12 kyr. D_{wan} and D_{wax} are calculated by combining Equations (6) and (7). (b)-(d) Normalized deviations of vent temperature, and depths to the 650°C and 1000°C isotherms, calculated by differences between values at the end of waxing (or waning) phases and at the steady state of the control simulation with $\tau = \tau_{wax}$ (or $\tau = \tau_{wan}$), which are normalized by the difference between two control simulations.

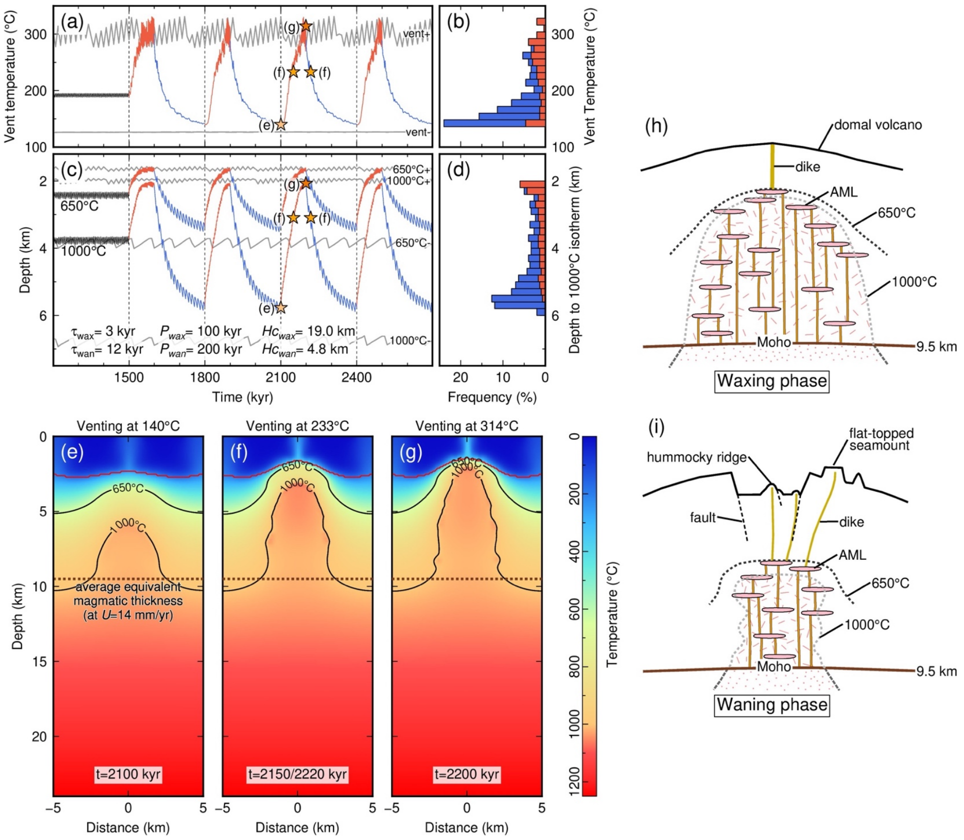

Figure 5.9. Simulation of cyclic changes in time intervals of melt injection.

Time interval is set as $\overline{\tau} = 6$ *kyr for the first 1.5 Myr, and then set to alternating* $\tau_{wax} = 3$ *kyr for* $D_{wax} = 100$ *kyr (*$Hc_{wax} = 19.0$ *km) and* $\tau_{wan} = 12$ *kyr for* $D_{wan} = 200$ *kyr (*$Hc_{wan} = 4.8$ *km). See Figure 5.15 to Figure 5.22 for the other 8 configurations. The AML dimension is set to* $W_{AML} = 4$ *km and* $H_{AML} = 0.2$ *km in total, emplaced beneath Tr = 650/1000°C. The hydrothermal domain is confined above* $Z_{H0} = 3$ *km with a permeability of* $k = 10^{-15}$ m^2*. (a) Maximum vent temperatures between 1200 and 2700 kyr. Red and blue lines represent waxing and waning phases, respectively. Gray lines represent two control simulations with* $\tau_{wax} = 3$ *kyr (marked as vent+) and* $\tau_{wan} = 12$ *kyr (marked as vent-). (b) Frequency of the maximum vent temperatures within a complete cycle. Red and blue bins represent waxing and waning phases, respectively. (c) Depth to the isotherms of 650℃ and 1000℃, distinct by labels. Gray lines represent the two control simulations for the depths to the isotherms of 650℃ (marked as 650℃+ and 650℃-) and 1000℃ (marked as 1000℃+ and 1000℃-). (d) Frequency of the depth of 1000℃ isotherm within a complete cycle. (e)-(g) Snapshots (timing indicated in Figures 5.9a and 5.9c) of the thermal regimes at the end of a waning phase (2100 kyr), middle of a waxing/waning phase (2150/2220 kyr), and end of a waxing phase (2200 kyr). The time-average equivalent magmatic thickness is calculated for the SWIR spreading rate of 14 mm/yr. (h) and (i) Geological interpretations for waxing and waning phases at the SWIR 50°28'E, modified from Chen et al. (2021).*

Figure 5.9 shows the results of the configuration with the greatest contrast between endmember magma supplies, i.e., $\tau_{wax} = 3$ kyr and $\tau_{wan} = 12$ kyr, yielding $D_{wax} = 100$ kyr and $D_{wan} = 200$ kyr upon combining Equations (6) and (7). We expect that the variability of the thermal regime within a complete cycle should be limited by the steady states of the two control simulations with $\tau = 3$ kyr and $\tau = 12$ kyr, which were run previously as part of the simulations that vary the isotherm of melt emplacement Tr (triangles in Figures 5.5a and 5.5b). Their steady-state vent temperatures (301±18°C and 127°C) and depths to the 650°C (1.6 and 3.8±0.1 km) and 1000°C (2.0 and 6.7±0.1 km) isotherms are shown in Figures 5.9a and 5.9c, marked as '+' for $\tau = 3$ kyr and '–' for $\tau = 12$ kyr, respectively. Four complete cycles with time series of vent temperatures and depths to the 650°C and 1000°C isotherms, clearly bracketed by the results of two control simulations, are also shown in Figures 5.9a and 5.9c.

During waxing phases, isotherms move upward rapidly at a near-constant velocity, resulting in shallowing of the AML, shrinking of the conductive boundary layer, and warming of the hydrothermal system (from Figures 5.9e to 5.9g). For over 70% of the waxing phase, the thermal regime resembles the hot-endmember $\tau = 3$ kyr control simulation with the 1000°C isotherm lying shallower than 4 km, and vent temperatures in excess of 200°C (Figures 5.9b and 5.9d). At the end of the waxing phase, the thermal regime almost reaches the steady state at the level of the constant $\tau = 3$ kyr control simulation. In contrast, during the waning phases, isotherms migrate downward first rapidly, then more and more slowly over time (from Figures 5.9g to 5.9e). In the simulations shown in Figure 5.9, the thermal regime does not have enough time to reach the steady state at the level of the $\tau = 12$ kyr control simulation (Figures 5.9a and 5.9c). The thermal regime spends over 80% of the waning phase in states with the 1000°C isotherm lying deeper than 4 km and vent temperatures < 200°C (Figures 5.9b and 5.9d).

Figures 5.8b to 5.8d quantify the extent to which the oscillatory thermal regimes described above deviate from their respective endmember steady states depending on the respective durations of the waxing and waning phase of the magmatic cycle (Figure 5.8a). Specifically, for each observable of interest (depths to the 650°C and 1000°C isotherms, and vent temperatures), we measure the deviation between the values at the ends of waxing or waning phases and at the steady states of the control simulations with $\tau = \tau_{wax}$ or $\tau = \tau_{wan}$, respectively. All results are normalized by the difference between the two steady-state values. We find that the normalized deviations of all observables during waning phases decrease significantly as D_{wan} increases (Figures 5.8b-5.8d). This is simply because the longer duration of D_{wan} leaves more time for the system to approach the steady state. The shortest value of $D_{wan} = 86$ kyr (i.e., $\tau_{wax} = 5$ kyr and $\tau_{wan} = 12$ kyr; Figure 5.8a) leads to the largest normalized deviations from the cold-endmember steady state. Only two configurations have waning phases almost reaching (all deviations < 0.1) the cold-endmember steady state, i.e., $\tau_{wax} = 4$ kyr and $\tau_{wan} = 8$ kyr ($D_{wan} = 200$ kyr) and $\tau_{wax} = 3$ kyr and $\tau_{wan} = 8$ kyr ($D_{wan} = 240$ kyr). By contrast, the corresponding waxing phases are in most runs long enough to allow the thermal regime to reach or nearly reach (all deviations < 0.1) the hot-endmember steady state (Figures 5.8b-5.8d).

5.6 Discussion

Our numerical modelling illustrates that not only the frequencies but also the depths of magmatic intrusions make a significant difference for the axial thermal regime at slow and ultraslow spreading ridges. Modes of melt injection (i.e., preferentially into cold or hot host rocks) provide an additional potential control for the variability of the axial thermal regime and a guideline for the formation of black-smoker hydrothermal circulation. The modelling of a cyclic melt supply shows that the thermal regime is significantly altered between waxing and waning phases, in a manner consistent with geological observations at the SWIR 50°28'E (Chen et al., 2021). This cyclic simulation also opens new perspectives on how the lower crust may be accreted at slow and ultraslow spreading ridges. Finally, we discuss the advantages and shortcomings of our treatment of hydrothermal convection.

5.6.1 Melt emplacement controls on the axial thermal regime

The thermal regime of MORs has been predicted to be overall hotter with increasing spreading rate, i.e., increasing melt supply assuming a constant magmatic crustal thickness (Phipps Morgan and Chen, 1993a; Theissen-Krah et al., 2011). Our simulations reproduce these previous numerical predictions (Figure 5.3) and are consistent, for example, with variations in BDT depths along the Knipovich Ridge, where the maximum depth of earthquakes is overall shallower at magmatic than at amagmatic ridge sections (Meier et al., 2021). We also successfully predict the persistence of a lower-crustal mush zone (enclosed by the 1000°C isotherm) at the center of the magmatically-robust SWIR 50°28'E and Lucky Strike segments, a persistence that was not predicted for slow and ultraslow rates by previous thermal models (Phipps Morgan and Chen, 1993a; Theissen-Krah et al., 2011).

However, changes in melt supply alone cannot explain why the maximum depth of earthquakes at the more magmatic Dragon Flag detachment of the SWIR is similar to or greater than at the nearly-amagmatic endmember 64°30'E region of the same ridge (18 vs. 15 km) (Chen et al., 2020; Tao et al., 2020; Yu et al., 2018), while spreading rates are the same. Here we show that the depth of melt emplacement, which we represent by the melt emplacement temperature (*Tr*, or temperature of the host rock upon melt emplacement), adds a new degree of freedom to the modeled thermal regimes (Figure 5.6). When melt is emplaced at a low *Tr* (e.g., 650ºC or less), the heat brought by the melt almost only warms the lithosphere above the *Tr* isotherm and is efficiently removed by hydrothermal circulation, while the lithosphere below is not heated. This effect, which had been conceptually proposed based on geological data (Cannat et al., 2019), provides a potential explanation for why the 18-km thick seismogenic lithosphere at the Dragon Flag segment of the SWIR (Tao et al., 2020; Yu et al., 2018) is similar in thickness to the seismogenic lithosphere in the nearly amagmatic 64°30'E ridge region (≥ 15 km; Chen et al., 2020): melt there may be mostly emplaced at shallow depths in cool host rocks, fueling robust hydrothermal circulation evidenced by numerous black smokers (Copley et al., 2016; Tao et al., 2012). This interpretation was proposed by Fan et al. (2021). It differs from that of Tao et al. (2020), calling for a permeable detachment fault that mines heat from a magma source lying at the BDT. We note, however, that our coldest run (no melt, and a maximum depth of Z_{H0} = 6 km and a permeability of $k = 10^{-14}$ m^2 for the hydrothermal system) predicts a BDT at 15.5 km, similar to the run with an equivalent magmatic crust of ~3 km (Zhao et al., 2013), melt emplaced at *Tr* = 400°C, and the SWIR spreading rate (a plausible context for the Dragon Flag; Figure 5.11). Such a configuration, therefore, leads to a thick axial lithosphere even with a non-zero melt supply.

5.6.2 Perspective on lower-crustal construction through cyclic melt supply

Cyclic changes of melt supply with alternating waxing and waning phases over periods on the order of a few 100s kyr have been documented at some magmatically-robust, segment-centered volcanos, such as ~300 kyr at the SWIR 50°28'E (Chen et al., 2021) and 300-500 kyr at the Menez Gwen areas of the MAR (Klischies et al., 2019). Our simulations of cyclic changes of melt injection frequencies for the reference case of the SWIR 50°28'E show an oscillatory thermal regime with a ~4 km fluctuation of the depth to the 1000°C isotherm during waxing and waning phases (Figures 5.9c and 5.9d). In this simulation, the waxing phases last 100 kyrs, and the waning phases last 200 kyrs, which correspond to the accretion of only 1.4 km and 2.8 km of new lithospheres at the SWIR spreading rate.

During waning phases, each newly injected AML is emplaced beneath its predecessor as the ridge axis cools, the hydrothermal domain deepens, and the mush zone gradually subsides to greater depths. During waxing phases, each newly injected AML is emplaced above its partly crystallized predecessor and into material that crystallized toward the end of the previous waning phase, including hydrothermally altered materials and dikes that fed the hummocky ridges typical of waning phases (Chen et al., 2021), and the top of the mush zone ascends until the thermal regime reaches a stationary state. Over the whole cycle, the lower crust is therefore constructed by a sequence of melt lenses emplaced at progressively shallower depths during the waxing phase and then at progressively deeper depths during the waning phase, while the upper lithosphere cools and crystallizes, and a progressively deeper BDT results in faulting of the crystallized material. We would expect differences in this crustal construction scheme depending on the duration of waxing and waning phases, resulting in different amplitudes for the oscillatory thermal regime and on the spreading rates, resulting in changes in the width of the affected new lithosphere.

Overall, this mode of lower-crustal construction would result in complex melt-rock interactions and in the assimilation of previously cooled, variably tectonized, and hydrothermally altered gabbros and dikes. The periodicity of melt supply and the fluctuation of the thermal regime documented at fast spreading ridges (Marjanović et al., 2014; Soule et al., 2009) are much lower than at slow and ultraslow ridges (Chen et al., 2021; Klischies et al., 2019). The predictions of our simulations are, however, consistent with the dynamics of magmatic systems documented at the gabbro/sheeted dikes transition zones of the Oman ophiolite and the fast spreading East Pacific Rise (Carbotte et al., 2021; Gillis, 2008; Nicolas et al., 2008). The AMLs migrate upward during waxing phases, corresponding to the reheating of the AML roof and hence the recrystallization of hydrothermally altered sheeted dikes into pyroxene and hornblende hornfels with the formation of xenoliths, while during waning phases, AMLs migrate downward, causing crystallization at the AML roof and/or sides to form isotropic gabbros that are crosscut by later dikes (France et al., 2009; Gillis, 2008; Nicolas et al., 2009, 2008). Samples of the lower crust formed at magmatically-robust segment centers of slow and ultraslow ridges are lacking to compare to fast spread examples and test these predictions.

Time variations of the melt supply are also inferred at several less magmatically-robust slow and ultraslow ridge sections, from systematic changes in seafloor morphology, volcanic facies, and apparent faulting patterns (Ballard and van Andel, 1977; Chen et al., 2021; Escartín et al., 2014; Klischies et al., 2019; MacLeod et al., 2009; Mendel et al., 2003; Parson et al., 1993). Axial Volcanic Ridges have been proposed to have a life cycle, constructed in magmatic periods and split in tectonic periods (Mendel et al., 2003; Parson et al., 1993), and melt-poor ridge sections with Oceanic Core Complexes (OCCs) also have cycles as the OCCs may be initiated by a local waning of melt supply and terminated by a higher melt supply (Cannat et al., 2009; MacLeod et al., 2009). The amplitude of these melt supply variations is, however, most probably lower than at the SWIR 50°28'E and Menez Gwen segment centers, with colder waxing phases and overall deeper mush zones and thicker brittle domains. Elements of the cyclic lower-crustal construction scheme we propose may still be relevant, but tectonic processes would thus play a much greater role. Overall, the lower-crustal construction and the thermal regime along slow and ultraslow spreading ridges can be expected to be conditioned by melt supply variations in both space and time, resulting in extreme variability.

5.6.3 Hydrothermal convection

High-temperature (> 300°C) black smokers at slow and ultraslow spreading ridges have been continuously documented over the last three decades (Beaulieu et al., 2015), including the highest vent temperatures (> 400°C) discovered at the MAR 5°S (Koschinsky et al., 2008) and at the Beebe vent field of the Mid-Cayman Spreading Center (Connelly et al., 2012). Vigorous black-smoker hydrothermal circulation is believed to extract heat from a hot magma body beneath, separated by a thin conductive boundary layer (e.g., Lowell et al., 2013; Wilcock et al., 2009). In our modelling, we do not predict high-temperature venting when melt is mostly emplaced at $Tr = 1000$°C, because the hydrothermal heat extraction is impeded by a thick boundary layer. However, when we allow melt to be emplaced at a low Tr or ascribe a deeper Z_{H0} to the hydrothermal domain, the boundary layer is thinner, and black-smoker hydrothermal circulation may be active for several thousand years. This condition may be met at detachment fault systems with shallow intermittent gabbroic intrusions (Cannat et al., 2009; Ildefonse et al., 2007) and deep-reaching hydrothermal fluids (Andersen et al., 2015; Tao et al., 2020). It should be noted that changing permeability and accounting for heterogeneities in the permeability field could also directly change hydrothermal venting temperatures and the efficiency of hydrothermal heat removal in our simulations. We chose not to explore these parameters and to rely on our straightforward porous convection model, as was first attempted by Theissen-Krah et al. (2011) and later by Fan et al. (2021), Hasenclever et al. (2014), and Olive and Crone (2018).

In this approach, the properties of the hydrothermal fluids, the confining depth of the hydrothermal system (Demartin et al., 2004), and the critical fluid temperature at ~400°C (Jupp and Schultz, 2000) define the Rayleigh number (Ra), written as (Fontaine and Wilcock, 2007; Lowell and Germanovich, 2004):

$$Ra = \frac{\alpha_f g \, (T_H - T_0) Z_H k}{\kappa_m \nu_f}, \tag{8}$$

where α_f and ν_f are the thermal expansion coefficient and kinematic viscosity of the hydrothermal fluid, respectively, and κ_m is the effective thermal diffusivity of the fluid-rock system. Representative values of these parameters are listed in Table S1, and can be used to estimate the Rayleigh number.

In simulations varying the maximum depths and permeabilities of the hydrothermal system with the same melt supply (τ = 6 kyr), the combination of Z_{H0} = 6 km and $k = 10^{-14}$ m^2 produces the highest $Ra = 5.2\times10^3$, corresponding to the most unstable vent temperatures and multiple, chaotic hydrothermal plumes that move horizontally (Figures 5.7c and 5.7g). By contrast, at the lowest $Ra = 0.3\times10^3$, corresponding to the combination of Z_{H0} = 3 km and $k = 10^{-15}$ m^2, hydrothermal circulation is stable with a single, robust, and vertically upwelling plume (Figure 5.7f). The combination of Z_{H0} = 6 km and $k = 10^{-15}$ m^2 produces stable and elevated vent temperatures with horizontally moving plumes, corresponding to a relatively low $Ra = 0.7\times10^3$ (Figure 5.7d), and the combination of Z_{H0} = 3 km and $k = 10^{-14}$ m^2 produces a relatively high $Ra = 1.6\times10^3$, yet a single, weak, vertically upwelling plume (Figure 5.7e). Hydrothermal convection under different melt supplies (other τ) also produces different patterns of hydrothermal plumes and Rayleigh numbers (Figure 5.14). Consequently, we observe that hydrothermal plumes evolve differently in different simulations, presumably reflecting the realistic properties of hydrothermal convection. Therefore, although they do not explore the complex permeability structure of the natural systems, our simulations are a more accurate way of describing hydrothermal heat extraction compared to a Nusselt number approach (e.g., Phipps Morgan and Chen, 1993).

5.7 Conclusions

We used a 2D numerical thermal model (Fan et al., 2021) that couples repeated melt intrusions and hydrothermal convection to constrain the thermal regimes inferred from two magma supply endmembers at ultraslow spreading ridges: the most magmatically-robust SWIR 50°28'E and the nearly-amagmatic SWIR 64°30'E. The variability of the thermal regimes at slow and ultraslow spreading ridges was explored by varying parameters associated with melt supply, modes of magma emplacement (i.e., the frequencies and depths of melt injections), and hydrothermal circulation (i.e., the maximum hydrothermal domain depth and permeability).

Unsurprisingly, our simulations predict that higher frequencies of melt injections result in overall hotter thermal regimes. The novelty in our results is that the depth of melt emplacement also plays a significant role; shallower melt injections result in greater efficiency of hydrothermal heat removal with black-smoker hydrothermal circulation and thus in a cooler thermal regime. This provides a potential explanation for the unexpected thick seismogenic lithosphere at the Dragon Flag area. Alternatively, deeper melt injections result in a hotter regime and are a condition for the formation of persistent lower-crustal mush zones. In addition, the increases of permeability and the maximum hydrothermal domain depth result in the increase of efficiency of hydrothermal heat removal, downward shifting the depths to the brittle-ductile transition and mush zone. We also explored the effect of cyclic changes in melt supply documented at the reference case of the SWIR 50°28'E on the persistence of the lower-crustal mush zone, the depth to the brittle-ductile transition, and the formation of the high-temperature hydrothermal vent, which provide insights into the lower-crustal construction at slow and ultraslow spreading ridges.

5.8 Supplementary material

All the MATLAB codes to reproduce our results are available on figshare (https://figshare.com/s/7d4417e42340f9a1b724). Supplemental Figures 5.15-5.22 and Movies S19-S27 are available on figshare (https://figshare.com/s/b9f0a82eeb2d4d6ec0ea).

Table 5.1. Summary of model parameters.

Symbol	Definition	Value	Units
U	Full spreading rate	14	mm/yr
P_0	Pressure at seafloor	20	MPa
T_0	Temperature at seafloor	0	°C
Tb	Imposed bottom temperature	1250	°C
Hc	Equivalent magmatic thickness	4.8-19	km
W_{AML}	Width of axial melt lenses	4	km
H_{AML}	Thickness of axial melt lenses	0.2	km
Tr	Temperature of host rock upon melt emplacement	650-1000	°C
τ	Time interval of melt injections	3-18	kyr
Z_{H0}	Maximum depth of the cracking front	3 and 6	km
T_H	Temperature of the cracking front	-	°C
T_{ve}	Visco-elastic transition temperature	900	°C
T_S	Solidus temperature	1000	°C
T_M	Liquidus temperature	1200	°C
k	Permeability	10^{-14}-10^{-15}	m^2
A_T	Sensitivity coefficient of temperature	-	$Pa \cdot m^{0.5}/K$
A_P	Sensitivity coefficient of pressure	-	$m^{0.5}$
ρ_M	Magma density	2700	kg/m^3

ρ	Lithosphere density	2900	kg/m^3
g	Acceleration of gravity	9.81	m/s^2
K_{IC}	Fracture toughness	0.5×10^{-6}	Pa·m$^{0.5}$
Ra	Rayleigh number of hydrothermal convection system	-	
α_f	Thermal expansion coefficient of the hydrothermal fluid	3×10^{-3}	K^{-1}
ν_f	Kinematic viscosity of the hydrothermal fluid	10^{-7}	m^2/s
κ_m	Effective thermal diffusivity of the fluid-rock system	10^{-6}	m^2/s
$\overline{\tau}$	Mean time interval of melt injections within 3 Myr at SWIR 50°28'E	6	kyr
τ_{wax}	Time interval of melt injections during waxing phases	3-5	kyr
τ_{wan}	Time interval of melt injections during waning phases	8-12	kyr
D_{wax}	Time period of a waxing phase	-	kyr
D_{wan}	Time period of a waning phase	-	kyr
D_{cycle}	Time period of a magmatic cycle ($D_{cycle}=D_{wax}+D_{wan}$)	300	kyr

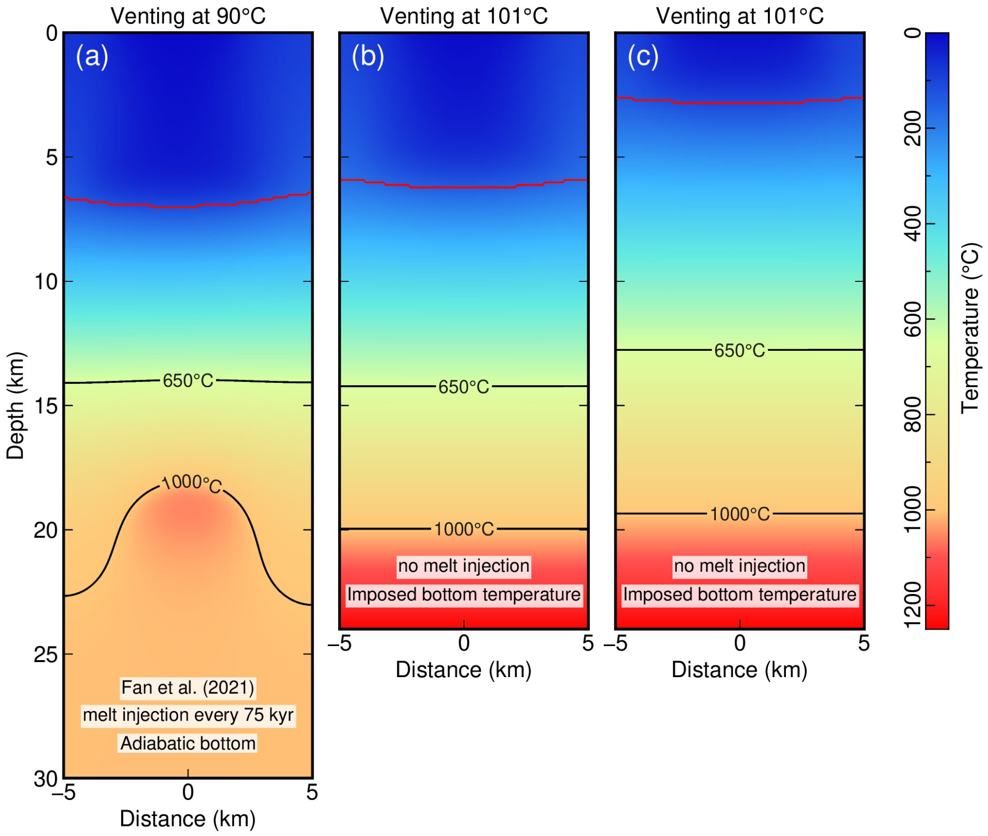

Figure 5.10. Snapshots of stationary-state thermal regimes from numerical simulations for fitting the 650℃ isotherms with the BDT depth of 15 km at the nearly-amagmatic SWIR 64°30'E (Chen et al., 2020).

All simulations are set to a permeability of k = 10-15 m2 within permeable layers. Red lines indicate the cracking fronts. Black lines indicate the 650℃ and 1000℃ isotherms. (a) Simulation by Fan et al. (2021), with a model thickness of 30 km and an adiabatic bottom. AMLs are set to WAML = 4 km and HAML = 0.5 km, emplaced beneath Tr = 1000℃ every τ

= 75 kyr. The hydrothermal domain is confined above ZH0 = 6 km. (b) and (c) No melt injection with a model thickness of 24 km and an imposed bottom temperature of 1250°C. The maximum hydrothermal domain depths are set to ZH0 = 6 in (b) and ZH0 = 3 km (c).

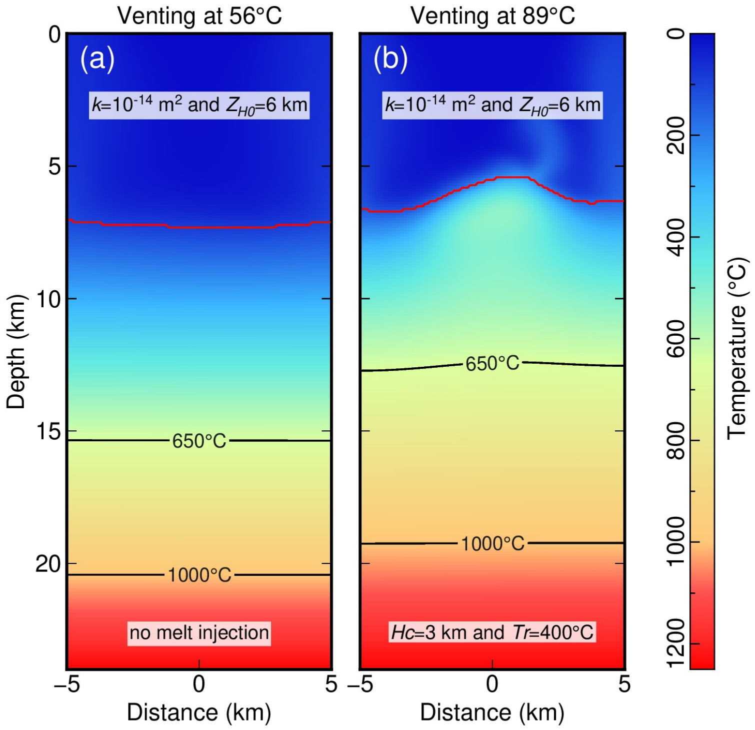

Figure 5.11. Snapshots of stationary-state thermal regimes from numerical simulations with hydrothermal domains confined above Z_{H0} = 6 km with a permeability of $k = 10^{-14}$ m^2. Red lines indicate the cracking fronts. Black lines indicate the 650°C and 1000°C isotherms. (a) No melt injection. (b) AMLs are set to W_{AML} = 4 km and H_{AML} = 0.2 km, emplaced beneath Tr = 400°C with the SWIR spreading rate to build an equivalent magmatic crust of ~3 km at the Dragon Flag (Zhao et al., 2013).

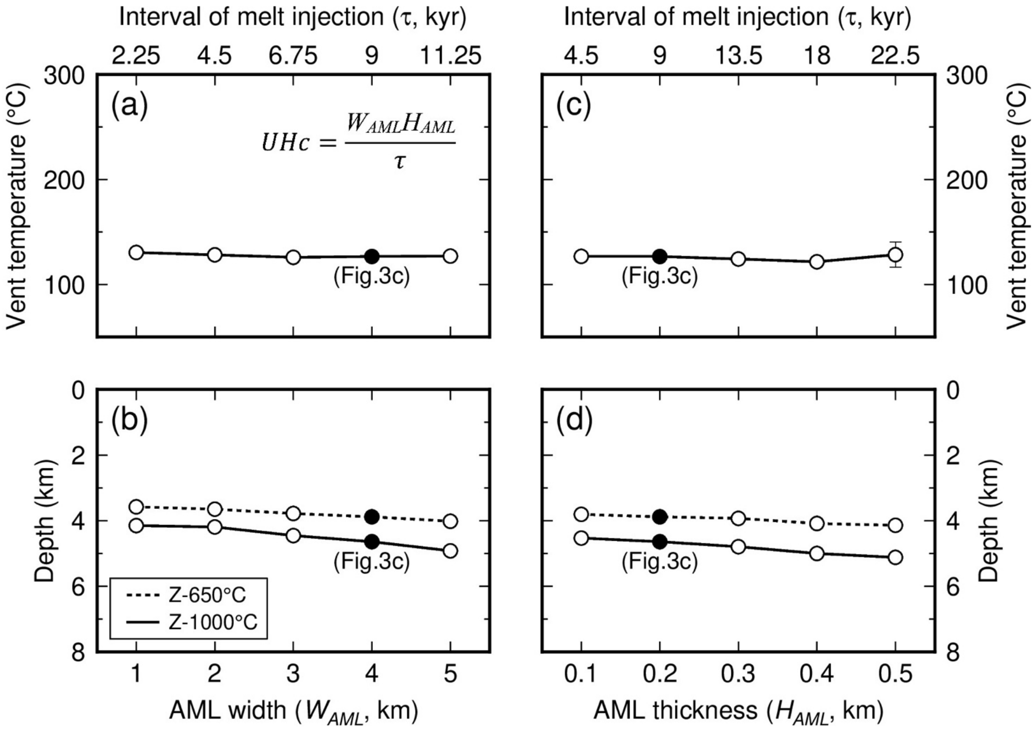

Figure 5.12. Effect of AML dimensions on key model outputs.

(a) and (b) Simulations of changing W_{AML} *from 1 to 5 km with a constant* $H_{AML} = 0.2$ *km. (c) and (d) Simulations of changing* H_{AML} *from 0.1 to 0.5 km with a constant* $W_{AML} = 4$ *km. In all simulations, τ is adjusted to keep the crustal thickness constant at Hc=6.3 km (for the SWIR spreading rate of 14 mm/yr), according to Equation (5). AMLs are emplaced beneath Tr = 1000°C, and hydrothermal domains are confined above* $Z_{H0} = 3$ *km with a permeability of* $k = 10^{-15}$ m^2*. (a) and (c) Maximum vent temperatures in stationary states. (b) and (d) Depths to the isotherms of 650°C (dashed lines) and 1000°C (solid lines). Black circles indicate the case of* $W_{AML} = 4$ *km and* $H_{AML} = 0.2$ *km (Figure 5.3c).*

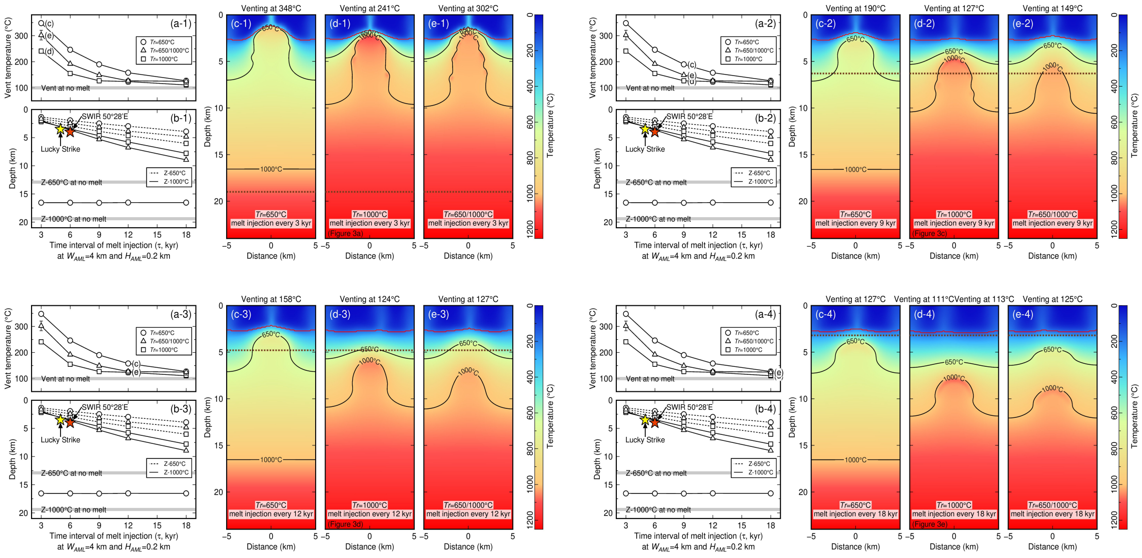

Figure 5.13. Stationary-state thermal regimes for three *Tr* at τ = 3 (a-1 to f-1), 9 (a-2 to f-2), 12 (a-3 to f-3), and 18 kyr (a-4 to f-4). See Figure 5.5 for τ = 6 kyr and details of model setup and the figure format.

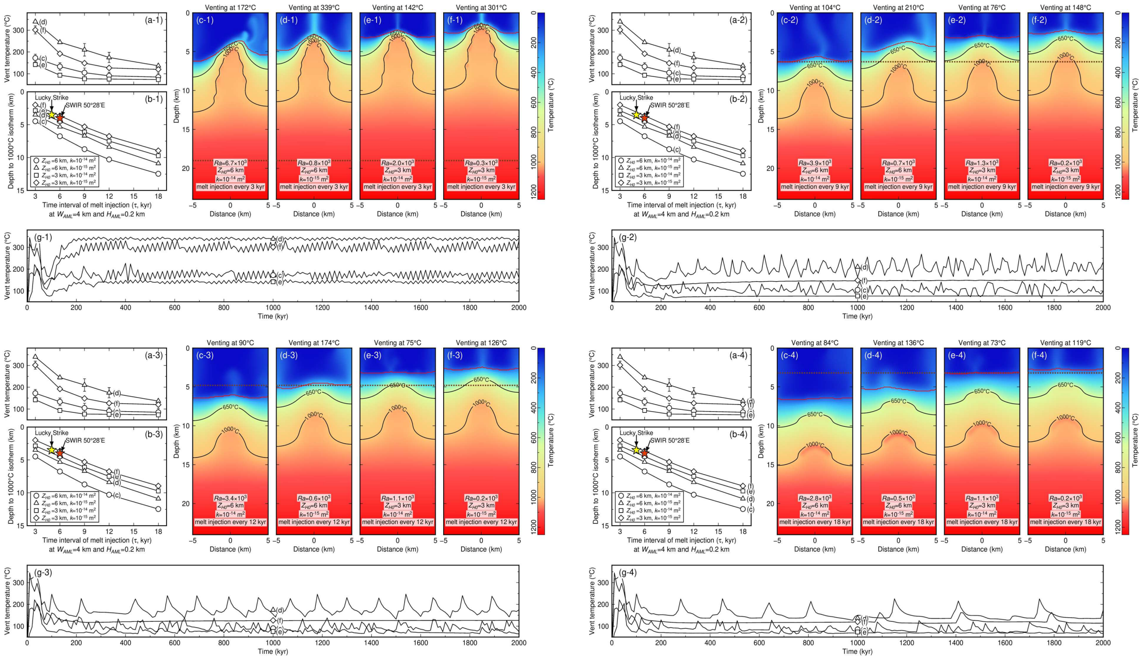

Figure 5.14. Stationary-state thermal regimes for four combinations of hydrothermal systems at $\tau = 3$ (a-1 to g-1), 9 (a-2 to g-2), 12 (a-3 to g-3), and 18 kyr (a-4 to g-4). See Figure 5.7 for $\tau = 6$ kyr and details of model setup and the figure format.

Figure 5.15. Cyclic changes in frequencies of melt injection with configurations of $\tau_{wax} = 3$ kyr and $\tau_{wan} = 8$ kyr, corresponding to $D_{wax} = 60$ kyr and $D_{wan} = 240$ kyr. See Figure 5.9 for $\tau_{wax} = 3$ kyr and $\tau_{wan} = 12$ kyr and details of model setup.

Figure 5.16. Cyclic changes in frequencies of melt injection with configurations of $\tau_{wax} = 3$ kyr and $\tau_{wan} = 10$ kyr, corresponding to $D_{wax} = 86$ kyr and $D_{wan} = 214$ kyr.

Figure 5.17. Cyclic changes in frequencies of melt injection with configurations of $\tau_{wax} = 4$ kyr and $\tau_{wan} = 8$ kyr, corresponding to $D_{wax} = 100$ kyr and $D_{wan} = 200$ kyr.

Figure 5.18. Cyclic changes in frequencies of melt injection with configurations of $\tau_{wax} = 4$ kyr and $\tau_{wan} = 10$ kyr, corresponding to $D_{wax} = 133$ kyr and $D_{wan} = 167$ kyr.

Figure 5.19. Cyclic changes in frequencies of melt injection with configurations of $\tau_{wax} = 4$ kyr and $\tau_{wan} = 12$ kyr, corresponding to $D_{wax} = 150$ kyr and $D_{wan} = 150$ kyr.

Figure 5.20. Cyclic changes in frequencies of melt injection with configurations of $\tau_{wax} = 5$ kyr and $\tau_{wan} = 8$ kyr, corresponding to $D_{wax} = 167$ kyr and $D_{wan} = 133$ kyr.

Figure 5.21. Cyclic changes in frequencies of melt injection with configurations of τ_{wax}=5 kyr and τ_{wan}=10 kyr, corresponding to D_{wax}=200 kyr and D_{wan}=100 kyr.

Figure 5.22. Cyclic changes in frequencies of melt injection with configurations of $\tau_{wax} = 5$ kyr and $\tau_{wan} = 12$ kyr, corresponding to $D_{wax} = 214$ kyr and $D_{wan} = 86$ kyr.

Movie S 1. Simulations of group 1 at τ = 3, 6, 9, 12, and 18 kyr (Figures 5.3a-5.3e).

Movie S 2. Simulations of group 2 with changing WAML from 1 to 5 km (from left to right) with a constant HAML = 0.2 km and a constant Hc = 9.5 km (Figures 5.4a and 5.4b).

Movie S 3. Simulations of group 2 with changing HAML from 0.1 to 0.5 km (from left to right) with a constant WAML = 4 km and a constant Hc = 9.5 km (Figures 5.4c and 5.4d).

Movie S 4. Simulations of group 2 with changing WAML from 1 to 5 km (from left to right) with a constant HAML = 0.2 km and a constant Hc = 6.3 km (Figures 5.12a and 5.12b).

Movie S 5. Simulations of group 2 with changing HAML from 0.1 to 0.5 km (from left to right) with a constant WAML = 4 km and a constant Hc = 6.3 km (Figures 5.12c and 5.12d).

Movie S 6. Simulations of group 3 for Tr = 650°C, Tr = 1000°C, and Tr = 650/1000°C at τ = 6 kyr (Figures 5.5c-5.5e).

Movie S 7. Simulations of group 3 for Tr = 400°C at τ = 6, 9, 12, and 18 kyr (Figure 5.6).

Movie S 8. Simulations of group 3 for Tr = 650°C at τ = 3, 6, 9, 12, and 18 kyr (Figure 5.6).

Movie S 9. Simulations of group 3 for Tr = 800°C at τ = 3, 6, 9, 12, and 18 kyr (Figure 5.6). Simulations of group 3 for Tr = 1000°C at τ = 3, 6, 9, 12, and 18 kyr have been shown in Movie S1.

Movie S 10. Simulations of group 3 for Tr = 1100°C at τ = 3, 6, 9, 12, and 18 kyr (Figure 5.6).

Movie S 11. Simulations of group 3 for Tr = 400/1000°C at τ = 3, 6, 9, 12, and 18 kyr (Figure 5.6).

Movie S 12. Simulations of group 3 for Tr = 650/1000°C at τ = 3, 6, 9, 12, and 18 kyr (Figure 5.6).

Movie S 13. Simulations of group 3 for Tr = 800/1000°C at τ = 3, 6, 9, 12, and 18 kyr (Figure 5.6).

Movie S 14. Simulations of group 3 for Tr = 1000/1100°C at τ = 3, 6, 9, 12, and 18 kyr (Figure 5.6).

Movie S 15. Simulations of group 4 for four combinations of Z_{H0} = 6 km and $k = 10^{-14}$ m^2, Z_{H0} = 6 km and $k = 10^{-15}$ m^2, Z_{H0} = 3 km and $k = 10^{-14}$ m^2, and Z_{H0} = 3 km and $k = 10^{-15}$ m^2 (from left to right) at τ = 6 kyr (Figures 5.7c-5.7f).

Movie S 16. Simulations of group 4 for the combination of Z_{H0} = 6 km and $k = 10^{-14}$ m^2 at τ = 3, 6, 9, 12, and 18 kyr (Figure 5.7).

Movie S 17. Simulations of group 4 for the combination of Z_{H0} = 6 km and $k = 10^{-15}$ m^2 at τ = 3, 6, 9, 12, and 18 kyr (Figure 5.7).

Movie S 18. Simulations of group 4 for the combination of Z_{H0} = 3 km and $k = 10^{-14}$ at τ = 3, 6, 9, 12, and 18 kyr (Figure 5.7). Simulations of group 4 for the combination of Z_{H0} = 3 km and $k = 10^{-15}$ m^2 at τ = 3, 6, 9, 12, and 18 kyr have been shown in Movie S24.

Movie S 19. Cyclic changes in frequencies of melt injection with configurations of τ_{wax} = 3 kyr and τ_{wan} = 12 kyr, corresponding to D_{wax} = 100 kyr and D_{wan} = 200 kyr. See Figure 5.9 for details of model setup.

Movie S 20. Cyclic changes in frequencies of melt injection with configurations of τ_{wax} = 3 kyr and τ_{wan} = 8 kyr, corresponding to D_{wax} = 60 kyr and D_{wan} = 240 kyr.

Movie S 21. Cyclic changes in frequencies of melt injection with configurations of τ_{wax} = 3 kyr and τ_{wan} = 10 kyr, corresponding to D_{wax} = 86 kyr and D_{wan} = 214 kyr.

Movie S 22. Cyclic changes in frequencies of melt injection with configurations of τ_{wax} = 4 kyr and τ_{wan} = 8 kyr, corresponding to D_{wax} = 100 kyr and D_{wan} = 200 kyr.

Movie S 23. Cyclic changes in frequencies of melt injection with configurations of τ_{wax} = 4 kyr and τ_{wan} = 10 kyr, corresponding to D_{wax} = 133 kyr and D_{wan} = 167 kyr.

Movie S 24. Cyclic changes in frequencies of melt injection with configurations of τ_{wax} = 4 kyr and τ_{wan} = 12 kyr, corresponding to D_{wax} = 150 kyr and D_{wan} = 150 kyr.

Movie S 25. Cyclic changes in frequencies of melt injection with configurations of τ_{wax} = 5 kyr and τ_{wan} = 8 kyr, corresponding to D_{wax} = 167 kyr and D_{wan} = 133 kyr.

Movie S 26. Cyclic changes in frequencies of melt injection with configurations of τ_{wax} = 5 kyr and τ_{wan} = 10 kyr, corresponding to D_{wax} = 200 kyr and D_{wan} = 100 kyr.

Movie S 27. Cyclic changes in frequencies of melt injection with configurations of τ_{wax} = 5 kyr and τ_{wan} = 12 kyr, corresponding to D_{wax} = 214 kyr and D_{wan} = 86 kyr.

Chapter 6

Conclusions and Prospects

In chapter 6, I wrap up new findings of the understanding of volcanic eruptions, faulting, and the thermal regime associated with melt supply at ultraslow spreading mid-ocean ridge, followed by future perspectives based on the work done in this thesis.

6.1 Conclusions

In this thesis, I have studied two endmembers in terms of melt supply at the ultraslow spreading Southwest Indian Ridge, a magmatically-robust endmember at the SWIR 50°28'E and a nearly-amagmatic endmember at the SWIR 64°30'E.

At the magmatically-robust SWIR 50°28'E, I mapped the fine-scale volcanic (seafloor and lava morphologies) and tectonic (faults and fissures) features and depicted an evolution of upper-crustal construction over the past 780 kyr, based on high-resolution bathymetry and backscatter data, near-bottom magnetic data, and seafloor photographs. Maps of the three different map-scale volcanic morphologies (smooth, smooth hummocky, and hummocky) are consistent with the abundance of photo-scale lava morphologies (sheet, lobate, and pillow), as the smooth morphology corresponds to a larger proportion of high-effusion-rate sheet-lobate lavas and the hummocky morphology corresponds to a larger proportion of low-effusion-rate pillow lavas. Smooth and smooth hummocky morphologies account for 64% of the mapped area, building dome-shaped volcanos, while hummocky morphology accounts for 29%, building hummocky ridges (the rest 7% is sedimented seafloor). In this magmatically-robust endmember, the proportion of lobate-sheet lavas is >40% and apparent tectonic strain is <8%, similar to what have been observed at intermediate- and fast-spreading ridges (Figure 3.15).

A temporal changes of upper-crustal construction modes was recognized at the SWIR 50°28'E, reflecting waxing and waning phases of melt supply over a cycle of ~300 kyr. During waxing phases of melt supply (V1 and V3), high-effusion-rate smooth lava flows are predominant and build domal volcanos, fed by localized dike injection zones. Combining with existing seismic velocity structure (Jian et al., 2017a), I propose that the lower-crustal magma plumbing systems are replenished by high frequency of melt injections, feeding long-lived, relatively shallow AMLs topping crystal mush zones. During waning phases of melt supply (V2 and V4+V5), delocalized dike injections zones fed low-effusion-rate hummocky ridges, with lower frequency of melt injections and shorter-lived AMLs. The brittle lithosphere should be colder and thicker during these waning phases, consistent with the observation of more faults.

At the nearly-amagmatic corridor of the SWIR 64°30'E, I used microseismicity data in the axial region. The recorded microearthquakes were located using a 1D velocity model (Momoh et al., 2017). The deepest microearthquakes at 15 km bsf constrain the seismogenic lithosphere in this nearly-amagmatic ultraslow spreading mid-ocean ridge context, providing a probable baseline for the ~600-700°C isotherm. The microearthquake hypocenters are collocated with seismically imaged damage zones of the south-dipping active axial detachment fault plane (Momoh et al., 2020, 2017). Focal mechanisms are consistent with normal faulting on this main fault, and on small-offset, north-dipping conjugate faults in the hanging wall. The occurrence of numerous hanging-wall earthquakes distinguishes this detachment system from others at more magmatically-robust slow and ultraslow spreading ridges where the hanging walls are nearly aseismic (de Martin et al., 2007; Parnell-Turner et al., 2017; Yu et al., 2018). A two-day seismic swarm with three clusters (deep-west, deep-east, and shallow) was recorded and interpreted as due to an upward-migrating melt intrusion in the detachment footwall (the deep-west cluster at 6-11 km), triggering a sequence of shallower tectonic earthquakes in the detachment fault plane (the shallow cluster at ~1.5 km). Combining with seismically imaged subhorizontal seismic reflectors that were interpreted as melt sills (Momoh et al., 2020), the larger number of microearthquakes at the transition between volcanic and smooth seafloor leads me to propose a link between sporadic magma injections and tectonic failure of crystallized mafic rocks at the ultramafic basement of melt-poor ultraslow ridges.

To wrap up the observations on the two endmembers of ultraslow spreading ridges and to explore the role of melt injection frequency and depth on the axial thermal regime of slow and ultraslow ridges, I used a modified version of a 2D numerical thermal model (Fan et al., 2021). Modelling was first applied to explore the melt supply controls on the thermal regimes inferred from geological and geophysical observations for the two SWIR endmembers. The model was also used to explore melt supply controls on the variability of the thermal regime at slow and ultraslow spreading ridges. For this modelling work, I considered parameters associated with melt supply (i.e., the frequency and depth of melt injections) and hydrothermal circulation (i.e., permeability and the maximum hydrothermal domain depth). Numerical simulations predict not surprisingly that the higher frequency of melt injections results in overall hotter thermal regimes. What is new is that I show that the depth of melt injections also plays a significant role. Shallower melt injections result in higher efficiency of hydrothermal heat removal and thus in a cooler thermal regime. Alternatively, deeper melt injections result in a hotter regime and are a condition for the formation of persistent lower-crustal mush zones. I also explore the effect of cyclic changes in melt supply on the persistence of lower-crustal mush zones, the formation of high-temperature hydrothermal vents, and the depth to the Brittle-Ductile Transition.

This thesis work provides a framework to advance the understanding of the role of melt supply and melt supply variations at slow and ultraslow spreading ridges. I confirm that magmatic, tectonic, and hydrothermal processes at these ridges are controlled by spatial and temporal variations in local melt supply, rather than by spreading rate alone, leading to a diversity of magma plumbing systems, crustal compositions, faulting styles, and axial thermal regimes.

6.2 Prospects

This thesis has improved our understanding on mid-ocean ridges processes associated with melt supply. However, a lot of work is necessary to be done for further studies in the future.

For the magmatically-robust SWIR 50°28'E, a detailed analysis of faulting pattern is necessary to provide more information for tectonic and volcanic history. One of the main concerns for the data interpretation is the estimation of crustal age, although I have tentatively classified 6 eruptive phases. Sediment cover from backscatter and seafloor photographs cannot provide accurate age information because the rates of sediment cumulation at different seafloor morphologies are different (higher rate at smooth seafloor morphology). One way to explore this issue would be to sample the upper crust across the boundary of different eruptive phases. To date these samples, U/Th (or other approaches) can be used to constrain crustal ages (e.g., Standish and Sims, 2010). Another issue at the SWIR 50°28'E is the existence of the AMLs. Seismic refraction data has shown a LVA at depth of 4-9 km bsf, referring to an AML on the top of the LVA (Jian et al., 2017a, 2017b). Seismic reflection experiments using multichannel streamers, therefore, need to be carried out at the SWIR 50°28'E. With imaged seismic reflectors, AMLs, boundary of layer 2A/2B, and subseafloor faults may be illustrated to improve the understanding of its upper-crustal magmatic and tectonic features, such as the Lucky Strike (Combier et al., 2015; Singh et al., 2006).

For the nearly-amagmatic SWIR 64°30'E, the existing two OBS deployments are short (27 days), probably offering only snapshots in time of the seismic activity. For example, most events in the shorter SMSMO catalog were less than 10 km bsf. A longer-term OBS experiment should be deployed. Earthquakes deeper than 15 km may then be recorded, which helps better understand the seismic activity of the detachment fault. One question to ask is the following: in this work I follow earlier studies (Anderson, 1995; McKenzie et al., 2005; Phipps Morgan and Chen, 1993a) and propose that the base of the seismogenic lithosphere corresponds to temperatures as low as 600-700°C. However, microstructural studies of sheared peridotites sampled in the region have shown evidence for semi-brittle deformation at a higher temperature (800-1000°C; Bickert et al., 2021). Could this high temperature deformation be associated to detectable earthquakes?

For the numerical thermal modelling, I did not consider the thermal effect of dikes, which may be significant at melt-rich endmembers (this effect at melt-poor endmembers is supposed to be neglected). Additionally, one question is for previous thermal models (Phipps Morgan and Chen, 1993a; Theissen-Krah et al., 2011): why these models cannot predict crustal mush zones at slow and ultraslow spreading ridges, e.g., centers of the MAR Lucky Strike segment (Combier et al., 2015; Seher et al., 2010; Singh et al., 2006) and the SWIR 50°28'E segment (Jian et al., 2017a, 2017b; Li et al., 2015). At least two things should be revisited in thermal models for slow and ultraslow spreading ridges: (1) the high heterogeneity of melt flux on the segment scale (Chapter 1.1.2), and (2) the differences of melt emplacement modes between slow-ultraslow (thicker lithosphere to enable more possibilities of melt emplacement depths) and fast-intermediate spreading ridges.

List of References

Aghaei, O., Nedimovič, M.R., Carton, H., Carbotte, S.M., Canales, J.P., Mutter, J.C., 2014. Crustal thickness and Moho character of the fast-spreading East Pacific Rise from 9°42′N to 9°57′N from poststack-migrated 3-D MCS data. Geochemistry, Geophys. Geosystems 15. https://doi.org/10.1002/2013GC005069

Allerton, S., Searle, R.C., Murton, B.J., 1996. Bathymetric segmentation and faulting on the Mid-Atlantic Ridge, 24°00'N to 24°40'N. Geol. Soc. Spec. Publ. 118, 49–60. https://doi.org/10.1144/GSL.SP.1996.118.01.04

Anderko, A., Pitzer, K.S., 1993. Equation-of-state representation of phase equilibria and volumetric properties of the system NaCl-H2O above 573 K. Geochim. Cosmochim. Acta 57. https://doi.org/10.1016/0016-7037(93)90105-6

Andersen, C., Rüpke, L., Hasenclever, J., Grevemeyer, I., Petersen, S., 2015. Fault geometry and permeability contrast control vent temperatures at the Logatchev 1 hydrothermal field, Mid-Atlantic Ridge. Geology 43. https://doi.org/10.1130/G36113.1

Anderson, D.L., 1995. Lithosphere, asthenosphere, and perisphere. Rev. Geophys. https://doi.org/10.1029/94RG02785

Anderson, J.A., Wood, H.O., 1925. Description and theory of the torsion seismometer. Bull. Seismol. Soc. Am. 15, 1–72.

Appelgate, B., Embley, R.W., 1992. Submarine tumuli and inflated tube-fed lava flows on Axial Volcano, Juan de Fuca Ridge. Bull. Volcanol. 54, 447–458. https://doi.org/10.1007/BF00301391

Arnulf, A.F., Harding, A.J., Kent, G.M., Wilcock, W.S.D., 2018. Structure, Seismicity, and Accretionary Processes at the Hot Spot-Influenced Axial Seamount on the Juan de Fuca Ridge. J. Geophys. Res. Solid Earth 123. https://doi.org/10.1029/2017JB015131

Baillard, C., Crawford, W.C., Ballu, V., Hibert, C., Mangeney, A., 2014. An automatic kurtosis-based P-and S-phase picker designed for local seismic networks. Bull. Seismol. Soc. Am. 104, 394–409. https://doi.org/10.1785/0120120347

Barreyre, T., Escartín, J., Garcia, R., Cannat, M., Mittelstaedt, E., Prados, R., 2012. Structure, temporal evolution, and heat flux estimates from the Lucky Strike deep-sea hydrothermal field derived from seafloor image mosaics. Geochemistry, Geophys. Geosystems 13. https://doi.org/10.1029/2011GC003990

Beaulieu, S.E., Baker, E.T., German, C.R., 2015. Where are the undiscovered hydrothermal vents on oceanic spreading ridges? Deep. Res. Part II Top. Stud. Oceanogr. 121. https://doi.org/10.1016/j.dsr2.2015.05.001

Behn, M.D., Ito, G., 2008. Magmatic and tectonic extension at mid-ocean ridges: 1. Controls on fault characteristics. Geochemistry, Geophys. Geosystems 9, 8–10. https://doi.org/10.1029/2008GC001965

Bickert, M., Cannat, M., Tommasi, A., Jammes, S., Lavier, L., 2021. Strain Localization in the Root of Detachment Faults at a Melt-Starved Mid-Ocean Ridge: A Microstructural Study of Abyssal Peridotites From the Southwest Indian Ridge. Geochemistry, Geophys. Geosystems 22, e2020GC009434. https://doi.org/10.1029/2020GC009434

Bickert, M., Lavier, L., Cannat, M., 2020. How do detachment faults form at ultraslow mid-ocean ridges in a thick axial lithosphere? Earth Planet. Sci. Lett. 533, 116048. https://doi.org/10.1016/j.epsl.2019.116048

Blacic, T.M., Ito, G., Canales, J.P., Detrick, R.S., Sinton, J., 2004. Constructing the crust along the Galapagos Spreading Center 91.3°-95.5°W: Correlation of seismic layer 2A with axial magma lens and topographic characteristics. J. Geophys. Res. Solid Earth 109. https://doi.org/10.1029/2004JB003066

Blackman, D.K., Canales, J.P., Harding, A., 2009. Geophysical signatures of oceanic core complexes. Geophys. J. Int. https://doi.org/10.1111/j.1365-246X.2009.04184.x

Boettcher, M.S., Hirth, G., Evans, B., 2007. Olivine friction at the base of oceanic seismogenic zones. J. Geophys. Res. Solid Earth 112. https://doi.org/10.1029/2006JB004301

Bohnenstiehl, D.W.R., Carbotte, S.M., 2001. Faulting patterns near 19°30′S on the East Pacific Rise: Fault formation and growth at a superfast spreading center. Geochemistry, Geophys. Geosystems 2, 1056. https://doi.org/10.1029/2001GC000156

Breton, T., Nauret, F., Pichat, S., Moine, B., Moreira, M., Rose-Koga, E.F., Auclair, D., Bosq, C., Wavrant, L.M., 2013. Geochemical heterogeneities within the Crozet hotspot. Earth Planet. Sci. Lett. 376, 126–136. https://doi.org/10.1016/j.epsl.2013.06.020

Briais, A., Sloan, H., Parson, L.M., Murton, B.J., 2000. Accretionary processes in the axial valley of the Mid-Atlantic Ridge 27°N-30° N from TOBI side-scan sonar images. Mar. Geophys. Res. 21, 87–119. https://doi.org/10.1023/a:1004722213652

Brunelli, D., Cipriani, A., Bonatti, E., 2018. Thermal effects of pyroxenites on mantle melting below mid-ocean ridges. Nat. Geosci. 11, 520–525. https://doi.org/10.1038/s41561-018-0139-z

Buck, W.R., Lavier, L.L., Poliakov, A.N.B., 2005. Modes of faulting at mid-ocean ridges. Nature 434, 719–723. https://doi.org/10.1038/nature03358

Canales, J.P., Detrick, R.S., Toomey, D.R., Wilcock, W.S.D., 2003. Segment-scale variations in the crustal structure of 150-300 kyr old fast spreading oceanic crust (East Pacific rise, 8°15’N-10°5’N) from wide-angle seismic refraction profiles. Geophys. J. Int. 152. https://doi.org/10.1046/j.1365-246X.2003.01885.x

Canales, J.P., Dunn, R.A., Arai, R., Sohn, R.A., 2017. Seismic imaging of magma sills beneath an ultramafic-hosted hydrothermal system. Geology 45. https://doi.org/10.1130/G38795.1

Canales, J.P., Tucholke, B.E., Xu, M., Collins, J.A., DuBois, D.L., 2008. Seismic evidence for large-scale compositional heterogeneity of oceanic core complexes. Geochemistry, Geophys. Geosystems 9. https://doi.org/10.1029/2008GC002009

Cande, S.C., Kent, D. V., 1995. Revised calibration of the geomagnetic polarity timescale for the Late Cretaceous and Cenozoic. J. Geophys. Res. Solid Earth 100, 6093–6095. https://doi.org/10.1029/94JB03098

Cann, J.R., Blackman, D.K., Smith, D.K., McAllister, E., Janssen, B., Mello, S., Avgerinos, E., Pascoe, A.R., Escartin, J., 1997. Corrugated slip surfaces formed at ridge-transform intersections on the Mid-Atlantic Ridge. Nature 385, 329–332. https://doi.org/10.1038/385329a0

Cann, J.R., Smith, D.K., 2005. Evolution of volcanism and faulting in a segment of the Mid-Atlantic Ridge at 25°N. Geochemistry, Geophys. Geosystems 6. https://doi.org/10.1029/2005GC000954

Cannat, M., 1993. Emplacement of mantle rocks in the seafloor at mid-ocean ridges. J. Geophys. Res. Solid Earth 98, 4163–4172. https://doi.org/10.1029/92JB02221

Cannat, M., Agrinier, J., Vitale Brovarone, A., Lecoeuvre, A., Corre, M., Fruh-Green, G., J., F.F., Chavagnac, V., Brunelli, D., Prampolini, M., Bickert, M., Hamelin, C., Lie Onstad, S., Maia, M., Roumejon, S., 2019a. A forest of carbonate-brucite chimneys at the Southwest Indian Ridge: the ultramafic-hosted Old City hydrothermal field, in: Goldschmidt Conference Abstract.

Cannat, M., Mevel, C., Maia, M., Deplus, C., Durand, C., Gente, P., Agrinier, P., Belarouchi, A., Dubuisson, G., Humler, E., Reynolds, J., 1995. Thin crust, ultramafic exposures, and rugged faulting patterns at the Mid-Atlantic Ridge (22°–24°N). Geology 23, 49. https://doi.org/10.1130/0091-7613(1995)023<0049:TCUEAR>2.3.CO;2

Cannat, M., Rommevaux-Jestin, C., Sauter, D., Deplus, C., Mendel, V., 1999. Formation of the axial relief at the very slow spreading Southwest Indian Ridge (49° to 69°E). J. Geophys. Res. Solid Earth 104, 22825–22843. https://doi.org/10.1029/1999JB900195

Cannat, M., Sauter, D., Bezos, A., Meyzen, C., Humler, E., Le Rigoleur, M., 2008. Spreading rate, spreading obliquity, and melt supply at the ultraslow spreading Southwest Indian Ridge. Geochemistry, Geophys. Geosystems 9, 1–26. https://doi.org/10.1029/2007GC001676

Cannat, M., Sauter, D., Escartín, J., Lavier, L., Picazo, S., 2009. Oceanic corrugated surfaces and the strength of the axial lithosphere at slow spreading ridges. Earth Planet. Sci. Lett. 288, 174–183. https://doi.org/10.1016/j.epsl.2009.09.020

Cannat, M., Sauter, D., Lavier, L., Bickert, M., Momoh, E., Leroy, S., 2019b. On spreading modes and magma supply at slow and ultraslow mid-ocean ridges. Earth Planet. Sci. Lett. 519, 223–233. https://doi.org/10.1016/j.epsl.2019.05.012

Cannat, M., Sauter, D., Mendel, V., Ruellan, E., Okino, K., Escartin, J., Combier, V., Baala, M., 2006. Modes of seafloor generation at a melt-poor ultraslow-spreading ridge. Geology 34, 605–608. https://doi.org/10.1130/G22486.1

Carbotte, S., Macdonald, K., 1992. East Pacific Rise 8°–10°30′N: Evolution of ridge segments and discontinuities from SeaMARC II and three-dimensional magnetic studies. J. Geophys. Res. 97, 6959. https://doi.org/10.1029/91JB03065

Carbotte, S.M., Arnulf, A., Spiegelman, M., Lee, M., Harding, A., Kent, G., Canales, J.P., Nedimović, M., 2020. Stacked sills forming a deep melt-mush feeder conduit beneath Axial Seamount. Geology. https://doi.org/10.1130/g47223.1

Carbotte, S.M., Detrick, R.S., Harding, A., Canales, J.P., Babcock, J., Kent, G., Van Ark, E., Nedimovic, M., Diebold, J., 2006. Rift topography linked to magmatism at the intermediate spreading Juan de Fuca Ridge. Geology 34, 209–212. https://doi.org/10.1130/G21969.1

Carbotte, S.M., Macdonald, K.C., 1994. Comparison of seafloor tectonic fabric at intermediate, fast, and super fast spreading ridges: Influence of spreading rate, plate motions, and ridge segmentation on fault patterns. J. Geophys. Res. Solid Earth 99, 13609–13631. https://doi.org/10.1029/93jb02971

Carbotte, S.M., Marjanović, M., Arnulf, A.F., Nedimović, M.R., Canales, J.P., Arnoux, G.M., 2021. Stacked Magma Lenses Beneath Mid-Ocean Ridges: Insights From New Seismic Observations and Synthesis With Prior Geophysical and Geologic Findings. J. Geophys. Res. Solid Earth 126, e2020JB021434. https://doi.org/10.1029/2020JB021434

Carbotte, S.M., Marjanović, M., Carton, H., Mutter, J.C., Canales, J.P., Nedimović, M.R., Han, S., Perfit, M.R., 2013. Fine-scale segmentation of the crustal magma reservoir beneath the East Pacific Rise. Nat. Geosci. 6. https://doi.org/10.1038/ngeo1933

Carbotte, S.M., Smith, D.K., Cannat, M., Klein, E.M., 2015. Tectonic and magmatic segmentation of the Global Ocean Ridge System: A synthesis of observations, in: Geological Society Special Publication. Geological Society of London, pp. 249–295. https://doi.org/10.1144/SP420.5

Caress, D.W., Clague, D.A., Paduan, J.B., Martin, J.F., Dreyer, B.M., Chadwick, W.W., Denny, A., Kelley, D.S., 2012. Repeat bathymetric surveys at 1-metre resolution of lava flows erupted at Axial Seamount in April 2011. Nat. Geosci. 5, 483–488. https://doi.org/10.1038/ngeo1496

Cashman, K. V., Sparks, R.S.J., Blundy, J.D., 2017. Vertically extensive and unstable magmatic systems: A unified view of igneous processes. Science (80-.). 355, eaag3055. https://doi.org/10.1126/science.aag3055

Chen, J., 2021a. The global Mid-Ocean Ridge system. https://doi.org/10.6084/m9.figshare.16628449.v1

Chen, J., 2021b. Bathymetry map of the Southwest Indian Ridge. https://doi.org/10.6084/m9.figshare.14933397.v2

Chen, J., Cannat, M., Crawford, W.C., 2020. Microseismicity constraints on brittle lithosphere thickness at a nearly amagmatic spreading corridor of the ultraslow Southwest Indian Ridge, in: AGU Fall Meeting.

Chen, J., Cannat, M., Tao, C., Sauter, D., Munschy, M., 2021. 780 thousand years of upper-crustal construction at a melt-rich segment of the ultraslow spreading Southwest Indian Ridge 50°28’E. J. Geophys. Res. Solid Earth. https://doi.org/10.1029/2021JB022152

Chen, Y., Morgan, W.J., 1990. Rift valley/no rift valley transition at mid-ocean ridges. J. Geophys. Res. 95, 17571–17581. https://doi.org/10.1029/jb095ib11p17571

Chen, Y.J., 1992. Oceanic crustal thickness versus spreading rate. Geophys. Res. Lett. 19, 753–756. https://doi.org/10.1029/92GL00161

Chen, Y.J., Lin, J., 2004. High sensitivity of ocean ridge thermal structure to changes in magma supply: The Galápagos Spreading Center. Earth Planet. Sci. Lett. 221. https://doi.org/10.1016/S0012-821X(04)00099-8

Christeson, G.L., Goff, J.A., Reece, R.S., 2019. Synthesis of Oceanic Crustal Structure From Two-Dimensional Seismic Profiles. Rev. Geophys. https://doi.org/10.1029/2019RG000641

Clague, D.A., Paduan, J.B., Caress, D.W., Chadwick Jr, W.W., Le Saout, M., Dreyer, B.M., Portner, R.A., Chadwick, W., Le Saout, M., Dreyer, B.M., Portner, R.A., 2017. High-resolution AUV mapping and targeted ROV observations of three historical lava flows at Axial Seamount. Oceanography 30, 82–99. https://doi.org/10.5670/oceanog.2017.426

Clague, D.A., Paduan, J.B., Dreyer, B.M., Chadwick, W.W., Rubin, K.R., Perfit, M.R., Fundis, A.T., 2018. Chemical Variations in the 1998, 2011, and 2015 Lava Flows From Axial Seamount, Juan de Fuca Ridge: Cooling During Ascent, Lateral Transport, and Flow. Geochemistry, Geophys. Geosystems 19, 2915–2933. https://doi.org/10.1029/2018GC007708

Coffin, M.F., Gahagan, L.M., Lawver, L.A., 1997. Present-day plate boundary digital data compilation. Institute for Geophysics.

Collins, J.A., Smith, D.K., McGuire, J.J., 2012. Seismicity of the Atlantis Massif detachment fault, 30N at the Mid-Atlantic Ridge. Geochemistry, Geophys. Geosystems 13. https://doi.org/10.1029/2012GC004210

Colman, A., Sinton, J.M., White, S.M., McClinton, J.T., Bowles, J.A., Rubin, K.H., Behn, M.D., Cushman, B., Eason, D.E., Gregg, T.K.P., Grönvold, K., Hidalgo, S., Howell, J., Neill, O., Russo, C., 2012. Effects of variable magma supply on mid-ocean ridge eruptions: Constraints from mapped lava flow fields along the Galápagos Spreading Center. Geochemistry, Geophys. Geosystems 13, Q08014. https://doi.org/10.1029/2012GC004163

Combier, V., Seher, T., Singh, S.C., Crawford, W.C., Cannat, M., Escartín, J., Dusunur, D., 2015. Three-dimensional geometry of axial magma chamber roof and faults at Lucky Strike volcano on the Mid-Atlantic Ridge. J. Geophys. Res. Solid Earth 120, 5379–5400. https://doi.org/10.1002/2015JB012365

Connelly, D.P., Copley, J.T., Murton, B.J., Stansfield, K., Tyler, P.A., German, C.R., Van Dover, C.L., Amon, D., Furlong, M., Grindlay, N., Hayman, N., Hühnerbach, V., Judge, M., Le Bas, T., McPhail, S., Meier, A., Nakamura, K.I., Nye, V., Pebody, M., Pedersen, R.B., Plouviez, S., Sands, C., Searle, R.C., Stevenson, P., Taws, S., Wilcox, S., 2012. Hydrothermal vent fields and chemosynthetic biota on the world's deepest seafloor spreading centre. Nat. Commun. 3. https://doi.org/10.1038/ncomms1636

Copley, J.T., Marsh, L., Glover, A.G., Hühnerbach, V., Nye, V.E., Reid, W.D.K., Sweeting, C.J., Wigham, B.D., Wiklund, H., 2016. Ecology and biogeography of megafauna and macrofauna at the first known deep-sea hydrothermal vents on the ultraslow-spreading Southwest Indian Ridge. Sci. Rep. 6. https://doi.org/10.1038/srep39158

Corbalán, A., Nedimović, M.R., Louden, K.E., Cannat, M., Grevemeyer, I., Watremez, L., Leroy, S., 2021. Seismic Velocity Structure Along and Across the Ultraslow-Spreading Southwest Indian Ridge at 64°30'E Showcases Flipping Detachment Faults. J. Geophys. Res. Solid Earth n/a, e2021JB022177. https://doi.org/https://doi.org/10.1029/2021JB022177

Cordier, C., Benoit, M., Hémond, C., Dyment, J., Le Gall, B., Briais, A., Kitazawa, M., 2010. Time scales of melt extraction revealed by distribution of lava composition across a ridge axis. Geochemistry, Geophys. Geosystems 11, Q0AC06. https://doi.org/10.1029/2010GC003074

Corliss, J.B., Dymond, J., Gordon, L.I., Edmond, J.M., Von Herzen, R.P., Ballard, R.D., Green, K., Williams, D., Bainbridge, A., Crane, K., Van Andel, T.H., 1979. Submarine thermal springs on the Galápagos Rift. Science (80-.). 203. https://doi.org/10.1126/science.203.4385.1073

Cowie, P.A., Scholz, C.H., Edwards, M., Malinverno, A., 1993. Fault strain and seismic coupling on mid-ocean ridges. J. Geophys. Res. 98, 17911–17920. https://doi.org/10.1029/93jb01567

Davis, A.S., Clague, D.A., 2000. President Jackson Seamounts, northern Gorda Ridge: Tectonomagmatic relationship between on- and off-axis volcanism. J. Geophys. Res. Solid Earth 105, 27939–27956. https://doi.org/10.1029/2000jb900291

de Martin, B.J., Reves-Sohn, R.A., Canales, J.P., Humphris, S.E., 2007. Kinematics and geometry of active detachment faulting beneath the Trans-Atlantic geotraverse (TAG) hydrothermal field on the Mid-Atlantic Ridge. Geology 35, 711–714. https://doi.org/10.1130/G23718A.1

Demartin, B., Hirth, G., Evans, B., 2004. Experimental constraints on thermal cracking of peridotite at oceanic spreading centers, in: Geophysical Monograph Series. Blackwell Publishing Ltd, pp. 167–185. https://doi.org/10.1029/148GM07

DeMets, C., Gordon, R.G., Argus, D.F., Stein, S., 1994. Effect of recent revisions to the geomagnetic reversal time scale on estimates of current plate motions. Geophys. Res. Lett. 21. https://doi.org/10.1029/94GL02118

Deschamps, A., Tivey, M., Embley, R.W., Chadwick, W.W., 2007. Quantitative study of the deformation at Southern Explorer Ridge using high-resolution bathymetric data. Earth Planet. Sci. Lett. 259, 1–17. https://doi.org/10.1016/j.epsl.2007.04.007

Deschamps, A., Tivey, M.A., Chadwick, W.W., Embley, R.W., 2013. Waning magmatic activity along the Southern Explorer Ridge revealed through fault restoration of rift topography. Geochemistry, Geophys. Geosystems 14, 1609–1625. https://doi.org/10.1002/ggge.20110

Detrick, R.S., Buhl, P., Vera, E., Mutter, J., Orcutt, J., Madsen, J., Brocher, T., 1987. Multi-channel seismic imaging of a crustal magma chamber along the East Pacific Rise. Nature 326, 35–41. https://doi.org/10.1038/326035a0

Detrick, R.S., Mutter, J.C., Buhl, P., Kim, I.I., 1990. No evidence from multichannel reflection data for a crustal magma chamber in the MARK area on the Mid-Atlantic Ridge. Nature 347, 61–64. https://doi.org/10.1038/347061a0

Detrick, R.S., Needham, H.D., Renard, V., 1995. Gravity anomalies and crustal thickness variations along the Mid-Atlantic Ridge between 33°N and 40°N. J. Geophys. Res. Solid Earth 100, 3767–3787. https://doi.org/10.1029/94JB02649

Dick, H.J.B., 1981. Low-angle faulting and steady-state emplacement of plutonic rocks at ridge-transform intersections. EOS Trans. Am. Geophys. Union 62 62, 406.

Dick, H.J.B., Lin, J., Schouten, H., 2003. An ultraslow-spreading class of ocean ridge. Nature 426, 405–412. https://doi.org/10.1038/nature02128

Dick, H.J.B., Natland, J.H., Alt, J.C., Bach, W., Bideau, D., Gee, J.S., Haggas, S., Hertogen, J.G.H., Hirth, G., Holm, P.M., Ildefonse, B., Iturrino, G.J., John, B.E., Kelley, D.S., Kikawa, E., Kingdon, A., Leroux, P.J., Maeda, J., Meyer, P.S., Miller, D.J., Naslund, H.R., Niu, Y.L., Robinson, P.T., Snow, J., Stephen, R.A., Trimby, P.W., Worm, H.U., Yoshinobu, A., 2000. A long in situ section of the lower ocean crust: Results of ODP Leg 176 drilling at the Southwest Indian Ridge. Earth Planet. Sci. Lett. 179. https://doi.org/10.1016/S0012-821X(00)00102-3

Dunn, R.A., Lekić, V., Detrick, R.S., Toomey, D.R., 2005. Three-dimensional seismic structure of the Mid-Atlantic Ridge (35°N): Evidence for focused melt supply and lower crustal dike injection. J. Geophys. Res. Solid Earth 110. https://doi.org/10.1029/2004JB003473

Dunn, R.A., Toomey, D.R., Solomon, S.C., 2000. Three-dimensional seismic structure and physical properties of the crust and shallow mantle beneath the East Pacific Rise at 9°30'N. J. Geophys. Res. Solid Earth 105, 23537–23555. https://doi.org/10.1029/2000JB900210

Dusunur, D., Escartín, J., Combier, V., Seher, T., Crawford, W., Cannat, M., Singh, S.C., Matias, L.M., Miranda, J.M., 2009. Seismological constraints on the thermal structure along the Lucky Strike segment (Mid-Atlantic Ridge) and interaction of tectonic and magmatic processes around the magma chamber. Mar. Geophys. Res. 30, 105–120. https://doi.org/10.1007/s11001-009-9071-3

Dziak, R.P., Haxel, J.H., Bohnenstiehl, D.R., Chadwick, W.W., Nooner, S.L., Fowler, M.J., Matsumoto, H., Butterfield, D.A., 2012. Seismic precursors and magma ascent before the April 2011 eruption at Axial Seamount. Nat. Geosci. 5. https://doi.org/10.1038/ngeo1490

Engels, J.L., Edwards, M.H., Fornari, D.J., Perfit, M.R., Cann, J.R., 2003. A new model for submarine volcanic collapse formation. Geochemistry, Geophys. Geosystems 4, 1077. https://doi.org/10.1029/2002GC000483

Escartín, J., Canales, J.P., 2011. Detachments in Oceanic Lithosphere: Deformation, Magmatism, Fluid Flow, and Ecosystems. Eos, Trans. Am. Geophys. Union 92. https://doi.org/10.1029/2011eo040003

Escartín, J., Cowie, P.A., Searle, R.C., Allerton, S., Mitchell, N.C., MacLeod, C.J., Slootweg, A.P., 1999. Quantifying tectonic strain and magmatic accretion at a slow spreading ridge segment, Mid-Atlantic Ridge, 29°N. J. Geophys. Res. Solid Earth 104, 10421–10437. https://doi.org/10.1029/1998jb900097

Escartín, J., Mével, C., Petersen, S., Bonnemains, D., Cannat, M., Andreani, M., Augustin, N., Bezos, A., Chavagnac, V., Choi, Y., Godard, M., Haaga, K., Hamelin, C., Ildefonse, B., Jamieson, J., John, B., Leleu, T., MacLeod, C.J., Massot-Campos, M., Nomikou, P., Olive, J.A., Paquet, M., Rommevaux, C., Rothenbeck, M., Steinfuhrer, A., Tominaga, M., Triebe, L., Campos, R., Gracias, N., Garcia, R., 2017. Tectonic structure, evolution, and the nature of oceanic core complexes and their detachment fault zones (13°20′N and 13°30′N, Mid Atlantic Ridge). Geochemistry, Geophys. Geosystems 18, 1451–1482. https://doi.org/10.1002/2016GC006775

Escartín, J., Smith, D.K., Cann, J., Schouten, H., Langmuir, C.H., Escrig, S., 2008. Central role of detachment faults in accretion of slow-spreading oceanic lithosphere. Nature 455, 790–794. https://doi.org/10.1038/nature07333

Escartín, J., Soule, S.A., Cannat, M., Fornari, D.J., Düşünür, D., Garcia, R., 2014. Lucky Strike seamount: Implications for the emplacement and rifting of segment-centered volcanoes at slow spreading mid-ocean ridges. Geochemistry, Geophys. Geosystems 15, 4157–4179. https://doi.org/10.1002/2014GC005477

Escartín, J., Soule, S.A., Fornari, D.J., Tivey, M.A., Schouten, H., Perfit, M.R., 2007. Interplay between faults and lava flows in construction of the upper oceanic crust: The East Pacific Rise crest 9°25′–9°58′N. Geochemistry, Geophys. Geosystems 8, Q06005. https://doi.org/10.1029/2006GC001399

Fan, Q., Olive, J.A., Cannat, M., 2021. Thermo-Mechanical State of Ultraslow-Spreading Ridges With a Transient Magma Supply. J. Geophys. Res. Solid Earth 126, e2020JB020557. https://doi.org/10.1029/2020JB020557

Ferrini, V.L., Fornari, D.J., Shank, T.M., Kinsey, J.C., Tivey, M.A., Soule, S.A., Carbotte, S.M., Whitcomb, L.L., Yoerger, D., Howland, J., 2007. Submeter bathymetric mapping of volcanic and hydrothermal features on the East Pacific Rise crest at 9°50′N. Geochemistry, Geophys. Geosystems 8, Q01006. https://doi.org/10.1029/2006GC001333

Fontaine, F.J., Olive, J.A., Cannat, M., Escartin, J., Perol, T., 2011. Hydrothermally-induced melt lens cooling and segmentation along the axis of fast-and intermediate-spreading centers. Geophys. Res. Lett. 38. https://doi.org/10.1029/2011GL047798

Fontaine, F.J., Wilcock, W.S.D., 2007. Two-dimensional numerical models of open-top hydrothermal convection at high Rayleigh and Nusselt numbers: Implications for mid-ocean ridge hydrothermal circulation. Geochemistry, Geophys. Geosystems 8. https://doi.org/10.1029/2007GC001601

Fornari, D.J., 1986. Submarine lava tubes and channels. Bull. Volcanol. 48, 291–298. https://doi.org/10.1007/BF01081757

Fornari, D.J., Haymon, R.M., Perfit, M.R., Gregg, T.K.P., Edwards, M.H., 1998. Axial summit trough of the East Pacific Rice 9°-10°N: Geological characteristics and evolution of the axial zone on fast spreading mid-ocean ridge. J. Geophys. Res. Solid Earth 103, 9827–9855. https://doi.org/10.1029/98JB00028

France, L., Ildefonse, B., Koepke, J., 2009. Interactions between magma and hydrothermal system in Oman ophiolite and in IODP Hole 1256D: Fossilization of a dynamic melt lens at fast spreading ridges. Geochemistry, Geophys. Geosystems 10, Q10O19. https://doi.org/10.1029/2009GC002652

Fundis, A.T., Soule, S.A., Fornari, D.J., Perfit, M.R., 2010. Paving the seafloor: Volcanic emplacement processes during the 2005–2006 eruptions at the fast spreading East Pacific Rise, 9°50′N. Geochemistry, Geophys. Geosystems 11, Q08024. https://doi.org/10.1029/2010GC003058

Georgen, J.E., Lin, J., Dick, H.J.B., 2001. Evidence from gravity anomalies for interactions of the Marion and Bouvet hotspots with the southwest Indian Ridge: Effects of transform offsets. Earth Planet. Sci. Lett. 187. https://doi.org/10.1016/S0012-821X(01)00293-X

Gillis, K.M., 2008. The roof of an axial magma chamber: A hornfelsic heat exchanger. Geology 36, 299–302. https://doi.org/10.1130/G24590A.1

Gregg, T.K.P., Fink, J.H., 1995. Quantification of submarine lava-flow morphology through analog experiments. Geology 23, 73–76. https://doi.org/10.1130/0091-7613(1995)023<0073:QOSLFM>2.3.CO;2

Grevemeyer, I., Hayman, N.W., Lange, D., Peirce, C., Papenberg, C., van Avendonk, H.J.A., Schmid, F., de La Peña, L.G., Dannowski, A., 2019. Constraining the maximum depth of brittle deformation at slow-and ultraslow-spreading ridges using microseismicity. Geology 47, 1069–1073. https://doi.org/10.1130/G46577.1

Grevemeyer, I., Reston, T.J., Moeller, S., 2013. Microseismicity of the Mid-Atlantic Ridge at 7°S-8°15′S and at the Logatchev Massif oceanic core complex at 14°40′N- 14°50′N. Geochemistry, Geophys. Geosystems 14, 3532–3554. https://doi.org/10.1002/ggge.20197

Griffiths, R.W., Fink, J.H., 1992. Solidification and morphology of submarine lavas: a dependence on extrusion rate. J. Geophys. Res. 97. https://doi.org/10.1029/92jb01594

Grindlay, N.R., Madsen, J.A., Rommevaux-Jestin, C., Sclater, J., 1998. A different pattern of ridge segmentation and mantle Bouguer gravity anomalies along the ultra-slow spreading Southwest Indian Ridge (15°30′E to 25°E). Earth Planet. Sci. Lett. 161. https://doi.org/10.1016/s0012-821x(98)00154-x

Gutenberg, B., Richter, C.F., 1944. Frequency of earthquakes in California. Bull. Seismol. Soc. Am. 34, 185–188.

Hardebeck, J.L., Shearer, P.M., 2002. A new method for determining first-motion focal mechanisms. Bull. Seismol. Soc. Am. 92. https://doi.org/10.1785/0120010200

Harding, A.J., 1989. Structure of young oceanic crust at 13°N on the East Pacific Rise from expanding spread profiles. J. Geophys. Res. 94, 12163–12196. https://doi.org/10.1029/jb094ib09p12163

Harding, A.J., Kent, G.M., Orcutt, J.A., 1993. A multichannel seismic investigation of upper crustal structure at 9°N on the East Pacific Rise: implications for crustal accretion. J. Geophys. Res. 98. https://doi.org/10.1029/93jb00886

Hasenclever, J., Theissen-Krah, S., Rüpke, L.H., Morgan, J.P., Iyer, K., Petersen, S., Devey, C.W., 2014. Hybrid shallow on-axis and deep off-axis hydrothermal circulation at fast-spreading ridges. Nature 508. https://doi.org/10.1038/nature13174

Havskov, J., Ottemöller, L., 1999. SeisAn earthquake analysis software. Seismol. Res. Lett. 70, 532–534. https://doi.org/10.1785/gssrl.70.5.532

Haymon, R.M., Fornari, D.J., Von Damm, K.L., Lilley, M.D., Perfit, M.R., Edmond, J.M., Shanks, W.C., Lutz, R.A., Grebmeier, J.M., Carbotte, S., Wright, D., McLaughlin, E., Smith, M., Beedle, N., Olson, E., 1993. Volcanic eruption of the mid-ocean ridge along the East Pacific Rise crest at 9°45-52′N: Direct submersible observations of seafloor phenomena associated with an eruption event in April, 1991. Earth Planet. Sci. Lett. 119. https://doi.org/10.1016/0012-821X(93)90008-W

Head, J.W., Wilson, L., Smith, D.K., 1996. Mid-ocean ridge eruptive vent morphology and substructure: Evidence for dike widths, eruption rates, and evolution of eruptions and axial volcanic ridges. J. Geophys. Res. B Solid Earth 101. https://doi.org/10.1029/96jb02275

Hess, H.H., 1962. History of Ocean Basins, Petrologic Studies. https://doi.org/10.1130/petrologic.1962.599

Holzbecher, E.O., 1998. Modeling Density-Driven Flow in Porous Media, Modeling Density-Driven Flow in Porous Media. https://doi.org/10.1007/978-3-642-58767-2

Hooft, E.E.E., Detrick, R.S., Toomey, D.R., Collins, J.A., Lin, J., 2000. Crustal thickness and structure along three contrasting spreading segments of the Mid-Atlantic Ridge, 33.5°-35°N. J. Geophys. Res. Solid Earth 105, 8205–8226. https://doi.org/10.1029/1999jb900442

Horner-Johnson, B.C., Gordon, R.G., Cowles, S.M., Argus, D.F., 2005. The angular velocity of Nubia relative to Somalia and the location of the Nubia-Somalia-Antarctica triple junction. Geophys. J. Int. 162, 221–238. https://doi.org/10.1111/j.1365-246X.2005.02608.x

Horning, G., Sohn, R.A., Canales, J.P., Dunn, R.A., 2018. Local Seismicity of the Rainbow Massif on the Mid-Atlantic Ridge. J. Geophys. Res. Solid Earth 123, 1615–1630. https://doi.org/10.1002/2017JB015288

Howell, S.M., Ito, G., Behn, M.D., Martinez, F., Olive, J.-A., Escartín, J., 2016. Magmatic and tectonic extension at the Chile Ridge: Evidence for mantle controls on ridge segmentation. Geochemistry, Geophys. Geosystems 17, 2354–2373. https://doi.org/10.1002/2016GC006380

Humphris, S.E., Fornari, D.J., Scheirer, D.S., German, C.R., Parson, L.M., 2002. Geotectonic setting of hydrothermal activity on the summit of Lucky Strike Seamount (37°17′N, Mid-Atlantic Ridge). Geochemistry, Geophys. Geosystems 3, 1–25. https://doi.org/10.1029/2001gc000284

Ildefonse, B., Blackman, D.K., John, B.E., Ohara, Y., Miller, D.J., MacLeod, C.J., Abe, N., Abratis, M., Andal, E.S., Andréani, M., Awaji, S., Beard, J.S., Brunelli, D., Charney, A.B., Christie, D.M., Delacour, A.G., Delius, H., Drouin, M., Einaudi, F., Escartin, J., Frost, B.R., Fryer, P.B., Gee, J.S., Godard, M., Grimes, C.B., Halfpenny, A., Hansen, H.E., Harris, A.C., Hayman, N.W., Hellebrand, E., Hirose, T., Hirth, J.G., Ishimaru, S., Johnson, K.T.M., Karner, G.D., Linek, M., Maeda, J., Mason, O.U., McCaig, A.M., Michibayashi, K., Morris, A., Nakagawa, T., Nozaka, T., Rosner, M., Searle, R.C., Suhr, G., Tamura, A., Tominaga, M., von der Handt, A., Yamasaki, T., Zhao, X., 2007. Oceanic core complexes and crustal accretion at slow-speading ridges. Geology 35. https://doi.org/10.1130/G23531A.1

Illsley-Kemp, F., Keir, D., Bull, J.M., Ayele, A., Hammond, J.O.S., Kendall, J.M., Gallacher, R.J., Gernon, T., Goitom, B., 2017. Local earthquake magnitude scale and b-value for the Danakil region of northern afar. Bull. Seismol. Soc. Am. 107. https://doi.org/10.1785/0120150253

Jian, H., Chen, Y.J., Singh, S.C., Li, J., Zhao, M., Ruan, A., Qiu, X., 2017a. Seismic structure and magmatic construction of crust at the ultraslow-spreading Southwest Indian Ridge at 50°28’E. J. Geophys. Res. Solid Earth 122, 18–42. https://doi.org/10.1002/2016JB013377

Jian, H., Singh, S.C., Chen, Y.J., Li, J., 2017b. Evidence of an axial magma chamber beneath the ultraslowspreading Southwest Indian Ridge. Geology 45, 143–146. https://doi.org/10.1130/G38356.1

Jokat, W., Ritzmann, O., Schmidt-Aursch, M.C., Drachev, S., Gauger, S., Snow, J., 2003. Geophysical evidence for reduced melt production on the Arctic ultraslow Gakkel mid-ocean ridge. Nature 423, 962–965. https://doi.org/10.1038/nature01706

Jupp, T., Schultz, A., 2000. A thermodynamic explanation for black smoker temperatures. Nature 403. https://doi.org/10.1038/35002552

Jupp, T.E., Schultz, A., 2004. Physical balances in subseafloor hydrothermal convection cells. J. Geophys. Res. Solid Earth 109. https://doi.org/10.1029/2003JB002697

Karson, J.A., Dick, H.J.B., 1983. Tectonics of ridge-transform intersections at the Kane fracture zone. Mar. Geophys. Res. 6. https://doi.org/10.1007/BF00300398

Karson, J.A., Lawrence, R.M., 1997. Tectonic setting of serpentinite exposures on the western median valley wall of the MARK area in the vicinity of Site 920, in: Proceedings of the Ocean Drilling Program, 153 Scientific Results. https://doi.org/10.2973/odp.proc.sr.153.001.1997

Keir, D., Stuart, G.W., Jackson, A., Ayele, A., 2006. Local earthquake magnitude scale and seismicity rate for the Ethiopian rift. Bull. Seismol. Soc. Am. 96. https://doi.org/10.1785/0120060051

Kennish, M.J., Lutz, R.A., 1998. Morphology and distribution of lava flows on mid-ocean ridges: a review. Earth Sci. Rev. https://doi.org/10.1016/S0012-8252(98)00006-3

Kissling, E., Ellsworth, W.L., Eberhart-Phillips, D., Kradolfer, U., 1994. Initial reference models in local earthquake tomography. J. Geophys. Res. 99, 19635–19646. https://doi.org/10.1029/93jb03138

Klein, E.M., White, S.M., Nunnery, J.A., Mason-Stack, J.L., Wanless, V.D., Perfit, M.R., Waters, C.L., Sims, K.W.W., Fornari, D.J., Zaino, A.J., Ridley, W.I., 2013. Seafloor photo-geology and sonar terrain modeling at the 9°N overlapping spreading center, East Pacific Rise. Geochemistry, Geophys. Geosystems 14, 5146–5170. https://doi.org/10.1002/2013GC004858

Klischies, M., Petersen, S., Devey, C.W., 2019. Geological mapping of the Menez Gwen segment at 37°50′N on the Mid-Atlantic Ridge: Implications for accretion mechanisms and associated hydrothermal activity at slow-spreading mid-ocean ridges. Mar. Geol. 412, 107–122. https://doi.org/10.1016/j.margeo.2019.03.012

Kong, L.S.L., Solomon, S.C., Purdy, G.M., 1992. Microearthquake characteristics of a mid-ocean ridge along-axis high. J. Geophys. Res. 97. https://doi.org/10.1029/91JB02566

Korger, E.I.M., Schlindwein, V., 2013. Seismicity and structure of the 85°E volcanic complex at the ultraslow spreading gakkel ridge from local earthquake tomography. Geophys. J. Int. 196. https://doi.org/10.1093/gji/ggt390

Koschinsky, A., Garbe-Schönberg, D., Sander, S., Schmidt, K., Gennerich, H.H., Strauss, H., 2008. Hydrothermal venting at pressure-temperature conditions above the critical point of seawater, 5°S on the Mid-Atlantic Ridge. Geology 36. https://doi.org/10.1130/G24726A.1

Krischer, L., 2015. hypoDDpy: hypoDDpy 1.0. https://doi.org/10.5281/ZENODO.18907

Kuo, B.Y., Forsyth, D.W., 1988. Gravity anomalies of the ridge-transform system in the South Atlantic between 31 and 34.5° S: Upwelling centers and variations in crustal thickness. Mar. Geophys. Res. 10, 205–232. https://doi.org/10.1007/BF00310065

Kurras, G.J., Fornari, D.J., Edwards, M.H., Perfit, M.R., Smith, M.C., 2000. Volcanic morphology of the East Pacific Rise crest 9 49′–52′: implications for volcanic emplacement processes at fast-spreading mid-ocean ridges. Mar. Geophys. Res. 21, 23–41. https://doi.org/10.1023/A:1004792202764

Langmuir, C., Humphris, S., Fornari, D., Van Dover, C., Von Damm, K., Tivey, M.K., Colodner, D., Charlou, J.L., Desonie, D., Wilson, C., Fouquet, Y., Klinkhammer, G., Bougault, H., 1997. Hydrothermal vents near a mantle hot spot: The Lucky Strike vent field at 37°N on the Mid-Atlantic Ridge. Earth Planet. Sci. Lett. 148. https://doi.org/10.1016/s0012-821x(97)00027-7

Lavier, L.L., Buck, W.R., Poliakov, A.N.B., 1999. Self-consistent rolling-hinge model for the evolution of large-offset low-angle normal faults. Geology 27, 1127–1130. https://doi.org/10.1130/0091-7613(1999)027<1127:SCRHMF>2.3.CO;2

Le Saout, M., Thibaud, R., Gente, P., 2018. Detailed Analysis of Near Tectonic Features Along the East Pacific Rise at 16°N, Near the Mathematician Hot Spot. J. Geophys. Res. Solid Earth 123, 4478–4499. https://doi.org/10.1029/2017JB015301

Li, J., Huang, X.-L., Li, X.-H., Chu, F.-Y., Zhu, J.-H., Zhu, Z.-M., Wang, H., 2021. Anomalously hot mantle source beneath the Dragon Flag Supersegment of the

Southwest Indian Ridge: New evidence from crystallisation temperatures of mid-ocean ridge basalts. Lithos 396–397, 106221. https://doi.org/10.1016/j.lithos.2021.106221

Li, J., Jian, H., Chen, Y.J., Singh, S.C., Ruan, A., Qiu, X., Zhao, M., Wang, X., Niu, X., Ni, J., Zhang, J., 2015. Seismic observation of an extremely magmatic accretion at the ultraslow spreading Southwest Indian Ridge. Geophys. Res. Lett. 42, 2656–2663. https://doi.org/10.1002/2014GL062521

Li, W., Jin, Z., Li, H., Tao, C., 2017. High water content in primitive mid-ocean ridge basalt from Southwest Indian Ridge (51.56ºE): Implications for recycled hydrous component in the mantle. J. Earth Sci. 28, 411–421. https://doi.org/10.1007/s12583-017-0731-y

Lin, J., Purdy, G.M., Schouten, H., Sempere, J.-C., Zervas, C., 1990. Evidence from gravity data for focused magmatic accretion along the Mid-Atlantic Ridge. Nature 344, 627–632. https://doi.org/10.1038/344627a0

Lissenberg, C.J., MacLeod, C.J., Bennett, E.N., 2019. Consequences of a crystal mush-dominated magma plumbing system: A mid-ocean ridge perspective. Philos. Trans. R. Soc. A Math. Phys. Eng. Sci. 377. https://doi.org/10.1098/rsta.2018.0014

Lister, C.R.B., 1974. On the Penetration of Water into Hot Rock. Geophys. J. R. Astron. Soc. 39. https://doi.org/10.1111/j.1365-246X.1974.tb05468.x

Liu, C., Li, J., Tao, C., Fan, Q., Song, J., Luo, Y., Feng, B., 2020. Variations in faulting style of the Southwest Indian Ridge (46°–53.5°E): Implications for crustal accretion process at ultraslow-spreading ridges. Tectonophysics 790, 228552. https://doi.org/10.1016/j.tecto.2020.228552

Liu, X., Wang, S., Zhang, D., Cao, J., Wang, H., 2016. Sounding data quality assessment method and result of high-resolution bathymetric sidescan sonar system, in: OCEANS 2016 - Shanghai. Institute of Electrical and Electronics Engineers Inc. https://doi.org/10.1109/OCEANSAP.2016.7485446

Liu, Z., Buck, W.R., 2020. Global Trends of Axial Relief and Faulting at Plate Spreading Centers Imply Discrete Magmatic Events. J. Geophys. Res. Solid Earth 125. https://doi.org/10.1029/2020JB019465

Lomax, A., Virieux, J., Volant, P., Berge-Thierry, C., 2000. Probabilistic Earthquake Location in 3D and Layered Models. Springer, Dordrecht, pp. 101–134. https://doi.org/10.1007/978-94-015-9536-0_5

Lonsdale, P., 1977. Clustering of suspension-feeding macrobenthos near abyssal hydrothermal vents at oceanic spreading centers. Deep. Res. 24. https://doi.org/10.1016/0146-6291(77)90478-7

Lowell, R.P., 1991. Modeling continental and submarine hydrothermal systems. Rev. Geophys. https://doi.org/10.1029/91RG01080

Lowell, R.P., Farough, A., Hoover, J., Cummings, K., 2013. Characteristics of magma-driven hydrothermal systems at oceanic spreading centers. Geochemistry, Geophys. Geosystems 14. https://doi.org/10.1002/ggge.20109

Lowell, R.P., Germanovich, L.N., 2004. Hydrothermal processes at mid-ocean ridges: Results from scale analysis and single-pass models, in: Geophysical Monograph Series. Blackwell Publishing Ltd, pp. 219–244. https://doi.org/10.1029/148GM09

Lowell, R.P., Rona, P.A., Von Herzen, R.P., 1995. Seafloor hydrothermal systems. J. Geophys. Res. 100. https://doi.org/10.1029/94JB02222

Lucazeau, F., 2019. Analysis and Mapping of an Updated Terrestrial Heat Flow Data Set. Geochemistry, Geophys. Geosystems 20. https://doi.org/10.1029/2019GC008389

Macdonald, K.C., 1982. Mid-Ocean Ridges: Fine Scale Tectonic, Volcanic and Hydrothermal Processes Within the Plate Boundary Zone. Annu. Rev. Earth Planet. Sci. 10, 155–190. https://doi.org/10.1146/annurev.ea.10.050182.001103

Macdonald, K.C., Fox, P.J., Perram, L.J., Eisen, M.F., Haymon, R.M., Miller, S.P., Carbotte, S.M., Cormier, M.H., Shor, A.N., 1988. A new view of the mid-ocean ridge from the behaviour of ridge-axis discontinuities. Nature. https://doi.org/10.1038/335217a0

Macdonald, K.C., Luyendyk, B.P., 1977. Deep-tow studies of the structure of the Mid-Atlantic Ridge crest near lat 37°N. GSA Bull. 88, 621–636. https://doi.org/10.1130/0016-7606(1977)88<621:DSOTSO>2.0.CO;2

Macdonald, K.C., Scheirer, D.S., Carbotte, S.M., 1991. Mid-ocean ridges: Discontinuities, segments and giant cracks. Science (80-.). 253, 986–994. https://doi.org/10.1126/science.253.5023.986

MacLeod, C.J., Searle, R.C., Murton, B.J., Casey, J.F., Mallows, C., Unsworth, S.C., Achenbach, K.L., Harris, M., 2009. Life cycle of oceanic core complexes. Earth Planet. Sci. Lett. 287, 333–344. https://doi.org/10.1016/j.epsl.2009.08.016

Manning, C.E., MacLeod, C.J., Weston, P.E., 2000. Lower-crustal cracking front at fast-spreading ridges: Evidence from the East Pacific Rise and the Oman ophiolite. Spec. Pap. Geol. Soc. Am. 349. https://doi.org/10.1130/0-8137-2349-3.261

Marjanović, M., Carbotte, S.M., Carton, H., Nedimović, M.R., Mutter, J.C., Canales, J.P., 2014. A multi-sill magma plumbing system beneath the axis of the East Pacific Rise. Nat. Geosci. 7, 825–829. https://doi.org/10.1038/ngeo2272

McCaig, A.M., Cliff, R.A., Escartin, J., Fallick, A.E., MacLeod, C.J., 2007. Oceanic detachment faults focus very large volumes of black smoker fluids. Geology 35. https://doi.org/10.1130/G23657A.1

McClinton, J.T., White, S.M., 2015. Emplacement of submarine lava flow fields: A geomorphological model from the Niños eruption at the Galápagos Spreading Center. Geochemistry, Geophys. Geosystems 16, 899–911. https://doi.org/10.1002/2014GC005632

McClinton, T., White, S.M., Colman, A., Sinton, J.M., 2013. Reconstructing lava flow emplacement processes at the hot spot-affected Galápagos Spreading Center, 95°W and 92°W. Geochemistry, Geophys. Geosystems 14, 2731–2756. https://doi.org/10.1002/ggge.20157

McKenzie, D., Jackson, J., Priestley, K., 2005. Thermal structure of oceanic and continental lithosphere. Earth Planet. Sci. Lett. 233. https://doi.org/10.1016/j.epsl.2005.02.005

Meier, M., Schlindwein, V., 2018. First In Situ Seismic Record of Spreading Events at the Ultraslow Spreading Southwest Indian Ridge. Geophys. Res. Lett. 45, 10,360-10,368. https://doi.org/10.1029/2018GL079928

Meier, M., Schlindwein, V., Scholz, J.R., Geils, J., Schmidt-Aursch, M.C., Krüger, F., Czuba, W., Janik, T., 2021. Segment-Scale Seismicity of the Ultraslow Spreading Knipovich Ridge. Geochemistry, Geophys. Geosystems 22. https://doi.org/10.1029/2020GC009375

Mendel, V., Sauter, D., Rommevaux-Jestin, C., Patriat, P., Lefebvre, F., Parson, L.M., 2003. Magmato-tectonic cyclicity at the ultra-slow spreading Southwest Indian Ridge:

Evidence from variations of axial volcanic ridge morphology and abyssal hills pattern. Geochemistry, Geophys. Geosystems 4, 9102. https://doi.org/10.1029/2002GC000417

Mével, C., 2003. Serpentinisation des péridotites abysales aux dorsales océaniques. Comptes Rendus - Geosci. 335, 825–852. https://doi.org/10.1016/j.crte.2003.08.006

Meyer, J.D., White, S.M., 2007. Lava morphology mapping by expert system classification of high-resolution side-scan sonar imagery from the East Pacific Rise, 9°-10°N. Mar. Geophys. Res. 28, 81–93. https://doi.org/10.1007/s11001-007-9015-8

Minshull, T.A., Muller, M.R., White, R.S., 2006. Crustal structure of the Southwest Indian Ridge at 66°E: Seismic constraints. Geophys. J. Int. 166, 135–147. https://doi.org/10.1111/j.1365-246X.2006.03001.x

Momoh, E., Cannat, M., Leroy, S., 2020. Internal Structure of the Oceanic Lithosphere at a Melt-Starved Ultraslow-Spreading Mid-Ocean Ridge: Insights From 2-D Seismic Data. Geochemistry, Geophys. Geosystems 21. https://doi.org/10.1029/2019GC008540

Momoh, E., Cannat, M., Watremez, L., Leroy, S., Singh, S.C., 2017. Quasi-3-D Seismic Reflection Imaging and Wide-Angle Velocity Structure of Nearly Amagmatic Oceanic Lithosphere at the Ultraslow-Spreading Southwest Indian Ridge. J. Geophys. Res. Solid Earth 122, 9511–9533. https://doi.org/10.1002/2017JB014754

Moore, J.G., 1975. Mechanism of Formation of Pillow Lava: Pillow lava, produced as fluid lava cools underwater, is the most abundant volcanic rock on earth, but only recently have divers observed it forming, American Scientist.

Nicolas, A., Boudier, F., France, L., 2009. Subsidence in magma chamber and the development of magmatic foliation in Oman ophiolite gabbros. Earth Planet. Sci. Lett. 284. https://doi.org/10.1016/j.epsl.2009.04.012

Nicolas, A., Boudier, F., Koepke, J., France, L., Ildefonse, B., Mevel, C., 2008. Root zone of the sheeted dike complex in the Oman ophiolite. Geochemistry, Geophys. Geosystems 9. https://doi.org/10.1029/2007GC001918

Niu, X., Ruan, A., Li, J., Minshull, T.A., Sauter, D., Wu, Z., Qiu, X., Zhao, M., Chen, Y.J., Singh, S., 2015. Along-axis variation in crustal thickness at the ultraslow spreading Southwest Indian Ridge (50°E) from a wide-angle seismic experiment. Geochemistry, Geophys. Geosystems 16, 468–485. https://doi.org/10.1002/2014GC005645

Olive, J.-A., Crone, T.J., 2018. Smoke Without Fire: How Long Can Thermal Cracking Sustain Hydrothermal Circulation in the Absence of Magmatic Heat? J. Geophys. Res. Solid Earth 123. https://doi.org/10.1029/2017JB014900

Olive, J.A., Dublanchet, P., 2020. Controls on the magmatic fraction of extension at mid-ocean ridges. Earth Planet. Sci. Lett. 549, 116541. https://doi.org/10.1016/j.epsl.2020.116541

Panagiotakis, C., Kokinou, E., 2015. Linear pattern detection of geological faults via a topology and shape optimization method. IEEE J. Sel. Top. Appl. Earth Obs. Remote Sens. 8, 3–11. https://doi.org/10.1109/JSTARS.2014.2363080

Parnell-Turner, R., Sohn, R.A., Peirce, C., Reston, T.J., Macleod, C.J., Searle, R.C., Simão, N.M., 2017. Oceanic detachment faults generate compression in extension 45. https://doi.org/10.1130/G39232.1

Parnell-Turner, R., Sohn, R.A., Peirce, C., Reston, T.J., MacLeod, C.J., Searle, R.C., Simão, N.M., 2020. Seismicity trends and detachment fault structure at 13°N, Mid-Atlantic

Ridge. Geology XXX–XXX. https://doi.org/10.1130/g48420.1

Parson, L.M., Murton, B.J., Searle, R.C., Booth, D., Evans, J., Field, P., Keeton, J., Laughton, A., McAllister, E., Millard, N., Redbourne, L., Rouse, I., Shor, A., Smith, D., Spencer, S., Summerhayes, C., Walker, C., 1993. En echelon axial volcanic ridges at the Reykjanes Ridge: a life cycle of volcanism and tectonics. Earth Planet. Sci. Lett. 117, 73–87. https://doi.org/10.1016/0012-821X(93)90118-S

Patriat, P., Segoufin, J., 1988. Reconstruction of the Central Indian Ocean. Tectonophysics 155. https://doi.org/10.1016/0040-1951(88)90267-3

Patriat, P., Sloan, H., Sauter, D., 2008. From slow to ultraslow: A previously undetected event at the Southwest Indian Ridge at ca. 24 Ma. Geology 36, 207–210. https://doi.org/10.1130/G24270A.1

Penrose, 1972. Penrose field conference on ophiolites. Geotimes 17, 24–25.

Perfit, M.R., Chadwick, W.W., 1998. Magmatism at mid-ocean ridges: Constraints from volcanological and geochemical investigations. Geophys. Monogr. Ser. 106, 59–115. https://doi.org/10.1029/GM106p0059

Perfit, M.R., Soule, S.A., 2016. Submarine Lava Types, in: Harff, J., Meschede, M., Petersen, S., Thiede, Jö. (Eds.), Encyclopedia of Marine Geosciences. Springer Netherlands, Dordrecht, pp. 808–817. https://doi.org/10.1007/978-94-007-6238-1_22

Phipps Morgan, J., Chen, Y.J., 1993a. Dependence of ridge-axis morphology on magma supply and spreading rate. Nature 364, 706–708. https://doi.org/10.1038/364706a0

Phipps Morgan, J., Chen, Y.J., 1993b. The genesis of oceanic crust: Magma injection, hydrothermal circulation, and crustal flow. J. Geophys. Res. Solid Earth 98, 6283–6297. https://doi.org/10.1029/92JB02650

Pitzer, K.S., Peiper, J.C., Busey, R.H., 1984. Thermodynamic Properties of Aqueous Sodium Chloride Solutions. J. Phys. Chem. Ref. Data 13. https://doi.org/10.1063/1.555709

Pontbriand, C.W., Sohn, R.A., 2014. Microearthquake evidence for reaction-driven cracking within the Trans-Atlantic Geotraverse active hydrothermal deposit. J. Geophys. Res. Solid Earth 119. https://doi.org/10.1002/2013JB010110

Pontbriand, C.W., Soule, S.A., Sohn, R.A., Humphris, S.E., Kunz, C., Singh, H., Nakamura, K.I., Jakobsson, M., Shank, T., 2012. Effusive and explosive volcanism on the ultraslow-spreading Gakkel Ridge, 85°E. Geochemistry, Geophys. Geosystems 13, Q10005. https://doi.org/10.1029/2012GC004187

Rabinowicz, M., Toplis, M.J., 2009. Melt Segregation in the Lower Part of the Partially Molten Mantle Zone beneath an Oceanic Spreading Centre: Numerical Modelling of the Combined Effects of Shear Segregation and Compaction. J. Petrol. 50, 1071–1106. https://doi.org/10.1093/petrology/egp033

Raitt, R.W., 1963. The crustal rocks. Sea 3, 84–102.

Reston, T., 2018. Flipping detachments: The kinematics of ultraslow spreading ridges. Earth Planet. Sci. Lett. 503, 144–157. https://doi.org/10.1016/j.epsl.2018.09.032

Reston, T.J., Ranero, C.R., 2012. The 3-D geometry of detachment faulting at mid-ocean ridges. Geochemistry, Geophys. Geosystems 12. https://doi.org/10.1029/2011GC003666

Richter, C.F., 1935. An instrumental earthquake magnitude scale [WWW Document]. Bull. Seismol. Soc. Am. URL https://pubs.geoscienceworld.org/ssa/bssa/articleabstract/25/1/1/115102/An-instrumental-earthquake-magnitude-scale (accessed 12.26.20).

Rioux, M., Cheadle, M.J., John, B.E., Bowring, S.A., 2016. The temporal and spatial distribution of magmatism during lower crustal accretion at an ultraslow-spreading ridge: High-precision U–Pb zircon dating of ODP Holes 735B and 1105A, Atlantis Bank, Southwest Indian Ridge. Earth Planet. Sci. Lett. 449. https://doi.org/10.1016/j.epsl.2016.05.047

Rommevaux-Jestin, C., Deplus, C., Patriat, P., 1997. Mantle Bouguer Anomaly along an ultra slow-spreading ridge: Implications for accretionary processes and comparison with results from central Mid-Atlantic Ridge. Mar. Geophys. Res. https://doi.org/10.1023/A:1004269003009

Rubin, A.M., Pollard, D.D., 1988. Dike-induced faulting in rift zones of Iceland and Afar. Geology 16, 413–417. https://doi.org/10.1130/0091-7613(1988)016<0413:DIFIRZ>2.3.CO;2

Sauter, D., Cannat, M., 2010. The ultraslow spreading Southwest Indian Ridge. pp. 153–173. https://doi.org/10.1029/2008GM000843

Sauter, D., Cannat, M., Meyzen, C., Bezos, A., Patriat, P., Humler, E., Debayle, E., 2009. Propagation of a melting anomaly along the ultraslow Southwest Indian Ridge between 46°E and 52°20′E: Interaction with the Crozet hotspot? Geophys. J. Int. 179, 687–699. https://doi.org/10.1111/j.1365-246X.2009.04308.x

Sauter, D., Cannat, M., Rouméjon, S., Andreani, M., Birot, D., Bronner, A., Brunelli, D., Carlut, J., Delacour, A., Guyader, V., MacLeod, C.J., Manatschal, G., Mendel, V., Ménez, B., Pasini, V., Ruellan, E., Searle, R., 2013. Continuous exhumation of mantle-derived rocks at the Southwest Indian Ridge for 11 million years. Nat. Geosci. 6, 314–320. https://doi.org/10.1038/ngeo1771

Sauter, D., Parson, L., Mendel, V., Rommevaux-Jestin, C., Gomez, O., Briais, A., Mével, C., Tamaki, K., 2002. TOBI sidescan sonar imagery of the very slow-spreading Southwest Indian Ridge: Evidence for along-axis magma distribution. Earth Planet. Sci. Lett. 199, 81–95. https://doi.org/10.1016/S0012-821X(02)00543-5

Sauter, D., Patriat, P., Rommevaux-Jestin, C., Cannat, M., Briais, A., 2001. The Southwest Indian Ridge between 49° 15′E and 57°E: Focused accretion and magma redistribution. Earth Planet. Sci. Lett. 192, 303–317. https://doi.org/10.1016/S0012-821X(01)00455-1

Schlindwein, V., Schmid, F., 2016. Mid-ocean-ridge seismicity reveals extreme types of ocean lithosphere. Nature 535, 276–279. https://doi.org/10.1038/nature18277

Schouten, H., Klitgord, K.D., 1982. The memory of the accreting plate boundary and the continuity of fracture zones. Earth Planet. Sci. Lett. 59, 255–266. https://doi.org/10.1016/0012-821X(82)90130-3

Schouten, H., Klitgord, K.D., Whitehead, J.A., 1985. Segmentation of mid-ocean ridges. Nature 317, 225–229. https://doi.org/10.1038/317225a0

Schweitzer, J., 2001. HYPOSAT — An Enhanced Routine to Locate Seismic Events BT - Monitoring the Comprehensive Nuclear-Test-Ban Treaty: Sourse Location, in: Ringdal, F., Kennett, B.L.N. (Eds.), . Birkhäuser Basel, Basel, pp. 277–289. https://doi.org/10.1007/978-3-0348-8250-7_17

Searle, R.C., Cannat, M., Fujioka, K., Mével, C., Fujimoto, H., Bralee, A., Parson, L., 2003.

FUJI Dome: A large detachment fault near 64°E on the very slow-spreading southwest Indian Ridge. Geochemistry, Geophys. Geosystems 4. https://doi.org/10.1029/2003GC000519

Searle, R.C., Escartín, J., 2004. The rheology and morphology of oceanic lithosphere and mid-ocean ridges, in: Geophysical Monograph Series. https://doi.org/10.1029/148GM03

Searle, R.C., Murton, B.J., Achenbach, K., LeBas, T., Tivey, M., Yeo, I., Cormier, M.H., Carlut, J., Ferreira, P., Mallows, C., Morris, K., Schroth, N., van Calsteren, P., Waters, C., 2010. Structure and development of an axial volcanic ridge: Mid-Atlantic Ridge, 45°N. Earth Planet. Sci. Lett. 299, 228–241. https://doi.org/10.1016/j.epsl.2010.09.003

Seher, T., Crawford, W.C., Singh, S.C., Cannat, M., Combier, V., Dusunur, D., 2010. Crustal velocity structure of the Lucky Strike segment of the Mid-Atlantic Ridge at 37°n from seismic refraction measurements. J. Geophys. Res. Solid Earth 115. https://doi.org/10.1029/2009JB006650

Sempéré, J.-C., Purdy, G.M., Schouten, H., 1990. Segmentation of the Mid-Atlantic Ridge between 24° N and 30°40’ N. Nature 344, 427–431. https://doi.org/10.1038/344427a0

Sempéré, J.C., Lin, J., Brown, H.S., Schouten, H., Purdy, G.M., 1993. Segmentation and morphotectonic variations along a slow-spreading center: The Mid-Atlantic Ridge (24°00′ N- 30°40′ N). Mar. Geophys. Res. 15, 153–200. https://doi.org/10.1007/BF01204232

Seton, M., Müller, R.D., Zahirovic, S., Williams, S., Wright, N.M., Cannon, J., Whittaker, J., Matthews, K.J., McGirr, R., 2020. A global dataset of present-day oceanic crustal age and seafloor spreading parameters. Geochemistry, Geophys. Geosystems. https://doi.org/10.1029/2020gc009214

Singh, S.C., Crawford, W.C., Carton, H., Seher, T., Combier, V., Cannat, M., Canales, J.P., Düsünür, D., Escartin, J., Miranda, J.M., 2006. Discovery of a magma chamber and faults beneath a Mid-Atlantic Ridge hydrothermal field. Nature 442, 1029–1032. https://doi.org/10.1038/nature05105

Sinha, M.C., Navin, D.A., Macgregor, L.M., Constable, S., Peirce, C., White, A., Heinson, G., Inglis, M.A., 1997. Evidence for accumulated melt beneath the slow-spreading Mid-Atlantic Ridge. Philos. Trans. R. Soc. A Math. Phys. Eng. Sci. 355. https://doi.org/10.1098/rsta.1997.0008

Sinton, J., Bergmanis, E., Rubin, K., Batiza, R., Gregg, T.K.P., Grönvold, K., Macdonald, K.C., White, S.M., 2002. Volcanic eruptions on mid-ocean ridges: New evidence from the superfast spreading East Pacific Rise, 17°–19°S. J. Geophys. Res. 107, 2115. https://doi.org/10.1029/2000JB000090

Sinton, J., Detrick, R., Canales, J.P., Ito, G., Behn, M., 2003. Morphology and segmentation of the western Galápagos spreading center, 90.5°-98°W: Plume-ridge interaction at an intermediate spreading ridge. Geochemistry, Geophys. Geosystems 4. https://doi.org/10.1029/2003GC000609

Sinton, J.M., Detrick, R.S., 1992. Mid-ocean ridge magma chambers. J. Geophys. Res. 97, 197. https://doi.org/10.1029/91JB02508

Small, C., 1998. Global systematics of mid-ocean ridge morphology, in: Geophysical Monograph Series. https://doi.org/10.1029/GM106p0001

Smith, D.K., Cann, J.R., 1992. The role of seamount volcanism in crustal construction at the

Mid-Atlantic Ridge (24°-30°N). J. Geophys. Res. Solid Earth 97, 1645–1658. https://doi.org/10.1029/91JB02507

Smith, D.K., Cann, J.R., 1990. Hundreds of small volcanoes on the median valley floor of the Mid-Atlantic Ridge at 24-30°N. Nature 348, 152–155. https://doi.org/10.1038/348152a0

Smith, D.K., Cann, J.R., Dougherty, M.E., Lin, J., Spencer, S., MacLeod, C., Keeton, J., McAllister, E., Brooks, B., Pascoe, R., Robertson, W., 1995. Mid-Atlantic Ridge volcanism from deep-towed side-scan sonar images, 25 °-29 °N. J. Volcanol. Geotherm. Res. 67, 233–262. https://doi.org/10.1016/0377-0273(94)00086-V

Smith, D.K., Cann, J.R., Escartín, J., 2006. Widespread active detachment faulting and core complex formation near 13°N on the Mid-Atlantic Ridge. Nature 442. https://doi.org/10.1038/nature04950

Smith, D.K., Escartín, J., Schouten, H., Cann, J.R., 2008a. Fault rotation and core complex formation: Significant processes in seafloor formation at slow-spreading mid-ocean ridges (Mid-Atlantic Ridge, 13°-15°N). Geochemistry, Geophys. Geosystems 9. https://doi.org/10.1029/2007GC001699

Smith, D.K., Escartín, J., Schouten, H., Cann, J.R., 2008b. Fault rotation and core complex formation: Significant processes in seafloor formation at slow-spreading mid-ocean ridges (Mid-Atlantic Ridge, 13°-15°N). Geochemistry, Geophys. Geosystems 9. https://doi.org/10.1029/2007GC001699

Smith, D.K., Jordan, T.H., 1988. Seamount statistics in the Pacific Ocean. J. Geophys. Res. 93. https://doi.org/10.1029/jb093ib04p02899

Snoke, J., Munsey, J., Teague, A., Bollinger, G., 1984. A program for focal mechanism determination by combined use of polarity and SV-P amplitude ratio data. Earthq. notes 55, 15.

Soule, S.A., 2015. Mid-Ocean Ridge Volcanism, in: The Encyclopedia of Volcanoes. Elsevier, pp. 395–403. https://doi.org/10.1016/b978-0-12-385938-9.00021-3

Soule, S.A., Escartín, J., Fornari, D.J., 2009. A record of eruption and intrusion at a fast spreading ridge axis: Axial summit trough of the East Pacific Rise at 9–10°N. Geochemistry, Geophys. Geosystems 10. https://doi.org/10.1029/2008GC002354

Soule, S.A., Fornari, D.J., Perfit, M.R., Rubin, K.H., 2007. New insights into mid-ocean ridge volcanic processes from the 2005–2006 eruption of the East Pacific Rise, 9°46′N–9°56′N. Geology 35, 1079–1082. https://doi.org/10.1130/G23924A.1

Soule, S.A., Fornari, D.J., Perfit, M.R., Tivey, M.A., Ridley, W.I., Schouten, H., 2005. Channelized lava flows at the East Pacific Rise crest 9°–10°N: The importance of off-axis lava transport in developing the architecture of young oceanic crust. Geochemistry, Geophys. Geosystems 6. https://doi.org/10.1029/2005GC000912

Spudich, P., Orcutt, J., 1980. A new look at the seismic velocity structure of the oceanic crust. Rev. Geophys. https://doi.org/10.1029/RG018i003p00627

Stakes, D.S., Perfit, M.R., Tivey, M.A., Caress, D.W., Ramirez, T.M., Maher, N., 2006. The Cleft revealed: Geologic, magnetic, and morphologic evidence for construction of upper oceanic crust along the southern Juan de Fuca Ridge. Geochemistry, Geophys. Geosystems 7, Q04003. https://doi.org/10.1029/2005GC001038

Standish, J.J., Sims, K.W.W., 2010. Young off-axis volcanism along the ultraslow-spreading Southwest Indian Ridge. Nat. Geosci. 3, 286–292. https://doi.org/10.1038/ngeo824

Stein, C.A., Stein, S., 1994. Constraints on hydrothermal heat flux through the oceanic lithosphere from global heat flow. J. Geophys. Res. 99. https://doi.org/10.1029/93JB02222

Takeuchi, C.S., Sclater, J.G., Grindlay, N.R., Madsen, J.A., Rommevaux-Jestin, C., 2010. Segment-scale and intrasegment lithospheric thickness and melt variations near the Andrew Bain megatransform fault and Marion hot spot: Southwest Indian Ridge, 25.5°E-35°E. Geochemistry, Geophys. Geosystems 11, n/a-n/a. https://doi.org/10.1029/2010GC003054

Tan, Y.J., Tolstoy, M., Waldhauser, F., Wilcock, W.S.D., 2016. Dynamics of a seafloor-spreading episode at the East Pacific Rise. Nature 540, 261–265. https://doi.org/10.1038/nature20116

Tao, C., Li, H., Jin, X., Zhou, J., Wu, T., He, Y., Deng, X., Gu, C., Zhang, G., Liu, W., 2014. Seafloor hydrothermal activity and polymetallic sulfide exploration on the southwest Indian ridge. Chinese Sci. Bull. https://doi.org/10.1007/s11434-014-0182-0

Tao, C., Lin, J., Guo, S., Chen, Y.J., Wu, G., Han, X., German, C.R., Yoerger, D.R., Zhou, N., Li, H., Su, X., Zhu, J., 2012. First active hydrothermal vents on an ultraslow-spreading center: Southwest Indian Ridge. Geology 40, 47–50. https://doi.org/10.1130/G32389.1

Tao, C., Seyfried, W.E., Lowell, R.P., Liu, Y., Liang, J., Guo, Z., Ding, K., Zhang, H., Liu, J., Qiu, L., Egorov, I., Liao, S., Zhao, M., Zhou, J., Deng, X., Li, H., Wang, H., Cai, W., Zhang, G., Zhou, H., Lin, J., Li, W., 2020. Deep high-temperature hydrothermal circulation in a detachment faulting system on the ultra-slow spreading ridge. Nat. Commun. 11, 1–9. https://doi.org/10.1038/s41467-020-15062-w

Thébault, E., Finlay, C.C., Beggan, C.D., Alken, P., Aubert, J., Barrois, O., Bertrand, F., Bondar, T., Boness, A., Brocco, L., Canet, E., Chambodut, A., Chulliat, A., Coïsson, P., Civet, F., Du, A., Fournier, A., Fratter, I., Gillet, N., Hamilton, B., Hamoudi, M., Hulot, G., Jager, T., Korte, M., Kuang, W., Lalanne, X., Langlais, B., Léger, J.M., Lesur, V., Lowes, F.J., Macmillan, S., Mandea, M., Manoj, C., Maus, S., Olsen, N., Petrov, V., Ridley, V., Rother, M., Sabaka, T.J., Saturnino, D., Schachtschneider, R., Sirol, O., Tangborn, A., Thomson, A., Tøffner-Clausen, L., Vigneron, P., Wardinski, I., Zvereva, T., 2015. International geomagnetic reference field: The 12th generation international geomagnetic reference field - The twelfth generation. Earth, Planets Sp. 67, 79. https://doi.org/10.1186/s40623-015-0228-9

Theissen-Krah, S., Iyer, K., Rüpke, L.H., Morgan, J.P., 2011. Coupled mechanical and hydrothermal modeling of crustal accretion at intermediate to fast spreading ridges. Earth Planet. Sci. Lett. 311. https://doi.org/10.1016/j.epsl.2011.09.018

Tilmann, F., Flueh, E., Planert, L., Reston, T., Weinrebe, W., 2004. Microearthquake seismicity of the Mid-Atlantic Ridge at 5°S: A view of tectonic extension. J. Geophys. Res. Solid Earth 109. https://doi.org/10.1029/2003JB002827

Tolstoy, M., Waldhauser, F., Bohnenstiehl, D.R., Weekly, R.T., Kim, W.-Y.Y., 2008. Seismic identification of along-axis hydrothermal flow on the East Pacific Rise. Nature 451, 181. https://doi.org/10.1038/nature06424

Tucholke, B.E., Behn, M.D., Buck, W.R., Lin, J., 2008. Role of melt supply in oceanic detachment faulting and formation of megamullions. Geology 36, 455–458. https://doi.org/10.1130/G24639A.1

Tucholke, B.E., Fujioka, K., Ishihara, T., Hirth, G., Kinoshita, M., 2001. Submersible study of an oceanic megamullion in the central North Atlantic. J. Geophys. Res. Solid Earth 106. https://doi.org/10.1029/2001jb000373

Waldhauser, F., Ellsworth, W.L., 2000. A Double-difference Earthquake location algorithm: Method and application to the Northern Hayward Fault, California. Bull. Seismol. Soc. Am. 90, 1353–1368. https://doi.org/10.1785/0120000006

Wang-Pin Chen, Molnar, P., 1983. Focal depths of intracontinental and intraplate earthquakes and their implications for the thermal and mechanical properties of the lithosphere. J. Geophys. Res. 88. https://doi.org/10.1029/jb088ib05p04183

Wang, J., Zhou, H., Salters, V.J.M., Dick, H.J.B., Standish, J.J., Wang, C., 2020. Trace element and isotopic evidence for recycled lithosphere from basalts from 48 to 53°E, Southwest Indian Ridge. J. Petrol. 61. https://doi.org/10.1093/petrology/egaa068

Wang, W., Kelley, K.A., Li, Z., Chu, F., Dong, Yunpeng, Chen, L., Dong, Yanhui, Li, J., 2021. Volatile element evidence of local MORB mantle heterogeneity beneath the Southwest Indian Ridge, 48-51°E. Geochemistry, Geophys. Geosystems e2021GC009647. https://doi.org/10.1029/2021GC009647

Weatherall, P., Marks, K.M., Jakobsson, M., Schmitt, T., Tani, S., Arndt, J.E., Rovere, M., Chayes, D., Ferrini, V., Wigley, R., 2015. A new digital bathymetric model of the world's oceans. Earth Sp. Sci. 2, 331–345. https://doi.org/10.1002/2015EA000107

Wessel, P., Luis, J.F., Uieda, L., Scharroo, R., Wobbe, F., Smith, W.H.F., Tian, D., 2019. The Generic Mapping Tools Version 6. Geochemistry, Geophys. Geosystems 20. https://doi.org/10.1029/2019GC008515

White, R.S., McKenzie, D., O'Nions, R.K., 1992. Oceanic crustal thickness from seismic measurements and rare earth element inversions. J. Geophys. Res. 97. https://doi.org/10.1029/92jb01749

White, S.M., Haymon, R.M., Fornari, D.J., Perfit, M.R., Macdonald, K.C., 2002. Correlation between volcanic and tectonic segmentation of fast-spreading ridges: Evidence from volcanic structures and lava flow morphology on the East Pacific Rise at 9°–10°N. J. Geophys. Res. Solid Earth 107, EPM 7-1-EPM 7-20. https://doi.org/10.1029/2001JB000571

White, S.M., Mason, J.L., Macdonald, K.C., Perfit, M.R., Wanless, V.D., Klein, E.M., 2009. Significance of widespread low effusion rate eruptions over the past two million years for delivery of magma to the overlapping spreading centers at 9°N East Pacific Rise. Earth Planet. Sci. Lett. 280, 175–184. https://doi.org/10.1016/j.epsl.2009.01.030

Wiens, D.A., Stein, S., 1983. Age dependence of oceanic intraplate seismicity and implications for lithospheric evolution. J. Geophys. Res. 88. https://doi.org/10.1029/JB088iB08p06455

Wilcock, W.S.D., Delaney, J.R., 1996. Mid-ocean ridge sulfide deposits: Evidence for heat extraction from magma chambers or cracking fronts? Earth Planet. Sci. Lett. 145. https://doi.org/10.1016/s0012-821x(96)00195-1

Wilcock, W.S.D., Hooft, E.E.E., Toomey, D.R., McGill, P.R., Barclay, A.H., Stakes, D.S., Ramirez, T.M., 2009. The role of magma injection in localizing black-smoker activity. Nat. Geosci. https://doi.org/10.1038/ngeo550

Wilcock, W.S.D., Tolstoy, M., Waldhauser, F., Garcia, C., Tan, Y.J., Bohnenstiehl, D.R., Caplan-Auerbach, J., Dziak, R.P., Arnulf, A.F., Mann, M.E., 2016. Seismic constraints on caldera dynamics from the 2015 Axial Seamount eruption. Science (80-.). 354, 1395–1399. https://doi.org/10.1126/science.aah5563

Wolfe, C.J., Purdy, G.M., Toomey, D.R., Solomon, S.C., 1995. Microearthquake characteristics and crustal velocity structure at 29°N on the Mid-Atlantic Ridge: the architecture of a slow spreading segment. J. Geophys. Res. 100. https://doi.org/10.1029/95jb02399

Wu, T., Tao, C., Zhang, J., Wang, A., Zhang, G., Zhou, J., Deng, X., 2019. A hydrothermal investigation system for the Qianlong-II autonomous underwater vehicle. Acta Oceanol. Sin. 38, 159–165. https://doi.org/10.1007/s13131-019-1408-4

Yang, A.Y., Zhao, T.P., Zhou, M.F., Deng, X.G., 2017. Isotopically enriched N-MORB: A new geochemical signature of off-axis plume-ridge interaction—A case study at 50°28′E, Southwest Indian Ridge. J. Geophys. Res. Solid Earth 122, 191–213. https://doi.org/10.1002/2016JB013284

Yang, W., Tao, C., Li, H., Liang, J., Liao, S., Long, J., Ma, Z., Wang, L., 2017. 230Th/238U dating of hydrothermal sulfides from Duanqiao hydrothermal field, Southwest Indian Ridge. Mar. Geophys. Res. 38, 71–83. https://doi.org/10.1007/s11001-016-9279-y

Yeo, I., Searle, R.C., Achenbach, K.L., Le Bas, T.P., Murton, B.J., 2012. Eruptive hummocks: Building blocks of the upper ocean crust. Geology 40, 91–94. https://doi.org/10.1130/G31892.1

Yeo, I.A., 2012. Detailed studies of mid-ocean ridge volcanism at the Mid-Atlantic Ridge (45° N) and elsewhere. Durham theses. Durham University. Available at Durham E-Theses Online: http://etheses.dur.ac.uk/4944/.

Yeo, I.A., Searle, R.C., 2013. High-resolution Remotely Operated Vehicle (ROV) mapping of a slow-spreading ridge: Mid-Atlantic Ridge 45°N. Geochemistry, Geophys. Geosystems 14, 1693–1702. https://doi.org/10.1002/ggge.20082

Yu, X., Dick, H.J.B., 2020. Plate-driven micro-hotspots and the evolution of the Dragon Flag melting anomaly, Southwest Indian Ridge. Earth Planet. Sci. Lett. 531, 116002. https://doi.org/10.1016/j.epsl.2019.116002

Yu, Z., Li, J., Niu, X., Rawlinson, N., Ruan, A., Wang, W., Hu, H., Wei, X., Zhang, J., Liang, Y., 2018. Lithospheric Structure and Tectonic Processes Constrained by Microearthquake Activity at the Central Ultraslow-Spreading Southwest Indian Ridge (49.2° to 50.8°E). J. Geophys. Res. Solid Earth 123, 6247–6262. https://doi.org/10.1029/2017JB015367

Yue, X., Li, H., Ren, J., Tao, C., Zhou, J., Wang, Y., Lü, X., 2019. Seafloor hydrothermal activity along mid-ocean ridge with strong melt supply: study from segment 27, southwest Indian ridge. Sci. Rep. 9, 9874. https://doi.org/10.1038/s41598-019-46299-1

Zhang, T., Lin, J., Gao, J.Y., 2013. Magmatism and tectonic processes in Area A hydrothermal vent on the Southwest Indian Ridge. Sci. China Earth Sci. 56, 2186–2197. https://doi.org/10.1007/s11430-013-4630-5

Zhao, D., Hasegawa, A., Horiuchi, S., 1992. Tomographic imaging of P and S wave velocity structure beneath northeastern Japan. J. Geophys. Res. 97. https://doi.org/10.1029/92jb00603

Zhao, M., Qiu, X., Li, J., Sauter, D., Ruan, A., Chen, J., Cannat, M., Singh, S., Zhang, J., Wu, Z., Niu, X., 2013. Three-dimensional seismic structure of the Dragon Flag oceanic core complex at the ultraslow spreading Southwest Indian Ridge (49°39′E). Geochemistry, Geophys. Geosystems 14, 4544–4563. https://doi.org/10.1002/ggge.20264